



# BALTEX

## Baltic Sea Experiment

---

World Climate Research Programme / Global Energy and Water Cycle Experiment  
WCRP GEWEX

---

**BALTEX-BASIS**  
**Final Report**  
**MAS3-CT97-0117 Contract with EC**



Jouko Launiainen and Timo Vihma  
(Editors)

---

International BALTEX Secretariat  
Publication No. 19  
May 2001

International BALTEX Secretariat  
GKSS Research Center  
Max Planck Straße  
D-21502 Geesthacht  
Germany  
Phone: +49 4152 87 1536  
Fax: +49 4152 87 2020  
e-mail: [baltex@gkss.de](mailto:baltex@gkss.de)



**BALTEX-BASIS**  
**Final Report**  
**MAS3-CT97-0117 Contract with EC**

Jouko Launiainen and Timo Vihma  
(Editors)

**Coordinator:**

Finnish Institute of Marine Research (FIMR)

**Partners:**

Universität Hamburg, Meteorologisches Institut, Germany (UHAM)

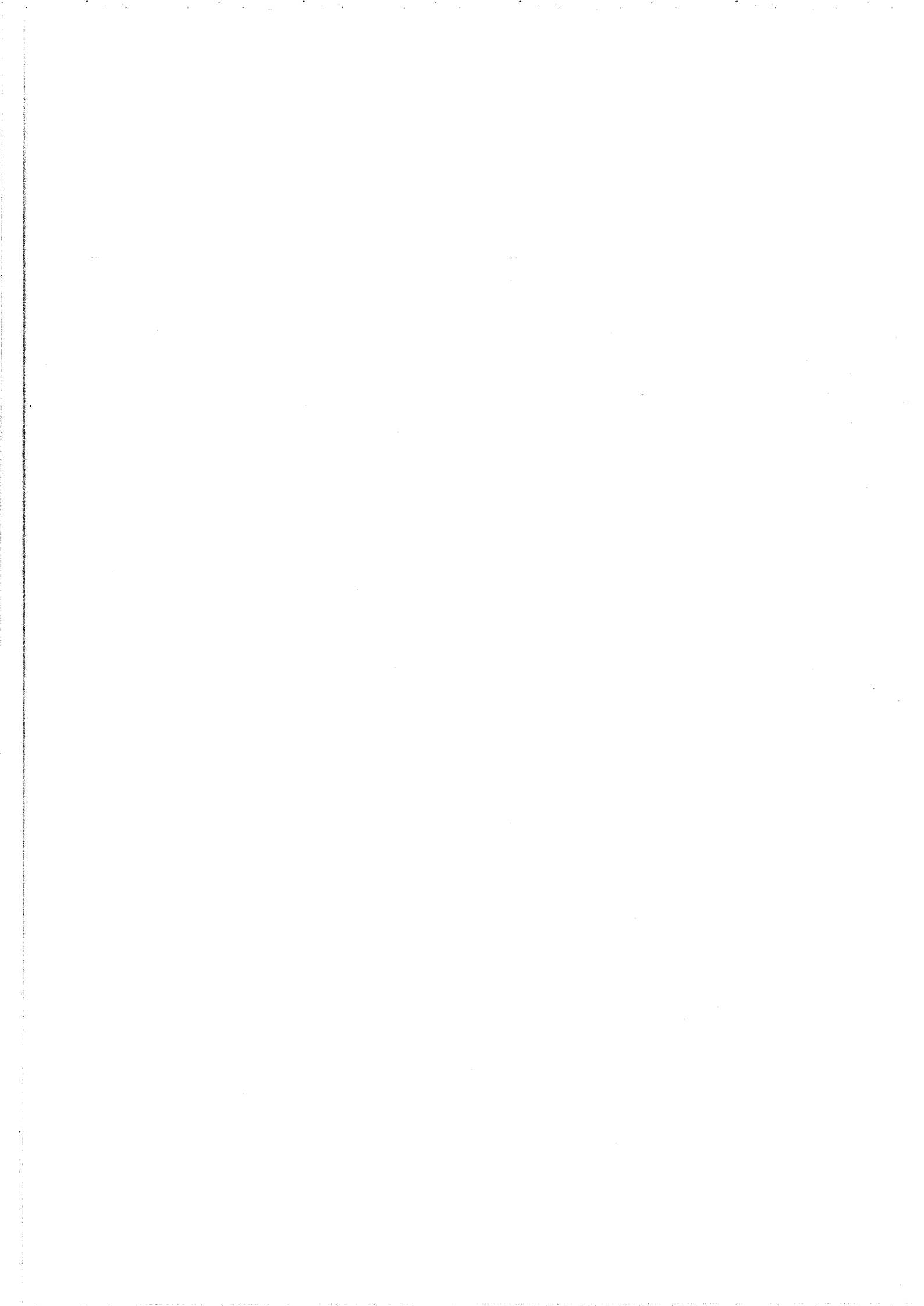
Universität Hannover, Inst. für Meteorologie und Klimatologie, Germany (UHAN)

Uppsala University, Dept. of Earth Sciences and Meteorology, Sweden (UUPP)

Swedish Meteorological and Hydrological Institute, Sweden (SMHI)

Chalmers Univ. of Technol., Dept. of Radio and Space Sci., Sweden (CUT, assoc. contr. to SMHI)

University of Hokkaido. (UHOK, subcontractor to FIMR).



## Preface

The Baltic Sea is located in a region with a seasonal ice cover forming and melting each year. As for the winter navigation, sea ice is of first-rate importance to various Baltic Sea countries and sea ice has a climatic importance as a sensitive indicator of a climatic change. In the Baltic Air-Sea-Ice Study (BALTEX-BASIS) marine meteorological, sea ice and oceanographic studies were carried out in order to study physical processes, parametrizations and modelling. The final goal is the optimization of coupled atmosphere-ocean models used in marine meteorological and ice navigation services. BALTEX-BASIS was carried out by Finnish, Swedish, German and Japanese institutes as an EC-supported project in 1997-2000. The overall objective of BALTEX-BASIS was:

- *to create and analyse an experimental data set for optimization and verification of coupled atmosphere-ice-ocean models.*

The main field experiment was carried out in the Gulf of Bothnia, Baltic Sea, in February-March, 1998. The experiment and the data are introduced in detail in the BALTEX-BASIS Data Report (BALTEX Secretariat, Publ. No. 14, Geestacht, Germany, 1999, 94p).

The specific objectives based on the BALTEX-BASIS joint data covered investigations of:


- atmospheric boundary layer (ABL), especially close to the sea ice margin
- momentum and thermal interaction at the air-ice-sea interfaces
- sea ice and its dynamics
- ocean boundary layer (OBL)
- ocean water and heat budget.

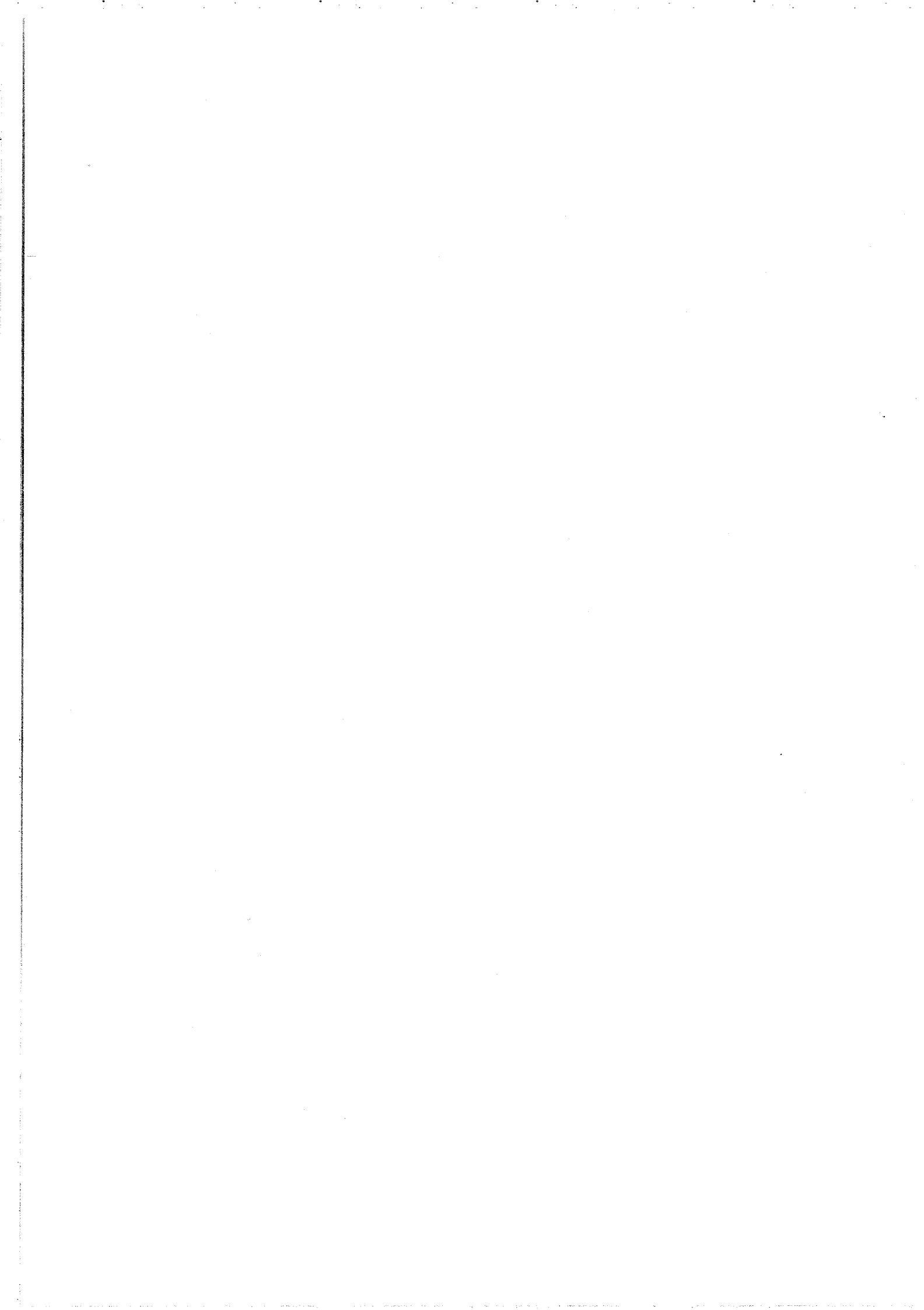
The field observations, process studies and modelling result in validation and development of coupled atmosphere-ice-ocean models.

This report summarizes the most prominent results gained in the project. In addition, various specific and more advanced studies are still in progress and we foresee still various reports based on BALTEX-BASIS data to be published in a couple of next years. Finally, we are happy to report that during the project the cooperation between various international scientists and institutions was exemplary good.

Helsinki, 26 January, 2001

  
Jouko Launiainen

  
Timo Vihma



## Executive Summary

The Baltic Air-Sea-Ice Study (BASIS) was a sub-project of BALTEX. The overall objective of the project was to create and analyse an experimental data set for verification and optimization of coupled atmosphere-ice-ocean models. The field campaign in February-March, 1998, formed the central experimental element. Observations were centered in the boundary zone between the open and ice-covered sea in the northern Baltic Sea. The aim was to gather meteorological, sea ice and hydrographic data to quantify the physical processes of energy and mass transfer between the atmosphere and the sea ice and the sea. An ice-going *R/V Aranda* (Finland) served as the central basis and platform in the sea. Airborne measurements were made by both a research aircraft and a helicopter. Several surface meteorological stations and buoys were used. The observations covered atmospheric turbulence, radiation, and clouds. Radiosonde soundings were made at five stations at the coasts of the Gulf of Bothnia. The sea ice was investigated by remote sensing, drifting buoys and surface-based measurements. The ocean boundary layer turbulence was investigated by measuring eddy fluxes below the ice.

The BASIS-98 experiment and the data are introduced in the BASIS Data Report (BALTEX Secretariat, Publ. No. 14, Geestacht, Germany, 1999, 94p.).

The data analyses in BASIS concentrated in three main branches: (1) the atmospheric boundary layer (ABL), (2) the ice and surface properties, and (3) the ocean boundary layer (OBL). Process oriented modelling was made applying the field data as a reference. A summary of the most essential results reads as follows.

The analyses of the atmospheric surface-layer turbulence indicated that the normalized standard deviations of the wind components increased during strong stability, and showed that the wall effect is important for the turbulence structure in the stable surface layer. The analyses of the stable boundary-layer depth agreed with new theoretical predictions.

Profile and turbulence measurements over the sea ice confirmed the validity of the Monin-Obukhov similarity theory, and suggested to a new formula for the ratio of local roughness lengths for momentum and heat. The ratio depends on the local roughness Reynolds number. The analyses further yielded a new formula for the flux-profile relationships in stable stratification. Different methods to determine the ice surface temperature, based on radiation, turbulence and profile measurements, were compared and the comparison demonstrated the applicability of a thermodynamic ice model in estimating the surface temperature and surface fluxes. The model was also fairly accurate in reproducing the temporal development of the temperature profile in the ice and snow in conditions of varying weather.

The airborne, land-based, and ice-based observations of the turbulent and radiative fluxes in the atmospheric surface layer showed a good agreement. The study revealed significant spatial and temporal variations in the surface fluxes which depended on the large-scale weather conditions and on the state of the surface, i.e. open water, compact land-fast sea ice, or broken sea ice. The spatial distribution of the net radiation flux depended even more on the inhomogeneous cloud fields. The spatial variability detected by the aircraft showed that area-representative fluxes for the whole ice edge zone cannot be derived from land-fast ice stations only.

The aircraft data were applied in parameterizing the turbulent surface fluxes over a broken ice cover. The analyses revealed that in order to get realistic area-averaged fluxes, the roughness lengths for heat and moisture must be 3 to 4 orders of magnitude smaller than the roughness length for momentum. The data were gathered from heights comparable to the lowest grid level of regional models, and the results are therefore considered applicable for such models (e.g. European HIRLAM and REMO). In conditions of stable stratification the lowest model level may often lie above the constant-flux layer, and the flux-divergence should be taken into account as reduced roughness lengths.

The BASIS observations of the ABL were compared with the analyses and 24-h forecasts of the regional model HIRLAM. The rawinsonde sounding data demonstrated that the differences were largest during passages of cold and warm fronts. The differences were largest near the surface, and the vertical gradients of air temperature and wind speed were smaller in HIRLAM than in the observations. The comparisons based on aircraft observations indicated some cases in which the HIRLAM surface temperature, wind speed and direction were strongly biased and the latent heat flux was unrealistically

large. In HIRLAM, particularly in the 24-h forecasts, the low-level jets (LLJs) were less common than in the observations. This may have resulted from a boundary-layer parameterization producing too much mixing. A mesoscale modelling study supported this conclusion.

Most of the analyses of the ABL were related to a stable or near-neutral boundary layer. A convective boundary layer was addressed in detail in two cases. In one case, the warm sea surface generated an ice-breeze, a mesoscale circulation resembling the classical land-breeze. The ice-breeze was also reproduced by a numerical model. In the second case a cold-air outbreak from over the sea ice to the open sea was documented by an aircraft flight mission and studied by applying two models. In the mesoscale modelling, it was important to take into account the leads among the sea ice, the counter-gradient transport of heat, a forest in an archipelago crossed by the air flow, and the water vapour condensation into ice crystals. In the large-eddy model simulation, the convection was mostly resolved by the model grid.

The analyses of the ice and surface properties concentrated on ice motion, ice and open ocean remote sensing, and snow influence in the ice thickness. The remote sensing and ice drifter data gathered demonstrated how useful a combined data set can be. It provides information on ice kinematics, ice leads and ice concentrations, which are of a great value for coupled air-ice-sea model verification. The ice drifter data showed a velocity variance found typical in semi-enclosed basins with seasonal ice cover, whereas the radar image data show closing and opening of leads and where ice deformation takes place.

The study of the wind forcing on the ice drift showed that in the centre of the Gulf of Bothnia the ice drift was highly wind-dependent, and a linear relationship between the wind and drift velocities explained 80% of the drift's variance. Close to the coast, internal ice stresses were important, and the modelling of the ice motion was only successful by using a high-resolution (5 km) model with a realistic ice rheology. In general, an improvement in the model results brought by using an accurate wind stress, depending on the thermal stratification and ice conditions, was comparable to that achieved by raising the grid resolution from 18 to 5 km.

An algorithm for determining sea ice concentration from Radarsat SAR was developed. The algorithm is based on local thresholds, which are partly manually extracted. The algorithm resolves the ice concentration with a resolution of 50 metres, and yielded good results for cases over the Gulf of Bothnia during the BASIS experiment.

The water and heat cycles of the Bothnian Bay were examined on the basis of observations and by using the model PROBE-Baltic. Observed and numerically simulated data from an 18-year period (1981-1998) were analyzed. The results can be summarized as follows. (1) The calculated long-term salinity and temperature structure are stable and in good agreement with observations. (2) The calculated ice concentration and thickness during the BASIS period were rather close to observations. (3) The Bothnian Bay water body heat balance during the BASIS period showed high temporal variation and with major contributions from the sensible heat flux, latent heat flux and net longwave radiation from the open water surface. (4) During the BASIS period the solar radiation as well as the heat flow from water to ice cannot be neglected in the heat balance. (5) From the heat balance calculations it was concluded that on long term mean the Bothnian Bay import heat from the Bothnian Sea.

The eddy-flux measurements below the ice revealed that the momentum flux at the depth of 5 m from the ice was ten times larger than that at the depth of 0.5 m, and the heat flux from the water to the ice was very small. Both the findings indicated an existence of a shallow very stable boundary layer just below the ice. This is likely to be related to inflow of river water into the sea below the sea ice. The small water-ice heat flux differs from the basin-scale analysis reported above, and demonstrates that spatial differences may be large not only in the ABL but also in the ocean boundary layer.

The BALTEX-BASIS study was financially supported by the European Commission under the Contract MAS3-CT97-0117.



TABLE OF CONTENTS	Page
PREFACE	
<b>EXECUTIVE SUMMARY</b>	1
<b>1. INTRODUCTION</b>	5
1.1 Physical Motivation and Aims	5
1.2 Tasks	6
1.3 Project Organization	7
<b>2. FIELD EXPERIMENT</b>	8
2.1 General layout of the field experiment	8
2.2 Ice Station	11
2.3 Airborne and Remote Sensing Observations	11
2.4 Coastal and Land-Fast Ice Stations	11
2.5 Pre- and Past-Intensive Period Hydrographic Monitoring, Other Operations	13
<b>3. ATMOSPHERIC BOUNDARY LAYER</b>	14
Surface-Layer Turbulence and the Structure of the Atmospheric Boundary-Layer <i>Ann-Sofi Smedman, Ulf Andre, Magnus Carlsson, Ulf Högström, Mikael Magnusson, Jutta Rost, and Sergej Zilitinkevich</i>	14
Turbulent Surface Fluxes and Air-Ice Coupling <i>Jouko Launiainen, Bin Cheng, Juha Uotila, and Timo Vihma</i>	42
Temporal and Spatial Variability of Surface Fluxes over the Ice Edge Zone in the Northern Baltic Sea <i>Burghard Brümmner, David Schröder, Jouko Launiainen, Timo Vihma, Ann-Sofi Smedman, and Mikael Magnusson</i>	55
On the Parameterization of Turbulent Surface Fluxes over Broken Sea Ice <i>Timo Vihma, David Schröder, Agathe Kerber, and Burghard Brümmner</i>	82
Evaluation of Radiosounding Data and Aircraft Observations in Comparison to HIRLAM Model Results <i>Anette Ganske, Dieter Etling, and David Schröder</i>	95
<b>4. ICE AND SURFACE PROPERTIES</b>	114
Sea Ice Concentration Derived from Radarsat Data <i>Maria Lundin</i>	114
BASIS Study of Wind Speed from SAR Images <i>Jan Askne, Nils Gustafsson, Bertil Håkansson, and Stephane Mugnier-Pollet</i>	119

Sea Ice Kinematics Using Argos Buoys and SAR Imagery <i>Bertil Håkansson, Sverre Dokken, and Juha Uotila</i>	127
Observed and Modelled Sea-Ice Response to Wind Forcing in the Northern Baltic Sea <i>Juha Uotila</i>	133
Modelling of Snow Influence on Land-Fast Ice Thickness <i>Maria Lundin</i>	154
<b>5. OCEAN BOUNDARY LAYER</b>	161
Modelling the Bothnian Bay Water and Heat Balance: the BALTEX-BASIS Experiment <i>Anders Omstedt</i>	161
Eddy Flux Measurements below Ice and Oceanic Boundary Layer (OBL) Studies <i>Kunio Shirasawa and Kunio Kobinata, and Toshiyuki Kawamura</i>	170
<b>6. MODELLING</b>	179
Modelling of Sea Ice Thermodynamics <i>Bin Cheng, Jouko Launiainen, Timo Vihma, Juha Uotila</i>	179
Case Studies of On-Ice and Off-Ice Air Flow Over the Gulf of Bothnia <i>Timo Vihma and Burghard Brümmer</i>	190
Large-Eddy-Simulation of an Off-Ice Airflow Case <i>Dieter Etling, G. Harbusch and Burghard Brümmer</i>	200
Three-Dimensional Mesoscale Modelling in BASIS <i>Mikael Magnusson</i>	204
<b>7. SUMMARY</b>	210
<b>8. DATA ARCHIEVE</b>	214
<b>9. LIST OF PUBLICATIONS</b>	217

# 1. INTRODUCTION

## 1.1 Physical Motivation and Aims

The Baltic Air-Sea-Ice Study (BALTEX-BASIS) was a sub-project of the Baltic Sea Experiment (BALTEX). BALTEX is a program of GEWEX/WCRP, and explores, models and quantifies the main physical processes that control the energy and water exchange within the Baltic Sea and its drainage area. The project BASIS aimed at an improved understanding of the energy and water cycles during winter conditions by conducting a versatile air-ice-sea experiment in the Baltic Sea. BASIS was carried out in 1997-2000, during which the winter experiment in 1998 formed the central element. A pilot experiment was organized in March 1997, and a past-experiment in March 1999. BASIS had cooperation with the Northern Hemisphere Climate-Processes Land-Surface Experiment (NOPEX) and its winter experiment (WINTEX).

The Baltic Sea is a semi-enclosed sea located in the seasonal sea ice zone with an ice cover forming and melting each year, at least in the northern areas. By acting as a thermal insulator and a mechanical cover, the sea ice strongly influences the air-sea exchange of energy, water and momentum, and prominently affects to weather and meteorological conditions. Since the sea ice is typically less than 1 m thick, its presence and extent are highly sensitive indicators to a climate change. Considering the winter navigation, sea ice is of practical importance to various countries, and therefore has major economical influences.

The overall objective of the BASIS was

- to create and analyse an experimental data set for optimization and verification of coupled atmosphere-ice-ocean models.

The specific objectives covered

- a) Investigation of the physical structure of the atmospheric boundary layer (ABL), especially close to the sea ice margin.*
- b) Investigation of momentum and thermal interaction and water budget at the air-ice, air-sea and sea-ice boundaries.*
- c) Investigation of the physical structure of the ocean boundary layer (OBL).*
- d) Validation of coupled atmosphere-ice-ocean models.*

## 1.2 Tasks

The project was divided into four Tasks with subtasks:

### *Task 1. Atmospheric boundary layer*

- Task 1.1            Airborne measurements  
Objective: to measure the horizontal and vertical profiles of the air temperature and humidity, wind speed and direction, cloud properties, turbulent fluxes and radiation
- 1.2                Ground-based measurements  
to measure at five coastal sites the vertical profiles of the air temperature and humidity, wind speed and direction
- 1.3                Ship/Ice-based measurements  
to measure over the sea ice the turbulent and radiative fluxes and vertical profiles of the air temperature and humidity, wind speed and direction
- 1.4                ABL process studies  
to study the ABL structure, air-ice, and air-sea interaction processes on the basis of the field data obtained in Tasks 1.1-1.3.

### *Task 2. Ice and surface properties*

- Task 2.1            Sea ice concentration and movement  
Objective: to measure the sea ice concentration and its changes during the field experiment over the Gulf of Bothnia, and to detect the ice movement
- 2.2                Ice and snow properties, surface topography and roughness  
to measure the distribution of the ice and snow thickness, water content, temperature, and salinity, as well as that of the surface topography and roughness
- 2.3                Ice and surface process studies  
to study the role of ice and snow in the processes controlling the air-ice-sea exchange of momentum, heat and moisture.

### *Task 3. Ocean boundary layer*

- Task 3.1            Hydrographic and current measurements  
Objective: to measure the large-scale temperature and salinity distribution in the Gulf of Bothnia, the currents below the ice, and the temperature profiles below the ice and in the open sea
- 3.2                Eddy flux measurements  
to measure the turbulent fluxes of momentum, heat and salt below the ice.
- 3.3                OBL process studies  
to study the OBL structure, ice-sea, and air-sea interaction processes on the basis of the field data obtained in Tasks 3.1 and 3.2.

### *Task 4. Modelling Activities*

Objective: to model the physical processes during the experiment for planning and logistical purposes. In the study phase, models will be verified against the experimental data, and models will finally be improved and optimized with the analyzed project data sets.

The scale of the various experiments varied from microscale to meso- $\gamma$ -scale, i.e. the spatial scale from  $10^{-1}$  m to  $10^2$  km and the temporal scale from minutes to days.

The detailed research plan including the studies to be made by the data was defined in the Technical Annex of the Contract MAS3-CT97-0117 of EC.

The overall project investigation approach is given in Figure 2.1.

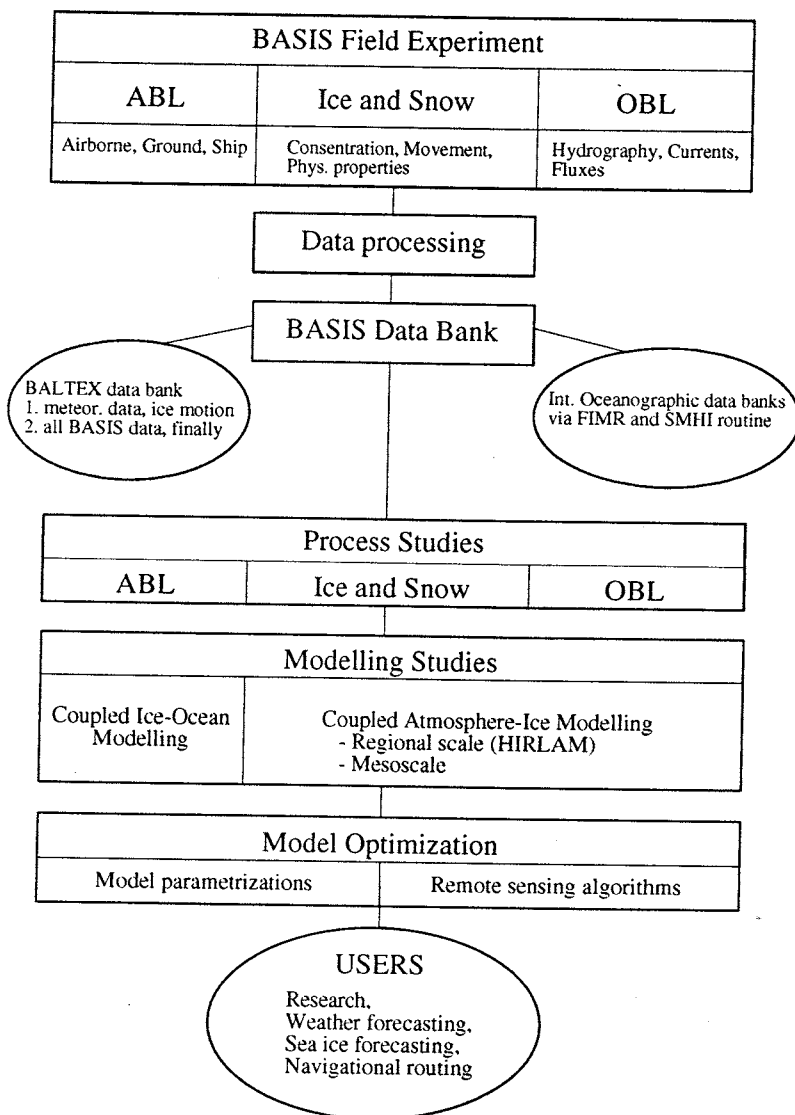


Figure 1.1. Research structure of BASIS.

### 1.3 Project Organization

#### *Project Contractors:*

Finnish Institute of Marine Research (FIMR)

Universität Hamburg, Meteorologisches Institut, Germany (UHAM)

Universität Hannover, Inst. für Meteorologie und Klimatologie, Germany (UHANN)

Uppsala University, Dept. of Earth Sciences and Meteorology, Sweden (UUPP)

Swedish Meteorological and Hydrological Institute, Sweden (SMHI)

Chalmers Univ. of Techn., Dept. of Radio and Space Sci., Sweden (CUT), Assoc. C.

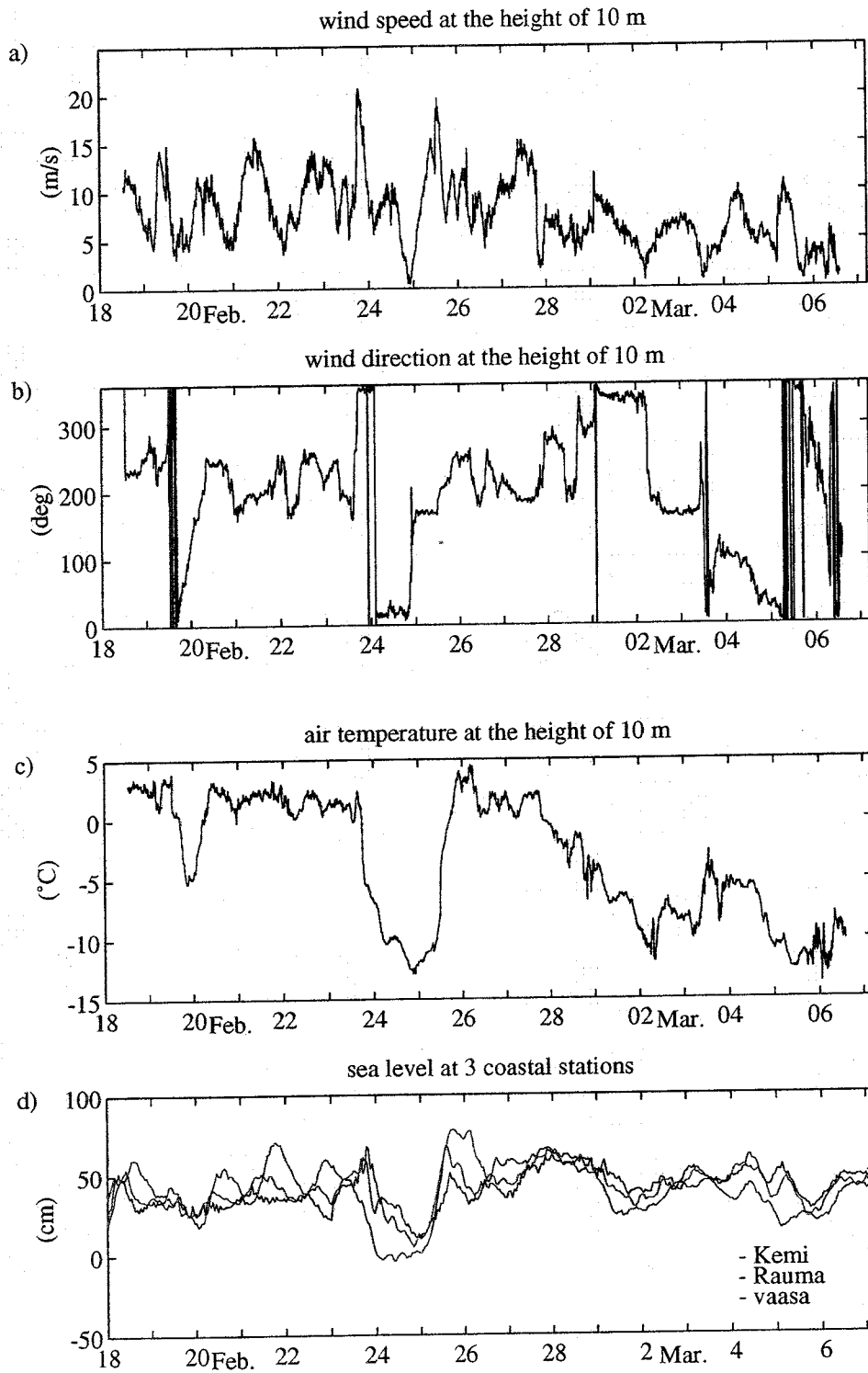


Figure 2.2. Time series of the wind speed (a) and direction (b) and air temperature (c) during the BASIS field experiment, as measured at a meteorological mast on the ice close to *R/V Aranda*. In (d) is given the time development of the sea level in Kemi, Vaasa, and Rauma.

## 2.2. Ice Station

*R/V Aranda* anchored in the Ice Station on 16 February, 1998, at the site 63° 08.12' N, 21° 14.66 E, and left the Ice Station on 6 March, 1998. The site of *R/V Aranda* and the measurements in the surroundings are shown in Figure 2.3 (scale 150 x 75 km) and Figure 2.4 (scale 0.7 x 0.4 km). The sea ice thickness at the *R/V Aranda* site varied in space and time from 0.25 to 0.45 m. During the intensive field experiment, a Finnish helicopter operated from *R/V Aranda* and deployed most of the equipment on the ice. A Swedish helicopter visited *R/V Aranda* on 18 February and on 5 March, 1998, to deploy and pick up ice drift buoys.

## 2.3. Airborne and Remote Sensing Observations

Airborne observations were made by the German research aircraft Falcon (UHAM), operating from Kokkola airport from 25 February to 6 March, 1998, and by the German Helipod (UHANN) helicopter, operating from *R/V Aranda* from 24 February to 1 March, 1998. The Falcon aircraft made six flight missions with a total duration of about 11.5 h. The missions took place under different large-scale flow directions with respect to the ice edge, i.e. under on-ice, off-ice and ice-parallel flows. The Helipod made three flights yielding a vertical sounding on each flight, and two horizontal legs of 8 km length at the height of 20 m. The observation quantities of both the aircraft and Helipod included the wind speed, air temperature and humidity, surface temperature, and the turbulent fluxes of momentum, heat and moisture. The aircraft additionally measured the upward and downward components of both the shortwave and longwave radiative fluxes, as well as the liquid water contents and particle sizes of cloud droplets. The ice surface roughness was measured by laser profilometry (FIMR) from a helicopter.

As a ground truth for utilizing radar satellite images (ERS-2, Radarsat), various sea and sea ice observations were carried out (by SMHI) in the near-site of the Ice Station and more remote areas by a helicopter. Data from the ice buoys were used as a ground truth for remote sensing as well.

## 2.4. Coastal and land-fast ice stations

Two stations were operated on the Finnish coast of the Gulf of Bothnia:

- a) Meteorological station for rawinsonde soundings (soundings with 6 h intervals) and surface-layer observations (UHAM), including turbulence and radiation measurements and cloud observations at Kokkola, Trullevi (63.8°N, 23.3°E)
- b) A meteorological rawinsonde station (UHANN, 6 h intervals) at Merikarvia, Mericamping (61.9°N, 21.5°E)

Three stations were operated on the Swedish coast of the Gulf of Bothnia:

- a) Meteorological station for radiosonde and pibal soundings (6 h intervals) and surface-layer observations (UUPP), including a 30-m mast, turbulence and radiation measurements at Umeå (63°40.5'N, 20°24.0'E)
- b) and c) Two meteorological rawinsonde stations (SMHI, 6 h intervals) at Sundsvall (62° 22.5'N, 17°19.5'E) and Kallax (65°30.7'N 22°6.5'E).

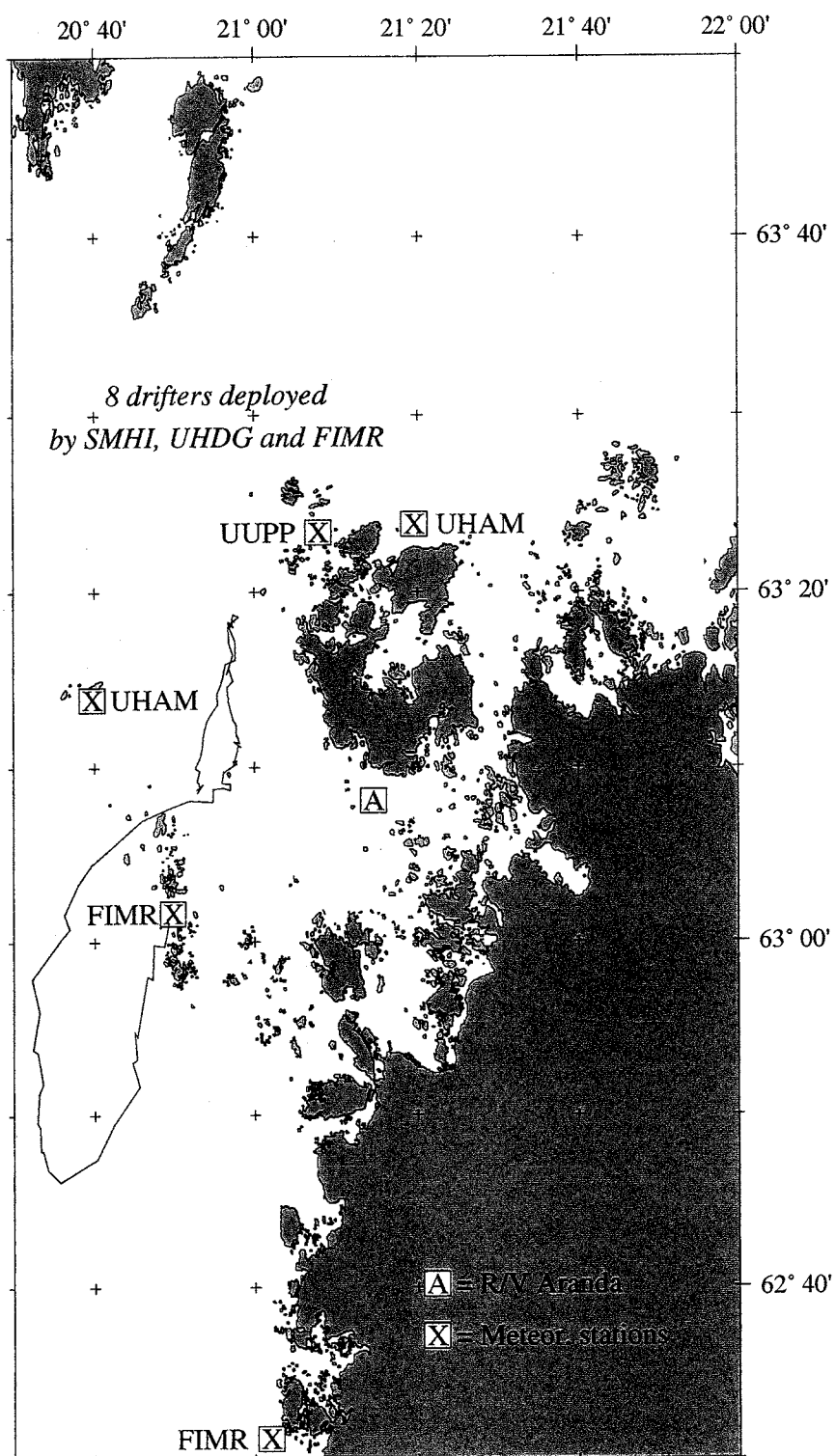


Figure 2.3. Meteorological stations and the near-site Ice Station (A; in the vicinity of *R/V Aranda*) on the sea ice during BASIS-98. (For sites of UUPP meteorological station at Umeå and UHAM meteorological station at Kokkola see Figure 2.1).



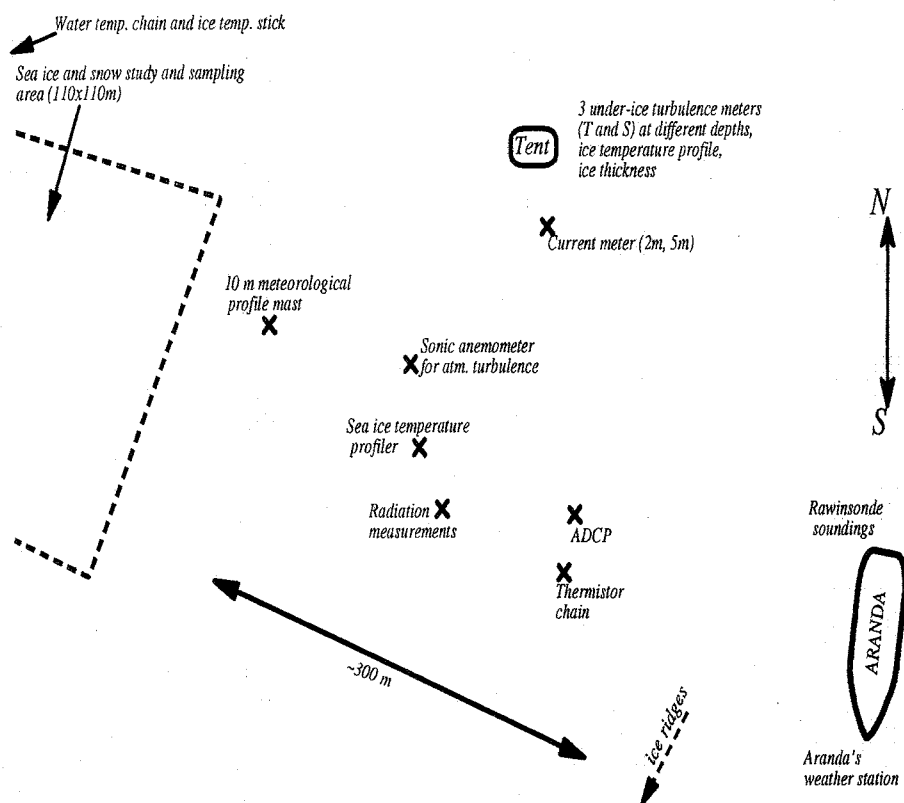


Figure 2.4. Near-site observation field at the *R/V Aranda* Ice Station during BASIS-98.

As a reference for the atmospheric conditions over open water, the Östergarnsholm station (UUPP,  $57^{\circ} 25,78' N$ ,  $18^{\circ} 54.25' E$ ) was used. It has a 30-m-high tower with temperature and wind sensors, as well as turbulence equipment.

The stations are marked in Figure 2.1. Most of the sounding stations started at 12 UTC of 18 February, 1998, and continued up to 12 UTC of 6 March, 1998.

## 2.5. Pre- and Past-Intensive Period Hydrographic Monitoring, Other Operations

A pre-experiment hydrographic monitoring was carried out in the Gulf of Bothnia by *R/V Argos* (SMHI) from 5 to 10 December, 1998. 22 hydrographic CTD stations were taken. Additionally, a vertical water temperature chain was deployed in the Bay of Bothnia. *R/V Aranda* made a hydrographic pre-experiment monitoring from 26 January to 5 February, 1998, by taking 38 CTD stations. *R/V Aranda* made a past-experiment monitoring from 9 to 13 March, 1998. In that time, the ice conditions and schedule allowed only 19 hydrographic stations in the Gulf of Bothnia.

For the BASIS research phase, daily ice maps and other ice information for the whole winter were obtained from FIMR and SMHI, which also supplied sea level data from various mareographs. Additionally, supportive meteorological data were obtained from the synoptic and automatic Finnish and Swedish coastal meteorological stations.

### 3. ATMOSPHERIC BOUNDARY LAYER

#### Surface-Layer Turbulence and the Structure of the Atmospheric Boundary-Layer

Ann-Sofi Smedman, Ulf Andre<sup>1)</sup>, Magnus Carlsson, Ulf Högström, Mikael Magnusson, Jutta Rost<sup>2)</sup> and Sergej Zilitinkevich

Department of Earth Sciences, Meteorology, Uppsala University, Sweden

<sup>1)</sup> Current address: SMHI, 601 76 Norrköping, Sweden

<sup>2)</sup> Current address: Meteorologisches Institut, University of Freiburg, Germany

#### 1. Turbulence structure in the stable and near-neutral atmospheric surface layer.

##### 1.1 Sites and measurements.

Data analysis from measurements made at three sites in the Bothnian Bay during a 3-week period 15 February –7 March 1998 has been performed (See Carlsson, 2000 for the complete analysis). The sites are Umeå at the Swedish east coast, Kokkola at the Finnish west coast and R/V Aranda, a ship anchored in the sea ice outside the Finnish coast. The sites are shown in Figure 1. At all sites small masts were erected and equipped with slow-response sensors for measurements of wind speed and temperature profiles. At one height on each mast a sonic anemometer was placed. With the sonic anemometer it is possible to measure the turbulent fluctuations of the three wind components ( $u, v, w$ ) as well as the virtual temperature.

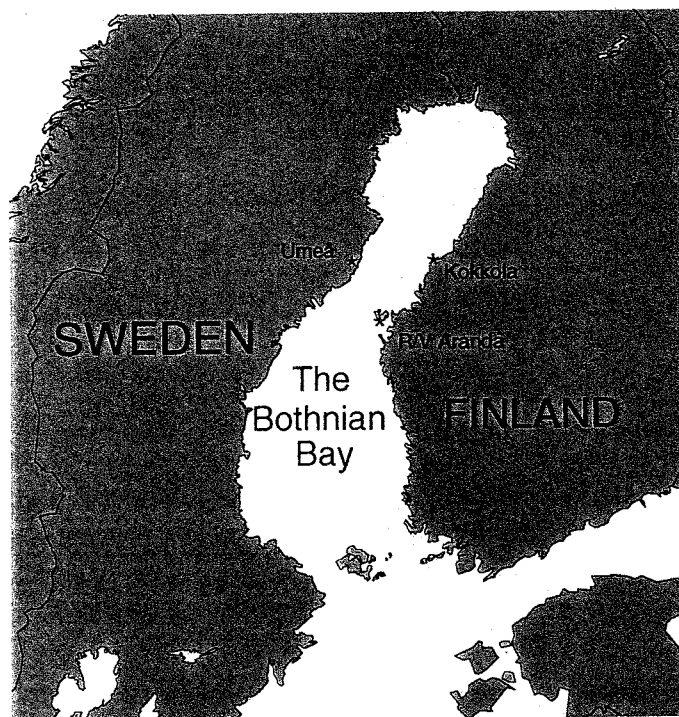


Figure 1. Map of the measuring area with the two sites Lövudden outside Umeå and the small mast near RV Aranda. The site Östergarnsholm is not shown.

The Umeå mast was located at Lövoudden (63° 40,5' N, 20° 24,0' E), a small peninsula about 25 km south of the town of Umeå at the Swedish east coast. The mast was placed just a few meters from the coastline. At 20-30 m behind the mast the woodland began. In the sector 50°-250° there was an open sea/ice fetch except for an island in the sector 130°-195°. Wind- and temperature measurements were made at the heights 1, 3.5 and 11 m. The sonic anemometer was placed at the height of 10 m for measuring turbulence.

The Kokkola-station was situated on the land-fast ice in a bay near Kokkola at the Finnish west coast (63° 95' N, 23° 08' E). On a 10×10 m area, four small masts were equipped to measure standard meteorological parameters and turbulence. Wind speed was measured at 2 m height, temperature and radiation at 1 m and turbulence at 3.5 m. There was at least 3 km open ice fetch in the sector 135°-315°. The sector 315°-135° was disturbed by woodland.

The ship R/V Aranda was anchored in the sea ice outside the Finnish West Coast (63° 08,12' N, 21° 14,66' E), outside the Finnish town Vaasa. The mast was situated about 300 m north-west of the ship. A 10 m high mast was used for measuring temperature- and wind profiles. Wind speed was measured at 0.4, 1.0, 2.3, 4.6 and 10.0 m height over the ice surface. Temperature measurements were made at 0.4, 2.3 and 10.0 m. The turbulence measurements were made at 2 m height with a sonic anemometer on a mast located 40 m from the mast measuring profiles. The Aranda station had open ice fetch long enough to consider all wind directions to be undisturbed.

The sampling rates for the turbulence measurements were 20 Hz at Umeå and Aranda and 50 Hz at Kokkola. All data used from the stations were saved as 10 min averages. In the forthcoming analysis these data are transformed to 1 hour averages. Only the undisturbed sectors are used, to be sure that it is the atmospheric conditions over sea ice/water that is considered. In addition wind speeds under 2 m/s are not used because of too large uncertainties in the measurements. The analysis of some turbulence parameters is given in the next Sections.

## 1.2 Variation of the normalised standard deviation of the vertical wind component

According to Monin-Obukhov similarity theory, normalised turbulence statistics and standard deviations of the velocity components and temperature in the surface layer should be unique functions of a stability parameter  $z/L$ . At least during neutral conditions the ratios are supposed to be constant. Figure 2 shows the normalised standard deviation of the vertical velocity component as a function of stability for the three sites Umeå (+), Aranda (x) and Kokkola (\*). The sonic anemometer was placed at a height of 10 m, 3.5 m and 2 m respectively at the different sites. During neutral stratification the values vary with increasing measuring height from 1.08 to 1.37. In the slightly stable regime the curves are almost constant but for strong stability there is a tendency for all three curves to increase with increasing stability.

The ratio  $\sigma_w/\sigma_u$  will be affected both by stability and the closeness of the ground (the wall effect). During neutral conditions the turbulent eddies in the vertical are determined by the height above the ground and during stable stratification buoyancy acts as a sink for the vertical component and will suppress energy and thus the eddy size. As stability increases the influence of the wall will decrease. But, at the same time stratification acts as a sink for the vertical component suppressing vertical motion. The effect of these two counteracting mechanisms on the ratio  $\sigma_w/\sigma_u$  can be seen in Figure 3. The curves for the stations Aranda

(x) and Kokkola (\*) ,2 m and 3.5 m above the ground respectively, follow very closely the corresponding curves given in Smedman (1991). In Figure 3 it can be seen that near the ground the stability overcomes the influence of the ground around  $z/L = 0.3 - 0.4$ .

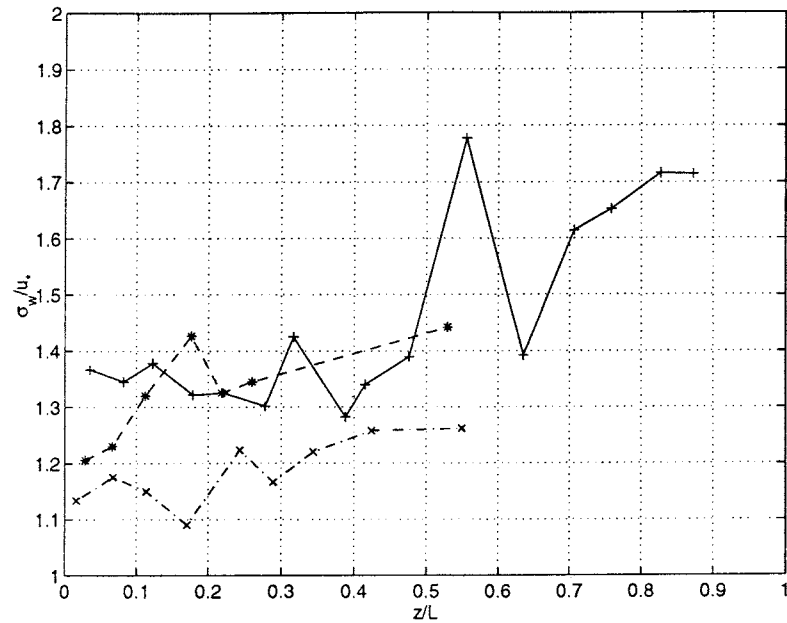


Figure 2. The normalised standard deviation of the vertical component of the wind speed as a function of stability. . +: Umeå, 10 m ; \*: Kokkola, 3.5 m ; x: Aranda 2m.

The curve for Umeå (+) in Figure 3 deviates from the other two showing much higher values for the ratio  $\sigma_w / \sigma_u$ . This is an indication that the measurements taken at Umeå at a height of 10 m is in the transition layer above the surface layer (see below).

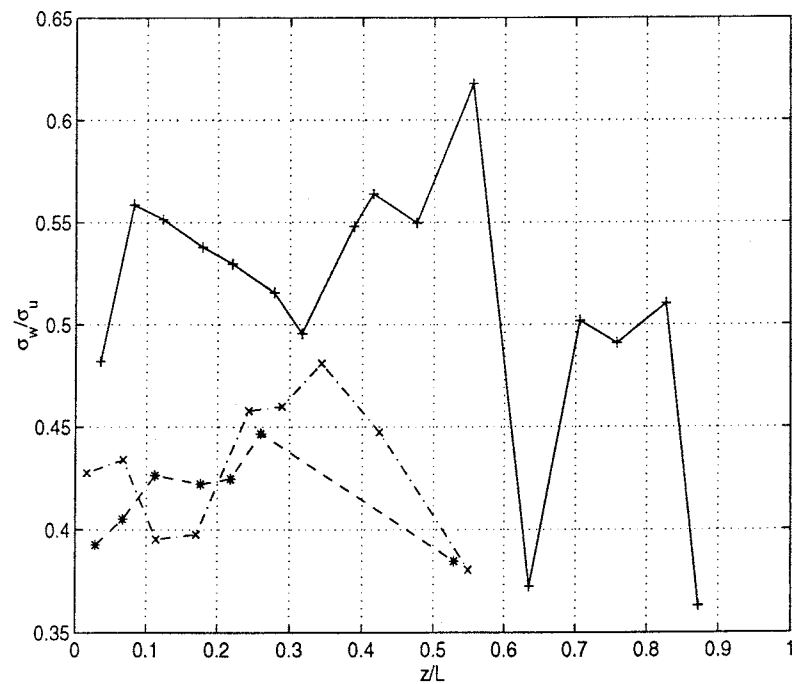


Figure 3. The ratio of standard deviations of the vertical and longitudinal components of the wind speed as a function of stability. Same sites as in Figure 2.

### 1.3 The drag coefficient ( $C_D$ )

During stable stratification, the surface drag coefficient  $C_D$  is related to its neutral value  $C_{DN}$  as:  $C_{DN} = \left( C_D^{-1/2} + \frac{1}{k} \psi_M \right)^{-2}$ , where  $k = 0.4$  and  $\psi_m = -6.8z/L$  for stable stratification. In Figure 4 the drag coefficient  $C_D$  is found for the three stations as a function of wind speed. For low wind speeds (strongly stable stratification) the curves from Kokkola (\*) and Aranda (x) give very low values indicating the effect of stability, while at high wind speeds (neutral stability) the three curves have almost the same value. The drag coefficients corrected for stability are shown in Figure 5 as a function of wind speed. The stability correction works very well for the Aranda (x) and Kokkola (\*) curves giving a value around  $1.3 \times 10^{-3}$ . The stability corrected curve for Umeå (+) is too high for very stable conditions (low wind speed) but gives about the same  $C_{DN}$  - value for neutral stratification (high wind speed) as the other two stations. The reason why the stability correction seems to fail for the Umeå data set is again an indication that 10 m is above the surface layer, where Monin-Obukhov similarity is supposed to be valid.

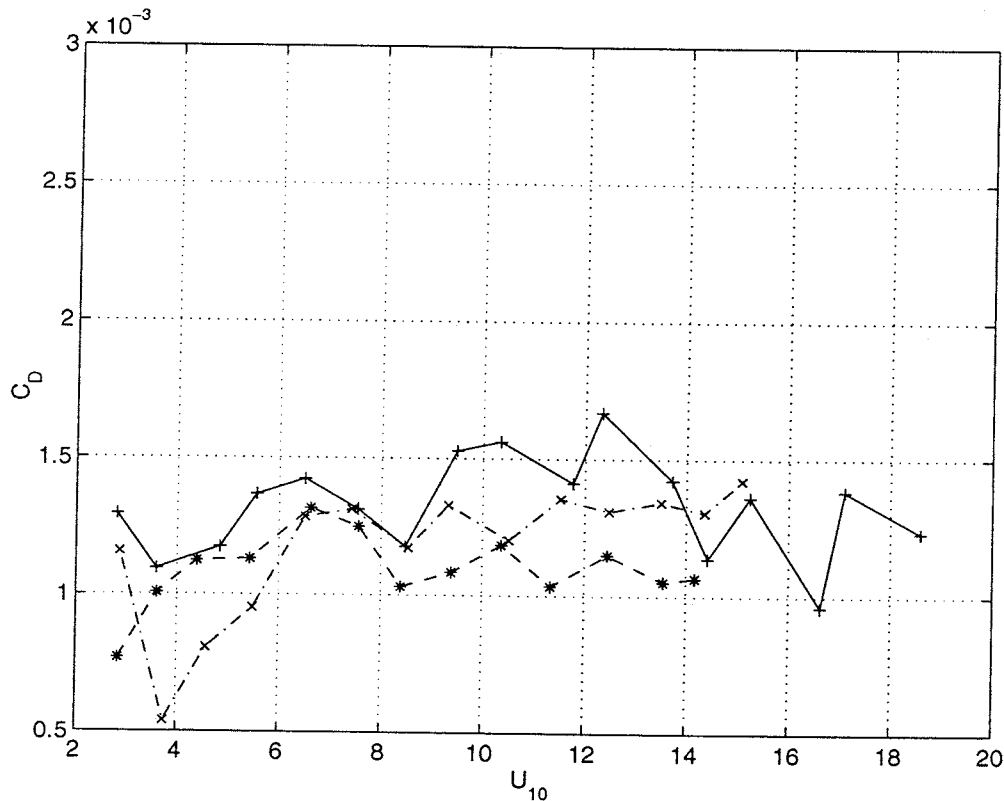


Figure 4. The drag coefficient as a function of wind speed at 10 m height. Same sites as in Figure 2.

It is possible to calculate the roughness length  $z_0$  from the  $C_D$  curves. If the logarithmic wind profile is used as an approximation

$$z_0 = \frac{z}{\frac{k}{e\sqrt{C_{DN}}}}$$

For high wind speeds, all the three  $C_{DN}$  curves show the same results as seen in Figure 4. If an average of  $C_{DN}$  taken over the three sites for wind speeds greater than  $12 \text{ ms}^{-1}$ ,  $z_0=9.4 \times 10^{-5} \text{ m}$ . This is a result that, according to Stull (1988), corresponds to *calm open sea*. If the term '*calm*' is translated into 'low wind speed regime', we are dealing with dynamically smooth flow. The result thus indicates that the ice cover is dynamically smooth, a result that is in general agreement with other findings.

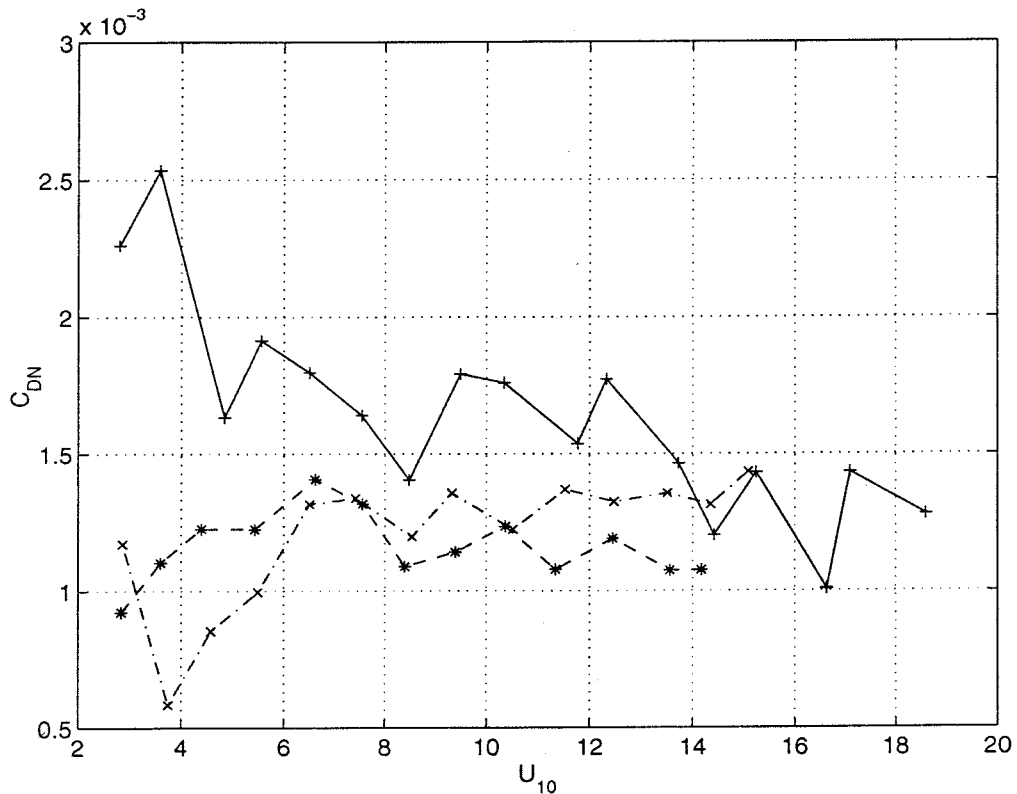


Figure 5. The drag coefficient corrected for stability as a function of wind speed at 10 m height. Same sites as in Figure 2.

#### 1.4 Buoyancy length scale ( $l_B$ )

The buoyancy length scale in stable air is given by:  $l_B = \sigma_w / N_{BV}$ , where  $N_{BV}$  is the Brunt-Väisälä frequency. The buoyancy length scale is a measure of the stability suppression of vertical motions and thus gives an idea of the eddy sizes in the SBL. The range of  $l_B$  is from the order of one meter for strong stability to some hundred meters for more neutral conditions.

Figure 6 shows the buoyancy length scale from the three sites as a function of stability. It is obvious from the Figure that the length scale and thus the size of the largest eddies increases with the height above ground. Again the Umeå curve deviates from the other two also in very stable air and again this is an indication of the shallow stable surface layer ( $h < 10 \text{ m}$ ).

#### 1.5 Conclusion

Several turbulence parameters were studied as a function of stability during stable conditions over snow covered ice. The stability dependence of the normalised standard deviations of the three wind components followed reasonably well the results of earlier studies (Panofsky and

Dutton, 1984). Especially notable is the increase with stability for stronger stability. This increase was seen in the standard deviation of all three wind components.

From the analysis it is clear that the turbulence structure in the stable boundary layer can be described according to Monin-Obukhov similarity theory. For some of the studied parameters the result from the Umeå site (10 m height) deviates from the two others (Kokkola 3.5 m and Aranda 2m height). This is especially clear for the buoyancy length scale  $l_B$  and the ratio of the standard deviations of the vertical and horizontal wind components,  $\sigma_w/\sigma_u$ . The deviation is an indication that the height of the surface layer, during stable conditions with homogeneous ice fetch, can be less than 10 m. The results of  $l_B$  and  $\sigma_w/\sigma_u$  also show that the influence of the surface (wall effect) is important for the turbulence structure in the stable surface layer.

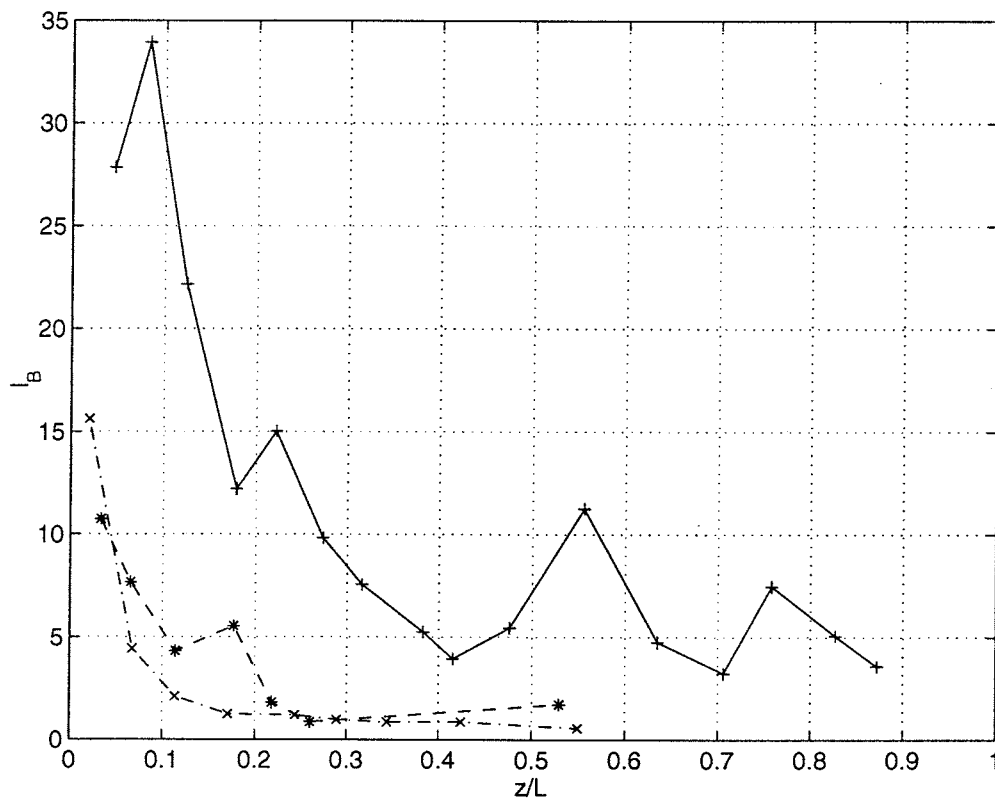


Figure 6. The buoyancy length scale as a function of stability. Same sites as in Figure 2.

## 2. Theory and measurements for the vertical wind variance in the atmospheric neutral surface layer

### 2.1 Introduction

Certain features of the near-neutral atmospheric surface layer are observed to be not wholly consistent with Monin-Obukhov theory (MO theory) nor with published measurements of laboratory non-accelerating flow over a flat plate, essentially because of non-local dynamics (Hunt and Morrison, 2000). Firstly, as observed by Högström (1990), the dimensionless vertical velocity standard deviation,  $\sigma_w/u_*$  (where  $u_*$  is the friction velocity) increases

systematically with height above the ground, whereas MO theory predicts it to be constant. Secondly, the measured turbulent kinetic energy budget showed that dissipation,  $\varepsilon$  was not in local balance with production,  $P$  as expected. Instead it was found that  $\varepsilon = 1.24P$ , the excess energy being brought down to the surface layer from above with the aid of the pressure transport term. The results of Högström (1990) were confirmed in a later experiment, Högström (1992) as well as in subsequent experiments.

Högström (1990) attempted to explain the above results in terms of the inactive turbulence concept introduced by Townsend (1961) and further elaborated by Bradshaw (1967), who also demonstrated effects of inactive turbulence in non-zero pressure gradient laboratory flow.

The origin and source of the 'inactive' motions in the atmospheric case needs further study. In Smedman et al. (1994) airborne measurements in a near neutral marine boundary layer showed that large scale eddies were formed in a strong shear zone at the top of the boundary layer at nearly 1000 m and brought down to the layers near the surface by the pressure transport term. Thus, an alternative mechanism which is directly linked to the fundamental dynamics of near-neutral boundary layers must be sought. As outlined below, such a mechanism is provided by a new theory for very high Reynolds number boundary layers proposed by Hunt and Morrison (2000) and Hunt and Carlotti (2001), based on earlier work by Townsend (1976), Marusic and Perry (1995).

## 2.2 General considerations and a prediction for the vertical velocity variance

The turbulent boundary layer of depth  $h$  is conveniently sub-divided into a *surface layer* of depth  $h_s = O(h/10)$ , where turbulence is in approximate local equilibrium, because production by strong mean shear approximately balances the rate of dissipation,  $\varepsilon$ , i.e.  $u_*^2 dU/dz/\varepsilon \sim 1$  (note, however the result of Högström, 1990 and 1992 that pressure transport in the neutral surface layer amounts to as much as 24% of the local production) and an *upper layer* where turbulence is not in equilibrium and with considerably weaker shear, and the energy and the dissipation rate are smaller, so that  $u_e^2 dU/dz/\varepsilon \ll 1$ ,  $u_e$  being a typical eddy velocity scale of order the friction velocity. For high enough values of the turbulent Reynolds number,  $Re_\tau = \frac{u_* L_e}{\nu} \gg 10^4$ , where  $\nu$  is kinematic viscosity, and  $L_e$  an eddy length scale above the

surface layer, the turbulence in the upper layer is generated more by the local shear than by diffusion from the surface layer. But the turbulence is not in equilibrium, because the turbulent energy diffuses or propagates outward to the top of the layer. The shear generated eddy motions also propagate downward to the surface layer where they are further distorted by the intense shear and also impact on the ground. The former process leads to groups of elongated sloping eddies which replicate themselves in line of 'cats paws' and honami waves (Hunt and Carlotti, 2001). This leads to amplified eddies and amplified horizontal components. These extended surface eddies, which are strongly affected by the surface friction at the ground, are significant in the *eddy surface layer* whose thickness  $h_e$  is less than that of the surface layer,  $h_s$ ,  $h_e$  being 2 – 4% of the boundary layer thickness, i.e. about  $1/3 h_s$  or, typically about 15 m. With or without shear, blocking at the surface creates a potential flow component which modifies the vertical velocity, where the variance  $\sigma_w^2$  is given, according to RDT calculations (Hunt, 1984; Mann, 1994)



$$\sigma_w^2 \approx u_e^2 \left(\frac{z}{L_e}\right)^{2/3} \quad (1)$$

The total vertical velocity variance in the surface layer is the sum of the contribution of the blocked eddies of the upper layer, Eq. (1), and that of small scale turbulence created near the surface, which scales on  $u_*$ , giving for the total variance

$$\sigma_w^2 = \alpha u_*^2 + \beta u_e^2 \left(\frac{z}{L_e}\right)^{2/3} \quad (2)$$

where  $\alpha \sim 1$ ,  $\beta \sim 1$ ,  $u_e \sim u_*$ , so that

$$\frac{\sigma_w^2}{u_*^2} \approx 1 + \left(\frac{z}{L_e}\right)^{2/3} \quad (3)$$

and where  $L_e$  is expected to scale with  $u_* / f_c$  and to be  $O(h_s)$  or  $O(h_e)$ .

This combination of local shear plus blocking of large scale eddies also occurs in unstable atmospheric boundary layers when there is both mean horizontal wind and significant thermal convection (Panofsky et al., 1977, Hunt, 1984).

For low Re flow, where the mean velocity gradient is much greater at the top of the surface layer, the shearing motion 'shelters' or decorrelates the surface layer eddies from those of the outer turbulence (Hunt et al., 1989). Then the second term in Eq. (3) is absent.

### 2.3 Validation against atmospheric near-neutral measurements

The prediction, Eq. (3) has been tested on well-documented near neutral atmospheric surface layer data from 10 sites, Table 1. The data have all been chosen to represent near-neutral conditions. In the selection of 'near-neutral data' the stability criteria has been:  $-0.1 < z_i/L < 0.1$ , where  $z_i$  is the highest measuring level for each site ( $z_i \geq 10$  m, except at site (5) where  $z_i = 6$  m). As shown in Högström (1990, 1992), the characteristic height variation in  $\sigma_w / u_*$  was observed in a stability interval of at least this magnitude. A general criterion of stationarity was also imposed. All measuring sites are flat but dynamically rough, and with a roughness length  $z_0$  varying from about  $10^{-4}$  m (open sea) to about 0.5 m (pine forest). The measurements are all in the constant flux layer but represent heights ranging from 1.6 m to about 30 m. In fact, most of them, except for two levels at site (6), one level at site (7) and two levels at site (10), are effectively in the eddy surface layer. Out of the 10 data sets, 8 are from experiments carried out in various parts of Sweden by the Uppsala group. The two remaining data sets, which are taken from the open literature, represent oceanic conditions. Unfortunately, most widely spread micro-meteorological data sets (such as the Kansas data, Haugen et al., 1971 or the Australian data, e.g. Dyer, 1974) represent land summertime fair weather mid-latitude conditions, which means that neutral conditions occur only during brief morning and evening transition periods, making these data sets unsuitable for the present analysis. Reviews of other spectral data are given by Hunt and Morrison (2000).

In testing Eq. (3), it is assumed that  $L_e$  is proportional to the depth of the neutral boundary layer  $u_* / f_c$ , because this scale determines the eddy motion in the upper layer. In Figure 7  $y = \sigma_w^2 / u_*^2$  has been plotted against  $x = 10^3 (z f_c / u_*)^{2/3}$ . It is clear from the figure that the non-dimensional vertical velocity variance increases with height in accordance with Eq. (3). The data points from the lowest measuring levels (1.6 and 3 m) deviate, however, from the general pattern in an interesting way. According to Hunt and Carlotti (2001), although the

forms of impinging eddies change in the thin eddy surface layer (see Section 2), the blocking mechanism itself is still significant. However, the distorted forms of the eddies, Figure 7, reduces the vertical velocity. This explains why, as Figure 7 indicates, the magnitude of the blocking term of Eq. (3) decreases where  $z \ll h_e$ , i.e. for the measurements at 1.6 and 3 m. From the above concept,  $L_e$  is proportional to  $u^*/f_c$ . Regression of the data in Figure 7 gives,  $L_e \approx 10^{-2} u^*/f_c$ . Taking the boundary layer height  $h = 0.3u^*/f_c$ , implies that  $L_e \sim h_e$ , i.e. the height of the eddy surface layer.

This statement implies that the length scale is a function of latitude. By taking data from sites with widely different latitude, this can be tested. Thus, in Figure 7, there are data from one site at  $44^\circ\text{N}$  (no 9, Sable Island) and one at  $64^\circ\text{N}$  (no 3, Bottenviken). Making regression with those two data sets only, gives a very similar regression expression to that obtained with the entire data set and with a correlation coefficient  $r = 0.75$  for the case when  $\phi$  is allowed to vary. If instead, a mean value for  $\phi$  is taken,  $r$  drops to 0.61, implying that the explained variance has dropped from 0.56 to 0.37.

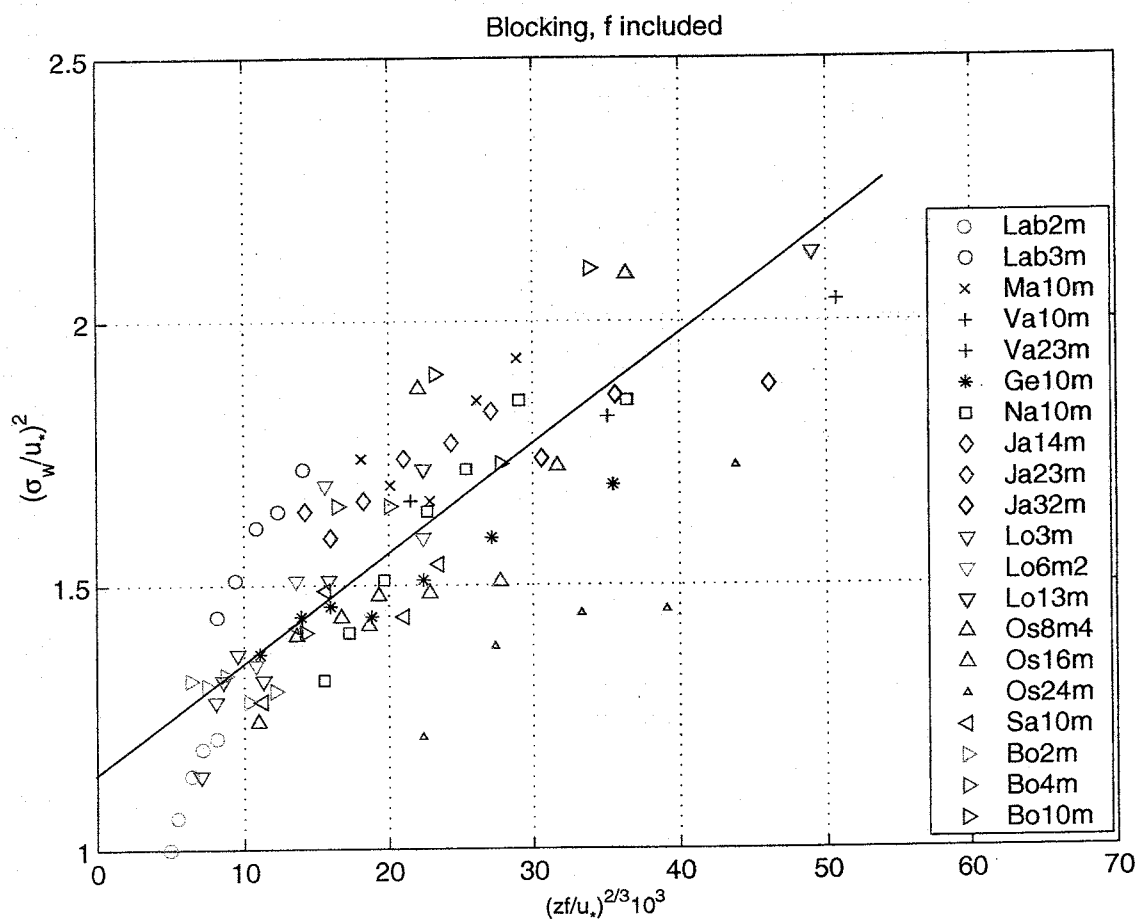


Figure 7. Normalized vertical velocity variance plotted against  $10^3(zf_c/u_*)^{2/3}$ . Symbols denote the sites; numbers in parenthesis refer to Table 1: ▽, Lövsta (1), agricultural, 3 levels; \*, North Sea (2), ocean; > Bottenviken (3), ice, 3 levels; x, Marsta (4), agricultural; o, Laban's mills (5), heath, 3 levels; ◇, Jädraås (6), pine forest, 3 levels; +, Vänersborg (7), agricultural, 2 levels; square, Näsudden (8), juniper heath; <, Sable Island (9), ocean; △, Östergarnsholm (10), ocean, 2 levels. Note, that each symbol represents the mean of a number of measurements from each particular site and height.

## 2.4 Conclusions

The various atmospheric neutral surface layer characteristics identified by Högström (1990, 1992) as effects of ‘inactive’ turbulence are explained here in terms of ‘top-down’ mechanisms that dominate at high Reynolds number over the ‘bottom-up’ instability mechanism that dominate at low Reynolds number. Detached eddies of relatively large scale, which are being brought down from above into the surface layer, cause the observed increase of dimensionless vertical velocity variance with height as well as other ‘anomalies’ (as compared to traditional theory). As shown by the analysis of the height variation of  $\sigma_w^2 / u_*^2$ , the detached eddies are, however, of eddy surface layer height scale and not of boundary layer height scale. Most importantly, as shown in a previous study (Högström and Bergström, 1996), these eddies are very effective means for momentum transport. This contrasts strongly to the statement of Townsend (1961) and Bradshaw (1967) that the ‘inactive’ eddies do not contribute to the shearing stress.

The high Reynolds number theory of Hunt and Morrison (2000), Hunt and Carloti (2001) predicts correctly not only the variation of  $\sigma_w^2 / u_*^2$  with height but also the low frequency fall-off of the dimensionless spectrum for the vertical velocity. The spectral level in this range is shown to be a factor three higher than given by the much quoted Kansas spectrum (Kaimal et al., 1972). Also the predictions for the co-spectrum between  $u$  and  $w$  is verified by the measurements.

Table 1. Measuring sites for test of  $\sigma_w / u_*$ -variation with height. The first column gives the name of the site and reference to the source (listed below the table). The second column gives general characteristics of the site, the third column measuring heights and the last column the latitude of the site.

Name and reference	Characteristics	Heights (m)	Latitude
Lövsta 1)	Agricultural	3, 6, 13	59°N
North Sea 2)	Ocean	10	53°N
Bottenviken 3)	Sea ice	2, 4, 10	64°N
Marsta 4)	Agricultural	10	59°N
Laban's mills 5)	Heath	1.6, 3, 6	57°N
Jädraås 6)	Pine forest	14, 26, 32*	61°N
Vänernborg 7)	Agricultural	10, 23	58°N
Näsudden 8)	Juniper heath	11	57°N
Sable island 9)	Ocean	10	44°N
Östergarnsholm 10)	Ocean	8, 16, 24	57°N

\* These heights are  $(z - d)$ , with  $d =$  zero plane displacement = 8 m.

- 1) Högström (1990)
- 2) From figure in: Geernaert and Plant (1990)
- 3) Data from three sites on the ice of the Bothnian Bay
- 4) Johansson et al. (2000)
- 5) Data from the ‘Laban’s mills’ site, Högström (1992)
- 6) Data from the Jädraås site, cf. Högström et al. (1989)
- 7) Data from the Vänernborg site, cf. Smedman (1991a)
- 8) Data from the Näsudden site, cf. Smedman (1991b)
- 9) Smith and Banke (1975)
- 10) Data from the Östergarnsholm site, cf. Smedman et al. (1999)

### 3 Validation of a diagnostic equation for the depth of the stably stratified boundary layer

#### 3.1 Introduction

The depth of geophysical (atmospheric and oceanic) turbulent boundary layers is an important value for many practical purposes such as pollution dispersing, wind engineering, air-sea interaction, weather prediction and climate modelling. The nature of these layers critically depends on the type of static stability: stable or unstable.

The data from the three experimental sites with surface measurements, RV Aranda, Umeå and Kokkola, have been used to validate a diagnostic equation for the depth of the stably stratified atmospheric boundary layer (SBL) which was developed by Sergej Zilitinkevich (Zilitinkevich and Calanca, 1999; Zilitinkevich et al., 2000).

#### 3.2 Theoretical background

This new developed equation focuses on the SBL at higher latitudes where there is no residual layer and the stably stratified free flow is adjacent to the SBL. In this case – especially if the temperature gradient in the free flow is larger than in the SBL – a energy exchange between the free flow and the SBL is possible due to the propagation of internal gravity waves.

This idea leads to an extended similarity theory that includes two length scales – the Monin Obukhov length  $L$  and a second which characterises the stability in the layer adjacent to the SBL (Brunt-Väisälä-frequency  $N$ ) while earlier estimates were mostly based on the balance between energy production by the wind velocity shear and the energy loss due to the buoyancy flux alone. The combination of these two length scales  $S=L/L_N$  expresses the influence of the free flow on the surface layer. Furthermore the equation considers earlier found depth scales for the equilibrium height as for

- (a) the neutral boundary layer in a rotating fluid (Rossby),
- (b) the SBL dominantly affected by the buoyancy flux (Kitaigorodskii),
- (c) the SBL affected by the buoyancy flux and rotation (Zilitinkevich),
- (d) the SBL affected by free flow stability and rotation (Pollard) and
- (e) the SBL dominantly affected by the free flow stability (Kitaigorodskii and Joffre).

Interpolation between the equations for the neutral boundary layer height

$$h_e^2 = (c_R \cdot \frac{u_*}{f})^2 \quad (\text{Rossby and Montgomery, 1935}) \quad (4)$$

and the equation for the SBL based on the extended Monin-Obukhov theory

$$h_e^2 = \frac{c_s^2 \cdot u_* \cdot L}{|f| \cdot (1 + c_{u2} \cdot S)} \quad (\text{Zilitinkevich, 2000}) \quad (5)$$

finally lead to the following equation:

$$h_e = \frac{c_R \cdot u_*}{|f| \cdot \sqrt{1 + \underbrace{\frac{c_R^2 \cdot u_*^2}{c_s^2 \cdot L \cdot f}}_A + \underbrace{\frac{c_R^2 \cdot c_{u2} \cdot N}{c_s^2 \cdot f}}_B}} \quad (\text{Zilitinkevich, 2000}). \quad (6)$$

Herein  $c_R$ ,  $c_s$  and  $c_{u2}$  are constants which were found in earlier studies to be 0.5, 0.7 and between 0.2 and 0.4 respectively.

### 3.3 Validation

For the validation of this equation and the three constants half hour averages of surface measurements for friction velocity  $u_*$  and the Monin-Obukhov length  $L$  from Kokkola, RV Aranda and Umeå have been used as well as the Brunt-Väisälä frequency from the radiosonde profiles. Using the constants as mentioned above the correlation is as high as 0.48 and the regression coefficient is 0.58 (Figure 8).

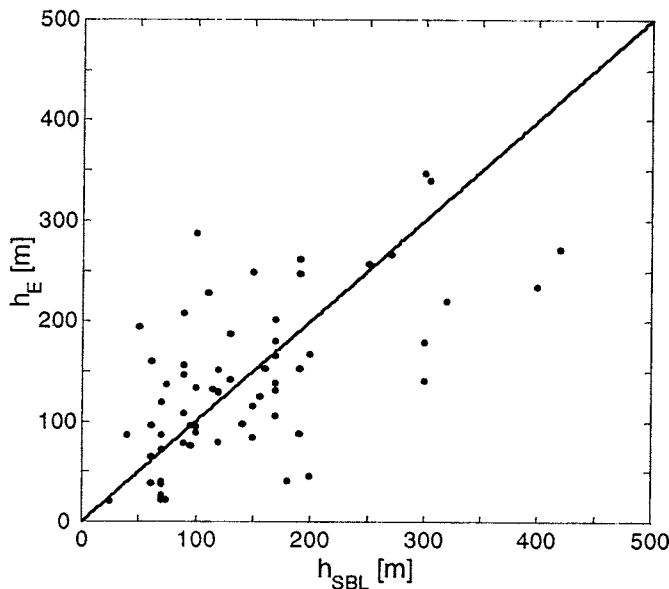


Figure 8. Comparison of the SBL depths: measured,  $h_{SBL}$ , and calculated after Eq. (6),  $h_e$ , taking the earlier estimates of the empirical constants  $c_R=0.5$ ,  $c_s=0.7$  and  $c_{u2}=0.2$ .

To improve the correlation a new estimation of the three constants have been made using two special cases. A near neutral free flow ( $S \rightarrow 0$ ) allows the determination of  $c_s$ . For in this case term B in equation (6) can be neglected compared to term A and equation (6) reduces to:

$$h_e \approx \frac{c_s \cdot u_*}{\sqrt{f \cdot \frac{u_*}{L}}} \quad (7)$$

Figure 9 shows equation (4) resolved for  $c_s$ . The regression line suggests that  $c_s=0.74$  with the correlation coefficient 0.84.

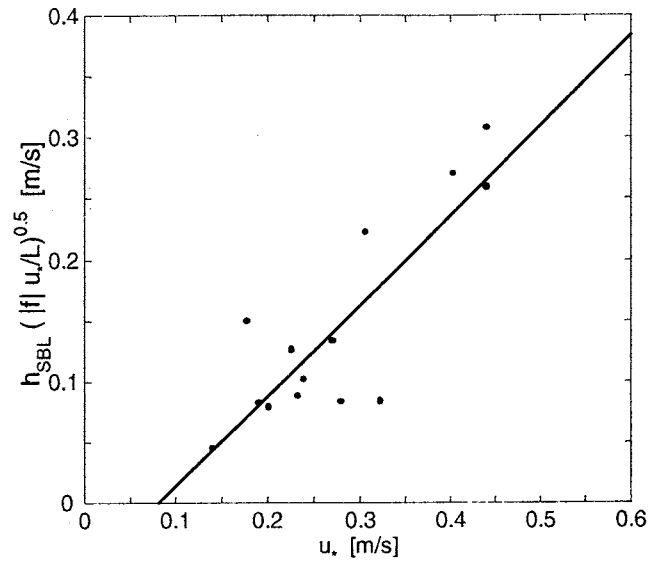


Figure 9. Re-estimation of the constant  $c_s$  from linear regression for the neutral-free-flow regime (nocturnal SBLs).

The second case assumes a near neutral boundary layer where Term A in equation (6) can be neglected compared to term B so that equation (6) simplifies to:

$$h_e = \frac{u_*}{|f|} \cdot \sqrt{\frac{c_s^2 \cdot f \cdot L}{u_* \cdot (1 + c_{u2} \cdot S)}} \quad (8)$$

Resolving equation (8) for  $c_{u2}$  linear regression suggests that  $c_{u2}$  varies between 0.04 and 0.4 with the mean value 0.1. Figure 10 shows the after Eq. (8) calculated SBL depth with this value.

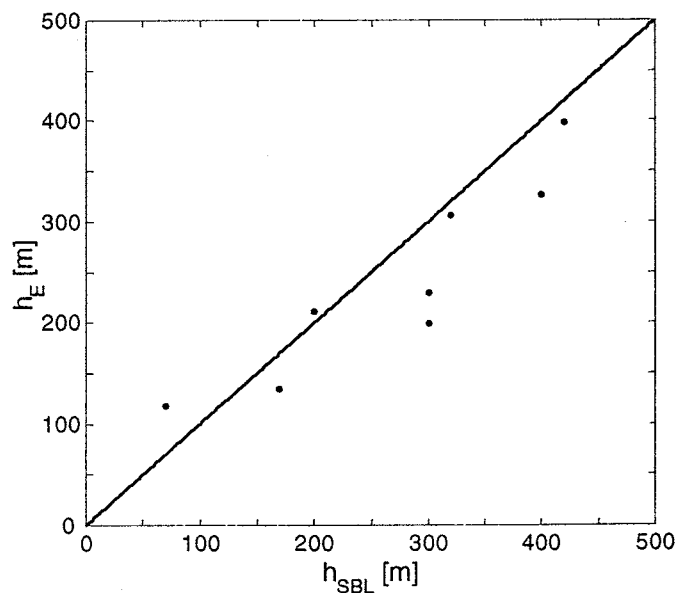


Figure 10. Comparison of the SBL depths: measured,  $h_{SBL}$ , and calculated after Eq. (8),  $h_e$ , taking  $c_s=0.74$  and  $c_{u2}=0.1$ .

In figure 11 a attempt is made to estimate the constant  $c_R$ . It shows that the SBL formulation equation (6) is practically insensitive to the choice of  $c_R$ . It can only be seen that this constant is larger than 0.4 (Table 2).

Table 2. The correlation and regression coefficients for various  $c_R$ . (Taking  $c_s=0.74$ ,  $c_{u2}=0.1$ ).

$c_R$	Regression coefficient	Correlation coefficient
0.2	0.63	0.67
0.4	0.73	0.69
0.6	0.75	0.70
0.8	0.76	0.70
1.0	0.76	0.70
1.4	0.77	0.70

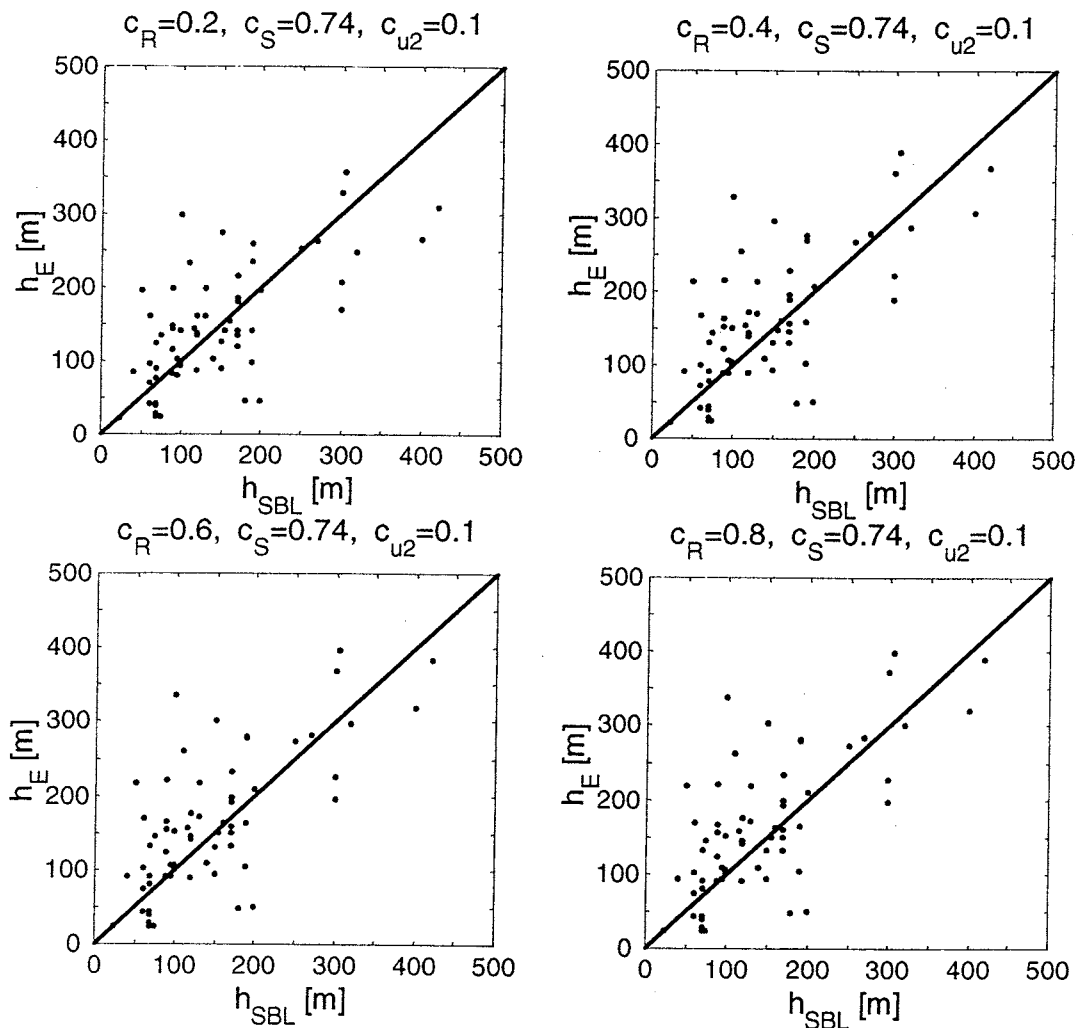


Figure 11. Comparison of the measured SBL depth,  $h_{SBL}$ , and the equilibrium SBL depth,  $h_e$ , calculated after Eq. (6) for  $c_R=0.2, 0.4, 0.6$  and  $0.8$  (taking  $c_s=0.74$  and  $c_{u2}=0.1$ ).

### 3.4 Concluding remarks

Calculation of the SBL depth using the new developed equation (6) that involves the influence of the free flow stability as well as rotation (Coriolis parameter) and surface layer properties (Monin-Obukhov length and friction velocity) gives reasonable results. A re-estimation of the three empirical constants confirmed earlier estimates of  $c_R$  to be about 0.5 and gave slightly higher values for  $c_s$  such as 0.74 compared to 0.7. For the estimation of the third constant  $c_{u2}$  only very few cases were available so that the statistical significance of the lower value is not given. Nevertheless these changes in the constants improved the correlation coefficient from 0.48 to 0.70 and the regression coefficient from 0.58 to 0.75.

Further validation based on a data set from Östergarnsholm, which is situated near the island of Gotland, showed the same trend for the constants.

## 4. Low-level jets over the frozen Gulf of Bothnia

### 4.1 Introduction

Low-level jets are a common phenomenon over the Baltic Sea as already found in earlier studies (Smedman et al., 1993; Källstrand, 1998). Also during the present campaign wind maxima within the lowest 2000 m could be observed quite often at all experimental sites which were located on the western and eastern coast of the Gulf of Bothnia south as well as north of the ice edge. Table 3 shows the different wind sectors for onshore and offshore flow at the different sites. For all sites wind and temperature profiles were available at least every six hours (00 UTC, 06 UTC, 12 UTC, 18 UTC). At all sites except Umeå GPS based systems have been used to determine wind velocity and direction. For Kallax and Sundsvall only significant levels were available, at Umeå a pibal tracking system has been used.

Table 3. Definition of the different wind sectors for the single sites.

location	offshore	Onshore	on-ice
Sundsvall	180°-45°	45°-180°	-
Umeå	225°-45°	45°-135°	135°-225°
Kallax	225°-90°	90°-225°	-
Merikarvia	340°-190°	190°-340°	-
RV Aranda	45°-170°	225°-45°	170°-225°
Kokkola	45°-225°	225°-45°	-

### 4.2 Statistical overview

The core heights of most wind maxima which lie between 250 m and 1600 m above ground are relative large compared to the depth of the SBL which lies between 50 m and 350 m or were combined with high wind speeds over several hundred meters. To be recorded as a Low Level Jet (LLJ) of following criteria had to be fulfilled:

- (I) Height of the wind maximum is within the lowest 600 m ( $h(U_{\max}) < 600$  m).
- (II) Maximum wind speed 15% stronger than the geostrophical wind ( $U_{\max} \geq U_g + 15\%$ ).
- (III) Minimum above the wind maximum is reached within the lowest 900 m ( $h(U_{\min}) \leq 900$  m,  $h > h(U_{\max})$ ).



Frequency of Wind Maxima and LLJs at the Single Sites

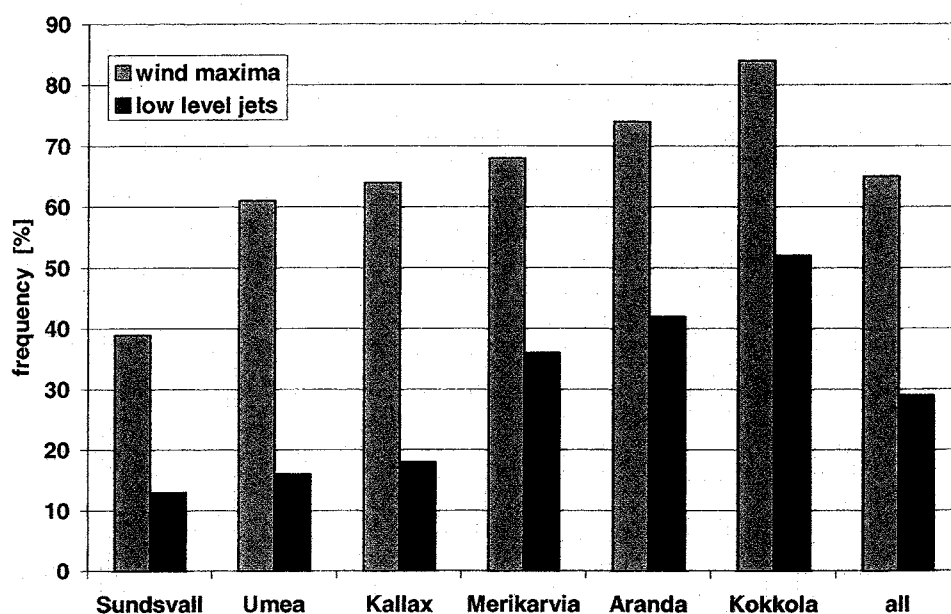


Figure 12. Frequency of wind maxima and LLJs at the single sites during the BASIS campaign.

Figure 12 shows the number of wind maxima and the number of LLJs. 63% of all wind profiles show wind maxima, 29% even LLJs. Looking at the distribution it is obvious that LLJs are more likely to occur on the eastern coast of the Gulf of Bothnia (Merikarvia, RV Aranda, Kokkola) where the air masses are advected over the sea by the mostly westerly winds (Tab. 2). Moreover the frequency of wind maxima /LLJs increases to the north where the Bothnian Bay is ice covered (at Kokkola 84% of all profiles show wind maxima).

Table 4. Percentage of the occurrence of LLJs at the single sites. The number of LLJ is related to the total number of profiles from the different wind directions.

direction	Sundsvall	Umeå	Kallax	Merikarvia	RV Aranda	Kokkola
offshore	7%	19%	18%	58%	57%	36%
onshore	36%	0%	20%	23%	42%	58%
on-ice	-	14%	-	-	14%	-
	12%	16%	18%	36%	39%	52%

### 4.3 Classification

To be able to register the form of the LLJs statistically a classification of the LLJs in respect to the origin of the air masses as suggested by Källstrand (1998) can be made (Table 5). The three classes, class 1, offshore flow, inertial oscillation due to stable stratification, class 2, land-sea-breeze/ sea-ice-breeze and class 3, baroclinic instability, fronts had to be extended for two other classes due to the ice covered sea: class 4, two distinct wind maxima and class 5, an onshore flow with inertial oscillation in stable stratification due to the ice covered sea.

In Figure 13 examples of profiles of wind speed and direction for each class are given. Note that the lower wind maximum of a class 4 LLJ (two wind maxima) might be caused by inertial oscillation or land-sea/ sea-ice-breeze while the upper maximum might have e.g. synoptic origin.

Table 5. Characteristics and possible origins of the LLJs for the classes 1 to 5.

class	Characteristics	possible origin
1	<ul style="list-style-type: none"> <li>• from upstream land area</li> <li>• distinct maximum</li> <li>• above max. wind speed constant wind</li> </ul>	<ul style="list-style-type: none"> <li>• inertial oscillation</li> <li>• fronts</li> </ul>
2	<ul style="list-style-type: none"> <li>• distinct but weak maximum</li> <li>• uniform onshore winds along the coast</li> <li>• with minimum above the maximum wind speed strong changes in dd</li> </ul>	land-sea/ice-breeze
3	<ul style="list-style-type: none"> <li>• no distinct maximum</li> <li>• high wind speeds over several hundred of meters</li> <li>• core height on high level</li> </ul>	<ul style="list-style-type: none"> <li>• fronts</li> <li>• baroclinic instability</li> <li>• etc</li> </ul>
4	two distinct wind maxima	
5	<ul style="list-style-type: none"> <li>• like class 1 with onshore winds</li> <li>• surface inversion</li> </ul>	inertial oscillation

Due to the changing synoptic situations LLJs in a classical way ('nocturnal jets') which correspond to the classes 1 and 5 represent only 38% of all LLJs (Figure 14). Jets caused by ageostrophic circulations (land-sea/ sea-ice) can be observed only very seldom. Nearly half of the LLJs have other origins which are partly unknown (class 3: 47%).

It is obvious that at the most southerly sites (Sundsvall and Merikarvia) class 3 is the wind directions most common LLJ-class which have probably baroclinic reasons. Due to the open water the PBL does not become stable when the air masses are advected over the sea and therefore no class 1 or 5 LLJs can develop. At Kokkola which has the widest sector for fetches over ice class 5 and 4 can be observed most.

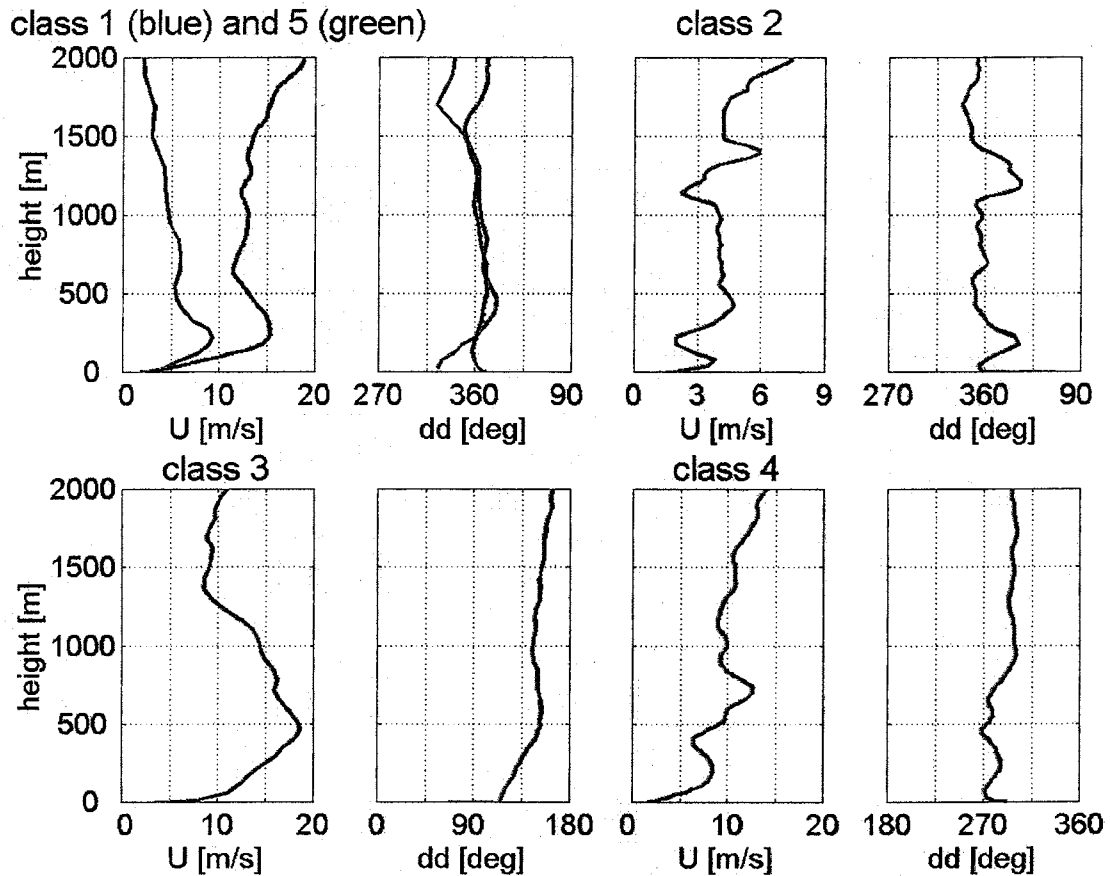


Figure 13. Examples for the classes 1 to 5. Class 1 and 5 are in one figure. The profiles are taken from Umeå, 05.03.98, 18 UTC (1), Kokkola, 01.03.98, 24 UTC (5), RV Aranda, 02.03.98, 06 UTC (2= and 04.03.98, 06 UTC (3), Kokkola, 06.03.98, 06 UTC (4).

Frequency of LLJ-Classes at the Single Sites (Absolut Amount)

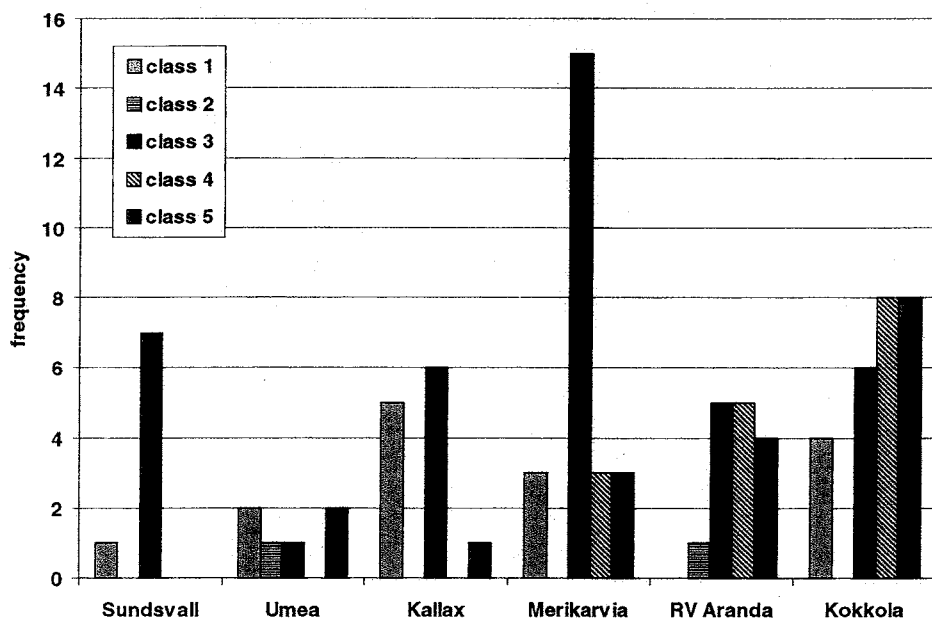


Figure 14. Absolute amount of the different classes of LLJ at the single sites for all wind directions.

#### 4.4 Time dependency

In mid latitudes LLJs can be observed mainly during clear sky nights when the PBL becomes stable. At higher latitudes LLJs throughout the day are expected due to the colder surface and therefore mostly stable stratified boundary layer. Looking at the time distribution of the occurrence of LLJs during BASIS (Umeå, Merikarvia, RV Aranda and Kokkola) it is conspicuous that despite of the ice covered Bothnian Bay and the winter conditions most LLJs can be observed during night time hours (00 UTC and 06 UTC). Distinguishing between the single classes only class 1 and 5 show significant dependency on time. Class 2 can only be observed just before sunrise when the temperature difference between the ice and the open water reaches its maximum.

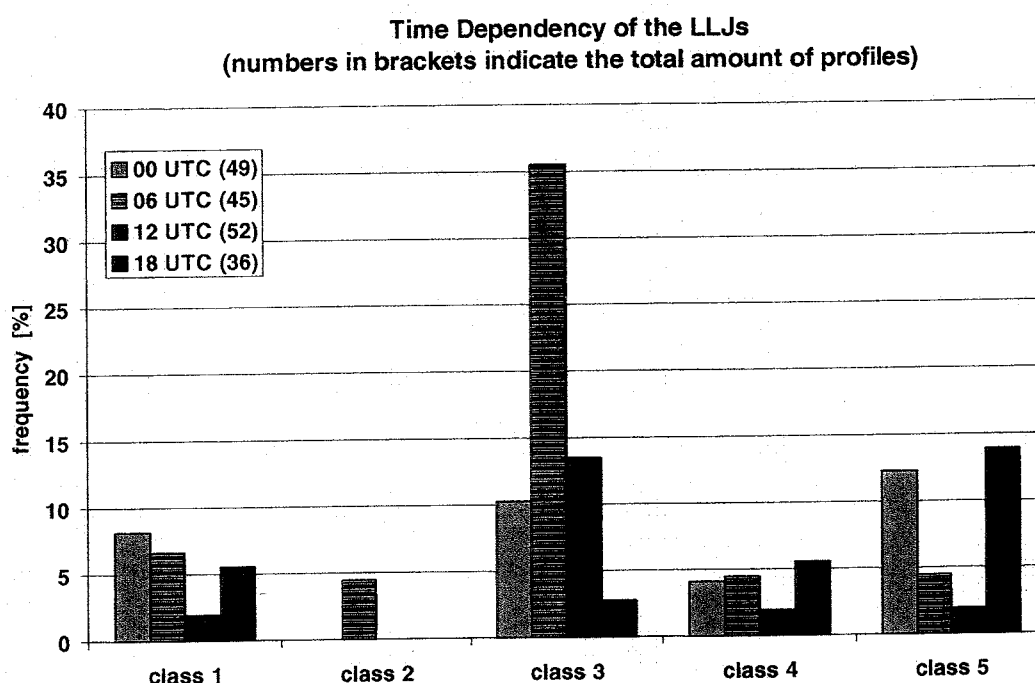


Figure 15. Frequency of the single LLJ-classes at Umeå, Merikarvia, RV Aranda and Kokkola divided into the time of occurrence.

#### 4.5 Concluding remarks

During the campaign wind maxima and even low-level jets occurred during onshore flows as well as during offshore flows. Low-level jets in a classical way such as 'nocturnal jets' (class 1 and 5) represent only 38% of all jets. There is no significant dependency on time.

### 5. Internal boundary layer and 'ice breeze circulation' in the marginal ice zone

#### 5.1 Background and theory

An internal boundary layer (IBL) is formed when air is advected over a discontinuity in surface properties. It is called *internal* since it is a layer within the boundary layer and it grows with distance downstream from the surface change. The discontinuity of surface properties can be a change in surface roughness, surface temperature, humidity or surface fluxes of heat or moisture. When the change is related to surface temperature or heat flux, the

IBL is called a thermal internal boundary layer (TIBL). The most common example of a TIBL is the one formed at the coast because of the often large temperature differences between land and sea. The knowledge of the IBL is important when mast measurements are analysed. To be sure that it is the properties over the local area that are measured, the fetch must be long enough so that the height of the IBL is larger than the measuring height.

Earlier studies of the IBL (from the 50's to the 70's) were related to neutral flow over a change in surface roughness (Garratt 1990). In the late part of this period also changes in temperature and surface heat flux were considered. Most studies were made on a smaller scale, with fetches less than 1 km.

During the last decades, the IBL studies have dealt mostly with mesoscale advection with long fetches. Special interest has been given the growth and structure of the TIBL, mainly because of its practical importance when dealing with pollution and dispersion from industries in coastal areas. Most work has been done on convective TIBL's arising when cold sea air flows over warmer land. The knowledge of stable TIBL's is far less. This is partly due to the fact that the stable TIBL normally needs very long fetches to be fully developed.

Most studies of the stable TIBL have been related to offshore flow, when warm continental air is advected over cool sea. The main interest has been to find an equation for the TIBL height. The fact that the stable TIBL has a less well defined top than the convective one, is another thing that makes the stable TIBL harder to study. Mulhearn (1981) studied offshore flow in Massachusetts Bay, USA. Using dimensional analysis, he found an expression for the TIBL height as a function of the square root of the fetch. Garratt (1987) used a mesoscale model to investigate growth and inner structure of a stable TIBL, formed by warm continental air flowing offshore. He used a physical model to find the following expression for the TIBL height:

$$h = \alpha \cdot x^{1/2} \cdot U \cdot \left( \frac{g \cdot \Delta\theta}{\theta} \right)^{-1/2} \quad (9)$$

which principally is the same expression as Mulhearn (1981) found with dimensional analysis. In Eq. (9),  $x$  is the fetch,  $U$  is the large-scale wind,  $g$  the acceleration due to gravity,  $\Delta\theta$  the difference between the continental air and the sea surface and  $\theta$  is the mean potential temperature.  $\alpha$  is a numerical coefficient defined as:

$$\alpha = \left( \frac{2AR_f C_{DG}}{\cos^3 \beta} \right)^{1/2} \quad (10)$$

where  $R_f$  is the flux Richardson number,  $\beta$  denotes the deviation angle from the normal to the coast and  $A$  is a parameter describing the shape of the temperature profile.  $C_{DG}$  is the geostrophic drag coefficient defined as:

$$C_{DG} = \frac{u_*^2}{V_g^2} \quad (11)$$

where  $V_g$  is the geostrophic wind.. Using least-square regression, Garratt obtained the value  $\alpha=0.014$ .

## 5.2 Observation of the stable internal boundary layer

When the turbulence measurements from 1.8 m and 10 m height on 2 March are compared, a distinct difference in turbulent heat flux is seen. At first there is a weaker positive heat flux at the 1.8 m level than at the 10 m level. During the day the heat flux at both levels decrease and after 15.00 UTC there is a negative heat flux at 1.8 m height while it is still positive at 10 m height. The different signs of the heat flux at the two levels indicate stable stratification at the 1.8 m level and unstable stratification at the 10 m level. It seems that the two levels measure conditions over two different surfaces. Hence one has reason to believe that there is a stable internal boundary layer with a height between 1.8 and 10 m at the Umeå mast.

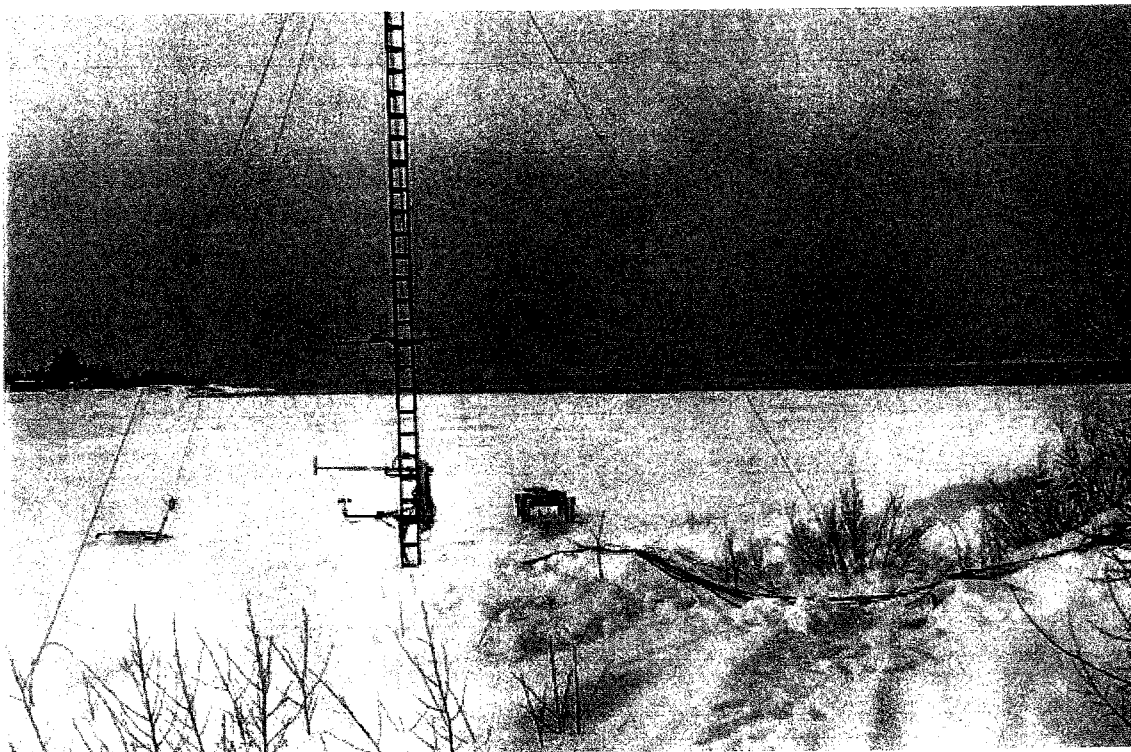


Figure 16. Picture of the Umeå site showing the fetch in the wind direction the 2 March 1998. In the background the edge between thick fast ice and thin new ice can be seen.

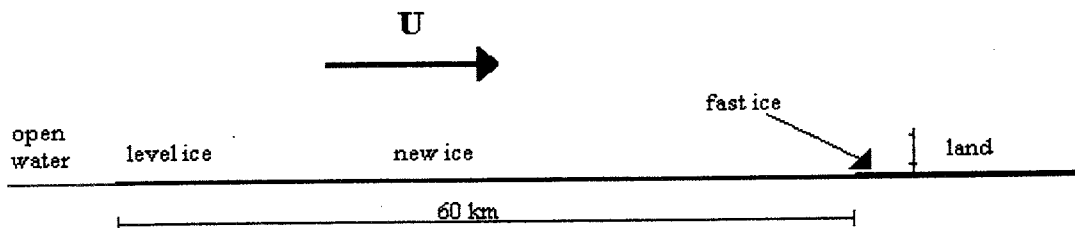


Figure 17. The ice conditions in the wind direction at the Umeå site the 2 March 1998.

The ice conditions in the wind direction on 2 March is shown in Figure 16 and a schematic picture is drawn in Figure 17. As can be seen, it is about 60 km in the wind direction from the mast to open water. If this surface change was responsible of the stable TIBL, the height  $h$  of

the TIBL should be much higher than 10 m at the Umeå site. Instead it appears to be the surface change between new ice and snow covered fast ice that causes the differences between the 1.8 m and 10 m height. The fast ice edge is located 260 m from the mast in the wind direction. While thick ice is assumed to have about the same temperature as the air above, thin new ice rather obtains the temperature of the water under the ice (personal communication oceanographer Dr. Johan Nilsson, MISU). As long as the air temperature above the ice is lower than the water temperature under the ice, there is always an upward heat flux through the ice that is larger the thinner the ice is. These two statements supports the theory of a stable TIBL, caused by the different surface properties of the new ice and the thick snow covered ice.

To investigate the theory of a stable TIBL, Garratt's (1987) expression (Eq. 9) has been used. Garratt used this expression on offshore flow with long fetch ( $x=100-900$  km). In the Umeå case there is a much smaller scale with a fetch of  $x=260$  m. The expression is used to see how it works on a smaller scale. Since, in the Umeå case, the flow is onshore,  $\Delta\theta$  in Eq. (9) will be the difference between the sea air temperature and the surface temperature on land.

There were no surface temperature measurements at the Umeå site but radiation measurements were made. By using the Stefan-Boltzmann law:

$$I \uparrow = \epsilon_{IR} \sigma_{SB} T^4 \quad (12)$$

it is possible to obtain the surface temperature  $T$  from the outgoing longwave radiation  $I \uparrow$ . In Eq. (12)  $\sigma_{SB}=5.67 \times 10^{-8} \text{ W} \cdot \text{m}^{-2} \cdot \text{K}^{-4}$  is the Stefan-Boltzmann constant. The infrared emissivity  $\epsilon_{IR}$  is 0.95 for permanent ice (Stull 1988). Unfortunately there are no radiation data from 2 March due to problems with the instruments. The day after, though, there are data and the shape of the temperature profiles that day are similar to the 2 March. Therefore the ground temperature data obtained from 3 March have been used to extrapolate the surface temperature on the 2 March, by assuming that the temperature difference between the ground and the 1 m level are the same on both days.

As  $\bar{\theta}$  the temperature at 11 m height has been used.  $\Delta\theta$  is obtained as the difference between the temperature on 11 m height and the extrapolated surface temperature. As the wind speed  $U$  in Eq. (9), the wind speed at 10 m height is used. Yet it remains to find a value of  $\alpha$  (Eq. 10). Eq. (11) is used to find a value of  $C_{DG}$ . Taking an average of the wind speed at the higher levels gives  $V_G=15 \text{ ms}^{-1}$ . An average of  $u_*$  during the day of 2 March gives  $u_*=0.3 \text{ ms}^{-1}$ . These two results yield, by using Eq. (11),  $C_{DG}=4 \times 10^{-4}$ . Since the wind direction is normal to the coast,  $\beta=0^\circ$ . As  $A$ , Garratt's value  $A=1.8$  is used. Instead of using  $R_f$ , the gradient Richardson number  $Ri$  has been estimated from  $z/L$  at the 1.8 m level. This has been done by using:

$$Ri = \frac{\phi_h}{\phi_m^2} \cdot \frac{z}{L} \quad (13)$$

Since the Richardson number is supposed to describe the stratification in the stable TIBL, only the stable values from the 1.8 m level has been used. An average of these values yields  $Ri=0.0039$ . Together with the other results above an  $\alpha=0.0024$  is obtained.

To see the development of the internal boundary layer during the day, the IBL height  $h$  has been estimated at five different times. The result is seen in Table 6.

Table 6. Temperature difference, mean temperature, wind speed and the IBL height at five different times during 2 March.

	$\Delta\theta$ [K]	$\bar{\theta}$ [K]	$U$ [ms <sup>-1</sup> ]	$h$ [m]
<b>12.30</b>	3.4	268.5	5.5	<b>0.59</b>
<b>14.30</b>	4.8	269.3	7.2	<b>0.66</b>
<b>16.30</b>	5.1	270.1	10.2	<b>0.90</b>
<b>18.30</b>	4.4	270.7	8.7	<b>0.83</b>
<b>20.30</b>	4.3	271.1	8.5	<b>0.82</b>

As can be seen the height of the stable TIBL increases during the afternoon. This is due to the increasing wind speed. The height has a maximum around 16.30 UTC and then decreases as the wind calms down. The reason why the wind speed has an effect on the height of the stable TIBL is connected with the large influence of the wind speed on the stratification. As the wind speed increases, both the stable TIBL and the unstable layer above the stable TIBL becomes more neutral. The increase of turbulence in the stable TIBL in combination with the decreasing instability in the layer above together yield the increase in height of the stable TIBL.

The values of  $h$  are somewhat smaller than expected. Since it was slightly stable at 1.8 m height in the afternoon, one could expect that the height of the stable TIBL should be higher than 1.8 m. The small values of  $h$  can be due to uncertainties when estimating for example  $\alpha$ . Since there were not enough levels measuring temperature, it was not possible to find a temperature profile for measuring  $A$ . Instead Garratt's value was used as an approximation. As can be seen in the small value of the obtained Richardson number, the conditions were close to neutral. It is possible that another type of expression should be used during such near neutral conditions on such a small scale.

### 5.3 Ice breeze circulation

On the morning of 3 March 1998 a vertical circulation started over the marginal ice zone outside the Umeå site. This phenomenon, called the ice breeze circulation was of somewhat larger scale than the TIBL formed on the 2 March. It was driven by the temperature contrast between land/ice and the open water 6 km south of the Umeå site. The ice breeze circulation is in fact the same thing as the land breeze that can develop during summer nights. They both are circulations with an offshore flow at the surface level and the mechanism responsible for the circulation is the same.

### 5.4 Theory - the sea/land breeze circulation

On clear calm days in coastal and lake-side areas it is common to find an onshore wind called sea breeze or lake breeze. At night the sea breeze is replaced by a weaker offshore flow. This is the land breeze. Both the sea breeze and the land breeze are parts of vertical circulation patterns based on the same mechanism. On clear days with low wind speed solar radiation heats up the land surface more quickly than the sea surface. This yields a temperature gradient between land and sea. Over land the air rises due to the heating of air by the warm land surface. Hydrostatic conditions make the vertical pressure gradient smaller over land



than over sea, so the pressure increase over land relative to the same height over sea. This horizontal pressure gradient causes a slight flow from land to sea. Over sea there is subsidence due to the cooling of air by the sea surface. The horizontal pressure gradient yields the flow from the sea towards land, which is the sea breeze. The opposite circulation occurs during night – the land breeze, from the land to the sea.

In the section above describing the circulation mechanism, conditions are simplified since the only factor, affecting the circulation that is considered is the temperature contrast between land and sea. In practice there are several factors that can have an effect on the development of a sea/land breeze circulation, one of the most important factors being the gradient wind. When strong gradient winds exist, the sea/land breeze does not develop. This is because the gradient wind simply destroys the much weaker sea/land breeze circulation or at least the temperature gradient responsible for it. On occasions with weaker gradient winds and a circulation, studies have concentrated on the effect of the gradient wind direction -onshore, offshore or parallel to the coast (Atkinson 1981). These studies have mostly been concerned with the sea breeze, since it is easier to observe than the land breeze. Because of the weakness of the land breeze, even small onshore gradient winds are likely to prevent the development of a land breeze circulation.

It is clear from the discussion above that the temperature contrast between land and sea must, in some manner, overcome the gradient wind. Lyons (1972) used the balance between the temperature contrast and the gradient wind in an effort to predict the Chicago lake breeze. He developed a simple forecasting scheme based on a dimensionless number,

$$\sigma = \frac{V_g^2}{C_p \Delta T} \quad (14)$$

where  $V_g$  is the geostrophic wind,  $C_p=1.005 \text{ Jg}^{-1}\text{K}^{-1}$  the specific heat of dry air and  $\Delta T$  the difference ( $^{\circ}\text{C}$ ) between the maximum air temperature over land and the mean water temperature. It was found that  $\sigma=10$  was a critical value. For values above 10 a lake breeze would not be expected at the shoreline.

### 5.5 Observation of the ice breeze

The ice breeze circulation was discovered on the morning of 3 March with pibal tracking technique. As seen in the wind profile from 6.30 UTC (Figure 18) the balloon started to change direction at 200-300 m height above ground. In the lowest 200 m the wind direction is about  $0^{\circ}$  which is offshore flow. Between 600 and 800 m the wind direction has changed to about  $220^{\circ}$  which is onshore flow. The same clear pattern was seen in wind profiles from 10.30 UTC and 12.30 UTC. On the morning the geostrophic wind was onshore. At 12.30 UTC it had changed direction to offshore but during the day it was never larger than  $8 \text{ ms}^{-1}$  in magnitude. The ice breeze circulation probably started around 6.00 UTC in the morning after the large decrease in air temperature.

It lasted throughout the afternoon and probably faded out around 18.00 UTC according to a weaker change in wind direction with height in the 18.30 UTC wind profile. The height of the ice breeze circulation was in the order of 500 to 1000 m during the whole day. The horizontal extension of the circulation was 6 to 10 km. In Figure 19 a schematic figure of the circulation

can be seen. The idealized streamlines as well as the trajectory of the pilot balloons are shown.

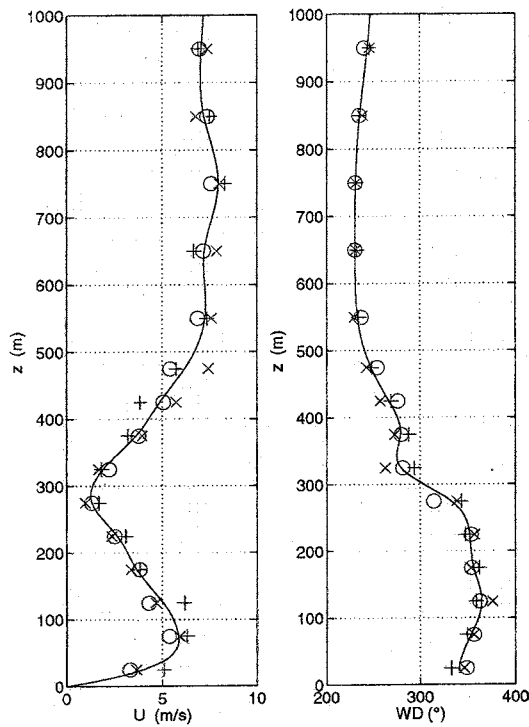


Figure 18. Wind speed and wind direction profile from the Umeå site at 6.30 the 3 March 1998. The different symbols indicate different balloons.

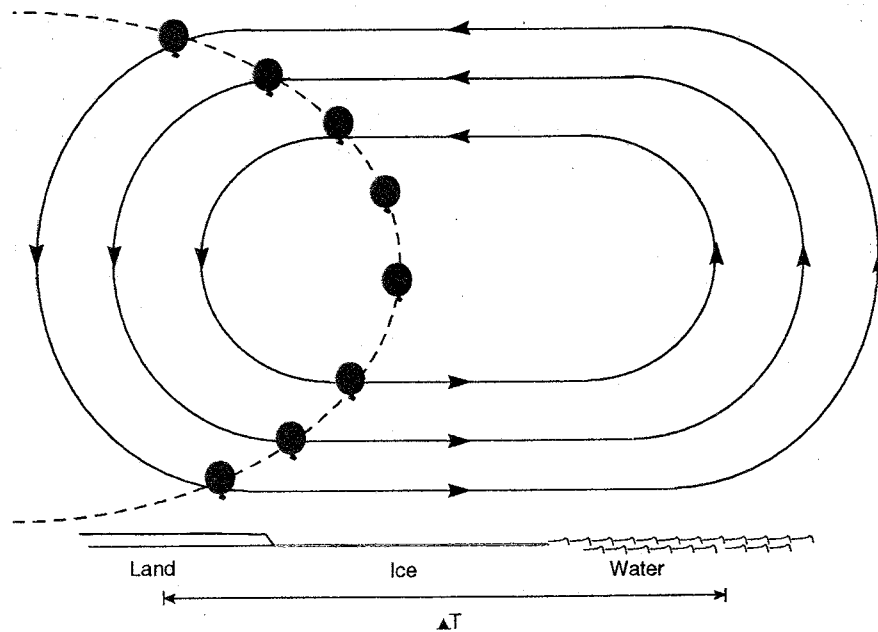


Figure 19. Schematic figure of the ice breeze circulation. The trajectory of the balloons is also shown.

## 5.6 Test of circulation criterion

As in the sea/land breeze case, the driving force of the ice breeze circulation is the temperature difference between sea and land/ice. In both cases the circulation is hindered if the gradient wind is too large. Since both cases depend on the same parameters it should be possible to use the same type of criterion for occurrence in the ice breeze case as in the sea breeze case. To see if this is true, Lyons criterion (Eq. 14) has been applied on the ice breeze case. The geostrophic wind is obtained from the wind profile and  $\Delta T$  is taken as the difference between the temperature at 3.5 m height at the Umeå mast and the water surface temperature. The latter is assumed to be 0 °C.

The criterion is applied on two occasions; at 6.30 UTC the 3 March, when it is known that an ice breeze was formed and at 14.30 UTC the 2 March when it is known that an ice breeze did not develop. At 6.30 the 3 March  $V_g=7 \text{ ms}^{-1}$  and  $\Delta T=10 \text{ °C}$ . Eq. (14) then yields  $\sigma=4.9$  which, with Lyons critical value  $\sigma=10$ , means that a circulation will start. At 14.30 UTC the 2 March  $V_g=12 \text{ ms}^{-1}$  and  $\Delta T=4 \text{ °C}$  which yields  $\sigma=36$ . Thus, with Lyons critical value, an ice breeze will not occur. According to these two results it appears that a criterion of the type that Lyons used, applies for the ice breeze. Even the critical value of  $\sigma=10$  seems to be of the right order. Numerical simulations of the ice breeze are presented in Magnusson (this issue).

## 5.8 Conclusions

It was shown that thermally induced phenomena develop over the marginal ice zone, just as they do at the coast during summer. Phenomena that can occur are thermal internal boundary layers (TIBLs) and 'ice breezes'. What kind of phenomenon that starts depends on the temperature difference between ice and sea as well as the large-scale wind.

During the study of the TIBL it was found that new ice and snow covered fast ice can be very different with respect to surface temperature and heat flux. This difference can be large enough to be responsible for the formation of a TIBL. The expression Garratt (1987) used to find the TIBL-height during offshore flow with long fetch is used on a much smaller scale with onshore flow. A somewhat lower height than expected is obtained, possibly due to the smaller scale and the more neutral conditions.

In the last section the 'ice breeze' was studied. It is the same type of circulation as the land/sea breeze but it occurs during winter at the marginal ice zone. A weak synoptic pressure field is important for the ice breeze to develop, since the geostrophic wind tends to destroy the circulation. Lyons (1972) used a criterion, based on the ratio of the geostrophic wind and the temperature difference between land and sea, to forecast the sea breeze. The same type of criterion appears to be applicable also for the ice breeze.

## References

- Atkinson, B. W., 1981: *Meso-scale Atmospheric Circulations*. Academic press, inc., 495 pp.
- BASIS, 2000: Second Annual Report from the Meteorology Group, Uppsala University to the EU-project BALTIC-BASIS (Baltic Sea Ice Study), contract no MAS-CT97-0117.
- Bradshaw, P., 1967: Inactive motion and pressure fluctuations in turbulent boundary layers. *J. Fluid Mech.*, **30**, Part 2, 241 – 258.

- Dyer, A.J., 1974: A review of flux-profile relationships. *Boundary-Layer Meteorol.*, **7**, 363 – 372.
- Garratt, J. R., 1987: The Stably Stratified Internal Boundary Layer for Steady and Diurnally Varying Offshore Flow. *Boundary-Layer Meteorology*, **38**, 369-394.
- Garratt, J. R., 1990: The Internal Boundary Layer – A Review. *Boundary-Layer Meteorology*, **50**, 171-203.
- Geernaert, G.L. and W.J. Plant, 1990: *Surface waves and fluxes*. Vol. 1 Current theory, 336 pp. Kluwer Acad., Norwell, Mass.
- Haugen, D.A., J.C. Kaimal and E.F. Bradley, 1971: An experimental study of Reynolds stress and heat flux in the atmospheric surface layer. *Quart. J. Roy. Met. Soc.*, **97**, 168 – 180.
- Hunt, J.C.R., 1984: Turbulence structure in thermal convection and shear-free boundary layers. *J. Fluid Mech.*, **138**, 161 – 184.
- Hunt, J.C.R., P. Moin, M. Lee, R.D. Moser, P. Spalart, N.N. Mansour, J.C. Kaimal and E. Gaynor, 1989: Cross correlations and length scales in turbulent flows near surfaces. *Advances in Turbulence*, **2** (ed.H. Fiedler and H. Fernholtz), Springer- Verlag pp 128 – 134.
- Hunt, J.C.R. and J.F. Morrison, 2000: Eddy structure in turbulent boundary layers. *Euro J. Mech, B – Fluids* **19**, 673 – 694.
- Hunt, J.C.R. and P. Carlotti, 2001: Statistical structure of the high Reynolds number turbulent boundary layer. *Flow, Turbulence, Combustion*, submitted.
- Högström, U., 1990: Analysis of turbulence structure in the surface layer with a modified similarity theory formulation for neutral conditions. *J. Atm. Sci.*, **47**, 1949 – 1972.
- Högström, U., 1992: Further evidence of inactive turbulence in the near neutral atmospheric surface layer. Proceedings, 10<sup>th</sup> Symposium of Turbulence and Diffusion, 29 Sept. – 2 Oct. 1992, Portland, Oregon, 188 – 191.
- Högström, U., H. Bergström, A. Smedman, S. Halldin and A. Lindroth, 1989: Turbulent exchange above a pine forest. I: Fluxes and gradients. *Boundary-Layer Meteorol.*, **49**, 197 – 217.
- Högström, U. and H. Bergström, 1996: Organized turbulence structures in the near-neutral surface layer. *J. Atm. Sci.*, **53**, 2452 – 2464.
- Johansson, C., A. Smedman, U. Högström, J.G. Brasseur and S. Khanna, 2000: Critical test of Monin-Obukhov similarity during convective conditions. *J. Atm. Sci.*, accepted.
- Källstrand, B., 1998: Low-Level Jets in a Marine Boundary Layer During Spring. *Contrib. Atmos. Phys.*, **71**, 359-373.
- Lyons, W. A., 1972: The Climatology and Prediction of the Chicago Lake Breeze. *J. Appl. Meteor.*, **11**, 1259-1270.
- Magnusson, M. 1999: Meso Scale Circulation Observed in a Coastal Area During Winter Conditions. Proc. AMS 13<sup>th</sup> Symposium on Boundary Layers and Turbulence, Dallas, January 199, 640-641.
- Mann, J., 1994: The spatial structure of neutral atmospheric surface-layer turbulence. *J. Fluid Mech.*, **273**, 141 – 168.
- Marusic, I. And Perry, A.E., 1995: A wake model for the turbulence structure of boundary layers. Part 2. Further experimental support. *J. Fluid Mech.*, **298**, 389 – 407.
- Mulhearn, P. J., 1981: On the Formation of a Stably Stratified Internal Boundary-Layer by Advection of Warm Air over a Cooler Sea. *Boundary-Layer Meteorology*, **21**, 247-254.
- Panofsky, H.A., H. Tennekes, D.H. Lenschow and J.C. Wyngaard, 1977: The

- characteristics of turbulent velocity components in the surface layer under convective conditions. *Boundary-Layer Meteorol.*, **11**, 355 – 361.
- Panofsky, H. A. and Dutton, J. A., 1984: *Atmospheric Turbulence-Models and Methods for Engineering Applications*. John Wiley & Sons, Inc., 397 pp.
- Smedman, A., 1991a: Some turbulence characteristics in stable atmospheric boundary layer flow. *J. Atm. Sci.*, **48**, 856 – 868.
- Smedman, A., 1991b: Occurrence of roll circulations in a shallow boundary layer. *Boundary-Layer Meteorology*, **57**, 343 – 358.
- Smedman, A.-S., Tjernström, M., Högström, U., 1993: Analysis of the Turbulence Structure of a Marine Low-Level Jet. *BLM*, **6**, 105-126.
- Smedman, A., M. Tjernström and U. Högström, 1994: The near-neutral marine atmospheric boundary layer with no surface shearing stress: a case study. *J. Atm. Sci.*, **51**, 3399 – 3411.
- Smedman, A.-S., Bergström, H., Högström, U., 1995: Spectra, Variances and Length Scales in a Marine Stable Boundary Layer Dominated by a Low-Level Jet. *BLM*, **76**, 211-232.
- Smedman, A., U. Högström, H. Bergström, A. Rutgerson, K.K. Kahma and H. Pettersson, 1999: A case study of air-sea interaction during swell conditions. *J. Geophys. Res.*, **104**, 25,833-25,851.
- Smith, S.D. and E.G. Banke, 1975: Variation of the sea surface drag coefficient with wind speed. *Quart. J. Roy. Met. Soc.*, **101**, 665 – 673.
- Stull, R. B., 1988: *An Introduction to Boundary Layer Meteorology*. Kluwer Acad. Publishers, 666 pp.
- Townsend, A.A., 1961: Equilibrium layers and wall turbulence. *J. Fluid Mech.*, **11**, 97-120.
- Townsend, A.A., 1976: *The structure of turbulent shear flow*. Cambridge University Press
- Zilitinkevich, S. and Calanca, P., 1999: An extended similarity-theory formulation for the stably stratified atmospheric surface layer. Accepted for publication in *Quart. J. Roy. Meteorol. Soc.*
- Zilitinkevich, S. et al., 2000: Diagnostic and prognostic equations for the depth of the stably stratified Ekman boundary layer. Submitted to *Quart. J. Roy. Meteorol. Soc.*

## Turbulent Surface Fluxes and Air-Ice Coupling

Jouko Launiainen, Bin Cheng, Juha Uotila and Timo Vihma

Finnish Institute of Marine Research, Helsinki

### 1. Introduction

Accurate estimation of local turbulent surface fluxes form a central question in air-ice studies (Hicks and Martin, 1972; Banke et al., 1980; Andreas, 1987; King and Anderson, 1994; Smeets et al., 1999) and modelling (Launiainen and Cheng, 1998) as well as in those of regional estimation and modelling (Claussen, 1991; Vihma, 1995; Essery, 1997). The regional approach most frequently involves to the estimation of spatially representative values over a heterogeneous surface, formed by a mosaic of ice of various thickness, and cracks and leads. Estimation of the local surface fluxes is even then a prerequisite for areal estimation.

Accurate determination of the turbulent fluxes and air-ice-ocean coupling and modelling were important goals of BASIS. In the air-ice coupling, the primary quantities to be studied include fluxes of momentum, heat and water vapour (latent heat), radiative fluxes, and air-ice interfacial (surface) temperature. In the report, we introduce the FIMR process studies of local air-ice coupling based on the measurements carried out at the *RV Aranda* Ice Station. Some results are given in Launiainen et al. 2001. The experiment and the data are introduced in the BALTEX-BASIS Data Report (Launiainen, 1999).

### 2. Observations and methods

#### 2.1 Measurements

Measurements focused on the air-ice coupling included momentum and sensible heat eddy-flux measurements (sonic anemometer Metek USA-1 with a path length of 180 mm, at a height of 2.25 m), and wind and air temperature measurements on a 10 m high profile mast on the sea ice. The wind speed was measured at 5 levels (at nominal heights of 10.13, 4.73, 2.43, 1.23, 0.53m by cup anemometers, Aanderaa Instruments Co.) and temperature at 3 levels (10.08, 2.38, 0.48m by film-type platinum resistors Aanderaa Instruments Co.). The profile gradients from the mast allow us to calculate the fluxes of momentum and sensible heat for comparison with the eddy-flux results. The sonic anemometer data were corrected by a geometric redress procedure for a potential tilt error of the axis, especially a deviation of the z-axis from the vertical. Sensor calibration of the mast was carried out in a wind tunnel and a temperature test tank before and after the field work, and specific attention was paid to the mutual comparison of the sensors. In addition to the sonic and mast measurements, radiation fluxes were measured and, in-ice and in-snow temperature time series were observed.

For general meteorological conditions, see Chapt. 2 and the report by Brümmer et al. in Chapt. 3 in this volume.

## 2.2 Methods .

### *Fluxes, gradient and bulk aerodynamic calculations*

In the surface layer, the turbulent fluxes (a-forms) of momentum ( $\tau$ ) and sensible heat ( $H$ ) can be expressed in the gradient (b) and bulk forms (c):

$$\tau = -\rho \overline{u'w'} = \rho K_M \frac{\partial V}{\partial z} = \rho u_*^2 = \rho C_D V_z^2 \quad (1)$$

$$H = \rho c_p \overline{\Theta'w'} = -\rho c_p K_H \frac{\partial \Theta}{\partial z} = \rho c_p C_H (\Theta_s - \Theta_z) V_z \quad (2)$$

$$E = \rho \overline{q'w'} = -\rho K_E \frac{\partial q}{\partial z} = \rho C_E (q_s - q_z) V_z \quad (3)$$

(a)                      (b)                      (c)

where  $V_z$  denotes wind speed at a height  $z$ ,  $u_*$  friction velocity,  $\Theta$  potential temperature,  $\rho$  air density, and  $c_p$  specific heat capacity of air.  $\Theta_s - \Theta_z$  and  $q_s - q_z$  are the differences in potential temperature and specific humidity between the surface and the atmosphere, respectively. Multiplying (3) by the latent heat of fusion, the latent heat flux is obtained.  $K_M$  and  $K_H$  and  $K_E$  are the gradient method eddy diffusivities for momentum, heat and water vapour. For most marine and over-ice studies, the fluxes have to be estimated using the bulk formulae (c-forms). The task to find relevant estimates for the local bulk transfer coefficients was a primary goal of BASIS.

From the Monin-Obukhov (M-O) similarity theory, which connects the flux-profile relationships and the bulk transfer coefficients (see Garratt, 1992; Launiainen, 1995), the bulk transfer coefficients for momentum ( $C_D$ ) and heat ( $C_H$ ) are defined as

$$C_D = C(z, z_0, \Psi_M(z/L)), \quad C_H = C(z, z_0, z_T, \Psi_M(z/L), \Psi_H(z/L)) \quad (4)$$

where  $z_0$  and  $z_T$  are the roughness lengths for velocity and temperature, respectively.  $\Psi_M$  and  $\Psi_H$  are universal functions which give the effect of atmospheric stratification, in terms of the Obukhov length  $L$ . The effects of stability and the universal functions vanish in neutral conditions. The above formulation indicates that for estimation of fluxes by bulk formulae, the local aerodynamic roughness lengths ( $z_0$ ,  $z_T$ ) or the local bulk transfer coefficients ( $C_D$ ,  $C_H$ ) must be known. In addition, because the case-specific parameter  $L$  (in the argument of the universal functions) includes the fluxes to be defined, the bulk calculation leads to an iterative solution, except in a rough first-order estimation not taking the stability explicitly into account. Additionally, it is common to assume and supported by theoretical arguments that the bulk coefficient for water vapour follows close to that of sensible heat i.e.  $C_E \cong C_H$ .

### *Eddy flux method*

Using an eddy fluctuation measuring equipment, the fluxes can be measured directly according to the (a) forms of (1) to (3). Having other necessary meteorological data for bulk aerodynamic calculation those yield data for derivation of the diabatic bulk transfer coefficients. By using relevant universal functions, the neutral bulk transfer coefficients  $C_{DN}$  and  $C_{HN}$  can be derived from the diabatic coefficients of (4).

### *Gradient method*

Based on the M-O similarity theory, the fluxes can also be defined from profile gradient measurements, because the profile gradient form (b) transfer coefficients are defined as

$$K_M = \frac{ku_*z}{\Phi_M(z/L)}, \quad K_H = \frac{ku_*z}{\Phi_H(z/L)} \quad (5)$$

where the functions  $\Phi_M$  and  $\Phi_H$  are the gradient-form universal functions for velocity and temperature, and  $k$  is the von Karman constant. By making accurate gradient measurements, we may solve for the fluxes from (1b), (2b) and (5). Accordingly, the gradient of wind speed gives  $u_*$  and  $\tau$  from (5) and (1b). Then, the temperature gradient yields the heat flux  $H$ . We should again note, however, that because the argument ( $z/L$ ) in the universal functions  $\Phi_M$  and  $\Phi_H$  includes the fluxes to be solved ( $u_*$ ,  $H$ ), the final solution is iterative. For our study, a modified algorithm developed by Launiainen and Vihma (1990) was applied. Regarding the universal functions, for the unstable regions the Businger (1971) - Dyer (1974) type forms with Högrström's (1988) coefficients were adopted, while for the stable region those of Holtslag and De Bruin (1988) were used. For the formulae, see e.g. Launiainen (1995; pp. 177-178).

As for the water vapour flux and latent heat, M-O similarity-theory-based forms analogic to those for the sensible heat can be given. In our study, however, no eddy-flux equipment or profile measurements were used. Instead, we estimated these fluxes using a single-level moisture measurement and the bulk aerodynamic method (3c). For the latter, calculation of the specific saturation humidity, to correspond to the surface temperature, forms a difficulty because accurate snow and ice temperature estimation is not any trivial. We first estimated the surface temperature using eq. (7) below, and then we used the bulk form to calculate the fluxes. We believe the gradient method for the water vapour and latent heat flux to be inaccurate in cold conditions, due to the smallness of the humidity gradients. Inaccuracy in the snow and ice surface temperature estimation forms a general problematic of application of the bulk method for the sensible heat calculation as well.

### *Coupled model*

As the third method to determine the turbulent surface fluxes, a coupled one-dimensional multi-layer thermodynamic model (Launiainen and Cheng, 1998; Cheng and others, 2001) was used. In the model, air and snow/ice are coupled by the heat fluxes and the interface temperature calculated at each time step. In addition to the ice thermodynamics, the model produces air-ice fluxes and stability parameter, and profiles of wind speed, temperature and moisture. As a meteorological input the model uses a level wind speed, temperature and moisture. Those may be arbitrary and mutually different. The model has been tested and yields heat flux, momentum flux, surface energy balance, surface temperature and in-ice temperatures rather accurately. For bulk calculation of the fluxes, the modelled surface temperature is used, so that the method is practically independent of the eddy flux and gradient methods described above.



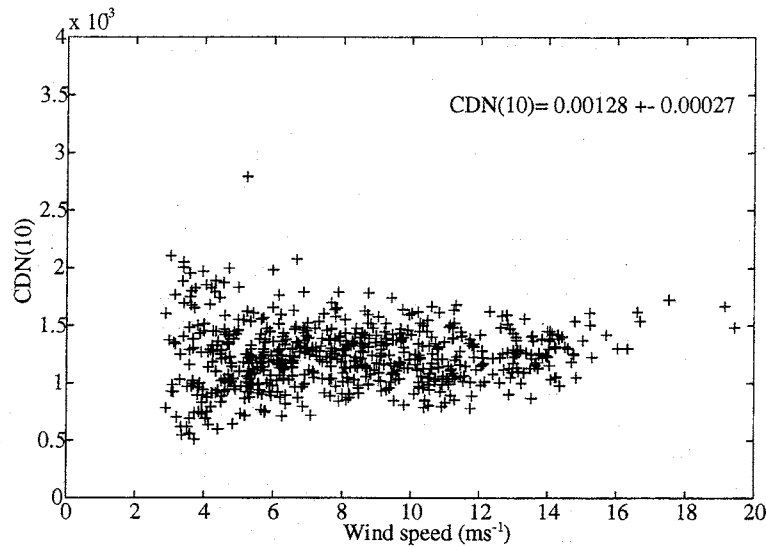


Figure 1. Eddy flux derived drag coefficient  $C_{DN}(10)$  as a function of wind speed at the Aranda Ice Station during BASIS-98, 17 February - 6 March, 1998. (0.5 h means).

### 3. Results and discussion

#### 3.1 Drag coefficient and aerodynamic roughness length

The neutral drag coefficient derived from the momentum flux measurements, eq. (1a), and corrected for stability  $C_{DN} = k^2 / (\ln z/z_0)^2$ , is shown as a function of wind speed in Figure 1. The results show no apparent wind speed dependence, and the mean  $C_{DN}(10) = 1.28 \times 10^{-3}$  corresponds to a mean aerodynamic roughness length  $z_0 = 1.2 \times 10^{-4}$  m. Actually, all the points (13 in all) corresponding to the highest wind velocities and a higher drag coefficient are from the same snowstorm episode. During this storm blowing snow and sastrugi were observed on the surface which might explain the higher drag coefficients. Generally, the results are to be regarded as reliable, because the results based on the above-described profile gradient method from (1b), (5) and (1c) resulted in very comparable drag coefficients, as can be seen from the comparison in Figure 2.

The experimental site was located in an archipelago in a coastal area surrounded by an asymmetric island and coast-line geometry and orography and asymmetric roughness along the wind direction. Investigation of the neutral drag coefficient indicated an apparent dependence on the wind direction, i.e. a dependence on the geometric roughness of the sea ice and of that of the land and archipelago in the coast. This can be seen from Figure 3, which gives the neutral drag coefficient versus the wind direction, as projected on a map of the observation area. The drag coefficient shows an interesting behaviour. From the direction of the archipelago, in the north and north-east, with a short fetch, the drag coefficient is comparatively high. From the south, west and north-west, the drag coefficients pretty well correspond with the main observed characteristics of the sea ice along the upwind fetch. Although the results seem quite reasonable, the upwind fetch in the direction of the deformed ice was unfortunately, not homogenous enough and the strict geometric to aerodynamic sea ice roughness ratio quantification still seems to remain as semi-quantitative. An analysis with respect to the helicopter laser roughness profiling data is still in progress. Based on visual

observations, Radarsat images and photographs from a helicopter we can assume the drag coefficient  $C_{DN}(10)$  to be  $1.0 \times 10^{-3}$  ( $z_0 \cong 2.7 \times 10^{-5}$  m) for smooth snow-covered ice, and  $1.5 \times 10^{-3}$  ( $z_0 \cong 2.9 \times 10^{-4}$  m) for the rougher ice in the west, refrozen from broken ice fields. Even so, no apparent wind speed dependence of the aerodynamic roughness or drag coefficient was found for any of the surface types.

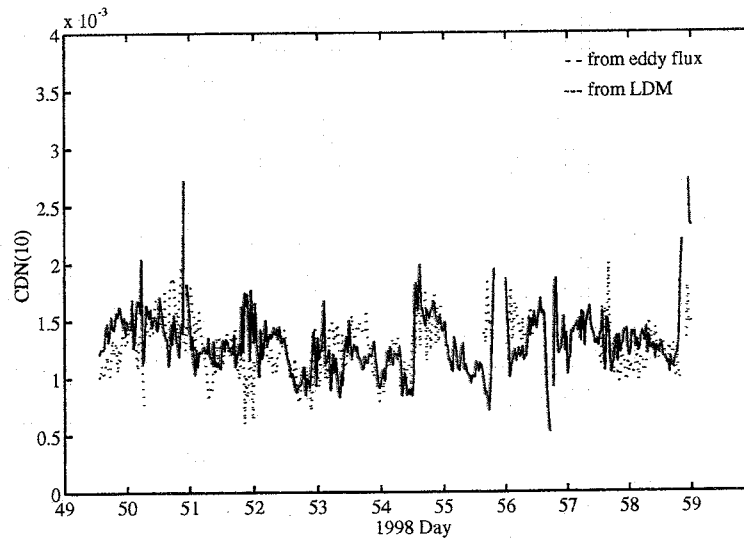


Figure 2. Neutral drag coefficient  $C_{DN}(10)$  time series as defined from the eddy flux (blue dotted) and profile-gradient method (red continuous line).

As for the roughness characterization in terms of a “rougher” sea ice, we are speaking about a deformed sea ice composed in this case of thin (0.3 - 0.4 m) Baltic Sea coastal ice of 100 % concentration, including no ridges and roughness elements higher than 0.3 to 0.6 m. Therefore, when referred e.g. to the northern polar sea ice roughness classification by Guest and Davidson (1991), our field site would correspond to smooth first- or multiyear sea ice with no pressure ridges. Actually, the (more or less subjective) ice roughness characterization and numerical drag coefficient results in the literature vary quite a lot, as is evident from e.g. Hofmann (1998; Table 4.1). The sea ice roughness information is given almost without exception in qualitative or semi-quantitative terms. The above definition and numerical uncertainty may be reflected in part e.g. as a large variability in the drag coefficients used by models in atmosphere-ice momentum flux calculations (Harder and Fischer, 1999). We believe that for a universal resistance quantification and characterization of sea ice we still need additional high-quality aerodynamic roughness data as well as quantification of the height and distribution of the geometric roughness elements (cf. the nice first effort by Banke et al., 1980).

### 3.2 Heat transfer coefficient and temperature roughness length

For the study period, the sensible heat flux was measured by the sonic anemometer and derived from the profile gradient measurements, but an estimation of the bulk heat exchange coefficient  $C_{HN} = k^2 / (\ln z / z_0)(\ln z / z_T)$  and the temperature roughness length ( $z_T$ ) is more problematic. For determination of the bulk heat transfer coefficient from (2c), very accurate surface temperature needs to be known. Experience gained from BASIS suggests that derivation of the surface temperature, even from radiation measurements, is not trivial and

was insufficiently accurate for the purpose. Therefore, we studied the temperature roughness length in conditions for which we believe the estimation of the surface temperature to have been most accurate, i.e. when the temperature remained at the freezing point. We first calculated the air-ice interface temperature using the coupled thermodynamic model. In cases for which the model estimates an apparent positive surface heat balance and melting, we assume the surface temperature to be  $0^{\circ}\text{C}$ . Under variable and mild ( $\Theta_z > T_s$ ) weather during the field campaign, we had several periods of such conditions (cf. Figure 7). For those cases we could then calculate the bulk transfer coefficients and the roughness length for temperature from (2) and (3).

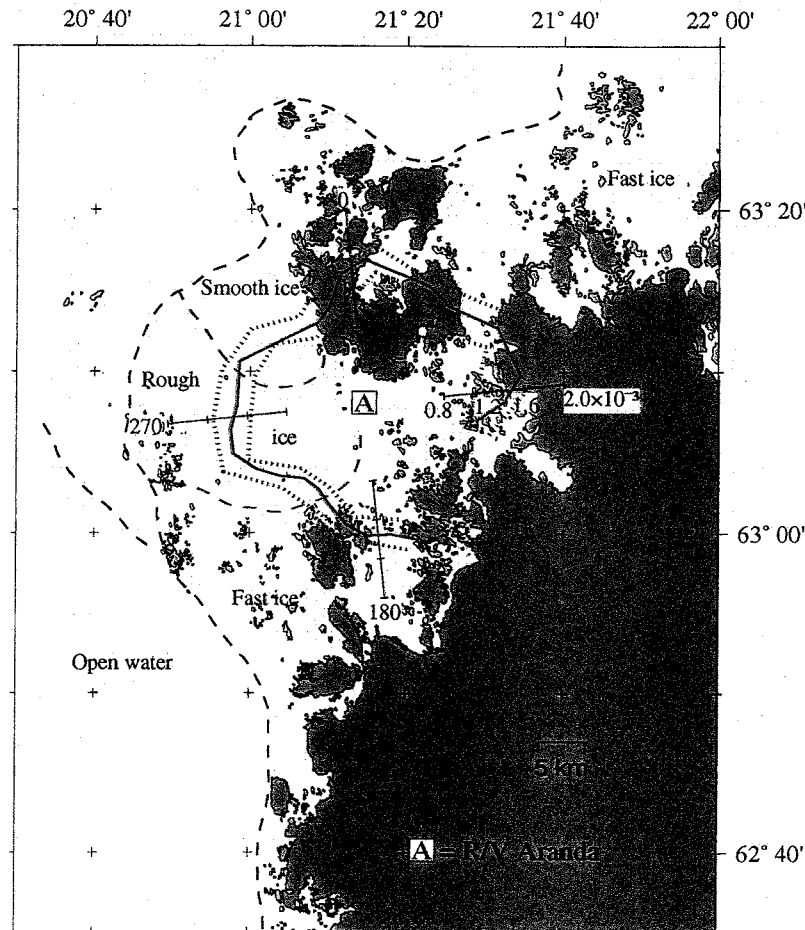


Figure 3. Drag coefficient and its deviation versus the wind direction (continuous red curve and broken green contours) observed at the *RV Aranda* Ice Station [A], as projected on a map of the observation area in the Archipelago in the Northern Baltic Sea.

The results indicate the temperature roughness and aerodynamic roughness to be of the same order of magnitude, and suggest the scalar roughness to be slightly larger than the aerodynamic roughness for low wind velocities, whereas  $z_T < z_0$  for winds higher than 4 - 5  $\text{ms}^{-1}$ . An apparent dependence of  $z_T$  on wind speed was found and  $z_T$  decreased with wind. The results are shown in terms of the aerodynamic to scalar roughness length ratio of  $\ln(z_0/z_T) = kB^{-1}$  in Figure 4 with respect to a roughness Reynolds number, in order to make the results

less case-specific. The Reynolds number we use is defined  $Re = (z_0 \cdot V)v^{-1}$ , where  $v$  is the kinematic viscosity. We prefer this Reynolds number to the commonly used  $Re = (z_0 \cdot u_* )v^{-1}$  (e.g. Owen and Thomson, 1960; Andreas, 1987) because we do not have an accurate method simultaneously to define  $z_0$  and  $u_*$  independently. In terms of  $Re$ , a fit with our  $\ln(z_0/z_T)$  data is given in Figure 4. As parameterized, our results of  $\ln(z_0/z_T)$  can be written in a linear form as

$$\ln(z_0/z_T) = s + a V \quad \text{or}$$

$$C_{HN} = kC_{DN}^{1/2} (\ln z/z_T)^{-1} \cong C_{DN} (1 + C_{DN}^{1/2} k^{-1} (s + aV))^{-1} \quad (6)$$

where  $C_{DN} = k^2 (\ln(z/z_0))^{-2}$  and  $s = -0.80$  and  $a = 0.15$  for wind speed at a height of 2 m. For a wind referred to 10 m,  $a = 0.13$ . For a site with  $C_{DN}$  or  $z_0$  known, (6) should give a reasonable estimate of  $C_H$  and  $z_T$ .

The region of our  $z_0$  observations in the analysis was limited of from  $3 \times 10^{-5}$  to  $9 \times 10^{-4}$  m, i.e.  $C_{DN}(10) = 1.0 \times 10^{-3}$  to  $1.9 \times 10^{-3}$  and wind speeds of from 3 to 15  $\text{ms}^{-1}$ . The analysis (Figure 4) suggests that for higher aerodynamic roughness and wind speeds an asymptotic value  $\ln(z_0/z_T) \cong 2$  is attained. This value is in good agreement with the findings of Garratt (1978,1992) for rough surfaces with  $z_0/z_T = 7.3$ . Accordingly, our results might serve as proper first estimates for even higher wind speeds and roughness lengths. Generally, the dependence of the roughness ratio found is in agreement with wind tunnel studies, theoretical arguments and parametrizations for conditions over natural surfaces (Owen Thomson, 1960; Garratt, 1992; Andreas, 1987) and with field studies (Hicks and Martin, 1972; Joffre, 1982). Strictly, our results cannot be compared with those of Andreas (1987) because of the different definition of  $Re$ . Still, if we estimate  $\ln(z_0/z_T)$  according to Andreas (1987), using our mean  $z_0$  and  $u_* = f(z_0, V, \text{stability})$ , the results are in rather good agreement with our data.

### 3.3 Fluxes of momentum and heat

As described above, the profile gradient data provided us an independent second method to determine the turbulent fluxes and transfer coefficients. The results of the gradient method calculations are compared with the eddy flux results in Figure 5a and 5b, and the fluxes calculated with the thermodynamic ice model are also shown for comparison. The gradient method (also called the level difference method LDM) results shown are based on measurements from the (nominal) levels of 2.4 m and 0.5 m. The results indicate the eddy flux and gradient methods to agree well. The sensible heat flux comparison is given in Figure 5a only up to the Julian day 59, 1998. The LDM results were not presented in the comparison after this date, because the LDM was inaccurate due to very low wind speeds, small turbulent fluxes and large daily short-wave radiation fluxes interfering.

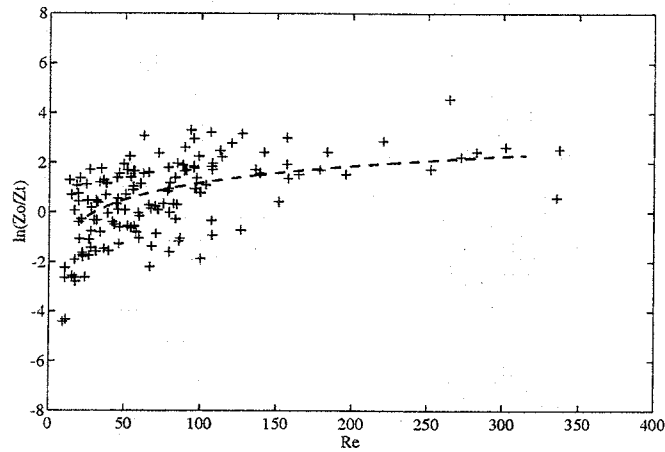


Figure 4. Ratio of the aerodynamic roughness to the temperature roughness  $\ln(z_0/z_T)$  as a function of the roughness Reynolds number ( $Re = z_0 \cdot V \nu^{-1}$ ). A fit  $z_0/z_T = 0.035 Re^{0.98}$  is given as broken curve ( $20 < Re < 300$ ).

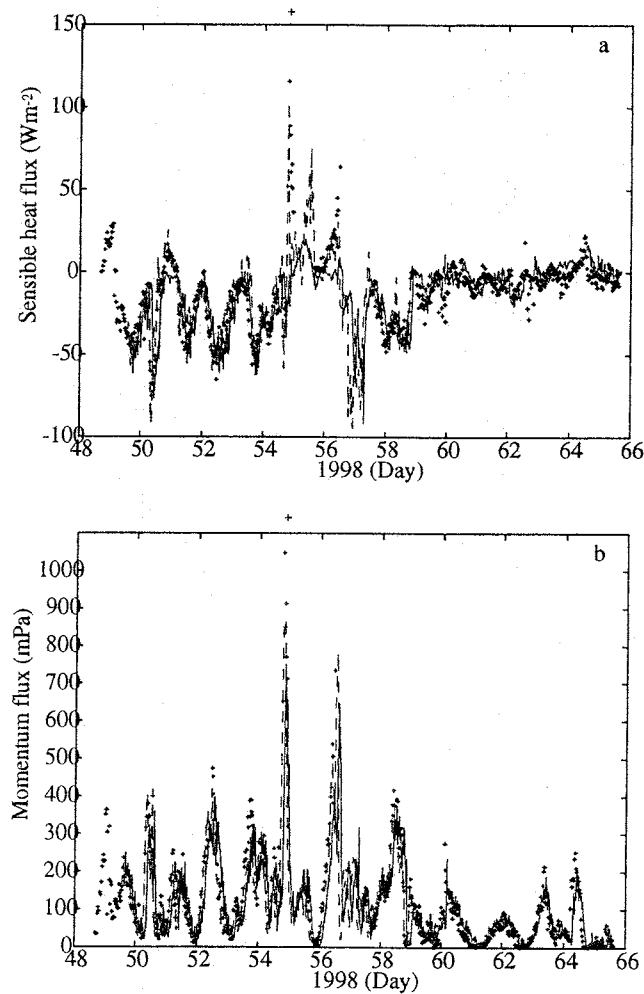


Figure 5. Time series of the sensible heat flux (4a) and momentum flux (4b). Crosses (black) give the results of the eddy flux observations. Broken line (red) gives the gradient method results (LDM) and the continuous line (blue) is the estimation by the coupled ice model. (Half hour means.)

The flux estimates by the coupled thermodynamic ice model generally agree with those of the two other methods. Actually, during the later part of the study period, from day 59 onwards, the magnitude of the sensible heat flux tends to be too small for any quantitative comparison (Figure 5a). During days 54 - 56, the ice model seems to smooth out the high, short-period flux variations. These were connected with cold snowstorms. Instead, the momentum flux is well estimated, even during the large peaks in Figure 5b. This gives us a reason to investigate whether the heat flux smoothing is due to a thermal "inertia" in the ice model. This will be studied using a shorter model time step.

The time series of the stability parameter  $z/L$  is given in Figure 6. As can be seen, the stability characteristics derived from the direct eddy-flux measurements and LDM are almost identical.

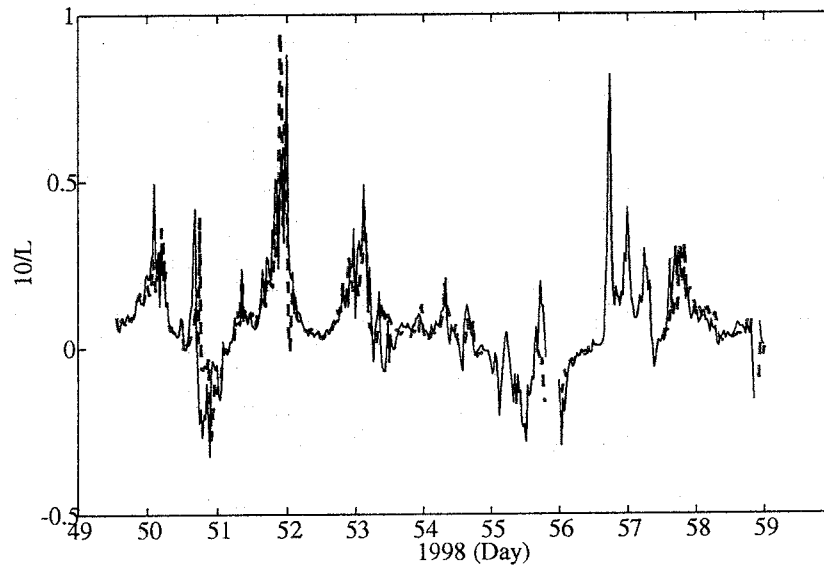


Figure 6. Time series of the stability parameter  $10z/L$  as calculated from the eddy flux results (broken) and profile gradient method (continuous).

### 3.4 Surface temperature

We may calculate and compare the various estimates of the surface temperature. The flux-profile gradient relation (2) gives as integrated (e.g. Launiainen and Vihma, 1990):

$$T_s = \Theta_z + \frac{H(\ln z/z_0 - \Psi_M(z/L))(\ln z/z_T - \Psi_H(z/L))}{\rho c_p k^2 V_z} \quad (6)$$

Estimates according to (6), based both on the sonic anemometer and LDM data, were calculated and the results are shown in Figure 7, together with the surface temperature predicted by the ice model. (For the LDM-based estimate, the  $z_T$  used was that derived above from the eddy flux data, but this has a minor effect on these results.) As can be seen, the three alternatives generally agree well and seem to be effective tools for surface temperature estimation. This was also supported by the temperature estimate based on thermal radiation

measurements for the first half of the measurement period, (for clarity, those are not shown in Figure 7). However, in conditions of small fluxes but large variations in meteorological forcing, as from day 59 onwards, the ice model may not follow all the variations. The other methods and especially the sonic anemometer based temperature estimation detected those well. This last conclusion was supported by the variations in the temperature estimate based on thermal radiation measurements.

### 3.5 Latent heat flux

The above  $T_s$  for determination of  $q_s$ , and  $C_E \equiv C_H = C(z, z_0, z_T, \Psi_M(z/L), \Psi_H(z/L))$  from (4) allow us to derive the water vapour and latent heat flux by the bulk method (3c), finally. Figure 8 gives the time series of the latent heat flux during BASIS. The surface temperature used for the bulk method is the one derived from the sonic based temperature profile. The latent heat flux calculated by the ice model is given for comparison. We may find a good overall agreement although we see the ice model to smoothen out the highest peaks and variations. It is noteworthy that the highest peak of over  $100 \text{ Wm}^{-2}$  is not any measurement error, likely. It is connected with a sudden rise of the cold snow storm from the north to over a warm and wet melting snow and ice. In the occasion, the sonic anemometer measured the sensible heat flux of over  $150 \text{ Wm}^{-2}$  (Figure 5a).

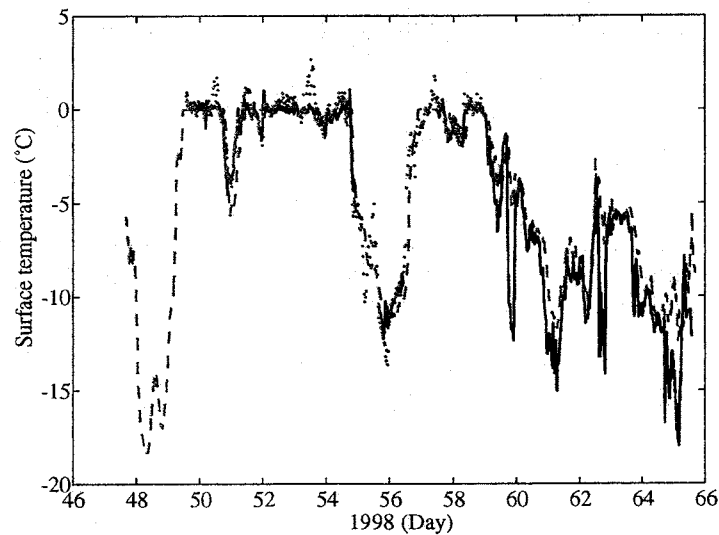


Figure 7. Surface temperature during BASIS as derived by the coupled model (broken, blue), and by eq. (6) using the eddy flux data (continuous, black) and profile gradient data (dotted, red).

### 3.6 Universal functions

The universal functions used for the determination of fluxes and transfer coefficients by the LDM method and the ice model) yielded results of reasonable agreement with those from the sonic anemometer. Strictly however, a detailed analysis of the observed diabatic eddy-flux based transfer coefficients with the observed fluxes and the  $M-O$  similarity-theory based flux-profile relationships suggests that the current universal functions for the stable region suppress the turbulence and transfer coefficients too much. This is to be seen in Figure 9.

For stability up to  $10/L = 0.5$ , the well-known universal functions of Webb (1972) and Holtslag and De Bruin (1988) yield 10 to 12 % lower bulk transfer coefficients than those defined from our data. For  $10/L = 1$  the above difference was 15 to 17 %. Actually, the non-linear Holtslag and De Bruin (1988) form, defined particularly for the strongly stable region, gives essentially the comparable results for less stable conditions with the usual linear form by Webb (1970), i.e.  $\Psi_M = \Psi_H = -5z/L$ . Up to  $10/L = 1$  our data well supports to these formulae. For strong stability, our data suggests  $\Psi_M = -3.5z/L$  and thus suggests stability to suppress turbulence and the bulk transfer coefficients less than estimated by those common universal functions. The search for an overall improved universal function form is still in progress. (Note that Figure 9 is given in terms of  $2/L$  corresponding to our measurement level).

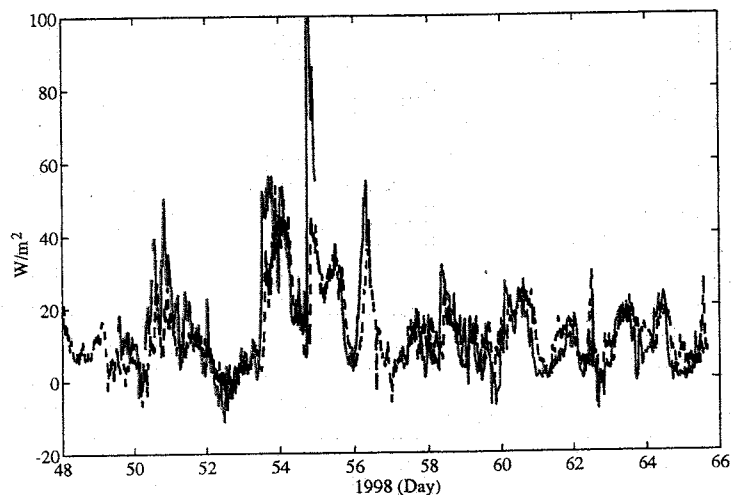


Figure 8. Latent heat flux ( $\text{W/m}^2$ ) during BASIS as calculated by the bulk aerodynamic method (continuous) and by the ice model (broken).

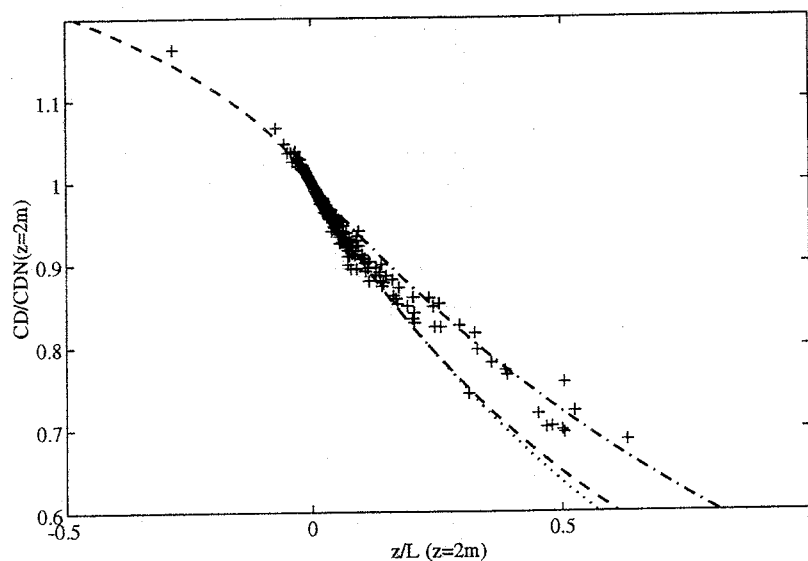


Figure 9. Observed stability dependence of the drag coefficient (crosses; from the sonic) compared with the estimations calculated by the universal functions of Webb (1970; dotted) and Holtslag and De Bruin (1988; broken). The dash-dot line corresponds to  $\Psi_M = -3.5z/L$ .



#### 4. Conclusions

To summary, we believe that the turbulent transfer coefficients and fluxes for the BASIS Ice Station are determined accurately. The drag coefficient (aerodynamic roughness) did not reveal a wind-speed dependence. The agreement of the gradient-method results with the eddy-flux results supports the validity of the Monin-Obukhov similarity theory, in conditions satisfying the preconditions for the theory. The third alternative for comparison, fluxes modelled by the coupled air-ice model compared reasonable well with the eddy flux and gradient methods.

Analysis of the roughness lengths indicated the temperature roughness to be comparable or slightly larger than the aerodynamic roughness for low wind speeds, but  $z_0 > z_T$  for moderate and strong winds. Accordingly, the temperature roughness length and bulk heat transfer coefficients can be reasonably approximated by eq. (6) for winds up to  $20 \text{ ms}^{-1}$ .

Surface temperature estimation by all three methods compared mutually well, and these may, except for some limitations regarding to the ice model, serve as a tool for temperature estimation. Then, methods to determine the relevant surface temperature allowed us to estimate the latent heat flux using a level moisture measurement and the bulk method.

For strong stability, our data suggest stability to suppress turbulence and the bulk transfer coefficients less than estimated by the most common current universal functions. The flux verification and temperature comparison justify the overall relevancy of the constructed ice model and indicate model's potential for process studies.

Finally, we cannot overemphasise the need for accurate and strict calibration of sensors, especially for the gradient method. In addition to the sensor calibration (temperature, wind speed), we note that an inaccuracy in the measuring heights, say 5 cm when defining gradients in the lowest few metres, causes significant error ( $\sim 10\%$ ) in fluxes and bulk transfer coefficients determined by the LDM method.

#### Acknowledgements

Captain Jarmo Jansson and his crew are acknowledged for the operations of the RV Aranda Ice Station. Milla Johansson, Pekka Kosloff, Tero Purokoski, Henry Söderman and Hannu Vuori are kindly acknowledged for the research assistance in the Ice Station.

#### References

- Anderson, R. J. 1987. Wind stress measurements over rough ice during the 1984 marginal ice zone experiment. *J. Geophys. Res.*, **92**(C7), 6933-6941.
- Andreas, E.L. 1987. A theory for the scalar roughness and the scalar transfer coefficient over snow and sea ice. *Boundary-Layer Meteorol.*, **38**, 159-184.
- Banke, E.G., S.D. Smith and R.J. Anderson. 1980. Drag coefficient at AIDJEX from sonic anemometer measurement. *International Association of Hydrological Sciences Publication 124* (Symposium at Seattle 1997 --- Sea Ice Processes and Models), 430-442.
- Cheng, B., J. Launiainen, T. Vihma and J. Uotila. 2001. Modelling sea ice thermodynamics in BALTEX-BASIS. *Ann. Glaciol.*, (in press).
- Claussen, M. 1991. Estimation of areally-averaged surface fluxes. *Boundary-Layer*

- Meteorol.*, **54**, 387-410.
- Essery, R. 1997. Modelling fluxes of momentum, sensible heat and latent heat over heterogeneous snow cover. *Quart. J. Roy. Meteorol. Soc.*, **123**, 1867-1883.
- Garratt, J. 1978. Flux-profile relations above tall vegetation. *Quart. J. Roy. Meteorol. Soc.*, **104**, 199-211.
- Garbrecht, T., C. Lupkes, E. Augstein and C. Wamser. 1999. Influence of a sea ice ridge on low-level air-flow. *J. Geophys. Res.*, **104**(D20), 24499-24507.
- Garratt, J. 1992. *The Atmospheric Boundary Layer*, Cambridge Univ. Press, Cambridge, 316 p.
- Guest, P.S. and K.L. Davidson. 1991. The aerodynamic roughness of different type of sea ice. *J. Geophys. Res.*, **96**(C3), 4709-4721.
- Harder, M. and H. Fischer. 1999. Sea ice dynamics in the Weddell Sea simulated with an optimized model. *J. Geophys. Res.*, **104**(C5), 11151-11162.
- Hicks, B. B. and H.C. Martin. 1972. Atmospheric turbulent fluxes over snow. *Boundary-Layer Meteorol.*, **2**, 255-265.
- Hofmann, M. 1998. Untersuchungen zur atmosphärischen turbulenz über arktischem meereis mit der hubschrauberschleppsonde HELIPOD. *Berichte des Instituts für Meteorologie und Klimatologie der Universität Hannover*, Band **59**, 94 p.
- Holtslag, A.A.M. and H.A.R. De Bruin. 1988. Applied modeling of the nighttime surface energy balance over land. *J. Appl. Meteorol.*, **37**, 689-704.
- Högström, U. 1988. Non-dimensional wind and temperature profiles in the atmospheric surface layer: a re-evaluation. *Boundary-Layer Meteorol.*, **42**, 55-78.
- King, J.C. and P.S. Anderson. 1994. Heat and water vapour fluxes and scalar roughness lengths over an Antarctic ice shelf. *Boundary-Layer Meteorol.*, **69**, 101-121.
- Joffre, S. M. 1982. Momentum and heat transfers in the surface layer over a frozen sea. *Boundary-Layer Meteorol.*, **24**, 211-229.
- Launiainen, J. 1983. Parameterization of the water vapour flux over a water surface by the bulk aerodynamic method. *Annales Geophysicae*, **1**(6), 481-492.
- Launiainen, J. and T. Vihma. 1990. Derivation of turbulent surface fluxes - an iterative flux-profile method allowing arbitrary observing heights. *Environmental Software.*, **5**, 113-124.
- Launiainen, J. 1995. Derivation of the relationship between the Obukhov stability parameter and the bulk Richardson number for flux-profile relationships. *Bound.-Layer Meteorol.*, **76**, 165-179.
- Launiainen, J. and B. Cheng. 1998. Modelling of ice thermodynamics in natural water bodies. *Cold Reg. Sci. Technol.*, **27**(3), 153-178.
- Launiainen, J., ed. 1999. *BALTEX-BASIS Data Report 1998*, Geesthacht, Germany. International BALTEX Secretariat. (Publication 14). 94 p.
- Launiainen, J., B. Cheng, J. Uotila, and T. Vihma. 2001. Turbulent surface fluxes and air-ice coupling in the Baltic-Air-Sea-Ice-Study (BASIS). *Ann. Glaciol.*, **33** (in press).
- Mai, S., C. Wamser and C. Kottmeier, 1996. Geometric and aerodynamic roughness of sea ice. *Boundary-Layer Meteorol.*, **77**, 233-248.
- Owen, P.R. and W.R. Thomson. 1963. Heat transfer across rough surfaces. *J. Fluid. Mech.*, **15**, 321-334.
- Smeets, C.J. P.P., P.G. Duynkerke and H.F. Vugts. 1999. Observed wind profiles and turbulence fluxes over an ice surface with changing surface roughness. *Boundary-Layer Meteorol.*, **92**, 101-123.
- Vihma, T. 1995. Subgrid parameterization of surface heat and momentum fluxes over polar oceans. *J. Geophys. Res.*, **100**, 22,625-22,646.

## Temporal and spatial variability of surface fluxes over the ice edge zone in the northern Baltic Sea

Burghard Brümmer<sup>1)</sup>, David Schröder<sup>1)</sup>, Jouko Launiainen<sup>2)</sup>, Timo Vihma<sup>2)</sup>, Ann-Sofi Smedman<sup>3)</sup>, and Mikael Magnusson<sup>3)</sup>

<sup>1)</sup> Meteorological Institute, University of Hamburg, Germany

<sup>2)</sup> Finish Institute of Marine Research, Helsinki, Finland

<sup>3)</sup> Department of Meteorology, Uppsala University, Sweden

### Abstract

During the Baltic Air-Sea-Ice Study (BASIS) from 16 February to 6 March 1998 turbulent fluxes of sensible and latent heat, and momentum as well as radiation fluxes were measured at three land-fast ice stations and by an aircraft flying over the ice edge zone of the northern Baltic Sea. The fluxes at the three ice stations show a high degree of temporal variability (sensible heat flux varied between  $-200 \text{ Wm}^{-2}$  and  $+100 \text{ Wm}^{-2}$ ), caused by rapidly passing weather systems. The aircraft-based fluxes were measured at levels between 10 and 30m during six flight missions under different weather and sea ice conditions. Spatial distributions and area-representative averages were determined. Fluxes from the surface stations and from the aircraft are in reasonable agreement. A mean northeast-southwest gradient of surface temperature and heat fluxes is present across the ice edge zone. The spatial variability of the heat fluxes in the ice edge zone is small during warm air advection and large under cold-air advection conditions. It is, however, often exceeded by the spatial variability of the net radiation flux caused by inhomogeneous cloud fields. Spatial variability from aircraft shows that area-representative fluxes for the whole ice edge zone cannot be derived from land-fast ice stations, only. The flux time series at the surface stations and the aircraft-based flux fields together are a unique data set for the validation of meso- and regional-scale models.

### 1. Introduction

The atmosphere is coupled with the local surface via the turbulent and radiative fluxes. The interaction between atmosphere and surface is particularly complex in case of an inhomogeneous surface such as fractured sea-ice with ice floes of different size and distribution. Ice and water have a wide difference of the relevant physical properties. These are primarily albedo, surface temperature, surface humidity, heat conductivity, transmissivity of solar radiation, and, to some degree, roughness (Guest and Davidson, 1991). In wintertime, the temperature difference between ice and water surface may exceed 30 K (e.g. Brümmer, 1996).

Climate and weather forecast models do not resolve the details of the interaction between the atmosphere and an inhomogeneous ice surface. The sub-grid-scale effects have to be parameterized (Stössel and Claussen, 1993; Vihma, 1995). Because ice floes and leads have typical horizontal scales of the order  $10^1$  to  $10^3$  m, the same problem holds for mesoscale models, although larger-scale features, for example the location of the ice edge and larger areas of open water, can be resolved by the mesoscale model grid.

The ice surface temperature adjusts faster to a change of the surface energy balance (e.g. caused by a changing cloud cover) than the sea surface temperature. In some weather and climate models the ice surface temperature is prescribed by climatological values. In that case, e.g. changes in low-level stratification which may be caused by cold and warm air

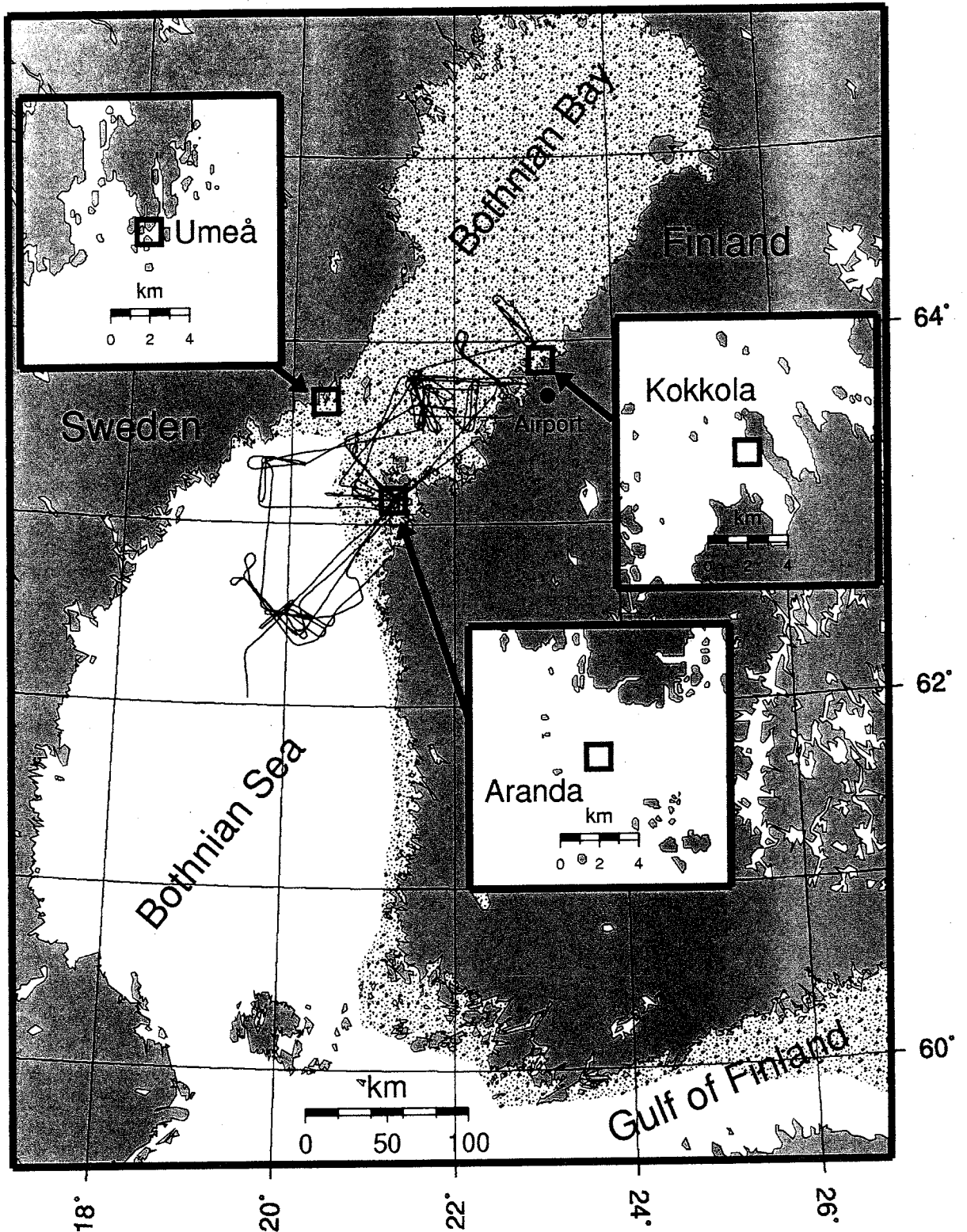


Figure 1: Field experiment BASIS in the northern Baltic Sea during 16 February to 6 March 1998: Positions of the three ice stations (squares) Aranda, Kokkola, and Umeå are given as well as the flight patterns (thin curves) of the six missions of research aircraft Falcon. The flight operation base, Kokkola airfield, is marked by a dot. The average sea-ice extension is indicated by the dotted area.

advection cannot be accounted for properly. The inclusion of at least a simple surface energy-balance scheme or a thermodynamic ice model would be an essential improvement.

During the field experiment BASIS (Baltic Air-Sea-Ice Study) lasting from 16 February to 6 March 1998 turbulent fluxes of heat, moisture, and momentum as well as radiation fluxes were measured over ice and water in the northern Baltic Sea (Figure 1). The measurements took place over an area of approximately 200 km times 100 km located around the ice edge. Three surface stations were deployed on land-fast ice and performed continuous measurements. In addition, an aircraft measured the spatial distribution of the fluxes over ice and water at particular times.

The objectives of this paper are (a) to present the temporal and spatial variability of the surface fluxes under various ice concentrations and various large-scale weather conditions, such as on-ice and off-ice air flow, (b) to give estimates of spatially and temporally averaged fluxes for the ice edge zone, (c) to discuss the conditions met in winter 1998 in relation to the climatic conditions, and (d) to discuss the accuracy and applicability of the flux data for validation of mesoscale models. Such comprehensive measurements of turbulent and radiation fluxes over the ice edge zone in the Baltic Sea have not been made before.

## 2. Platforms and instrumentation

Three ice stations and an aircraft were applied as platforms for the flux measurements. The locations of the ice stations and the flight patterns are shown in Figure 1 and the respective instrumentations are described below. Further details on the BASIS experiment are given in Launiainen (1999).

### 2.1 The three ice stations

One of the three ice stations was deployed close to research icebreaker Aranda on land-fast ice south of the isle of Vallgrund at a distance of about 40 km from the ice edge (Figure 1). The ice at Aranda was about 0.3 to 0.45 m thick. At a 10 m high mast temperature, humidity, wind speed, and wind direction were measured at several levels. A sonic instrument (METEK) was installed at a separate mast at 2.2 m height, from which the turbulent fluxes of heat and momentum were calculated for 10 min intervals. Downward ( $S\downarrow$ ) and upward ( $S\uparrow$ ) solar radiation were measured by pyranometers (CM-5) and upward long-wave radiation ( $L\uparrow$ ) as well as surface temperature  $T_s$  by infrared radiometers (Barnes PRT-5 and Everest Interscience 4000.4GL). The net radiation flux was determined by two Suomi-Franssila instruments and the downward long-wave radiation ( $L\downarrow$ ) was calculated as a residuum.

Unfortunately, surface temperature  $T_s$  could not be measured continuously. In order to fill the gaps, it was also calculated from the turbulent flux-profile relationships based on the universal Monin-Obukhov similarity theory. The necessary aerodynamic and scalar roughnesses were derived from the sonic anemometer and meteorological profile mast data (Launiainen et al., 2001). In most cases the calculated and the measured surface temperature compare well, so that we present in Table 2  $T_s$  estimates for those days on which no direct measurements were available.

The second surface station was placed near Kokkola on land-fast ice at a distance of about 100 m from the shore of a peninsula (Figure 1). The distance to the open sea was about 130 km. Air pressure, wind speed and direction installed at 2 m height, air temperature and dew-point temperature installed at 1 m height, and surface temperature (infrared radiometer

Heimann KT-19) were sampled every second and recorded as 1 minute averages. Surface fluxes of heat and momentum were determined by a sonic instrument (METEK) at 3.5 m height and were calculated for 5 min intervals. All four radiation fluxes  $S\downarrow$ ,  $S\uparrow$ ,  $L\downarrow$ , and  $L\uparrow$  were measured separately by pyranometers (Kipp and Zonen) and pyrgeometers (Eppley) at 1 m height.

The third ice station was situated near Umeå at a peninsula which was about 20 km north of the ice edge. A 12 m high mast was equipped with instruments for wind speed and direction at 1, 3.5 and 11.5 m above the ice surface. The fluxes of heat and momentum were measured by a sonic instrument (Solent) at 10 m height and were calculated for 10 min intervals. Radiation fluxes  $S\downarrow$ ,  $S\uparrow$ ,  $L\downarrow$ , and  $L\uparrow$  were measured by Eppley radiometers. Although the instruments were located on the shore a few meters from the sea ice, the Umeå station is regarded here as a land-fast ice station.

## 2.2 Research aircraft Falcon

The German research aircraft Falcon was equipped with a gust-probe system to measure the three wind components. The system includes a 5-hole wind probe (Rosemount 858J) at 4 m long nose boom for the relative wind velocity and an inertial reference system (Honeywell) for the aircraft velocity. Furthermore, Falcon carried sensors for temperature (Pt-100), water vapor (Lyman- $\alpha$ -humidometer, Vaisala humicap, and dewpoint mirror) and pressure (pitot tube, Rosemount). All quantities were sampled with 100 Hz corresponding to 1 m distance at the typical flight speed of  $100 \text{ ms}^{-1}$ . The radiation fluxes  $S\downarrow$ ,  $S\uparrow$ ,  $L\downarrow$ , and  $L\uparrow$  were measured by pyranometers (Eppley) and pyrgeometers (Eppley), respectively, and the surface temperature by an infrared radiometer (Heimann KT-19). All radiation parameters were sampled with 10 Hz.

The Falcon operated from Kokkola airfield. Six missions were flown: on 27 and 28 February and 2, 3, 5 and 6 March 1998. They covered the ice edge area between Kokkola in the north and locations up to 100 km south of Aranda over the open sea (Figure 1). During all missions the Falcon flew vertical profiles and horizontal legs at different levels in the lowest 3 km of the atmosphere. In this study, only the low-level flight legs between 10 and 30 m above the surface are used.

Turbulent fluxes of momentum, sensible and latent heat were calculated over 1, 2, 4, 8, and 20 km length intervals in order to estimate the effect of averaging length. The linear trend was removed before applying the eddy correlation technique. To retain a high spatial resolution, the intervals for the flux calculations were shifted by 50 m.

Accuracy of the aircraft flux measurements has been a topic of recent research. Various studies have addressed the statistical flux error as a function of the flight length (Lenschow et al., 1994; Mann and Lenschow, 1994; Lenschow and Stankov, 1986), the systematic error due to filtering or detrending (Grunwald et al., 1998; Grossmann, 1992), and the error caused by height extrapolation of the flux from the flight level to the surface (Grunwald et al., 1998; Emeis, 1995). The problem of flux estimates is that only time or space averaged fluxes can be measured instead of the flux ensemble average. The inherent error depends on length interval, flight level and turbulence characteristics. We will show below that the low flight levels allowed for short interval lengths for the surface flux determination.

Comparisons between aircraft and tower measurements have been performed e.g. by Mahrt (1998), Desjardins et al. (1997) and André (1990) and comparisons between various aircrafts

e.g. by Dobosy et al. (1997). Our study can be regarded also as a contribution to the aircraft-tower comparisons.

### 3. Weather conditions

The weather conditions in the experimental area during BASIS were characterized by a rapid sequence of synoptic systems: warm fronts, cold fronts, occluded fronts, troughs and ridges, lows and highs. The time of passage of these systems is marked in Figure 2 which shows the relevant meteorological quantities recorded at the three ice stations. Steady weather conditions lasted not much longer than one day. Unstationarity is a characteristic feature of mild winters in Scandinavia such as the winter of 1997/98.

Since a large-scale north-south temperature gradient is always present in Northeastern Scandinavia in winter, rapid temperature changes of 10 to 20 K occurred with corresponding changes especially in the wind direction. Particularly strong temperature drops occurred on 16, 19, and 23 February 1998 on the rear side of lows passing close to or directly over (23 February) the experimental area. In the latter case the highest wind speed during the campaign with more than  $20 \text{ ms}^{-1}$  was measured at Aranda. The three cold episodes lasted for only one to two days and ended on 18, 20, and 25 February, respectively, as suddenly as they began, with warm fronts advecting warm air from the open Baltic Sea in the southwest. These events were again accompanied with wind speeds up to  $19 \text{ ms}^{-1}$ .

Between the three mentioned cold-air episodes, fronts, troughs, and ridges passed in a fast sequence and air temperatures were above freezing. This caused snow melt and melting ponds on the sea ice and the ice surface was widely grey instead of white. After the passage of a low (the deepest one during BASIS) and its accompanying trough on 28 February air temperatures remained below  $0^\circ\text{C}$  until the end of the campaign and wind speeds were generally lower than before.

Nearly constant wind directions in the entire experimental area for more than 24 hours occurred only on 24 February and 1 March under two similar synoptic conditions between an eastward departing low and a high pressure zone approaching from northwest and passing later over the area. Furthermore, a meso-scale low (ML) which occurred on 3 March should be mentioned. It does not stand out in the pressure time series in Figure 2, but in a  $180^\circ$  wind shift accompanied with its passage. The ML is noted because it was recorded during the Falcon mission on 3 March and caused inhomogeneous fluxes in the area (Figure 11).

The six aircraft missions took place under different weather conditions. The flight times are marked in Figure 2. On 27 February, a strong on-ice air flow from south led to an air temperature higher than the local water and ice temperature. On 28 February, an on-ice to ice-parallel air flow occurred after the passage of the cold front of the deep and large low pressure system mentioned above. The mission on 2 March was characterized by weak turbulence and almost cloudless conditions. On 3 March, the mentioned meso-scale low passed the experimental area. On 5 March, a northerly off-ice air flow led to the lowest temperatures during all aircraft missions. The last mission took place on 6 March during about off-ice winds.

In the Baltic Sea, only first year ice is present. During the last 100 years, it has covered between 12 and nearly 100% of the area and lasted for 4 to 7 months depending on the site and weather conditions (Leppäranta and Seinä, 1985). The winter 1997/98 was a mild one. During BASIS, only the Bothnian Bay, parts of the Gulf of Finland and a small zone at the

Finnish coast were covered with ice (Figure 1).

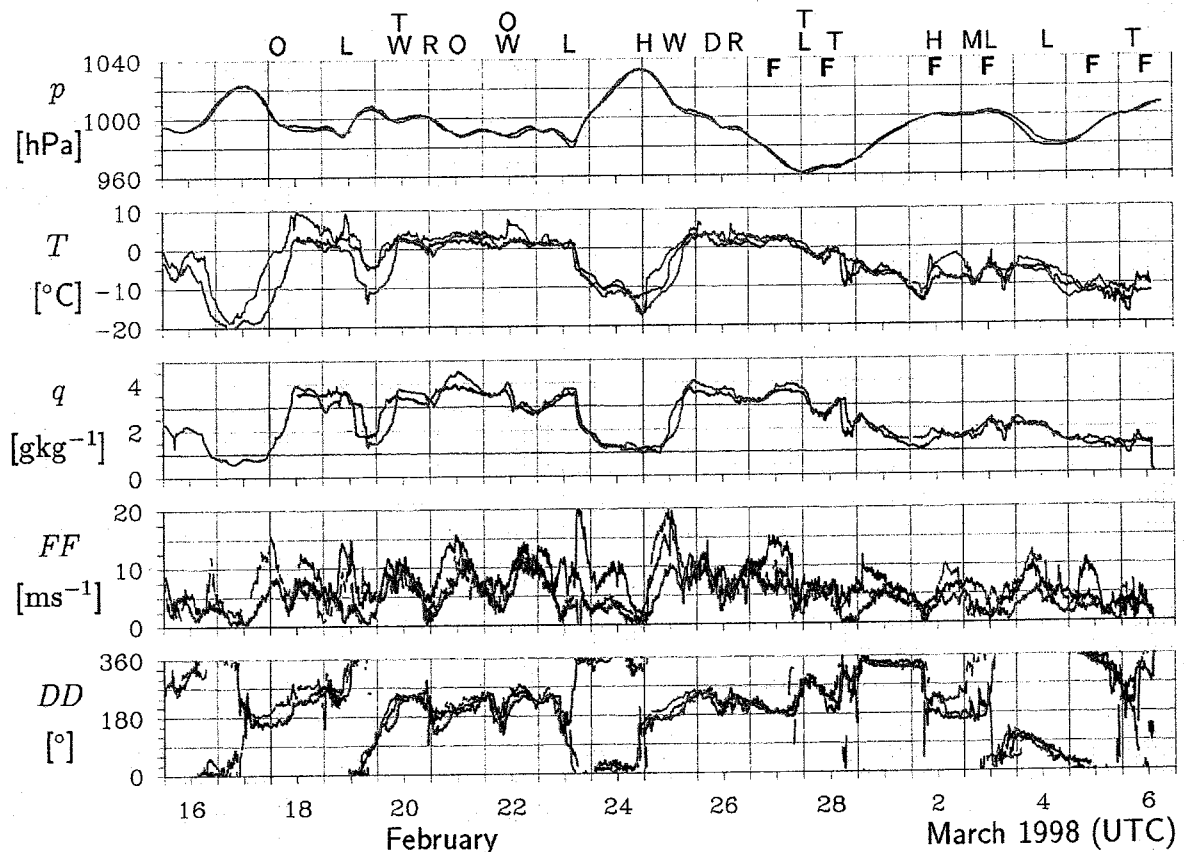


Figure 2: Time series (time in UTC) of 10 min averages of pressure  $p$ , temperature  $T$ , water vapor mixing ratio  $q$ , wind speed  $FF$ , wind direction  $DD$ , measured at Aranda (green line), Kokkola (red line) and Umeå (blue line). Measuring heights are: Aranda ( $T$ : 2.3 m,  $q$ : 4.6 m,  $FF$  and  $DD$ : 10 m), Kokkola ( $T$ : 1 m,  $q$ : 1 m,  $FF$  and  $DD$ : 2 m) and Umeå ( $T$ : 11 m,  $FF$  and  $DD$ : 11.5 m). Capitals on top indicate passage times of synoptic events: High (H), Low (L), Trough (T), Ridge (R), Warm Front (W), Cold Front (C), Occlusion (O), Disturbance (Convergence Line) (D), Mesoscale Low (ML), and the times of Falcon flight missions (F).

#### 4. Temporal variability of surface fluxes at the ice stations

##### 4.1 Time series of fluxes

The radiation and turbulent fluxes measured at Aranda, Kokkola, and Umeå are displayed in Figures 3, 4, and 5, respectively. To facilitate the interpretation, the time series of air and surface temperature and albedo are added to the Figures.

The albedo of the ice/snow surface varies between 0.3 and 0.9. It is high during freezing periods and freshly fallen snow and it is low during melting periods when the air temperature is above zero. The long term variations of albedo, e.g. in Figure 4, correspond well to the warm and cold episodes. Albedo changes follow temperature changes with some time delay because it takes some time for the snow/ice to melt. This can be seen e.g. in the Kokkola measurements on 20 February during noon when the albedo is still high although the air temperature is 2°C. One day later, after continuous melting the albedo is below 0.4. The same holds on 18/19 February and on 25/26 February.



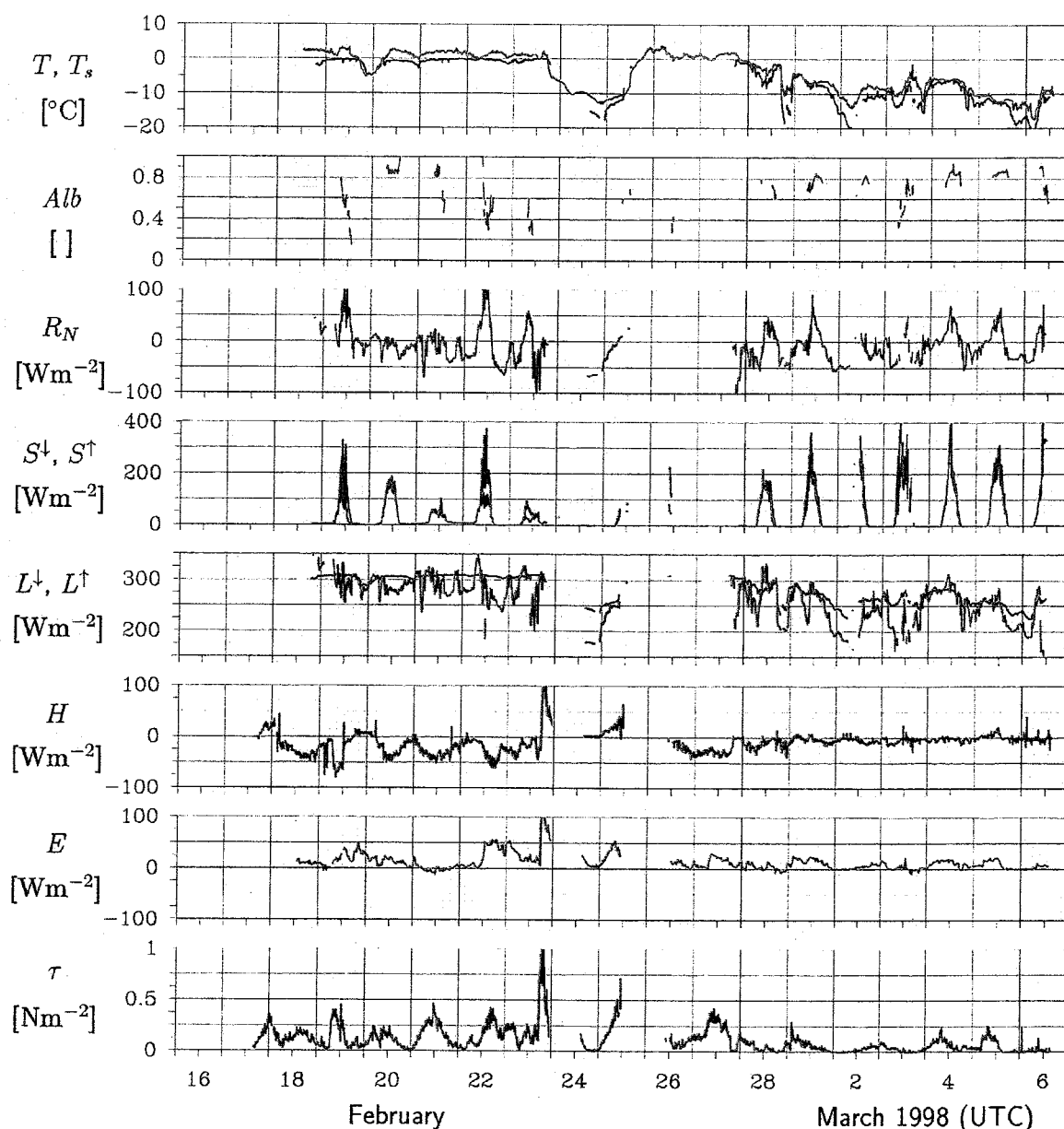


Figure 3: Air temperature  $T$ , surface temperature  $T_s$  (green line), albedo  $Alb$ , net radiation  $R_N$  (a positive sign means a source for the surface), downward solar radiation  $S_{\downarrow}$ , upward solar radiation  $S_{\uparrow}$ , downward long-wave radiation  $L_{\downarrow}$ , upward long-wave radiation  $L_{\uparrow}$  (green line), sensible heat flux  $H$ , latent heat flux  $E$  (positive upward), and magnitude of momentum flux  $\tau$  measured at Aranda (10 min averages).

The short-wave radiation,  $S_{\downarrow}$  reflects the variable cloud conditions caused by the passing synoptic systems. The daily maximum of  $S_{\downarrow}$  varied between 100 and 300  $Wm^{-2}$ . High values reflecting clear sky occurred e.g. under high pressure conditions on 17 and 24 February and 2 March. The lowest maximum values of  $S_{\downarrow}$  occurred on 21 and 25 February when an occluded front and a warm front passed the experimental area.

The long-wave radiation fluxes,  $L_{\downarrow}$  and  $L_{\uparrow}$ , varied between 180 and 320  $Wm^{-2}$ .  $L_{\downarrow}$  changes with cloud cover: it was low on the above-mentioned clear days 17 and 24 February and 2

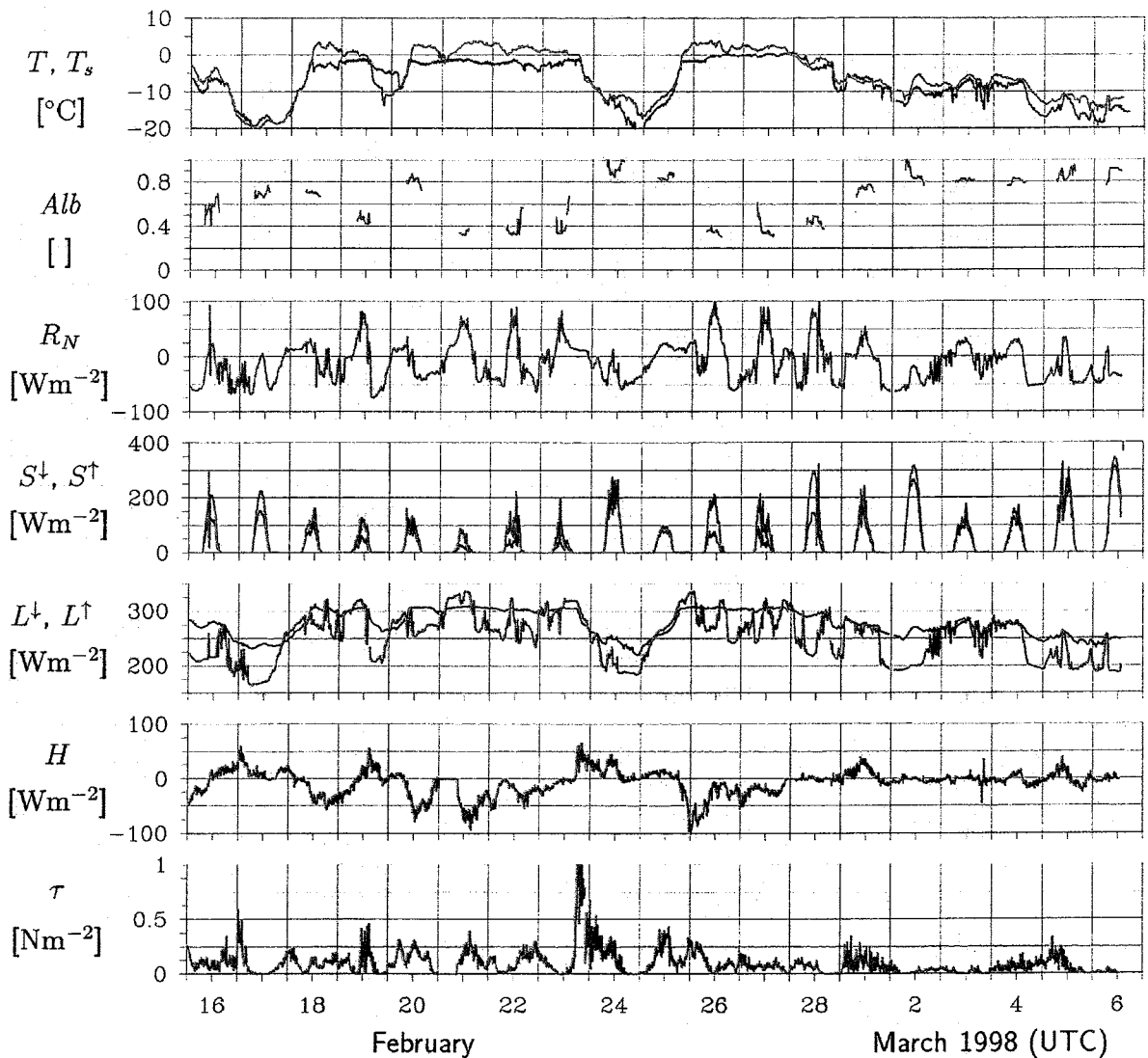


Figure 4: As Figure 3, but for Kokkola ice station.

March and high (above  $300 \text{ Wm}^{-2}$ ) on the overcast days (21 and 25/26 February) with warm air advection by fronts. Generally  $L\downarrow$  is smaller than  $L\uparrow$ . However, there are exceptions when  $L\downarrow$  was larger than  $L\uparrow$ . This was true during thaw, e.g. 21 and 25/26 February, when the air temperature was clearly above  $0^\circ\text{C}$  but the ice/snow surface temperature remained at the freezing point.

The net radiation flux,  $R_N = S\downarrow - S\uparrow + L\downarrow - L\uparrow$ , follows partly the daily cycle and partly the synoptically caused cloud variations.  $R_N$  changed between  $-60$  and  $+100 \text{ Wm}^{-2}$ . Night values were predominately negative (exception e.g. 24/25 February at Kokkola) and day values predominately positive (exception e.g. 2 March at Kokkola). The overall average of  $R_N$  is close to zero, because the smaller negative values during the night hold for a longer time of the day than the larger positive values during the day.

The sensible heat flux  $H$  varied mostly between  $-50$  and  $+50 \text{ Wm}^{-2}$  (positive means upwards), but in extreme cases values of  $-100 \text{ Wm}^{-2}$  or less (e.g. 25/26 February at Kokkola, 18 and 22 February at Umeå) and  $+100 \text{ Wm}^{-2}$  (e.g. 23 February at Aranda) occurred. Extreme negative

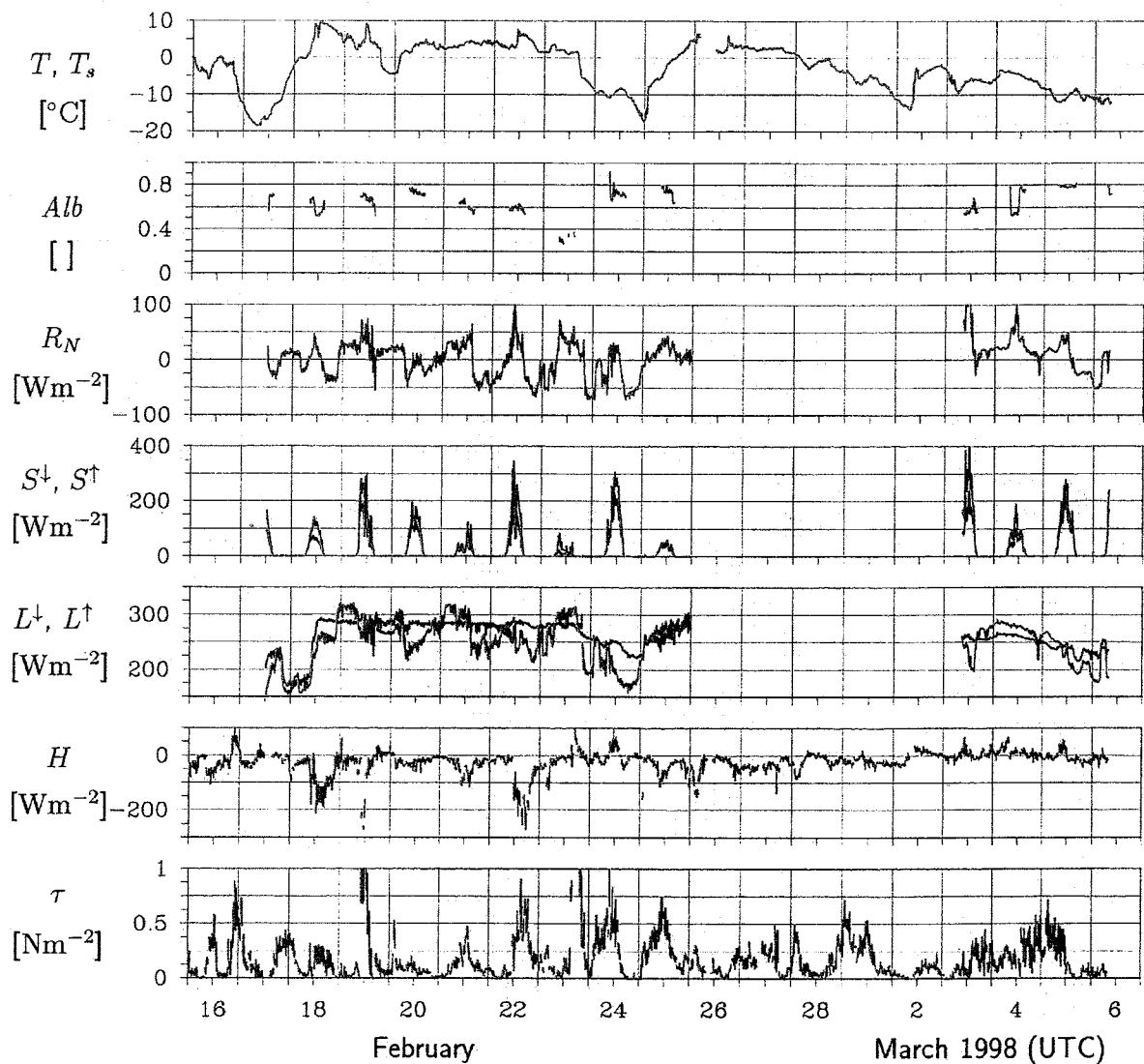


Figure 5: As Figure 3, but for Umeå ice station.

$H$  fluxes were observed after the passage of warm fronts (18, 20, 22, and 25/26 February) in situations with surface temperatures of  $0^{\circ}\text{C}$  and air temperatures above  $0^{\circ}\text{C}$  together with high wind speeds (Figure 2). Extreme positive  $H$  fluxes occurred e.g. on 19 and 23 February when the air temperature dropped rapidly on the rear side of a passing low. Obviously, the decrease of air temperature by advection took place faster than the net effect of the processes changing the ice/snow surface temperature.

Taken together, the temporal variability of the  $H$  fluxes was larger during the first 12 days of the experiment as a consequence of the synoptic variability (passing fronts, lows and highs and alternating melting and freezing episodes). During the last six days of the campaign with air temperatures permanently below  $0^{\circ}\text{C}$ ,  $H$  fluxes were often positive and the temporal variability was smaller. This is also a consequence of the generally weaker winds during that time.

The latent heat flux  $E$  was not measured. However, it was calculated by the bulk aerodynamic method (Launiainen and Vihma, 1990) using the humidity saturation deficit corresponding to the surface temperature and the relative humidity observed at the meteorological mast near Aranda. The stratification effect was taken into account. The  $E$  flux varied mostly between 0

and  $+50 \text{ Wm}^{-2}$ . During the low passage on 23 February more than  $100 \text{ Wm}^{-2}$  occurred. In contrast to the strong negative  $H$  fluxes no significant downward  $E$  fluxes were determined.

The momentum flux  $\tau$  reflects primarily the wind speed variations due to the synoptic variability. The temporal variations of  $\tau$  due to varying stability are comparably small.

Since the experimental area is smaller than the typical length scale of the passing pressure systems (highs, lows, ridges and troughs), the temporal variations of the turbulent and radiation fluxes were the same at the three stations. Differences caused by the local conditions (e.g. distance from obstacles) are discussed in section 4.2.

#### 4.2 Differences between the ice stations

Differences of the meteorological quantities and of the turbulent and radiation fluxes between the three ice stations may have many reasons: different locations within a gradient field, different distances from a marked contrast in surface properties such as the ice edge, different local surface properties (roughness and orography), different measuring heights and others.

The stations were deployed on land-fast ice with different distances from land (see maps in Figure 1). The local conditions are reflected in the dependence of the roughness length  $z_0$  on the wind direction  $DD$  (see Figure 6). Roughness length is calculated according to

$$z_0 = z / \exp \left[ 0.4 \cdot \frac{FF}{u_*} + \psi_M(z/L) \right] \quad (1)$$

where the stability functions  $\psi_M(z/L)$ , the one by Högström (1988) for the unstable region and by Holtslag and de Bruin (1988) for the stable region, were used. Those were calculated by an iterative algorithm from Launiainen and Vihma (1990). In Eq. (1)  $z$  is measuring height,  $FF$  wind speed,  $u_*$  friction velocity, and  $L$  Monin-Obukhov stability parameter.

The generally lowest  $z_0$  values and the lowest variations of  $z_0$  with  $DD$  are found at Aranda for directions which had the largest distance from land. The highest  $z_0$  values are found for Umeå, where the station was located close to land and small islands. In spite of some scatter, there is a distinct  $DD$ -dependence of  $z_0$  e.g. for Kokkola:  $z_0$  varies by about three orders of magnitude between  $10^{-4}$  m for southwesterly wind directions and  $10^{-1}$  m for northerly wind directions from the peninsula. At Umeå,  $z_0$  varies by about four orders of magnitude. For all three stations holds, that  $z_0$  is about  $10^{-4}$  m for land-fast ice without remarkable ridges and for "undisturbed" wind directions.

Table 1 summarizes the mean values of several quantities averaged over (a) the whole period and (b) only over sub-periods when all three stations measured simultaneously in order to enable comparisons.

There are significant air temperature differences in spite of the relatively small distances between the three stations. Mean temperatures range from  $-4.4^\circ\text{C}$  (Kokkola) to  $-2.1^\circ\text{C}$  (Umeå). Since surface temperatures were generally lower than air temperatures, the heat fluxes are - on the average - downward: Kokkola ( $-8 \text{ Wm}^{-2}$ ), Aranda ( $-10 \text{ Wm}^{-2}$ ), and Umeå ( $-24 \text{ Wm}^{-2}$ ).

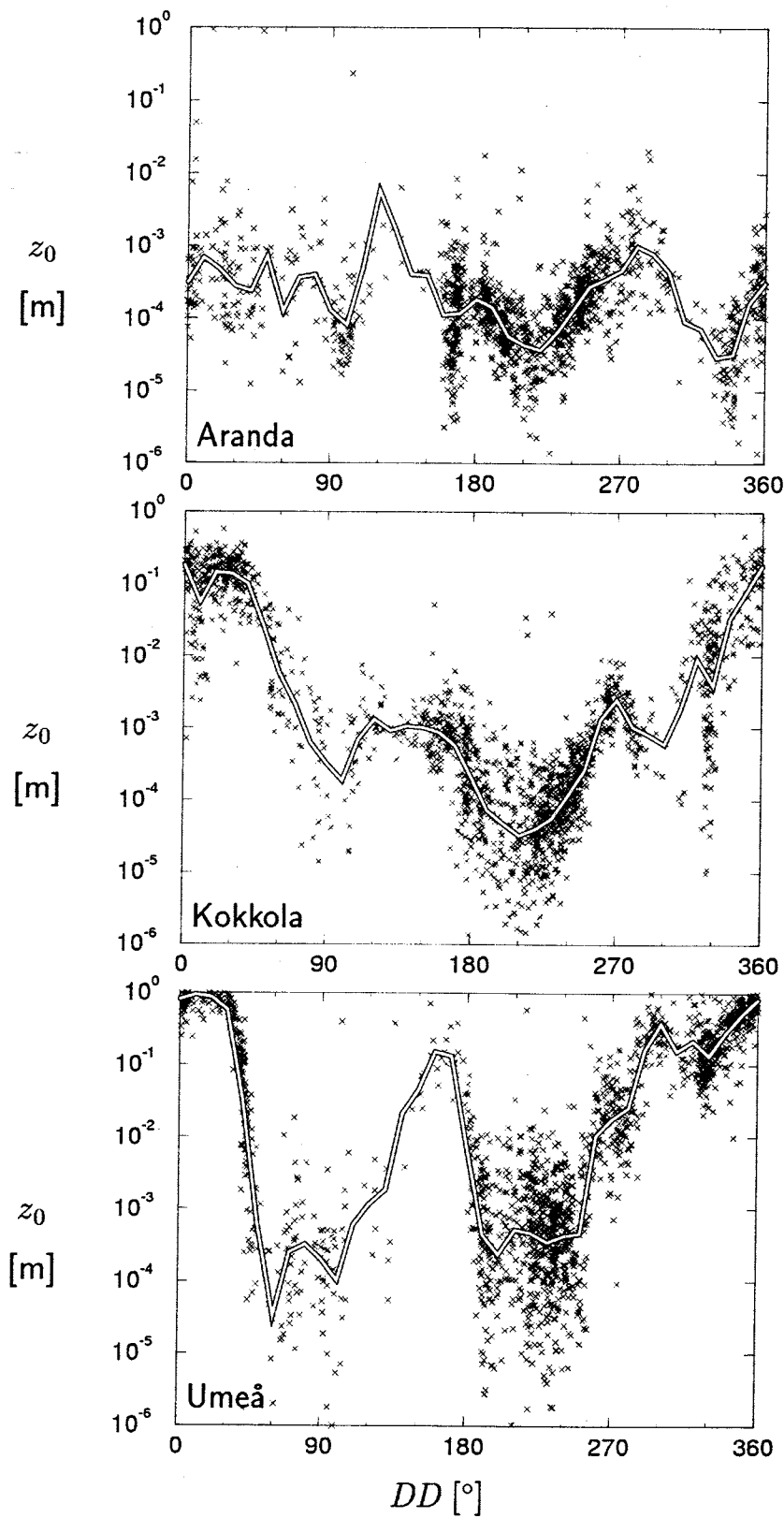


Figure 6: Dependence of roughness length  $z_0$  on wind direction  $DD$  at Aranda, Kokkola and Umeå. The white curve represents averages over  $DD$  intervals of  $10^\circ$ .

Table 1: Mean values of basic meteorological parameters as well as turbulent and radiation fluxes measured at Aranda, Kokkola and Umeå from 16 February to 6 March 1998. The first column for each station represents averages over the whole period, the second column averages only over periods when all three stations measured simultaneously. The last column gives the duration of simultaneous measurements.

Param.	Unit	Aranda		Kokkola		Umeå		time [h]
p	hPa	995.1	995.1	995.3	995.4			433
FF	ms <sup>-1</sup>	7.7	7.8	4.4	4.5	6.0	6.1	308
T	°C	-3.8	-3.8	-5.5	-4.4	-2.7	-2.1	369
T <sub>s</sub>	°C	-6.3	-6.3	-7.5	-7.0			288
q	gkg <sup>-1</sup>	2.46	2.47	2.39	2.54			383
Alb		0.74	0.73	0.68	0.68	0.66	0.67	46
S↓	Wm <sup>-2</sup>	53	43	43	32	38	37	195
S↑	Wm <sup>-2</sup>	38	32	31	22	25	24	195
L↓	Wm <sup>-2</sup>	263	269	253	260	251	260	195
L↑	Wm <sup>-2</sup>	283	286	278	280	260	267	195
S <sub>N</sub>	Wm <sup>-2</sup>	15	11	12	10	13	13	195
L <sub>N</sub>	Wm <sup>-2</sup>	-20	-17	-25	-20	-9	-7	195
R <sub>N</sub>	Wm <sup>-2</sup>	-5	-6	-13	-10	4	6	195
H	Wm <sup>-2</sup>	-7	-10	-10	-8	-24	-24	293
τ	Nm <sup>-2</sup>	0.11	0.11	0.07	0.09	0.15	0.18	293

The net solar radiation,  $S_N$ , is a heat source for the surface and with 10 to 13 Wm<sup>-2</sup> approximately the same at all three stations. The net long-wave radiation,  $L_N$ , plays a more important role at this time of the year and causes a heat loss for the surface of -20 Wm<sup>-2</sup> at Kokkola and -17 Wm<sup>-2</sup> at Aranda. The upward long-wave radiation,  $L↑$  measured at Umeå is obviously incorrect, because it would correspond to a much too low average surface temperature of -13°C. The average  $L↑$  value at Umeå is presumably close to those at Kokkola and Aranda, i.e. around 280 Wm<sup>-2</sup>. In that case  $L_N$  at Umeå would be -20 Wm<sup>-2</sup>.

The energy balance,  $B = S_N + L_N - H - E$ , at the surface of the three ice stations during the BASIS period may be roughly estimated from the flux data. Since the latent heat flux  $E$  was not measured, we assume the average value of +14 Wm<sup>-2</sup> calculated at Aranda to be valid for all three stations. Under these assumptions, the snow/ice surface lost some energy to the atmosphere at Kokkola ( $B \sim -14$  Wm<sup>-2</sup>) and Aranda ( $B \sim -10$  Wm<sup>-2</sup>), whereas the surface fluxes were balanced at Umeå ( $B \sim +1$  Wm<sup>-2</sup>) considering the corrected  $L↑$  value. In view of the different locations of the three ice stations with respect to the ice edge, the differences in  $B$  appear to be plausible.

Table 1 shows that the average wind speed  $FF$  differs considerably between the three stations. The highest wind speeds were present over the ice surface at Aranda. The small mean value at Kokkola is partly a consequence of the low anemometer height of 2 m compared to 10 m at Aranda and 11.5 m at Umeå. But even with a logarithmic extrapolation to 10 m height the wind at Kokkola is smaller than at the other stations. This is also reflected in the mean momentum flux  $\tau$  which is the smallest at Kokkola.

The different heights of the sonic instruments (2.2 m at Aranda, 3.5 m at Kokkola, and 10 m

at Umeå) cannot explain the  $\tau$  differences. The mean  $\tau$  value at Umeå appears to be rather large. Applying the bulk formula for momentum  $\tau = \rho C_D FF^2$ , where  $\rho$  is density and  $C_D$  transfer coefficient, a  $C_D$  value of  $3.7 \cdot 10^{-3}$  is computed for Umeå compared to  $C_D$  values of  $1.3 \cdot 10^{-3}$  for Aranda and  $2.3 \cdot 10^{-3}$  for Kokkola (after neutral logarithmic reduction of the  $FF$  value from 2 m to 10 m height). An error of the sonic instrument at Umeå cannot be excluded also in view of the rather large negative  $H$  value.

The mean albedo at three ice stations differs only by a few per cent and amounts to about 0.7 averaged for all. An accordance also holds for the humidity measurements at Aranda and Kokkola.

## 5. Horizontal variability of surface fluxes over ice and water measured by aircraft

The horizontal distribution of the turbulent and radiation fluxes was measured during six flight missions (see Figure 1). The aircraft measurements document the meteorological conditions during the one to two hours long mission time. The aspect of simultaneity is not exactly but approximately fulfilled, because the Falcon flight speed of  $100 \text{ ms}^{-1}$  is about one order of magnitude larger than the typical wind speed. The horizontal variability measured over the ice edge zone results primarily from surface inhomogeneities and only to a small degree from changes of the synoptic situation during the flight mission. In practise, there is no other method than aircraft measurements to obtain the horizontal variability of fluxes over an inhomogeneous surface.

In the following we discuss in Section 5.1 the small-scale horizontal variability of turbulent and radiation fluxes over ice and water demonstrated by two representative flight legs. Section 5.2 deals with the mesoscale horizontal variability of the fluxes. The small-scale details presented in Section 5.1 are intended to demonstrate (a) how closely changes of the turbulent fluxes are related to changes of the surface properties, (b) how reliable and concise the aircraft flux measurements are, and (c) which small-scale details are averaged out in the mesoscale flux fields presented in Section 5.2.

### 5.1 Small-scale horizontal variability

Two out of 30 low-level horizontal flight legs are selected for presentation. The two examples hold for an on-ice to ice parallel air flow on 28 February 1998 (Figure 7) and for an off-ice air flow on 5 March 1998 (Figure 8).

#### (a) First example: on-ice air flow on 28 February 1998

On 28 February 1998, a 58 km long leg was flown at 15 m height from the open water over the sea ice (Figure 7). The air temperature was lower than the water temperature (about  $-0.5^\circ\text{C}$ ) but higher than the ice surface temperature (between  $-2$  and  $-3.5^\circ\text{C}$ ). The ice edge was crossed after 7.5 km flight distance and the ice area had several small openings up to a few hundred meters width. The albedo of water was about 0.1, that of the ice between 0.3 to 0.6 increasing with distance from the ice edge. Openings in the ice cover below the aircraft are seen by the infrared surface temperature radiometer having an aperture angle of  $2^\circ$ . They are also presented in the albedo curve but "smoothed" to some degree because the aperture angle of both the downward and upward looking pyranometer is  $180^\circ$ . Thus the albedo does not reach 0.1 over the openings.

The net radiation  $R_N$  exhibits a longer-scale variation caused partly by the transition from

water to ice but mainly by the cloud field. Between 12 and 35 km distance the sun was shining on the ice; further downstream clouds were present.

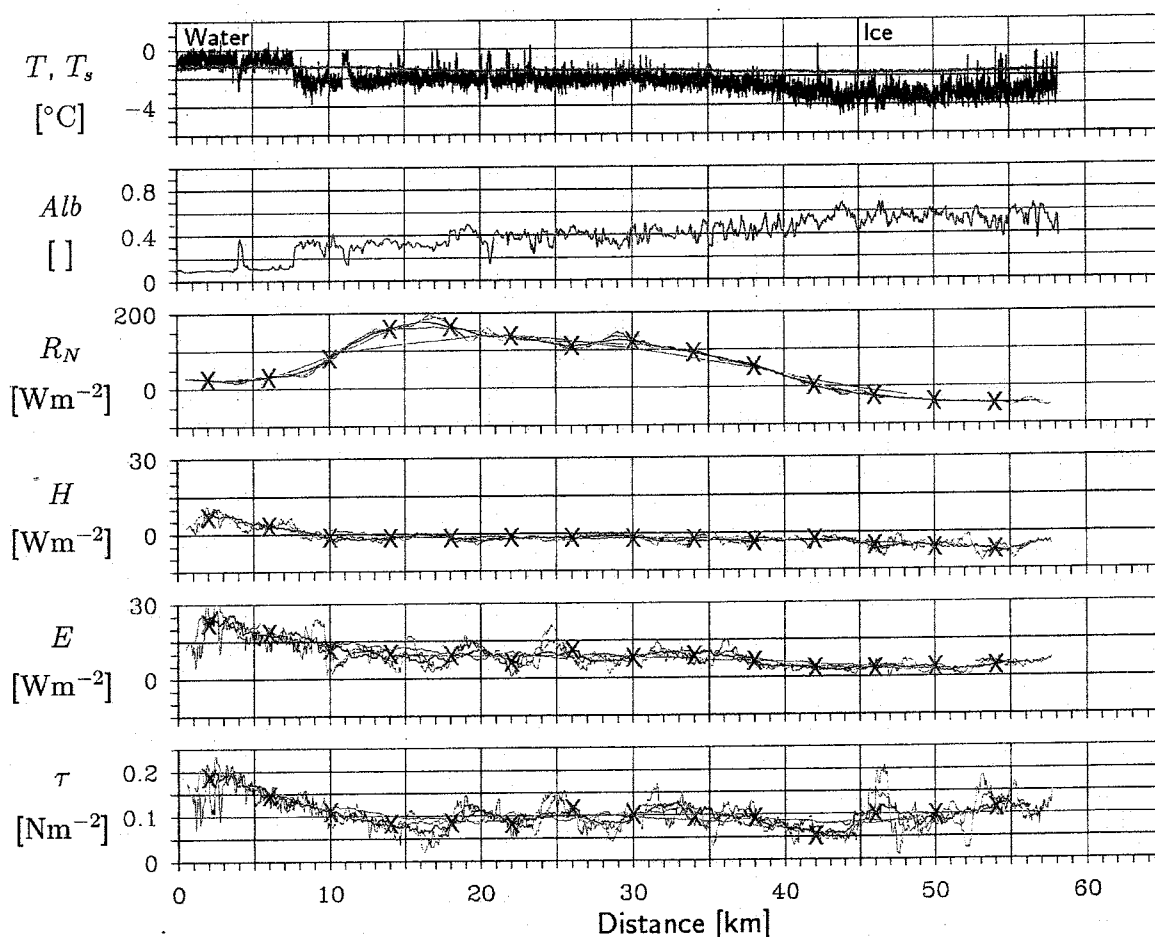


Figure 7: Air temperature  $T$ , surface temperature  $T_s$  (green line), albedo  $Alb$ , net radiation  $R_N$ , sensible heat flux  $H$ , latent heat flux  $E$ , and momentum flux  $\tau$  measured by the aircraft Falcon at 15 m height on 28 February 1998. Leg starts at  $63.85^\circ\text{N}$ ,  $21.54^\circ\text{E}$  and ends at  $64.00^\circ\text{N}$ ,  $22.89^\circ\text{E}$ . The fluxes are calculated according to Section 2.2 over 1, 2 (green line), 4 (red line), 8, and 20 km (blue line) intervals. Crosses mark 4 km average values as used in Figures 9 - 12.

The sensible heat flux  $H$  was rather small on this day, within  $\pm \text{Wm}^{-2}$ .  $H$  changed its sign at the ice edge in accordance with the air-surface stability change. This is an indication of the validity of the fluxes which were determined by the cross-correlation method independently of the air-surface temperature difference. The fluxes calculated for different length intervals (1, 2, 4, 8, and 20 km) agree well: fluxes for longer length intervals appear like averages of fluxes calculated for shorter length intervals. The consistency is confirmed by a significant correlation coefficient of the regression curve between  $H$  and the product  $(-\rho \cdot c_p \cdot \Delta\Theta \cdot FF)$  of independently measured parameters. The correlation coefficient  $r$  increases from  $r^2 = 0.63$  for the 1 km length interval to  $r^2 = 0.83$  for the 20 km length interval. This suggests that even fluxes calculated for short length intervals of 1 or 2 km are reasonable. They may be even more useful for inhomogeneous surfaces because they reflect more closely the varying surface conditions (this is even more obvious in the second example in Figure 8). All these facts support the reliability of the aircraft flux estimates. As a compromise between statistical significance and spatial resolution we use 4 km long intervals in Figures 9 to 12 to estimate the horizontal variability of the fluxes on the mesoscale.



## (b) Second example: off-ice air flow on 5 March 1998

The second example shows a 61 km long flight leg flown at 30 m height which led from land-fast ice over a transitional zone to the open water during off-ice air flow (Figure 8). The air temperature was colder than both the ice and the water surface. Thus, unstable stratification occurred everywhere. The ice surface was about 10 K colder than the water surface, so that ice/water surface inhomogeneities affected the turbulent and radiation fluxes much more than in the first example.

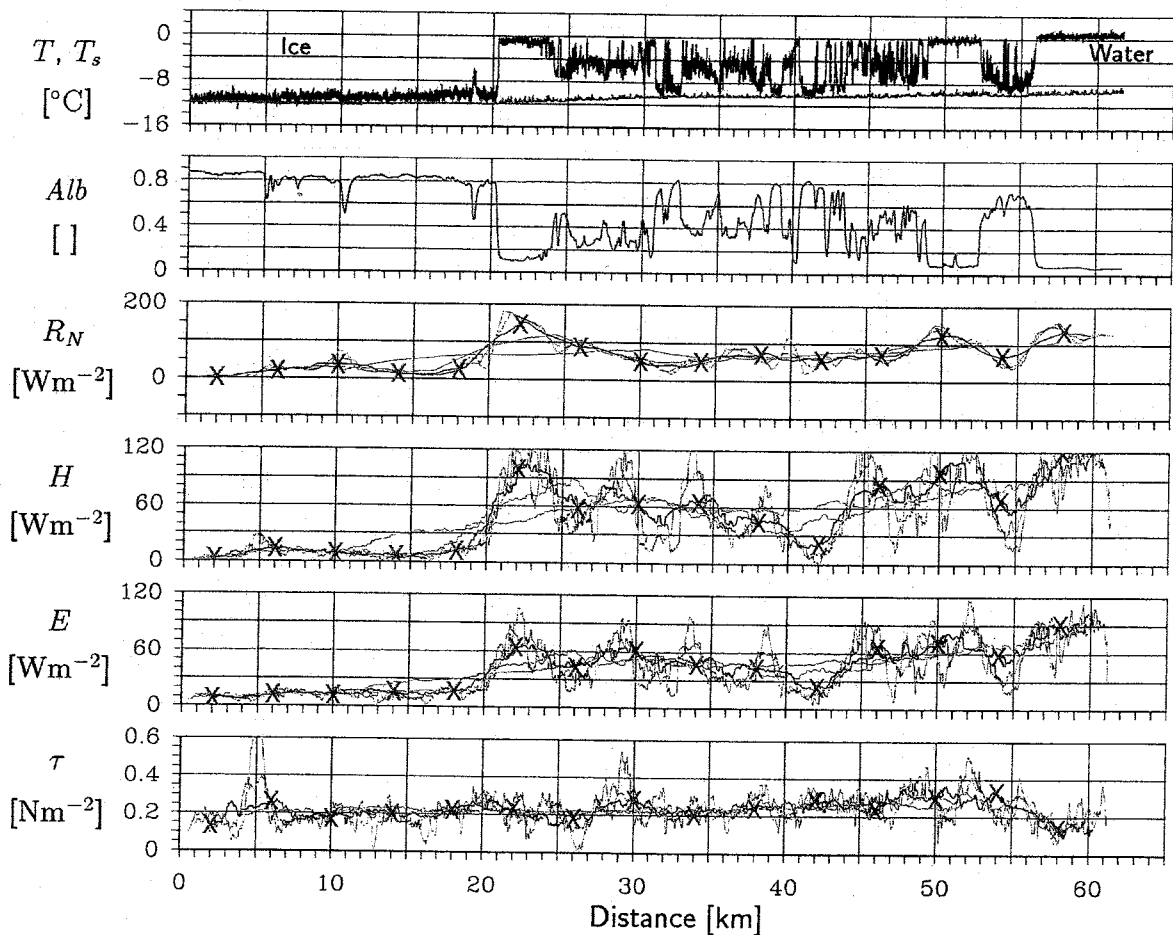


Figure 8: As for Figure 7, but for a flight at 30 m height on 5 March 1998. Leg starts at 63.05°N, 21.23°E and ends at 62.59°N, 20.18°E.

The albedo of the snow-covered land-fast ice was more than 0.8 and that of open water less than 0.1. In the 35 km broad transitional zone, there were sections with freshly frozen ice as can be seen from albedo values as low as 0.2 and moderately cold surface temperatures around  $-5^{\circ}\text{C}$ . The detection of new ice is only possible due to the small-scale horizontal resolution of the measurements. In case of a coarser horizontal resolution, it cannot be distinguished anymore between new ice and a mixture of old ice and open water resulting in equivalent mean values of albedo and  $T_s$ .

Although the cloud cover and thus  $S\downarrow$  and  $L\downarrow$  were inhomogeneous along the leg, the main variability of the net radiation  $R_N$  is caused by differences in ice cover.  $R_N$  was 10 to  $30\text{Wm}^{-2}$  over snow-covered ice and 110 to  $170\text{Wm}^{-2}$  over open water.

The sensible heat flux  $H$  was upward everywhere. In accordance with the temperature difference between air and surface,  $H$  was small over ice (5 to 15  $\text{Wm}^{-2}$ ) where the temperature difference is  $-1$  to  $-2$  K and larger over open water (90 to 120  $\text{Wm}^{-2}$ ) where the temperature difference is around  $-10$  K. The fluxes calculated for short intervals of 1 or 2 km reflect the frequent changes of ice and water in the ice edge transitional zone. Again, as mentioned in the first example, the fluxes for longer intervals cannot resolve the detailed surface structure but follow it in a kind of smoothed curve. The same holds for the latent heat flux  $E$  and the momentum flux  $\tau$ . The horizontal variability of  $E$  follows closely that of  $H$ .

$R_N$ ,  $H$  and  $E$  are all of comparable magnitude. The energy budget  $B$  results to about  $-5$   $\text{Wm}^{-2}$  over closed ice and to about  $-40$   $\text{Wm}^{-2}$  over open water. Thus, even during day time when  $S_N$  was about 90  $\text{Wm}^{-2}$  over ice and about 180  $\text{Wm}^{-2}$  over water both surfaces lost energy to the atmosphere under cold-air outbreaks conditions. During night time, the energy loss is increased since  $S_N$  vanishes, resulting in  $B = -95$   $\text{Wm}^{-2}$  over ice and  $B = -200$   $\text{Wm}^{-2}$  over water.

Taken together, the results of this subsection suggest, that (1) the turbulent fluxes measured by the Falcon are reliable, (2) the fluxes react immediately to horizontal variations of the underlying surface, (3) this flux variability can be resolved by choosing relatively short length intervals, and (4) the fluxes calculated over longer length intervals represent a kind of average of the fluxes calculated for shorter length intervals.

## 5.2 Mesoscale horizontal variability

In this Section we present the variability of the fluxes within a mesoscale area of about 200 km x 100 km (see Figure 1). Only low-level flight legs between 10 m and 30 m height are used. As mentioned above, the length interval for the flux calculations and for other averages is chosen as 4 km (non-overlapping), thus neglecting the small-scale variability as presented in Section 5.1. In order to combine the results from the mosaic-like distribution of the low-level legs during a flight mission to a coherent horizontal field an objective analysis (Cressman, 1959) is applied. By this method the 4 km aircraft-based averages are inter- and extrapolated on a regular square grid of 11 km side length. The grid size of 11 km was chosen to make it comparable to the grid resolution of the mesoscale model HIRLAM. In Figures 9 to 12 the mesoscale horizontal distribution of the fluxes is shown for four flight missions. Each figure contains both the original 4 km aircraft values and the 11 km grid values. In addition, the fluxes at the three ice stations averaged over the duration of the flight missions (1 to 1.5 hours) are included in the figures. The ice stations data did not enter into the 11 km grid interpolation.

On 27 February 1998 (Figure 9), a strong on-ice air flow of 15 to 18  $\text{ms}^{-1}$  led to an ice surface temperature close to the freezing point of  $-0.26^\circ\text{C}$  for the local sea water with a salinity of 0.5%. Without albedo information it would have been difficult in this situation to distinguish between water and ice using the surface temperature as an indicator only. The net radiation flux  $R_N$  was positive everywhere.  $R_N$  was larger over open water than over ice due to the albedo differences between water and ice and due to the fact that the net long-wave flux  $L_N$  was close to zero as a consequence of a warm, nearly closed low-level cloud deck. The sensible heat flux  $H$  was downward and not much different over water and ice. The latent heat flux was small and in the middle of the experimental area around Aranda even close to zero. The momentum flux  $\tau$  shows distinct mesoscale variations which are in accordance with those of wind speed and  $H$ .

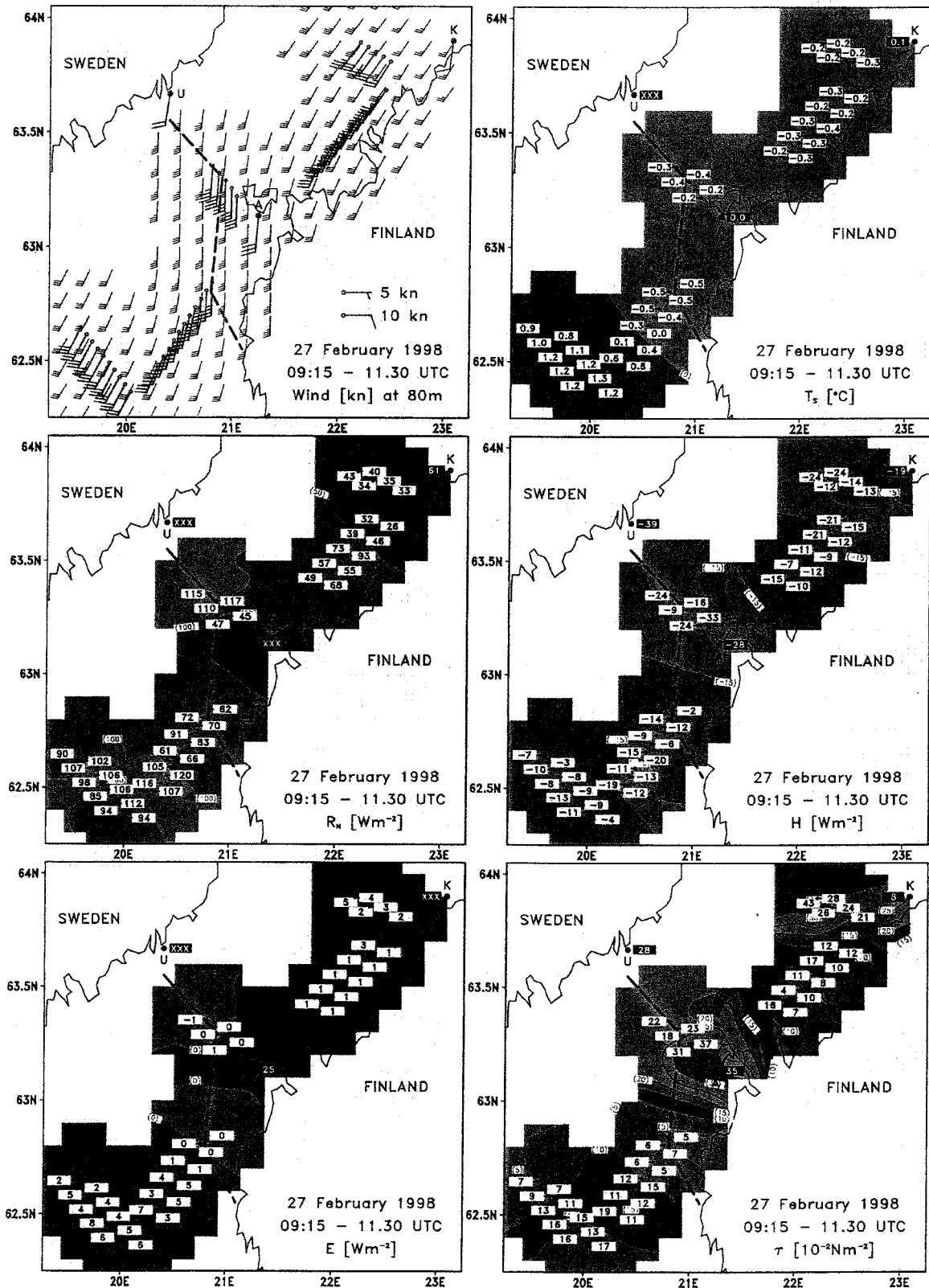


Figure 9: Spatial distribution of wind, surface temperature  $T_s$ , net radiation  $R_N$ , sensible heat flux  $H$ , latent heat flux  $E$ , and momentum flux  $\tau$  between 09:15 to 11:30 UTC on 27 February 1998. 4 km-grid averages (white rectangles) are valid for the position of the small black dots, ice station values (black rectangles) are valid for the position of the black dots. The 11 km grid values are represented by different colours and contoured by isolines (labelled). The outermost observed ice edge is marked by a dashed line.

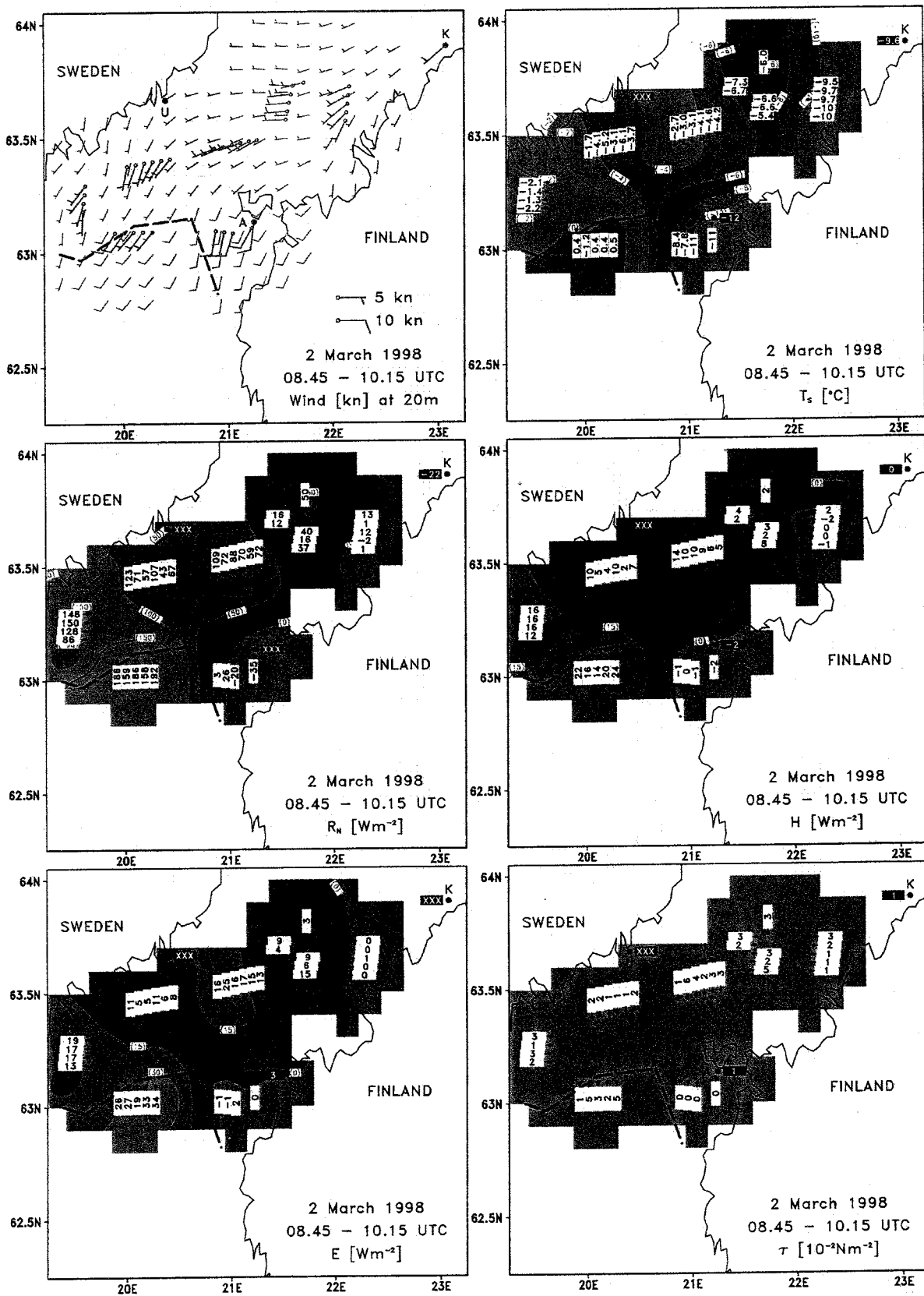


Figure 10: As Figure 9, but for 2 March 1998 between 08.45 - 10.15 UTC.

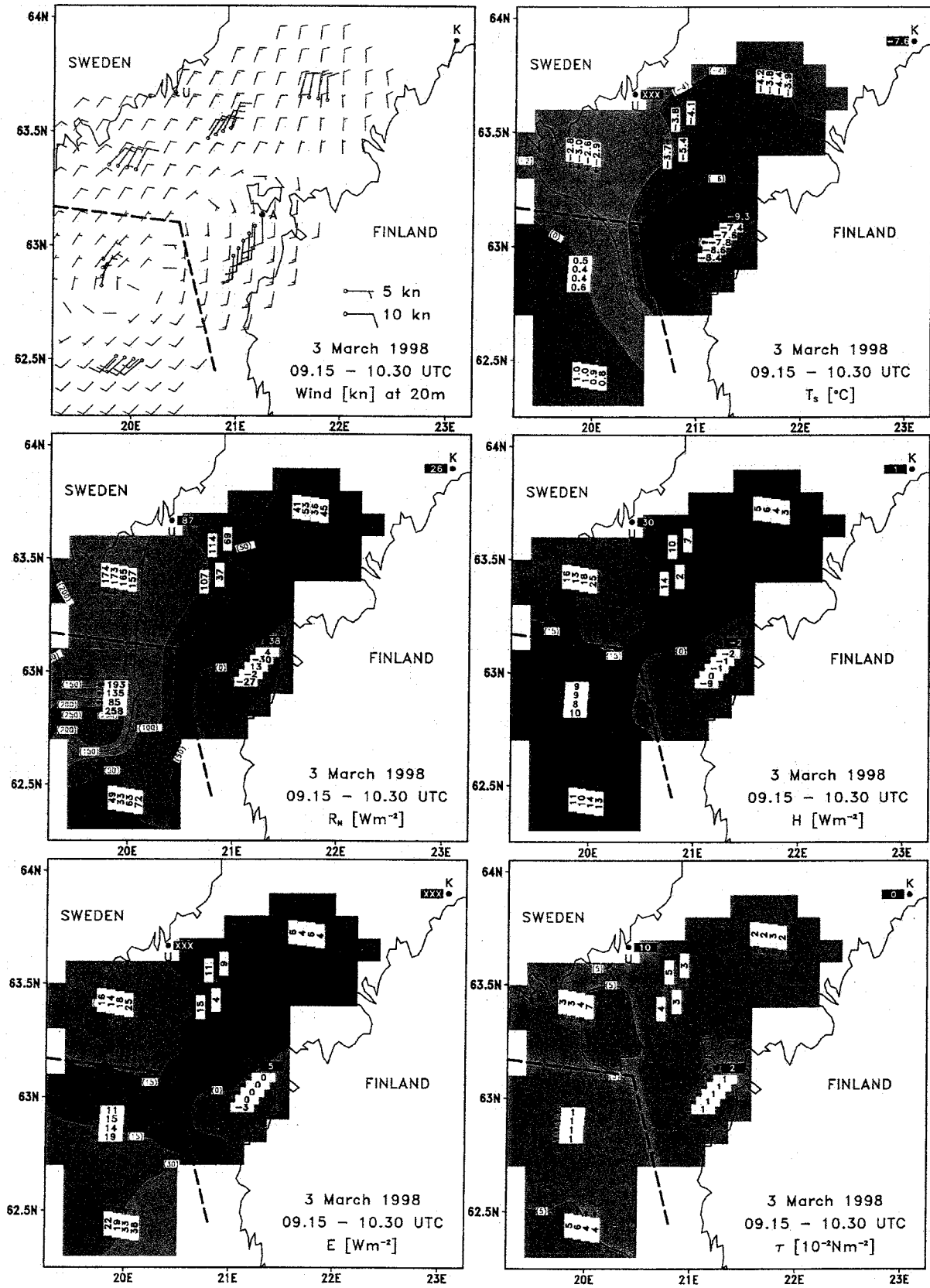


Figure 11: As Figure 9, but for 3 March 1998 between 09.15 to 10.30 UTC.

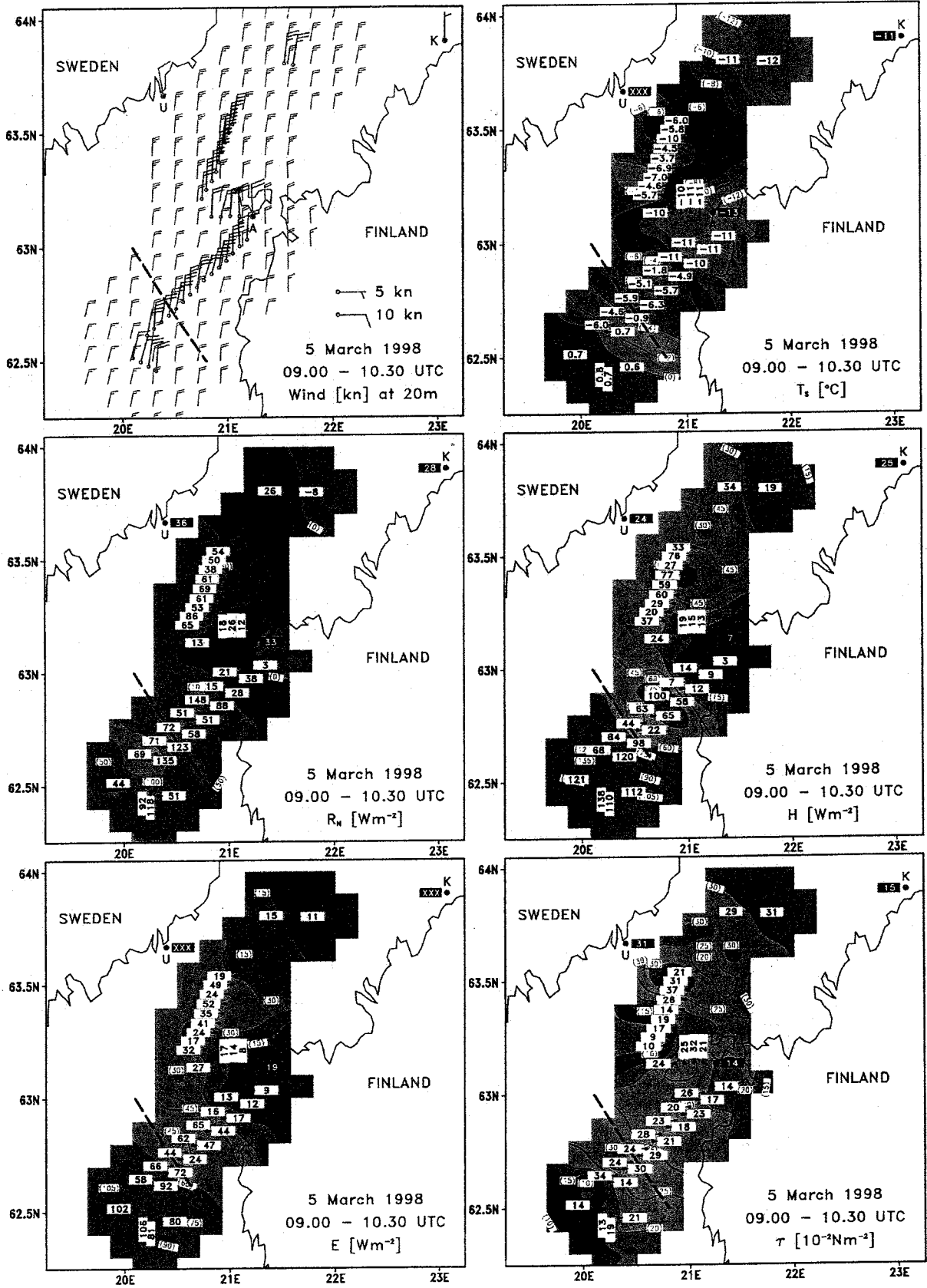


Figure 12: As Figure 9, but for 5 March 1998 between 09.00 to 10.30 UTC.

It has to be mentioned that, only on this day, the lowest flight legs had to be placed around 80 m because of bad visibility and high turbulence. Nevertheless, the aircraft and ice station data are in good agreement.

In general, during warm air advection over a colder surface, a shallow internal boundary layer (IBL) develops and the turbulent fluxes within the IBL are downwards (Garratt, 1990). The IBL may be further partitioned into very shallow sublayers. Thus, the agreement between our surface-based and aircraft results is surprisingly good. This suggests that the IBL was rather uniform and the vertical flux divergence was minor. The measured sensible heat fluxes are approximately in agreement with other observations of on-ice flows (Andreas, 1985; Fairall and Markson, 1987; Brümmer et al., 1994), although much larger downward fluxes have also been reported (Andreas et al., 1984).

On 2 March 1998 (Figure 10), a weak southwesterly to westerly flow of 3 to 5  $\text{ms}^{-1}$  and nearly cloudless conditions prevailed during the flight mission. The surface temperature generally decreased from the ice edge (about  $-1^\circ\text{C}$ ) in the southwest to less than  $-10^\circ\text{C}$  at the Finnish coast. A region with higher  $T_s$  was present between Umeå and the Isle of Vallgrund. All fluxes follow more or less the mean  $T_s$  distribution and, thus, the ice distribution. Even the region with higher  $T_s$  values southeast of Umeå appears as a region of higher fluxes. The net radiation  $R_N$  has a strong gradient from southwest to northeast. The largest  $R_N$  values (nearly  $200 \text{ Wm}^{-2}$ ) occurred over the open water. Over the ice,  $R_N$  was clearly smaller and decreased to zero or below over the closed and thick land-fast ice in the east. Heat fluxes were upward over the open water, thin ice, and regions of low ice concentration, but they were zero or even downward over regions of higher ice concentration, where the ice was also thicker. The same horizontal distribution as for  $H$  holds for the latent heat flux  $E$ . In accordance with the low wind speed the momentum flux was very small, but linked to the  $T_s$  distribution as well. The ice station measurements at Kokkola and Aranda fit well into the general horizontal distribution.

On 3 March 1998 (Figure 11), a weak mesoscale low (marked as ML in Figure 2) crossed the experimental area from west to east just during the flight mission. Thus, inhomogeneous meteorological conditions occurred in the experimental area. The sky was overcast to the south and southwest of Aranda with cloud bases below 100 m in the southwesterly air flow. On the other hand, nearly clear sky (0 - 1 octa) was present in the northeasterly flow south and southwest of Umeå, while east of Umeå 2 - 4 octas low-level clouds were present. The distribution of  $R_N$  was mainly caused by this cloud distribution and to a lesser extent by the water/ice distribution. The horizontal distributions of  $H$  and  $E$  follow the mesoscale distribution of  $T_s$  with a general decrease from southwest to northeast with an enclosed weak maximum south/southeast of Umeå where again a weak  $T_s$  maximum was present. We also mention the situation south of Aranda where a warm, moist air was advected over the rather cold land-fast ice leading to a weak downward  $H$  flux and a nearly vanishing  $E$  flux. Again the measurements at the ice stations agree well with the nearest aircraft data. Turbulent fluxes at Umeå are, however, an exception because the wind had a component from the coast.

On 5 March 1998 (Figure 12), a moderate northerly air flow of 10 to 12  $\text{ms}^{-1}$  transported cold air over the experimental area. This led to the coldest ice surface temperatures and largest sensible and latent heat fluxes (both over ice and water) measured during all six flight missions. Again, there was a clear northeast/southwest gradient of  $T_s$  with the embedded higher  $T_s$  region at and south of Aranda.  $H$  and  $E$  closely followed the ice/water distribution with values of more than  $100 \text{ Wm}^{-2}$  above the open water and less than  $20 \text{ Wm}^{-2}$  over compact ice. The maximum heat loss ( $H$  plus  $E$ ) amounted to  $240 \text{ Wm}^{-2}$ . This is a large but not an

extreme heat loss in cold-air outbreaks. Brümmer (1996) reports on heat losses of nearly  $700 \text{ Wm}^{-2}$  at the ice edge near Spitsbergen. Net radiation  $R_N$  follows both the ice/water distribution and the cloud coverage. The latter increased from 2 - 4 octas in the north to 7 - 8 octas at Aranda and south of it.

Data from all six flight missions and the simultaneous ice station measurements are summarized in Table 2. The surface temperature  $T_s$  at Aranda and Kokkola is up to 7 K colder than  $T_s$  averaged over all ice-covered parts of the aircraft legs. The ice in the ice edge zone is obviously warmer and, thus, thinner than the land-fast ice. This implies that the areally averaged heat flux for the ice-covered part of the ice edge zone is higher than at the ice stations.

Table 2: Surface temperature  $T_s$ , sensible heat flux  $H$ , net radiation flux  $R_N$ , and momentum flux  $\tau$  measured by Falcon (F) and simultaneously at the ice stations Aranda (A), Kokkola (K), and Umeå (U). Falcon data are averaged over the entire flight (F) and separately for the ice-covered ( $F_{ice}$ ) and open water part ( $F_{wat}$ ). The ice coverage  $n_{ice}$  is determined from the  $T_s$  data.

		27 Feb.	28 Feb.	2 March	3 March	5 March	6 March
$T_s$ °C	F	0.0	-1.6	-5.5	-3.1	-6.4	-5.2
	$F_{ice}$	-0.4	-2.2	-6.2	-4.3	-8.0	-7.6
	$F_{wat}$	0.4	-0.1	0.4	0.8	1.1	1.1
	A	0.0	-6.0	-12.0	-9.3	-12.8	-11.8
	K	-0.1	-3.6	-9.6	-7.6	-11.3	-14.5
	U						
$H$ [ $\text{Wm}^{-2}$ ]	F	-14	2	7	8	55	25
	$F_{ice}$	-14	-1	5	7	40	16
	$F_{wat}$	-14	11	22	11	130	47
	A	-28	-8	-2	-2	7	-6
	K	-19	0	-0	0	25	-1
	U	-39	-2		30	24	
$R_N$ [ $\text{Wm}^{-2}$ ]	F	73	96	61	82	46	63
	$F_{ice}$	70	44	47	73	41	49
	$F_{wat}$	76	215	185	113	70	98
	A		36		38	33	15
	K	61	63	-22	26	28	-32
	U				87	36	
$\tau$ [ $10^{-2} \text{ Nm}^{-2}$ ]	F	17	12	2	3	23	8
	$F_{ice}$	14	11	2	3	23	5
	$F_{wat}$	18	14	3	3	15	13
	A	35	2	1	2	14	4
	K	8	5	1	0	15	1
	U	28	5		10	31	
$n_{ice}$		0.47	0.69	0.90	0.76	0.83	0.73



Taken together, it can be concluded from the mesoscale fields in Figures 9 to 12:

- (a) Ice station fluxes and closest aircraft fluxes agree well.
- (b) The fluxes at the ice stations only hold for that particular location. They cannot be taken to estimate the average fluxes over the inhomogeneous sea ice area.
- (c) There is a general northeast/southwest gradient of surface temperature in the Gulf of Bothnia. The  $H$  and  $E$  distribution is closely related to the  $T_s$  distribution. This also holds for embedded mesoscale variations.
- (d) The mesoscale variability of the net radiation  $R_N$  is generally much larger than that of  $H$  and  $E$ . The variability of  $R_N$  is caused by the variability of both the cloud and the ice cover. The variability caused by cloud cover is dominating. Since  $R_N$  is mostly the largest term in the surface energy budget (particularly during day time) the proper knowledge of the cloud field is most important.

### 5.3 Time-averaged horizontal distributions

The six aircraft missions took place during different weather conditions. We use the interpolated 11 km grid to estimate the time-averaged horizontal distribution of fluxes. For this average only those grid points are considered which are available during all flight missions. Since the second flight mission on 28 February 1998 covered only a small area west of Kokkola it is omitted in the averages presented in Figure 13 which is based on the flight missions on 27 February, 2 March, 3 March, 5 March, and 6 March 1998. The averages at the three ice stations are added both for the periods of the flight missions and for the entire BASIS period if the representative station data were available without gaps.

The  $T_s$  field (Figure 13) clearly represents the different surface types: open water in the southwest, the cold land-fast ice around Aranda, the fractured ice/water surface west and north of the Isle of Vallgrund, the increasingly colder ice towards northeast, and the even colder land-fast ice at Kokkola. Net radiation  $R_N$  - since it holds for conditions near noon - is positive everywhere but reflects the different surface types clearly. The same is, of course, true for the sensible ( $H$ ) and latent ( $E$ ) heat flux which closely follow the  $T_s$  distribution.

To obtain an approximate estimate of the surface energy budget  $B$  during the period from 27 February to 6 March 1998, we present two  $B$  estimates in Figure 13: one for the time around noon and the other for the night time neglecting the net short-wave radiation  $S_N$  and assuming that all other fluxes remain the same as during day time. Of course, the latter  $B$  estimates contain a lot of uncertainties. Nevertheless, we suppose that the two  $B$  estimates for day and night are not too far from reality. Both  $B$  distributions show a clear dependence on the water/ice surface conditions. The amplitudes of  $B$  are smaller over ice than over water. The positive  $B$  values during the day are over-compensated by negative ones during the night. During this time of the year the daily average can approximately be calculated as:  $B_{Total} = 0.28 \cdot B_{Noon} + 0.72 \cdot B_{Night}$ . We end up with a clearly negative energy balance  $B$  on the average for the last 8 days of the BASIS period. The mean value of  $B_{Total}$  ranged between  $-30$  and  $-60 \text{ Wm}^{-2}$  in the ice edge zone area, where the latter value holds for the open water.

The average of  $B$  at Kokkola and Aranda for the five flight days amounts to  $-22 \text{ Wm}^{-2}$ , respectively. This  $B$  estimate is about  $15 \text{ Wm}^{-2}$  higher than the aircraft-based estimate. When looking into the different terms contributing to  $B$  it can be seen that the

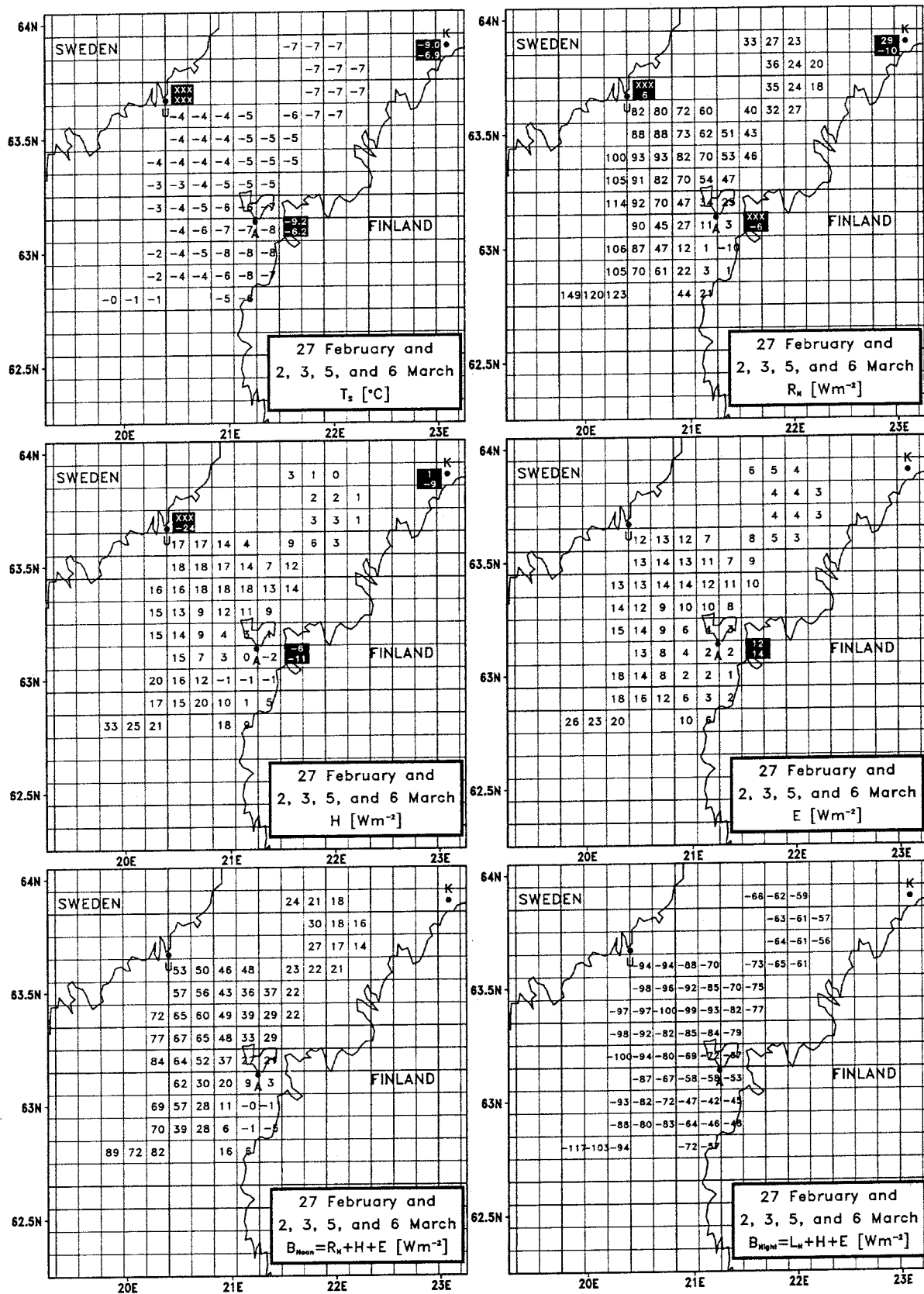


Figure 13: Time-averaged spatial distribution of surface temperature  $T_s$ , net radiation  $R_N$ , sensible heat flux  $H$ , latent heat flux  $E$ , energy budget  $B_{\text{Noon}}$  during noon, and  $B_{\text{Night}}$  during night based on the flight missions on 27 February, 2, 3, 5, and 6 March 1998. Ice station values (black rectangles) are averaged for the periods of the flight missions (top) and for the entire BASIS period (bottom).

difference is caused by  $L_N$ . Obviously, the aircraft  $L_N$  measurements during the day cannot simply be transferred to the night time conditions, because of the daily cycle of  $T_s$ .

## 6. Concluding remarks

In this paper, turbulent fluxes of heat and momentum as well as radiation fluxes are presented which were sampled over the ice edge zone of the northern Baltic Sea during the BASIS field experiment between 16 February and 6 March 1998. Two kinds of platforms were used: three surface stations deployed on land-fast ice and one aircraft flying at low levels over land-fast ice, broken ice, and open water at particular times.

In view of the relatively small distances of 50 to 100 km between the surface stations, mean meteorological quantities show remarkable differences such as the air temperature with a difference of 3 K (Table 1). This results primarily from the different fetches over sea ice.

Sensible heat flux  $H$  and net radiation flux  $R_N$  varied strongly during the campaign as consequence of the rapidly varying synoptic weather conditions. On the average,  $H$  was an energy source and  $R_N$  an energy sink for the land-fast ice. The role of sensible heat flux as a heat source is manifested when warm air from southwest is advected over the sea ice (Figures 2 - 5).

For the Arctic Ocean, it is well known that due to an effective radiative cooling a stable stratification prevails over the sea ice in winter, and the sensible heat flux is therefore directed downwards (Untersteiner, 1986; Jordan et al., 1999). Observations on the heat fluxes over the Baltic Sea ice do not seem to have been published previously. The predominantly downward sensible heat fluxes agree with the Arctic data, but the physical situation is apparently different. In our case, the observations were made in the ice edge zone, and the largest downward fluxes occurred during warm air advection, and these flux magnitudes were larger than typically observed in the Arctic (Jordan et al., 1999). This suggests that the advection was the primary reason for the large fluxes. During periods of cold air temperatures with strong long-wave cooling, the situation was more resembling that in the Arctic Ocean in winter. The downward sensible heat fluxes were smaller or even upward fluxes were observed. This was partly due to the short duration of the cold periods, during which the heat stored in the snow and ice conducted to the surface.

At the Finnish coast, our three-week average temperature was about 1 K warmer than the climatological mean for the region, and, in particular, the period was characterized by rapid variations in weather (Finnish Meteorological Institute, 1998). More experimental data are therefore required to understand the energy balance of the Baltic Sea ice cover also in a climatological level. This is necessary in particular for the radiative fluxes, for which the agreement of surface station and aircraft results was worse.

There is evidence that the aircraft measured turbulent fluxes are reliable for two reasons: the aircraft fluxes react immediately to horizontal changes of the underlying surface - as confirmed by a high correlation coefficient between flux and forcing - and they conformed well with the ice station fluxes. At the Aranda and Kokkola stations the aircraft- and surface-based sensible heat fluxes agreed well (typically within a few  $\text{Wm}^{-2}$ ) when compared to studies over land surfaces (Kelly et al., 1992; Desjardins et al., 1997). This was achieved because the land-fast ice surface is almost homogeneous and because the flat surface allowed lower flight levels than usually possible over a land surface. The good agreement at the land-fast ice close to the surface stations suggests that the fluxes measured over fractured ice in the

middle of the northern Baltic Sea are also of a good accuracy, and perhaps not as liable to errors as the aircraft flux measurements over more complex surfaces.

The fluxes measured at the ice stations only hold for that particular location, at most for the land-fast ice area in general. The mesoscale variability of the fluxes measured by aircraft over various ice conditions demonstrates that areally representative fluxes for the whole ice edge zone cannot be estimated from the fluxes at land-fast ice stations.

The mesoscale distributions in Figures 9 to 12 show that there is a general north to south gradient of surface temperature and sensible and latent heat flux in the northern Baltic Sea. Both  $H$  and  $E$ , and also to some extent the momentum flux  $\tau$ , follow mesoscale variations of  $T_s$  in a positively correlated way.

The energy budget  $B$  over the ice edge zone varies strongly with the underlying surface (ice or water). The dominating term in the energy budget is the net radiation flux  $R_N$ . In most situations  $R_N$  varies stronger than  $H$  and  $E$ .  $R_N$  variations are caused to a larger degree by the varying cloud cover and to a smaller degree by the varying ice cover. Therefore, even in the ice edge zone the proper knowledge of the cloud field is decisive for the energy budget.

Both the records of the three ice stations and the interpolated grid fields of the aircraft data are suited for validation of meso- and regional-scale models. The ice station data are useful to validate the energy exchange between atmosphere and land-fast ice near to the coast. Although aircraft data are only available for certain periods, only they can give the spatial distribution of surface properties and surface fluxes within the inhomogeneous ice edge area where no other data exist. Due to the low flight levels between 10 and 30 m and as manifested by comparison with the ice station values, the aircraft-based fields of turbulent fluxes and other meteorological quantities appear to be very close to reality.

## References

- André, J.-C., P. Bougeault, and J.-P. Goutorbe, 1990: Regional estimates of heat and evaporation fluxes over non-homogenous terrain. Examples from the HAPEX-MOBILY PROGRAMME. *Boundary-Layer Met.*, **50**, 77-108.
- Andreas, E.L., W.B. Tucker, and S.F. Ackley, 1984: Atmospheric boundary-layer modification, drag coefficient, and surface heat flux in the Antarctic marginal ice zone. *J. Geophys. Res.*, **89**, 649-661.
- Andreas, E.L., 1985: Heat and moisture advection over Antarctic sea ice. *Mon. Wea. Rev.*, **113**, 736-746.
- Brümmer, B., B. Busack, H. Hoerber, and G. Kruspe, 1994: Boundary-layer observation over water and Arctic sea-ice during on-ice air flow. *Boundary-Layer Met.*, **68**, 75-108.
- Brümmer, B., 1996: Boundary-layer modification in wintertime cold-air outbreaks from the Arctic sea ice. *Boundary-Layer Met.*, **80**, 109-125.
- Cressman, G.P., 1959: An operational objective analysis system *Mon. Wea. Rev.*, **87**, 367-474.
- Desjardins, R.L., J.I. Macpherson, L. Mahrt, P. Schuepp, E. Pattey, H. Neumann, D. Baldocchi, S. Wofsy, D. Fitzjarrald, H. Mccaughey, and D.W. Joiner, 1997: Scaling up flux measurements for the boreal forest using aircraft-tower combinations. *J. Geophys. Res.*, **102**, 29125-29133.
- Dobosy, R.J., T.L. Crawford, J.I. Macpherson, R.L. Desjardins, R.D. Kelly, S.P. Oncley, and D.H. Lenschow, 1997: Intercomparison among four flux aircraft at BOREAS in 1994. *J. Geophys. Res.*, **102**, 29101-29111.

- Emeis, S., 1995: Determination of the surface sensible heat flux from aircraft measurements. *Beitr. Phys. Atmosph.*, **68**, 143-148.
- Fairall, C.W., and R. Markson, 1987: Mesoscale variations in surface stress, heat fluxes, and drag coefficient in the marginal ice zone during the 1983 Marginal Ice Zone Experiment. *Geophys. Res.*, **92**, 6921-6932.
- Finnish Meteorological Institute, 1998: *Ilmastokatsaus (Climate Review, in Finnish)*, **02/98** and **03/98**.
- Garratt, J.R., 1990: The internal boundary layer - a review. *Boundary-Layer Met.*, **50**, 171-203.
- Grossman, R.L., 1992: Sampling error in the vertical fluxes of potential temperature and moisture measured by aircraft during FIFE. *J. Geophys. Res.*, **97**, 18439-18443.
- Grunwald J., N. Kalthoff, F. Fiedler, and U. Corsmeier, 1998: Application of different flight strategies to determine areally averaged turbulent fluxes. *Contr. Atmos. Phys.*, **71**, 283-302.
- Guest, P.S., and K.L. Davidson, 1991: The aerodynamic roughness of different types of sea ice. *J. Geophys. Res.*, **96**, 4709-4721.
- Högström, U., 1988: Non-dimensional wind and temperature profiles in the atmospheric surface layer: A re-evaluation. *Boundary-Layer Met.*, **42**, 55-78.
- Holtslag, A.A.M. and H.A.R. De Bruin, 1988: Applied modeling of the nighttime surface energy balance over land. *J. Appl. Met.*, **27**, 689-704.
- Jordan, R.E., E.L. Andreas, and A.P. Makshtas, 1999: Heat budget of snow-covered sea ice at North Pole 4. *J. Geophys. Res.*, **104**, 7785-7806.
- Kelly, R.D., E.A. Smith, and J.I. Macpherson, 1992: A comparison of surface sensible and latent heat fluxes from aircraft and surface measurements in FIFE 1987. *J. Geophys. Res.*, **97**, 18445-18453.
- Launiainen, J. and T. Vihma, 1990: Derivation of turbulent surface fluxes - an iterative flux-profile method allowing arbitrary observing heights. *Environmental Software*, **5**, 113-124.
- Launiainen, J. (Ed.), 1999: BALTEX-BASIS Data Report 1998. *BALTEX Secretariat Publ. No. 14*, Geesthacht, Germany.
- Launiainen, J., B.Cheng, J.Uotila and T.Vihma, 2001: Turbulent surface fluxes and air-ice coupling in BALTEX-BASIS. *Submitted to Annals Glaciology*.
- Lenschow, D.H. and B.B. Stankov, 1986: Length scales in the convective boundary layer. *J. Atm. Sci.*, **43**, 1198-1209.
- Lenschow, D.H., J. Mann, and L. Kristensen, 1994: How long is long enough when measuring fluxes and other turbulence statistics? *J. Atmos. and Oceanic Technol.*, **11**, 661-673.
- Leppäranta, M. and A. Seinä, 1985: Freezing, maximum annual ice thickness and breakup of ice on the Finnish coast during 1830-1984. *Geophysica*, **21**, 87-104.
- Mahrt, L. and M. Ek, 1993: Spatial variability of turbulent fluxes and roughness lengths in HAPEX-MOBILHY. *Boundary-Layer Met.*, **65**, 381-400.
- Mann, J. and D.H. Lenschow, 1994: Errors in airborne flux measurements. *J. Geophys. Res.*, **99**, 14519-14526.
- Stössel, A., and M. Claussen, 1993: On the momentum forcing of a large-scale sea-ice model. *Clim. Dyn.*, **9**, 71-80.
- Untersteiner, N., 1986: The geophysics of sea ice: overview, in *Geophysics of Sea Ice. Plenum Press, New York*, pp. 1-8.
- Vihma, T., 1995: Subgrid parameterization of surface heat and momentum fluxes over polar oceans. *J. Geophys. Res.*, **100**, 22625-22646.

# On the parameterization of turbulent surface fluxes over broken sea ice

Timo Vihma<sup>1)</sup>, David Schröder<sup>2)</sup>, Agathe Kerber<sup>2)</sup>, and Burghard Brümmer<sup>2)</sup>

<sup>1)</sup> Finnish Institute of Marine Research, Helsinki, Finland

<sup>2)</sup> Meteorological Institute, University of Hamburg, Germany

## 1. Introduction

The surface energy balance over sea is controlled by short-wave and long-wave radiative fluxes, turbulent air-ice fluxes of sensible and latent heat, and the conductive heat flux from the ocean through the ice and snow (e.g. Makshtas, 1991). The turbulent sensible heat flux may be directed either from air to ice or from ice to air, and in general it has a smaller magnitude than the dominating radiation component. The latent heat flux is generally smaller in magnitude than the sensible heat flux. The ice and snow thickness strongly affect the conductive heat flux, in particular when the ice and snow layers are thin. Hence, also the other components of the surface heat balance indirectly depend on the ice and snow thickness. In winter, over cracks, leads, and polynyas the surface may be even 30 K warmer than the air, and the sensible and latent heat fluxes together can amount to values of more than  $600 \text{ Wm}^{-2}$  (e.g. Brümmer, 1996). Thus, even a small fraction of open water may strongly affect the area-averaged surface energy balance.

The parameterization of surface fluxes over a broken ice cover is a problem for numerical atmospheric and ocean models because of three principal reasons: (1) The state of the surface changes rapidly in time, (2) the spatial scale of variations between sea ice and open water is often much smaller than the model grid size, and (3) the surface may be extremely inhomogeneous with respect to the temperature. The turbulent surface fluxes of momentum ( $\tau$ ), sensible heat (H) and latent heat (LE) are generally parameterized by the bulk formulae:

$$\tau = \rho C_D V^2 \quad (1)$$

$$H = \rho c_p C_H (\theta_s - \theta) V \quad (2)$$

$$LE = \rho \lambda C_E (q_s - q) V \quad (3)$$

where  $\rho$  is the density and  $c_p$  the specific heat of air,  $\lambda$  is the latent heat of vaporization, and  $V$  is the wind speed. The  $\theta_s - \theta$  and  $q_s - q$  are respectively the differences in potential temperature and specific humidity between the surface and the atmosphere. Applying the Monin-Obukhov similarity theory the transfer coefficients for momentum ( $C_D$ ), heat ( $C_H$ ), and moisture ( $C_E$ ) can be determined as a function of the roughness lengths for momentum  $z_0$ , heat  $z_T$ , and moisture  $z_q$  and of the universal functions  $\Psi_M$ ,  $\Psi_H$ , and  $\Psi_E$ :

$$C_D = \kappa^2 [\ln(z/z_0) - \Psi_M(z/L)]^2, \quad (4)$$

$$C_H = \kappa^2 [\ln(z/z_0) - \Psi_M(z/L)]^{-1} [\ln(z/z_T) - \Psi_H(z/L)]^{-1}, \quad (5)$$

$$C_E = \kappa^2 [\ln(z/z_0) - \Psi_M(z/L)]^{-1} [\ln(z/z_q) - \Psi_E(z/L)]^{-1}, \quad (6)$$

where  $\kappa$  is the von Karman constant ( $\kappa = 0.4$ ),  $z$  is the reference height, and  $L$  is the Obukhov length.

The problems in subgrid-scale parameterization of fluxes over polar oceans were addressed in Vihma (1995) with most emphasis in the spatial scale of polynyas. In this paper we concentrate on smaller scale variations between the sea ice and open water, and examine the effects of the roughness lengths on the turbulent exchange. The roughness lengths are calculated on the basis of aircraft observations. We present and discuss the absolute magnitudes and mutual ratios of the three roughness lengths  $z_0$ ,  $z_T$ , and  $z_q$  as well as the corresponding transfer coefficients, and study their dependence on the ice concentration and surface albedo.

## 2. Roughness lengths and their ratios

A lot of observations have been made on the roughness length for momentum over sea. A review is given by Overland and Davidson (1992). A widely applied equation relating  $z_0$  to the geometric properties of the surface has been presented by Banke et al. (1980). Over bluff roughness elements, like sea ice with ridges and patterns of snowdrift, the thermal roughness length  $z_T$  depends on  $z_0$  and the roughness Reynolds number  $Re = z_0 u_* / \nu$ , where  $u_*$  is the friction velocity and  $\nu$  the kinematic viscosity of air. An empirical relation for this dependence was derived by Andreas (1987). The BASIS results of Launiainen et al. (2001, this issue) are approximately comparable to it. The ratio  $z_0/z_T$  is less than 1 for a very smooth ice, about 10 for a typical sea ice with  $z_0 \approx 1$  mm, and then increases up to 300 for  $z_0 \approx 5$  mm. Over a water surface,  $z_0$  has a well-known dependence on the wind speed (e.g. Smith, 1988), while  $z_T$  shows little or no dependence on the wind speed (DeCosmo et al., 1996). The ratio  $z_0/z_T$  is approximately 2. Usually the roughness length  $z_q$  and the transfer coefficient for moisture  $C_E$  are taken equal to those for heat. Due to the difference between the Schmidt and Prandtl numbers, a slightly larger transfer coefficient for moisture, i.e.  $C_E/C_H = 1.05$  to  $1.2$ , has also been suggested (e.g. Brutsaert, 1975) and applied in models (e.g. Eppel et al., 1995).

The results mentioned above are basically only valid over homogeneous ice and water surfaces. When calculating the turbulent fluxes on the basis of the roughness lengths and Monin-Obukhov theory over a heterogeneous surface, we are applying the theory in conditions where it is not strictly valid. This is, however, a common practice in numerical models, and our goal is to provide relevant values for the roughness lengths in such conditions.

If a numerical model calculates the surface fluxes applying the mixture method (i.e. parameter aggregation), all the quantities in equations (1) to (6) are interpreted as grid-averages. Then the roughness lengths are not local parameters, but refer to the relations of the grid-averaged quantities and are called as effective roughness lengths. For the parameterization of momentum transfer, the effective roughness length  $z_0^{eff}$  should take into account the aggregated effects of the roughness of a heterogeneous surface. Over a broken sea ice,  $z_0^{eff}$  exceeds the  $z_0$  of compact sea ice because of the form drag due to floe edges (Mai et al., 1996), and parameterization schemes have been developed to take this effect into account. Uotila (2001) gives a successful example of this. Formulae for an effective roughness lengths for heat,  $z_T^{eff}$ , have been derived for heterogeneous surfaces (Wood and Mason, 1991), but we are not aware of results for  $z_T^{eff}$  particularly derived for broken sea ice.

In some models (e.g. Stössel and Claussen, 1993), the momentum flux is described by an effective roughness length, while a mosaic method, i.e. flux aggregation, is used to calculate the surface fluxes of sensible and latent heat. This requires, however, that the model applies information on the ice concentration to calculate the heat fluxes separately over the ice-covered and ice-free parts of the grid box. If this is not made,  $Z_T^{eff}$  should be applied, in principle, although in many models (e.g. ECHAM)  $Z_T^{eff}$  is equated with  $Z_0^{eff}$ . Over a heterogeneous surface in general, the ratio of the roughness lengths may differ drastically from the ratios which were presented above for homogeneous sea ice and open water. For example, Beljaars and Holtslag (1991) and Mahrt and Ek (1993) observed a ratio  $Z_0^{eff} / Z_T^{eff} = 10^4$  for heterogeneous land surfaces, and Beljaars and Viterbo (1994) concluded that using a ratio of  $10^3$  the ECMWF model produces better winter evaporation over land. Beljaars (1994) even observed a ratio of  $10^7$  for a heterogeneous pastureland.

### 3. Aircraft Observations

Six missions of the German research aircraft Falcon were flown over the ice edge zone of the Northern Baltic Sea on 27 and 28 February and on 2, 3, 5, and 6 March 1998 (see Figure map). They took place under different weather conditions: on-ice air flows on 27 and 28 February, weak turbulence and almost cloudless conditions on 2 March, a meso-scale low in the operation area on 3 March, and off-ice air flows on 5 and 6 March. The equipment of the aircraft are described by Brümmer et al. (2001, this issue). Our studies are based on the low-level flight legs. Ten horizontal legs were flown at heights between 10 and 30 m above the surface and lasted for 3.5 to 10 minutes each corresponding to distances of 20 to 60 km. The relevant values for our calculations – air and surface temperature, air humidity, and wind speed - were measured by a horizontal resolution of 1 m. The turbulent fluxes of momentum, sensible and latent heat were calculated using averaging lengths of 1, 2, 4, 8, and 20 km. The linear trend was removed before applying the eddy correlation technique.

### 4. Calculation of roughness lengths

Transforming the system of equations (4) to (6) and using (1) to (3) the effective roughness lengths  $Z_0^{eff}$ ,  $Z_T^{eff}$ , and  $Z_q^{eff}$  can be expressed as:

$$Z_0^{eff} = z \exp \left[ \left( \rho \kappa^2 V^2 / \tau^2 \right)^{-1/2} + \Psi_M(z/L) \right]^{-1} \quad (7)$$

$$Z_T^{eff} = z \exp \left[ \frac{\rho c_p \kappa^2 (\theta_s - \theta) V}{H \left[ \ln(z/Z_0^{eff}) - \Psi_M(z/L) \right]} + \Psi_H(z/L) \right]^{-1} \quad (8)$$

$$Z_q^{eff} = z \exp \left[ \frac{\rho \lambda \kappa^2 (q_s - q) V}{LE \left[ \ln(z/Z_0^{eff}) - \Psi_M(z/L) \right]} + \Psi_E(z/L) \right]^{-1} \quad (9)$$

The Obukhov length  $L$  can be calculated using the measured values of the turbulent fluxes. The universal functions are determined according to Holtslag and de Bruin (1988) for stable stratification and according to Högström (1988) for unstable stratification. Applying the measured values for  $\theta_s$ ,  $\theta$ ,  $q$ ,  $V$ ,  $H$ ,  $LE$ , and  $\tau$ , the roughness lengths can be calculated. These calculations are done for the 10 low-level flight legs varying the averaging lengths from 1 to



20 km. A weak turbulence and small heat fluxes cause large uncertainty for determination of the roughness lengths. Thus, cases of  $\tau < 0.01 \text{ Nm}^2$  and  $|H| < 2 \text{ Wm}^{-2}$  are excluded. The calculated roughness lengths are effective roughness lengths, because they are determined by the mixture method on the basis of spatial averages without any distinction between sea ice and open water. In the following the term "effective" is omitted and we use the symbols  $z_0$ ,  $z_T$ , and  $z_q$  for simplicity. Knowing the roughness lengths, the neutral transfer coefficients  $C_{DN}$ ,  $C_{HN}$ , and  $C_{EN}$  result from the equations (4), (5), and (6), respectively, setting in zero for the universal functions.

## 5. Results

### 5.1. Roughness lengths, transfer coefficients and their ratios

The roughness lengths  $z_0$ ,  $z_T$ , and  $z_q$ , their logarithmic ratios, the neutral transfer coefficients  $C_{DN}$ ,  $C_{HN}$ , and  $C_{EN}$ , and their ratios are presented for the all 10 flight legs separately and as an average in Table 1. For classification, the distance of the flight leg, the ice concentration, and albedo are added. All values are based on averages over 20 km long parts of the low-level flight legs. As the roughness lengths always enter into the model parameterizations in a logarithmic form, they are averaged as logarithmic means.

Table 1. Mean values of ice concentration ( $n_{ice}$ ), albedo (Alb), the roughness lengths  $z_0$ ,  $z_T$ , and  $z_q$ , and their ratios as well as the neutral transfer coefficients referred to 10 m height  $C_{DN}$ ,  $C_{HN}$ , and  $C_{EN}$ , and their ratios. All values are based on running means over 20 km long legs, shifted by 50 m. The low-level flight leg 1 took place on 28 February, legs 2 to 5 on 2 March, leg 6 on 3 March, legs 7 and 8 on 5 March, and legs 9 and 10 on 6 March 1998. The overall means at the lowest row are weighted by the length of the flight legs and based on the legs 3 to 10, only. The means of the roughness lengths are calculated as logarithmic means.

leg	Dist. [km]	$n_{ice}$	Alb	$z_0$ [m]	$z_T$ [m]	$z_q$ [m]	$\ln(z_0)/$ $\ln(z_T)$	$\ln(z_q)/$ $\ln(z_T)$	$C_{DN}$ $\times 10^3$	$C_{HN}$ $\times 10^3$	$C_{EN}$ $\times 10^3$	$C_{DN}/$ $C_{HN}$	$C_{EN}/$ $C_{HN}$
1	38.0	1.00	0.44	2E-4	3E-25	2E-1	0.16	0.03	1.3	0.3	3.5	5.4	14.0
2	20.6	1.00	0.55	7E-4	5	3E-7	-4.67	-9.68	1.8	22.3	1.0	0.1	0.0
3	27.2	0.98	0.34	5E-4	4E-6	3E-5	0.61	0.83	1.6	1.1	1.3	1.5	1.2
4	27.8	0.92	0.37	8E-5	2E-15	4E-9	0.28	0.57	1.2	0.4	0.6	3.1	1.7
5	23.3	0.16	0.13	8E-6	5E-6	3E-5	0.97	0.85	0.8	0.8	0.9	1.0	1.1
6	22.1	1.00	0.82	8E-3	1E-5	3E-3	0.44	0.53	3.1	1.7	2.7	1.9	1.6
7	28.1	0.99	0.39	4E-5	7E-10	2E-7	0.48	0.74	1.0	0.6	0.7	1.9	1.3
8	61.8	0.95	0.50	1E-3	6E-8	9E-6	0.41	0.70	1.9	0.9	1.3	2.1	1.4
9	35.5	1.00	0.63	2E-4	2E-7	4E-13	0.55	1.83	1.4	0.8	0.5	1.7	0.6
10	40.5	0.76	0.29	4E-4	9E-8	2E-8	0.48	1.08	1.6	0.9	0.8	1.8	0.9
Mean		0.87	0.44	3E-4	3E-8	2E-7	0.50	0.91	1.6	0.9	1.1	1.9	1.2

The values of  $z_0$  vary in orders of magnitude between  $10^{-6}$  m and  $10^{-3}$  m. The mean value of  $3 \cdot 10^{-4}$  m is somewhat smaller than the value of  $1 \cdot 10^{-3}$  m commonly used for sea ice roughness in models. The roughness length for sensible heat  $z_T$  varies more strongly and amounts to a mean value of  $3 \cdot 10^{-8}$  m being 4 orders of magnitude smaller than  $z_0$ . The  $z_T$ -values of  $3 \cdot 10^{-25}$  m and 5 m (leg 1 and 2) seem to be unrealistic. The first leg was flown in or above a shallow stable boundary layer on 28 February 1998, and it was not clear whether the measurements at the height of 15 m represented the surface fluxes. During the second leg, the turbulence and heat fluxes were very weak causing large errors in the determination of the roughness lengths. For this reason the first two legs were not taken into account in calculating

the mean values in the last row of Table 1. The roughness length for moisture  $z_q$  is on average one order of magnitude larger than  $z_T$ .

The calculated roughness lengths have a lot of scatter, but their logarithmic ratios are the momentous numbers. Table 1 shows that the ratio  $\ln(z_0)/\ln(z_T)$  is about 0.5. Only for leg 5, mostly over open water, the ratio is close to 1. Concerning the ratio  $\ln(z_q)/\ln(z_T)$ , values slightly smaller than 1 are calculated in most cases. The same information is given by the neutral transfer coefficients: the mean  $C_{HN}$  amounts to  $0.9 \cdot 10^{-3}$  m and is smaller than the mean  $C_{DN}$  of  $1.6 \cdot 10^{-3}$  m by a factor of almost 2.

## 5.2 Dependence on ice concentration and albedo

Before investigating the dependence of the ratio  $\ln(z_0)/\ln(z_T)$  on ice concentration and albedo in general, one flight leg (leg 8 in Table 1) is presented as an example. In Figure 1, the ice concentration and albedo ( $n_{ice}$ , Alb), roughness lengths ( $z_0$ ,  $z_T$ ), their logarithmic ratio  $\ln(z_0)/\ln(z_T)$ , surface and air temperature ( $T_s$ ,  $T$ ), and sensible heat flux ( $H$ ) are shown as determined using averaging lengths of 4, 8, and 20 km. The 60-km long leg was flown during an off-ice air flow on 5 March 1998, and led from land-fast ice over a transitional zone to the open water.

The calculated  $z_0$ -values are about  $10^{-3}$  m over the whole leg, whereas the  $z_T$ -values vary a lot in space and depend on the averaging length. The 4-km averages of  $z_T$  vary from  $10^{-18}$  m to  $10^{-3}$  m, but the extreme values disappear by averaging over longer distances. The resulting ratio  $\ln(z_0)/\ln(z_T)$  amounts to a quite constant value of 0.4 for the 20-km averages, whereas fluctuations between 0.2 and 0.9 are observed for the 4-km averages. These fluctuations can be interpreted to some degree with respect to the ice conditions. The largest values occur over the land-fast ice (Distance = 5 km in Figure 1) and over the open water (58 km). The other extreme values of the ratio  $\ln(z_0)/\ln(z_T)$  are affected by a delay of the sensible heat flux in responding to the temperature difference  $T-T_s$  (e.g. at 24 km), or by the heat flux changes while  $T-T_s$  remains constant (e.g. at 42 km). To reduce these effects we concentrate in the following on the 20-km averages.

In Figure 2, the ratio  $\ln(z_0)/\ln(z_T)$  is presented as a function of  $n_{ice}$  (a) and albedo (b) for all low-level flight legs. The 20-km averages are shifted by 1 km. Hence, 130 cases taken from the 9 legs are shown. The anomalous value calculated for leg 2 (see Table 1) is dropped out. The accuracy of the calculated roughness lengths depends on the stratification and the magnitude of  $H$ . Thus, cases of stable stratification are marked by squares, cases of small upward  $H$  ( $H < 10 \text{ Wm}^{-2}$ ) by crosses, and the other cases by circles. Two regression curves of second order are added in each figure: the solid line represents all cases, and the dotted line the cases of an upward  $H$ -flux of more than  $10 \text{ Wm}^{-2}$ .

In Figure 2a, always when  $n_{ice}$  is smaller than 0.9,  $H$  is larger than  $10 \text{ Wm}^{-2}$ , and the ratio  $\ln(z_0)/\ln(z_T)$  clearly follows the regression curve: for a low ice fraction ( $n_{ice} < 0.2$ ) the ratio is close to 1 and it drops to 0.4 with increasing ice fraction. When the ice concentration is close to 1, the ratio varies from 0.2 to 1.2. The smallest values were calculated for a stable stratification, and a part of the scatter can be explained by the small heat fluxes (crosses). In any case, it can be concluded that  $\ln(z_T)$  is clearly smaller than  $\ln(z_0)$  over a broken sea ice cover. However, there are many different ice types in the ice edge zone, so that the ice concentration alone cannot represent the ice conditions and their total effect on the energy

exchange with the atmosphere. Thus, the ratio  $\ln(z_0)/\ln(z_T)$  is also presented as a function of the surface albedo (Figure 2b). The distribution looks different from Figure 2a, because albedo values between 0.3 and 0.85 were observed while  $n_{ice}$  was almost 1. Nevertheless, the regression curves resemble each other. Based on the regression curves for  $H > 10 \text{ Wm}^{-2}$ , we present two functional forms for the ratio  $\ln(z_0)/\ln(z_T)$ :

$$\ln(z_0)/\ln(z_T) = 1.4 - 2.6 \cdot n_{ice} + 1.7 \cdot n_{ice}^2 \quad (10)$$

$$\ln(z_0)/\ln(z_T) = 1.2 - 2.6 \cdot Alb + 2.1 \cdot Alb^2 \quad (11)$$

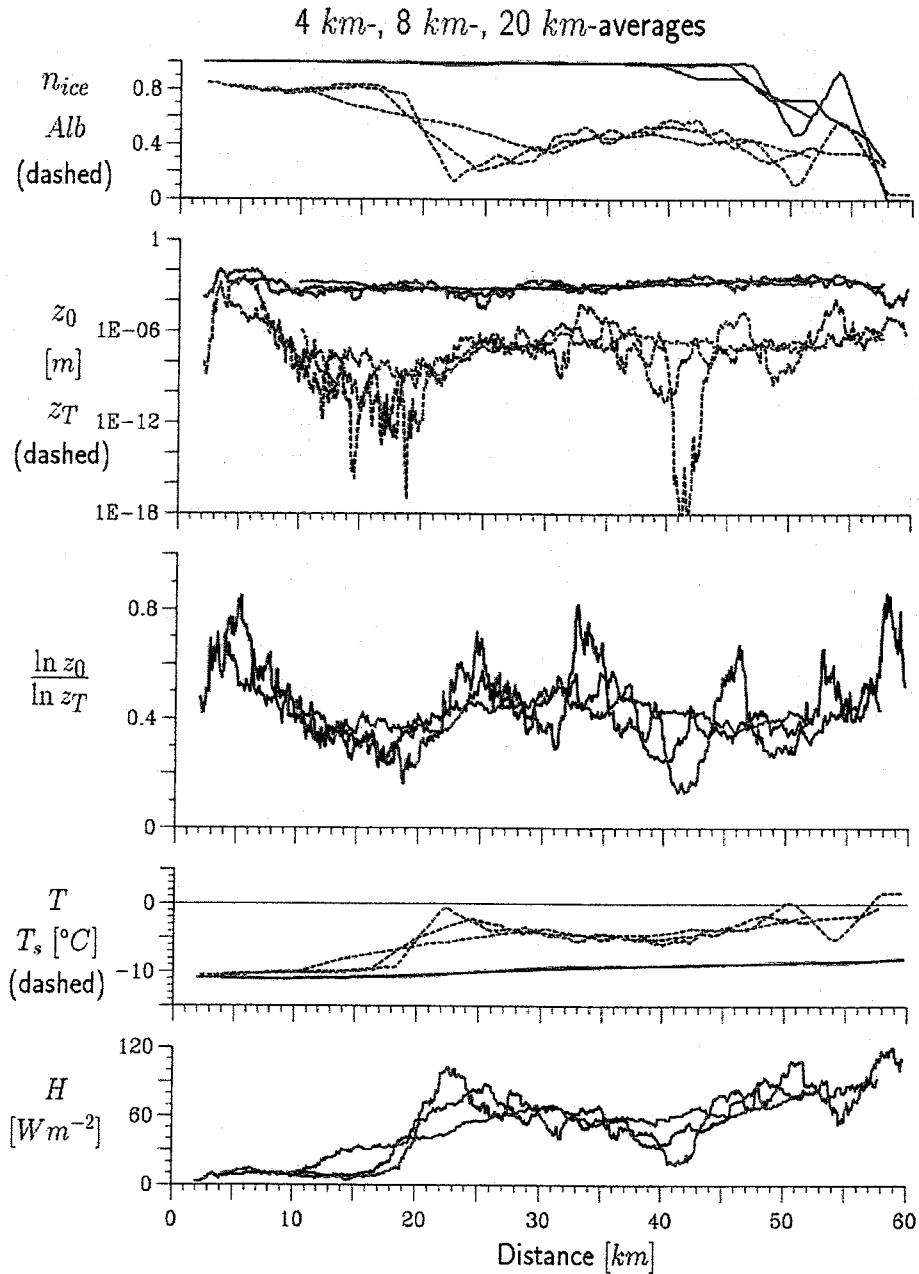


Figure 1. Ice concentration and albedo ( $n_{ice}$ ,  $Alb$ ), roughness lengths ( $z_0$ ,  $z_T$ ), their logarithmic ratio  $\ln(z_0)/\ln(z_T)$ , air and surface temperature ( $T$ ,  $T_s$ ), and surface heat flux ( $H$ ) as measured during a low-level flight leg on 5 March 1998 (leg 8 in Table 1), during an off-ice air flow. The results are presented for averaging lengths of 4 km, 8 km, and 20 km.

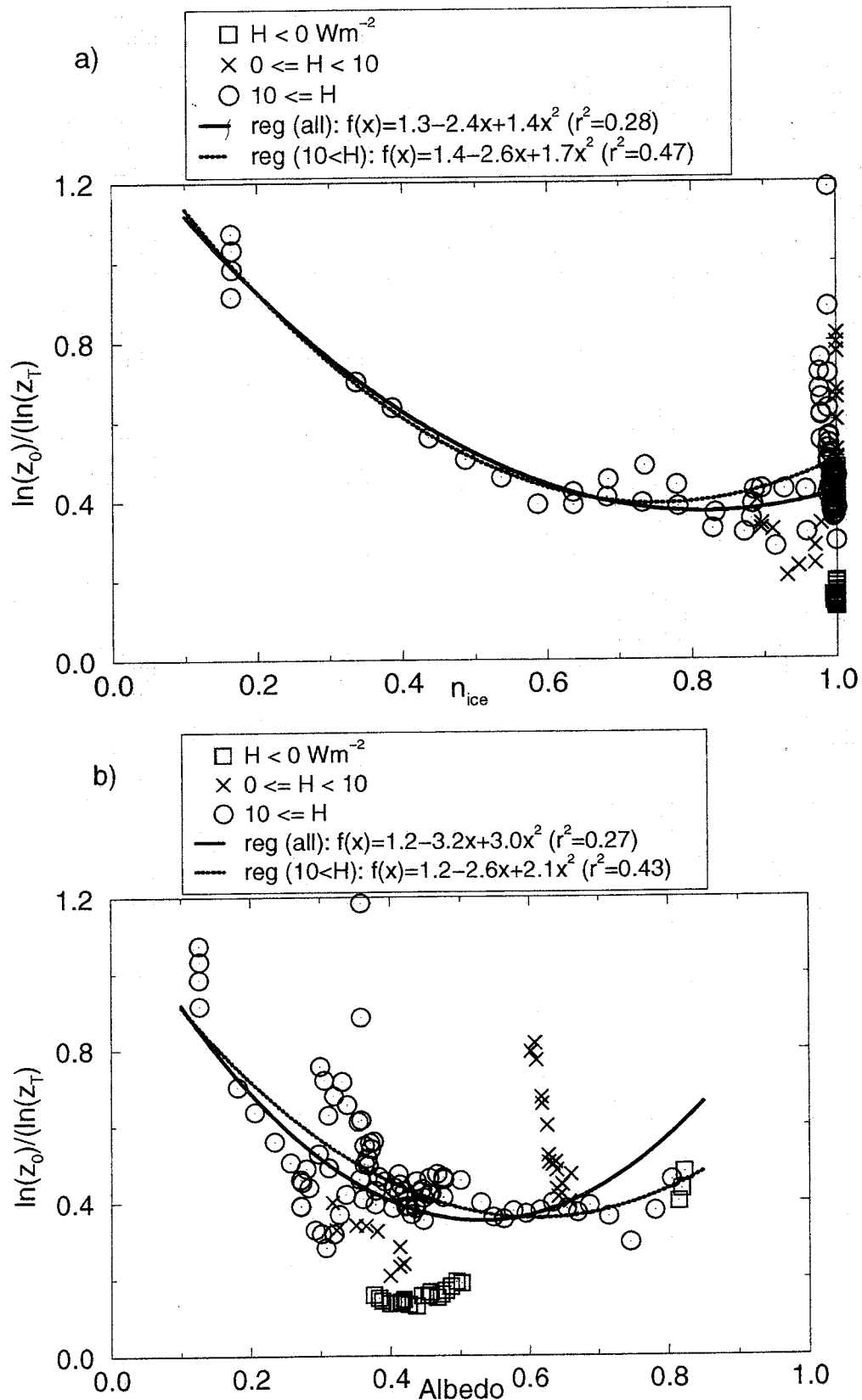


Figure 2. The logarithmic ratio  $\ln(z_0)/\ln(z_T)$  as function of  $n_{ice}$  (a) and albedo (b). The data are based on 20km-averages - shifted by 1km - of all BASIS low-level flight legs, except leg 2. Various symbols are used according to the sensible heat flux  $H$ . The regression curves of the second order and their coefficients are added.

We can see some physical reasons for such a relation between  $z_0$  and  $z_T$ . Over a broken sea ice the effective roughness length for momentum should be larger than a local  $z_0$  over open water or over smooth sea ice because of the effect of form drag due to floe edges (Mai et al., 1996). On the other hand, the effective roughness length for temperature is reduced, if the heat fluxes over the ice part and the open water part tend to balance for each other. The both effects together can lead to a minimum value of  $\ln(z_0)/\ln(z_T)$  (a maximum value of  $z_0/z_T$ ) for a broken sea ice cover with an ice concentration of 0.6-0.9.

## 6. Sensitivity of turbulent fluxes to the roughness lengths

To investigate the influence of the roughness lengths on the turbulent transfer, comparisons between the measured and parameterized sensible heat fluxes are presented in Figure 3. The 20-km averages of the all low-level flight legs are used to make the spatial averaging comparable to the size of the grid-squares of regional models. Because the average values are only shifted by 1 km, 153 cases exist for this study.

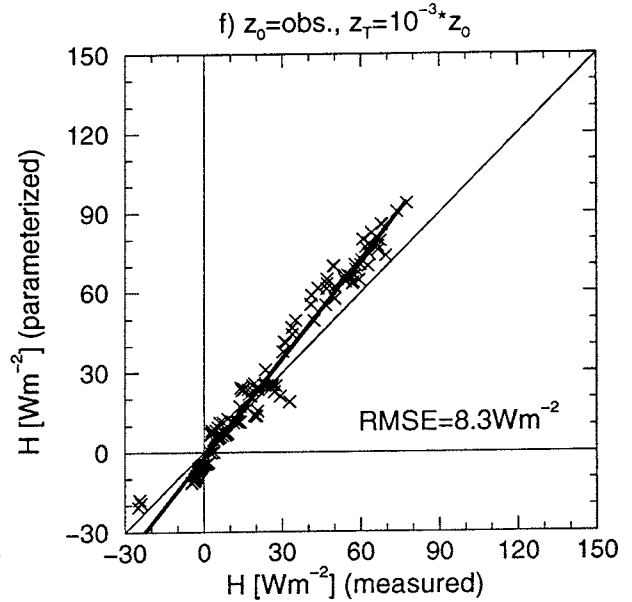
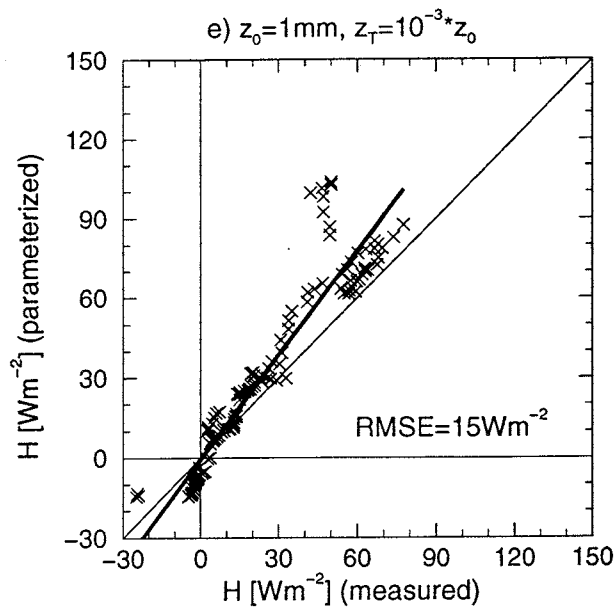
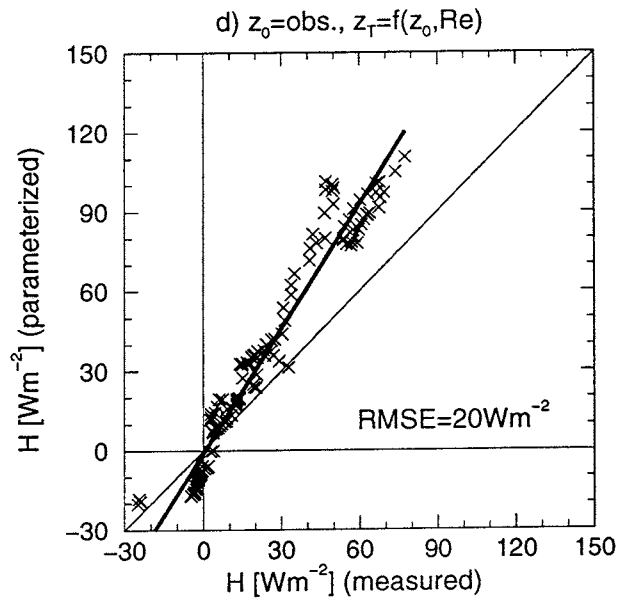
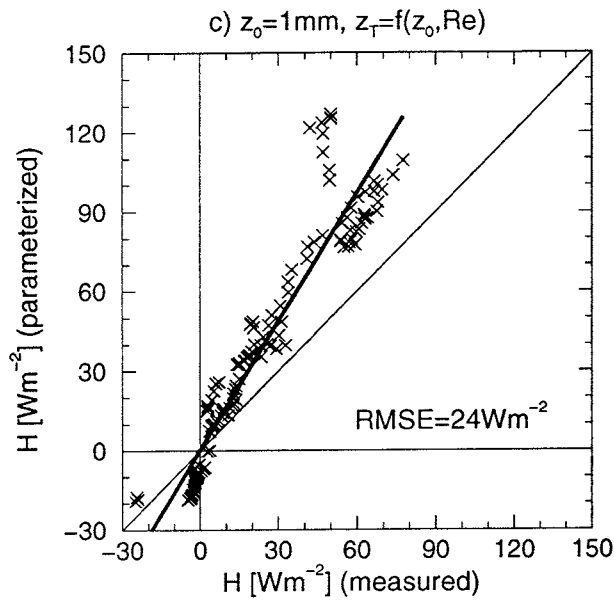
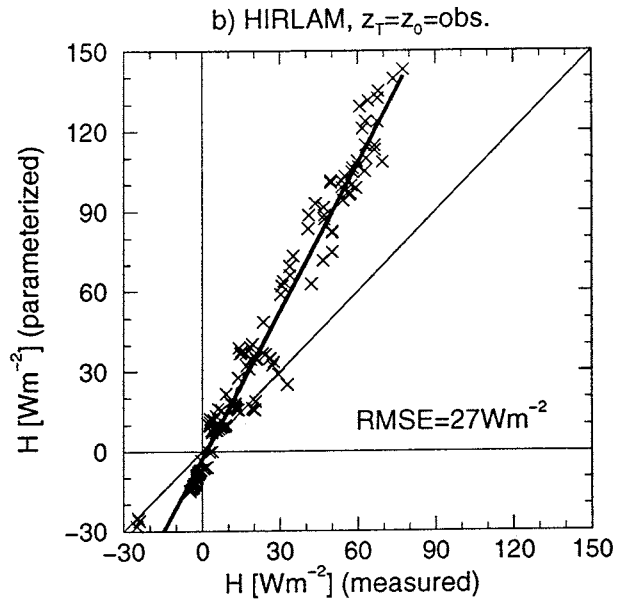
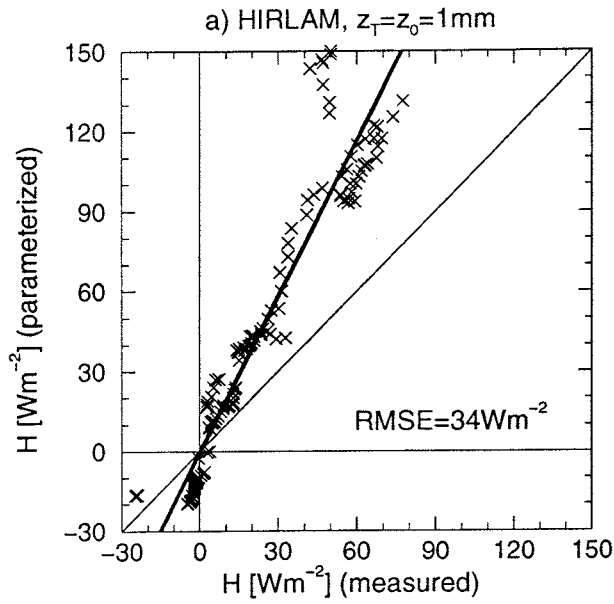
In Figure 3a,  $H$  is parameterized by analytic formulae (Louis et al, 1981) applied, for example, in the regional model HIRLAM and the global model ECHAM. The roughness lengths  $z_0$  and  $z_T$  are both set to  $10^{-3}$  m. The comparison shows that  $H$  is generally overestimated by a factor of approximately two. The root-mean-square error (RMSE) is  $34 \text{ Wm}^{-2}$ , and the observed fluxes vary between  $-30$  and  $+90 \text{ Wm}^{-2}$ . If the observed values of  $z_0$  are applied instead of the constant value of  $10^{-3}$  m, and  $z_T$  again set equal to  $z_0$ , the scatter is reduced, but the systematic discrepancy is similar (Figure 3b).

Next,  $H$  is parameterized according to Launiainen and Vihma (1990) applying the universal functions, setting  $z_0$  to  $10^{-3}$  m, and calculating  $z_T$  as a function of  $z_0$  and the roughness Reynolds number (Andreas, 1987) (Figure 3c). The results are slightly improved: the RMSE is  $24 \text{ Wm}^{-2}$ , but  $H$  is still systematically overestimated. Prescribing  $z_0$  according to the observations and calculating  $z_T$  from  $z_0$  and the roughness Reynolds number yields a bit better results (Figure 3d).

In the following the fluxes are parameterized on the basis of the universal functions, but  $z_T$  is varied over a wider range. Setting  $z_T$  three orders of magnitude smaller than  $z_0$ , as observed over heterogeneous land surfaces (Beljaars and Viterbo, 1994), the RMSE is reduced to  $15 \text{ Wm}^{-2}$  for  $z_0 = 10^{-3}$  m (Figure 3e), and to  $8.3 \text{ Wm}^{-2}$  if the observed values of  $z_0$  are applied (Figure 3f). A good agreement is reached for the whole range of values.

Finally our new functional forms for  $z_T$  depending on  $z_0$  and ice concentration (Eq. 10) or on  $z_0$  and albedo (Eq. 11) are applied. Setting  $z_0$  to  $10^{-3}$  m, the parameterized  $H$  (Figures 3g and 3i) is equally good as for  $z_T = z_0/1000$  (Figure 3e). Only by using the observed  $z_0$ -values the results are improved as confirmed by the RMSE of approx.  $6 \text{ Wm}^{-2}$  (Figures 3h and 3j).

The comparison shows that the roughness lengths have a large effect on the surface heat fluxes. A significantly smaller  $z_T$  than  $z_0$ , as previously observed over heterogeneous land surfaces, is necessary to realistically parameterize the heat fluxes over a broken sea ice cover.



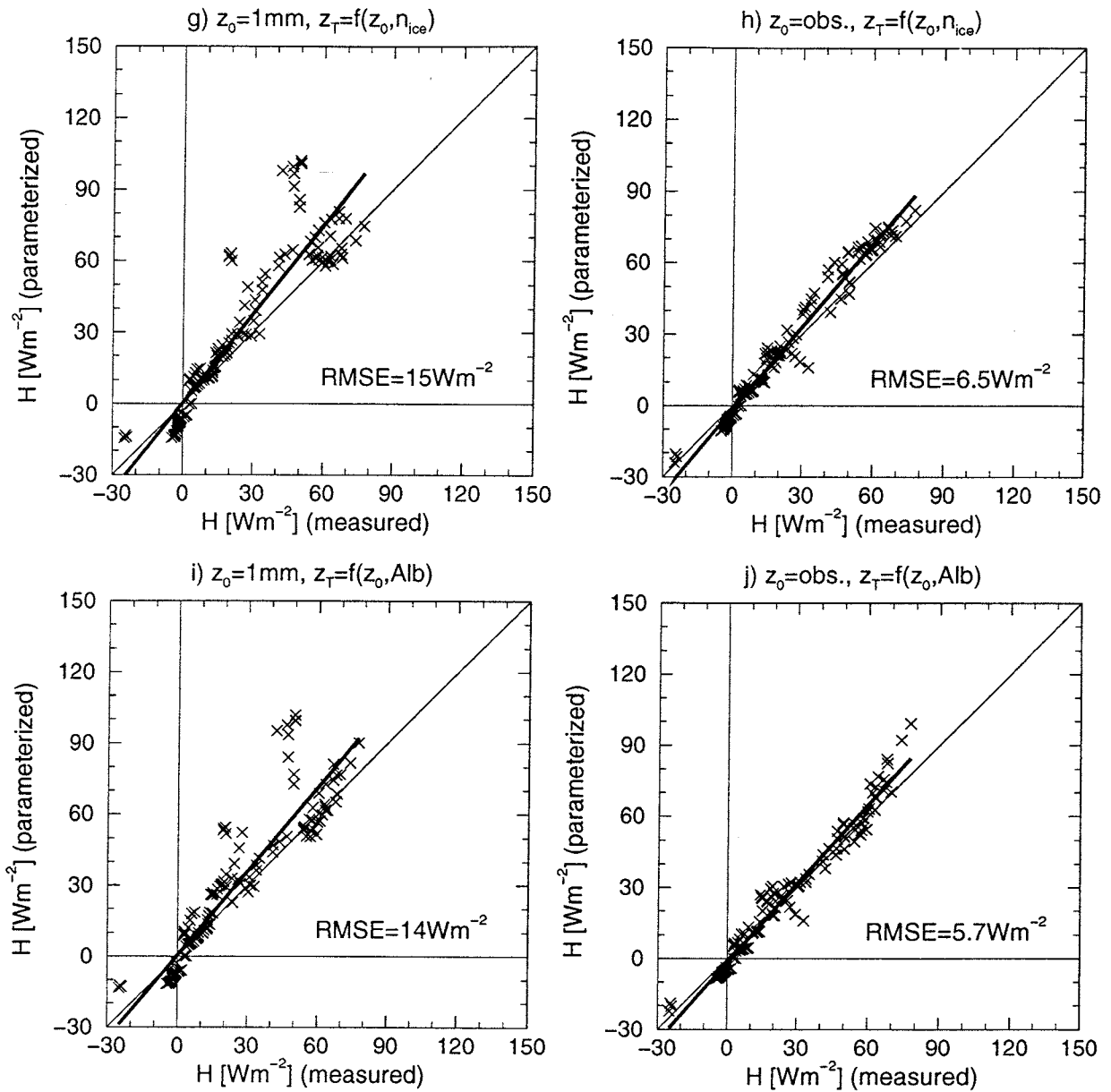


Figure 3: Comparison between measured and parameterized sensible heat flux  $H$  based on the 20-km averages (shifted by 1 km) from the all low-level flight legs during BASIS. At each of the ten figures a different parameterization technique is applied: In Figures a, c, e, g, and i  $z_0$  is set to  $10^{-3}$  m, whereas the observed  $z_0$  is used in the other figures. The heat fluxes are parameterized by analytic formulae used in HIRLAM and ECHAM in Figures a and b. In all other cases the universal functions are applied, but  $z_T$  is determined as a function of  $z_0$  and the roughness Reynolds number (Andreas, 1987) (c and d),  $z_T$  is set to  $z_0/1000$  (Beljaars and Viterbo, 1994) (e and f),  $z_T$  is determined as a function of  $z_0$  and  $n_{ice}$  (Eq. 10) (g and h), and  $z_T$  is determined as a function of  $z_0$  and albedo (Eq. 11) (i and j).

## 7. Discussion

We calculated the effective roughness lengths and corresponding transfer coefficients for momentum, heat, and moisture over a broken sea ice cover. The calculations were based on aircraft measurements of turbulent fluxes of momentum and sensible and latent heat. The data of 10 low-level flight legs at heights between 10 and 30 m were applied and averaged over horizontal legs 20 km long. The calculations were based on the mixture method (parameter aggregation) applying the universal functions. A good agreement between the aircraft-based and surface-based turbulent fluxes (Brümmer et al, 2001, this issue) permits this approach. The results show that the mean effective roughness length for heat ( $z_T = 3 \cdot 10^{-8}$  m) is 4 orders of magnitude smaller than that for momentum ( $z_0 = 3 \cdot 10^{-4}$  m). The corresponding neutral transfer coefficients are  $C_{HN} = 0.9 \cdot 10^{-3}$  and  $C_{DN} = 1.6 \cdot 10^{-3}$ . Considering the ratios of the roughness lengths and transfer coefficients, our results for a broken sea ice cover are approximately in agreement with several observational results obtained for heterogeneous land surfaces, being closest to those of Beljaars and Holtslag (1991) and Mahrt and Ek (1993). This is reasonable, because from the point of view of the surface temperature distribution, a mixture of sea ice and leads often more resembles heterogeneous land surfaces than a compact ice cover.

It has been suggested that over a homogeneous surface  $C_{EN}$  should slightly exceed  $C_{HN}$  due to the difference between the Schmidt and Prandtl numbers. Our observed ratio  $C_{EN}/C_{HN} = 1.2$  cannot, however, be interpreted as a support to this theory. In our case the difference may be mostly related to the following reasons. (1) In the case that the observations were made above the constant-flux layer, the vertical profiles of H and LE may have been different (e.g. Vihma and Brümmer, 2001). (2) H and LE may have different spatial distributions within the 20-km averaging domains. The sensible heat flux is more liable to change its direction according to the surface temperature, and therefore the effect of the local fluxes balancing each other has a greater potential to reduce the area-averaged H and  $C_{HN}$  than LE and  $C_{EN}$ . (3) The measurement of the latent heat flux in cold temperatures may be liable to errors.

A comparison between the measured and parameterized fluxes using different roughness lengths shows that (1) the commonly used parameterization techniques strongly overestimate the surface heat fluxes over a broken sea ice cover, (2) the roughness lengths have a large effect on the heat fluxes, and (3) realistic heat fluxes can be parameterized using significantly smaller values for  $z_T$  than for  $z_0$ . It is shown that  $z_T$  depends on  $z_0$  and the ice concentration and albedo. Our experimental functional forms lead to good results concerning the sensible heat flux, although there is some scatter due to different ice types. The proposed formulae are applicable for use in numerical models, because the ice concentration can be derived from satellite SSM/I data.

The possible flux divergence between the surface and the aircraft measurement level may have affected our results yielding smaller roughness lengths. The measurement heights between 10 and 30 m are, however, comparable to or smaller than the lowest grid level in most regional and large-scale models. This means that from the point of view of the models our results are more applicable than roughness lengths based on data from lower measurement heights.

Further studies are necessary to investigate the quality of the aircraft-based fluxes in various stratification conditions and the influence of the averaging length with respect to large step



changes in the surface temperature. Furthermore, it is important to address the topic from the point of view of application of the mosaic method (flux aggregation) in parameterizing the surface fluxes.

### Acknowledgements

Jouko Launiainen is acknowledged for fruitful discussions.

### References

- Andreas, E. L.: 1987, 'A theory for the scalar roughness and the scalar transfer coefficients over snow and sea ice', *Bound.-Layer Meteorol.* **38**, 159-184.
- Banke E. G., Smith, S. D., and Anderson, R. J.: 1980, 'Drag coefficients at AIDJEX from sonic anemometer measurements', In: Pritchard R. S. (Ed.): *Sea ice processes and models*, proceedings of the AIDJEX/ICSI Symposium, Seattle, pp. 430-442.
- Beljaars, A. C. M.: 1995, 'The parameterization of surface fluxes in large-scale models under free convection', *Quart. J. Roy. Meteorol. Soc.*, **121**, 255-270.
- Beljaars, A. C. M. and Holtslag, A. A. M.: 1991, 'Flux parameterization over land surfaces for atmospheric models', *J. Appl. Meteorol.* **30**, 327-341.
- Beljaars, A. C. M. and Viterbo, V.: 1994, 'The sensitivity of winter evaporation to the formulation of aerodynamic resistance in the ECMWF model', *Bound.-Layer Meteorol.* **71**, 135-149.
- Brümmer, B.: 1996, 'Boundary layer modification in wintertime cold-air outbreaks from the Arctic sea ice', *Bound.-Layer Meteorol.* **80**, 109-125.
- Brümmer, B., Schröder, D., Launiainen, J., Vihma, T., Smedman, A. S., and Magnusson, M.: 2001, 'Temporal and spatial variability of surface fluxes over the ice edge zone in the Gulf of Bothnia', this issue.
- Brutsaert, H. W.: 1975, 'The roughness length for water vapour, sensible heat and other scalars', *J. Atmos. Sci.* **32**, 2028-2031.
- DeCosmo, J., Katsaros, K. B., Smith, S. D., Anderson, R. J., Oost, W. A., Bumke, K., and Chadwick, H.: 1996, 'Air-sea exchange of water vapor and sensible heat: the Humidity Exchange Over the Sea (HEXOS) results', *J. Geophys. Res.* **101 (C5)**, 12001-12016.
- Eppel, D. P., Kapitza, H., Claussen, M., Jacob, D., Koch, W., Lenkov, L., Mengelkamp, H.-T., and Werrmann, N.: 1995, 'The non-hydrostatic mesoscale model GESIMA. Part II: Parameterizations and applications', *Contr. Atmos. Phys.* **68**, 15-41.
- Högström, U.: 1988, 'Non-dimensional wind and temperature profiles in the atmospheric surface layer: A re-evaluation', *Bound.-Layer Meteorol.* **42**, 55-78.
- Holtslag, A. A. M. and de Bruin, H. A. R.: 1988, 'Applied modelling of the nighttime surface energy balance over land', *J. Appl. Meteorol.* **27**, 689-704.
- Launiainen, J., Cheng, B., Uotila, J., and Vihma, T.: Turbulent surface fluxes and air-ice coupling, this issue.
- Launiainen, J. and Vihma, T.: 1990, 'Derivation of turbulent surface fluxes – an iterative flux-profile method allowing arbitrary observing heights', *Environm. Software* **5**, 113-124.
- Mahrt, L., and M. Ek.: 1993, 'Spatial variability of turbulent fluxes and roughness lengths in HAPEX-MOBILHY', *Bound.-Layer Meteorol.*, **65**, 381-400.
- Mai, S., Wamser, C., and Kottmeier, C.: 1996, 'Geometric and aerodynamic roughness of sea ice', *Bound.-Layer Meteorol.* **77**, 233-248.
- Makshtas, A. P.: 1991, 'The heat budget of Arctic ice in the winter', International Glaciological Society, Cambridge, England, 77 pp.

- Overland, J. E. and Davidson, K. L.: 1992, 'Geostrophic drag coefficients over sea ice', *Tellus* **44 A(1)**, 54-66.
- Smith, S. D.: 1988, 'Coefficients for sea surface wind stress, heat flux, and wind profiles as a function for wind speed and temperature', *J. Geophys. Res.* **93 (C12)**, 15467-15472.
- Stössel, A. and Claussen, M.: 1993, 'On the momentum forcing of a large-scale sea-ice model', *Clim. Dyn.* **9**, 71-80.
- Uotila, J.: 2001, 'Observed and modelled sea-ice drift response to wind forcing in the northern Baltic Sea', *Tellus*, reprinted in this issue.
- Vihma, T.: 1995, 'Subgrid parameterization of surface heat and momentum fluxes over polar Oceans', *J. Geophys. Res.* **100**, 22,625-22,646.
- Vihma, T., and Brümmer, B.: 2001, 'Observations and modelling of the on-ice and off-ice air flow over the northern Baltic Sea', submitted to *Bound.-Layer Meteorol.*
- Wood, N. and Mason, P.: 1991, 'The influence of static stability on the effective roughness lengths for momentum and heat transfer', *Quart. J. Roy. Met. Soc.* **117 (501)**, 1025-1056.

## Evaluation of Radiosounding Data and Aircraft Observations in Comparison to HIRLAM Model Results

A. Ganske<sup>1)</sup>, D. Etling<sup>1)</sup>, and D. Schröder<sup>2)</sup>

<sup>1)</sup> Institute of Meteorology and Climatology, University Hannover, Germany

<sup>2)</sup> Meteorological Institute, University Hamburg, Germany

### 1. Introduction

One of the aims of the BASIS project is the validation of numerical atmospheric models by comparison to experimental data. Especially the conditions of the boundary layer with its air – sea interactions should be studied.

HIRLAM is a high resolution limited area weather prediction model, which includes parameterizations among others for the ice-air interactions, see Källén (1996). As the HIRLAM model is used for operational weather forecasts for the Baltic Sea region, reanalysis and 24-hour forecasts of the 44 km grid version of HIRLAM were made for the period of the BASIS field experiment (18 February to 7 March, 1988). These results shall be compared to experimental data. Previous studies of Uotila et al. (1997) showed that there were discrepancies between observations, made in the years 1994 and 1995, and HIRLAM model output. Especially for inversions and low-level jets, differences between observations and 6-hour forecast results with the 55 km grid version of HIRLAM were found. Therefore the measurements of temperature and wind speed during BASIS were used for an additional comparison of experimental data with HIRLAM model output of the 44 km grid version. In the following, a comparison of HIRLAM results with radiosonde and aircraft observations will be presented.

### 2. Preparation of the radiosonde data

For the comparison of radiosounding data to HIRLAM reanalysis and 24-hour forecast results, we used radiosounding data of the four meteorological stations Merikarvia, Aranda, Kokkola and Umea. Details of the radiosonde network are given in the BASIS Data Report (Launiainen, 1999). In order to have the same variables for all stations, we calculated temperature, specific humidity, wind speed and wind direction as functions of height and pressure, if necessary. We further chose 4 grid points of the HIRLAM 44 km grid whose geographical coordinates are closest to those of the meteorological stations. Table 1 shows geographical coordinates of meteorological stations and the corresponding grid points of the HIRLAM model:

Table 1. Coordinates of meteorological stations and the corresponding HIRLAM grid points.

Station	Geogr. Position	Pos. of Grid Point
Merikarvia	61.85 N , 21.47 E	61.9N, 21.7E
Kokkola	63.95N, 23.08E	63.86N, 22.99E
Aranda	63.14N, 20.4E	62.97N, 20.96E
Umea	63.67N, 20.4E	63.51N, 20.57E

In the following the grid points of HIRLAM will be named as the corresponding meteorological stations.

HIRLAM data are given as discrete values on a vertical grid, where values on the full pressure levels  $p_k$  represent a mean value over a layer between half levels  $p_{k+1/2}$  and  $p_{k-1/2}$  with

$p_{k+1/2} < p_k < p_{k-1/2}$ . Radiosounding data are measured as discrete values on irregular pressure levels, which have much smaller distances from each other than HIRLAM grid levels. For a comparison of HIRLAM data to radiosounding data we evaluated mean values of measured temperature, specific humidity, wind speed and wind direction. For each measurement of the radiosonde launches at 0,6,12,18 UTC we calculated pressures  $p_k$  of full levels of the HIRLAM grid with  $k=1,\dots,31$  and  $p_{k+1/2}$  of half levels, using measured ground pressure for the evaluation. Mean values of a measured variable  $X$  between half levels  $p_{k+1/2}$  and  $p_{k-1/2}$  are calculated as

$$\bar{X}_k = \frac{1}{(\ln(p_{k+1/2}) - \ln(p_{k-1/2}))} \sum_{i=1}^N X_i \cdot \Delta \ln p_i$$

where  $N$  denotes the number of measured values  $X_i$  between  $p_{k+1/2}$  and  $p_{k-1/2}$  and  $X$  is e.g. measured temperature, specific humidity, or the wind components. These mean values  $\bar{X}_k$  ( $k=1,\dots,31$ ) were then associated to the pressures  $p_k$  of the full levels. As vertical profiles of wind speed, measured at Umea, are not as high as the profiles measured at the three other stations, mean measured wind speeds at Umea can not be calculated

Due to technical problems mean measured data and HIRLAM model output can not be presented as contour plots on the time-height or time-pressure plane. Instead we used the level indices of HIRLAM full levels as vertical coordinate and show mean measured data, HIRLAM reanalysis data and HIRLAM 24-hour forecast results as contour plots on the time-level index plane.

### 3. Results for radiosonde comparison

In the following we will compare only the mean measured data to results of HIRLAM reanalysis and HIRLAM 24-hour forecasts.

#### 3.1 Temperature

During the period of the BASIS experiment many cold fronts, warm fronts and occlusions passed the experimental region. The temperature changes due to these fronts can be seen in the contour plots on the time-level index plane of the temperature. As an example Figure 1 shows the mean measured temperature at Kokkola. Cooling in levels in the boundary layer can be found at 20.2. 18 UTC, 24.2. 0 UTC, 28.2. 6 UTC, and 4.3. 0 UTC. Between these passages of cold fronts warming of lower levels due to warm fronts can also be observed. Inversions with vertical temperature differences larger than  $3^\circ \text{C}$  can also be seen in the figure, e.g. at 19.2. 0 UTC, 20.2. 0 UTC, 21.2. 6 UTC, 26.2. 18 UTC and 6.3. 0 UTC.

Figure 2 shows the corresponding contour plot of temperatures, given by HIRLAM reanalysis at grid point Kokkola. Even though the qualitative structures of the temperature fields are comparable to those of mean measured temperatures, large differences of up to  $-4.3^\circ \text{C}$  between mean measured temperatures and those of HIRLAM reanalysis at constant date and level can be found especially in the levels 31, 30, and 29. These large differences are found close to the passing times of cold and warm fronts. Also at constant date the vertical profiles of mean measured and HIRLAM reanalysis temperatures are different. On the one hand vertical regions of temperature intervals are smaller in the reanalysis data than in the mean measured data, as can be seen e.g. for the 22.2. 0 UTC. On the other hand vertical gradients of temperature are in many cases smoother in the HIRLAM reanalysis data than in the mean measured data.

The comparison of HIRLAM 24-hour forecast temperatures at grid point Kokkola in Figure 3 to mean measured temperatures shows at constant level and date even larger differences of up to  $10^{\circ}\text{C}$  than those between reanalysis and mean measured data. The qualitative structure of the temperature as a function of time and level index is again comparable to mean measured data. Nevertheless maximum temperatures in inversions are smaller for HIRLAM 24-hour forecast than for experimental results. At constant time vertical gradients of temperature are smaller in the forecast than in the reanalysis. Also regions of temperature intervals with constant color are smaller in the contour plot of the forecast than in that of the reanalysis. Therefore differences of forecast temperatures to mean measured temperatures are not only due to the differences of the data at the beginning of the forecast but also due to the calculation of the forecast.

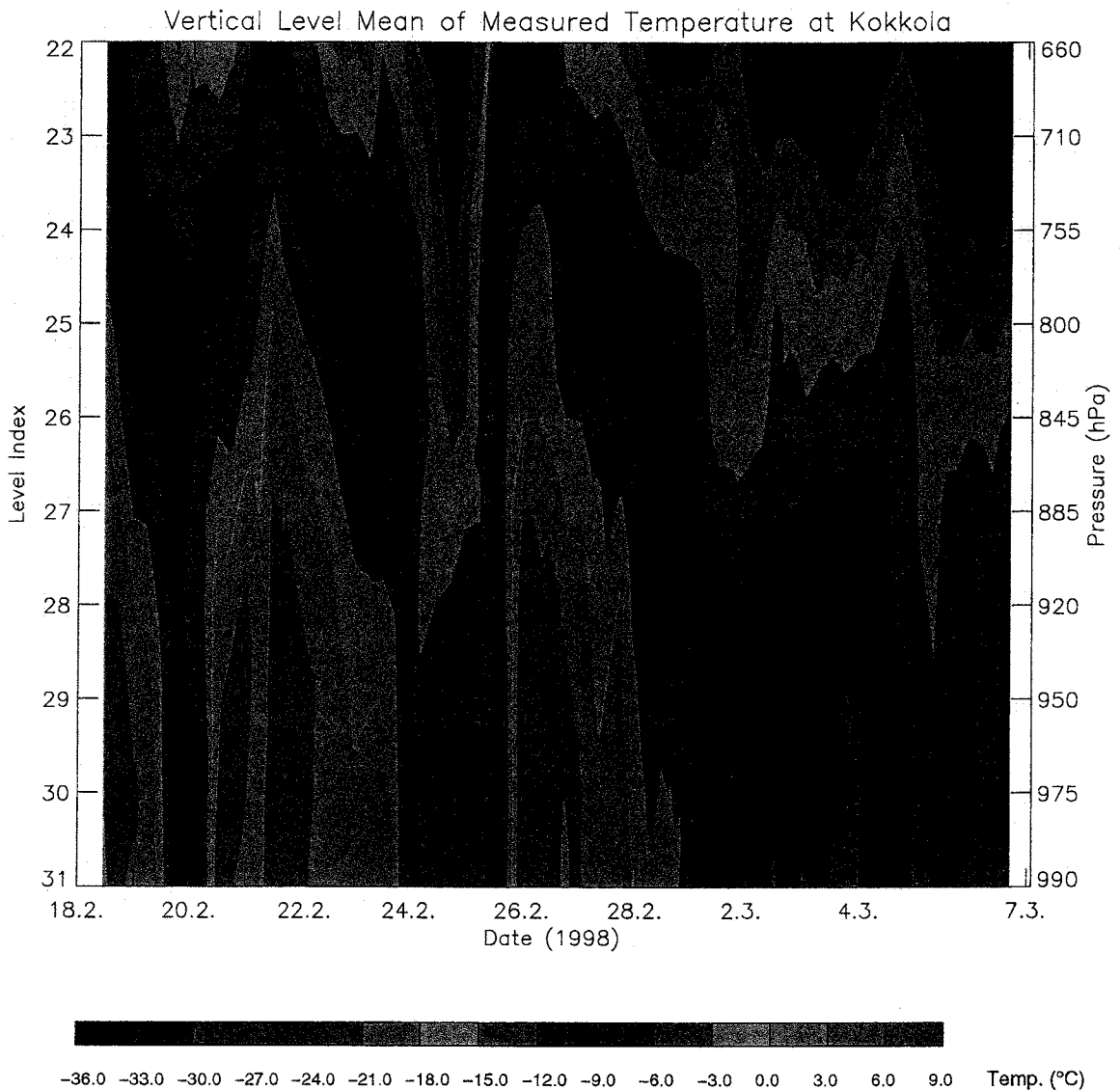


Figure 1: Vertical level mean of measured temperatures at Kokkola, drawn as contour plot in the time-level index plane. Horizontal axis: Date of measurement. Left vertical axis: Level index of full levels of HIRLAM model. Right vertical axis: Typical values of pressure at full levels of HIRLAM model.

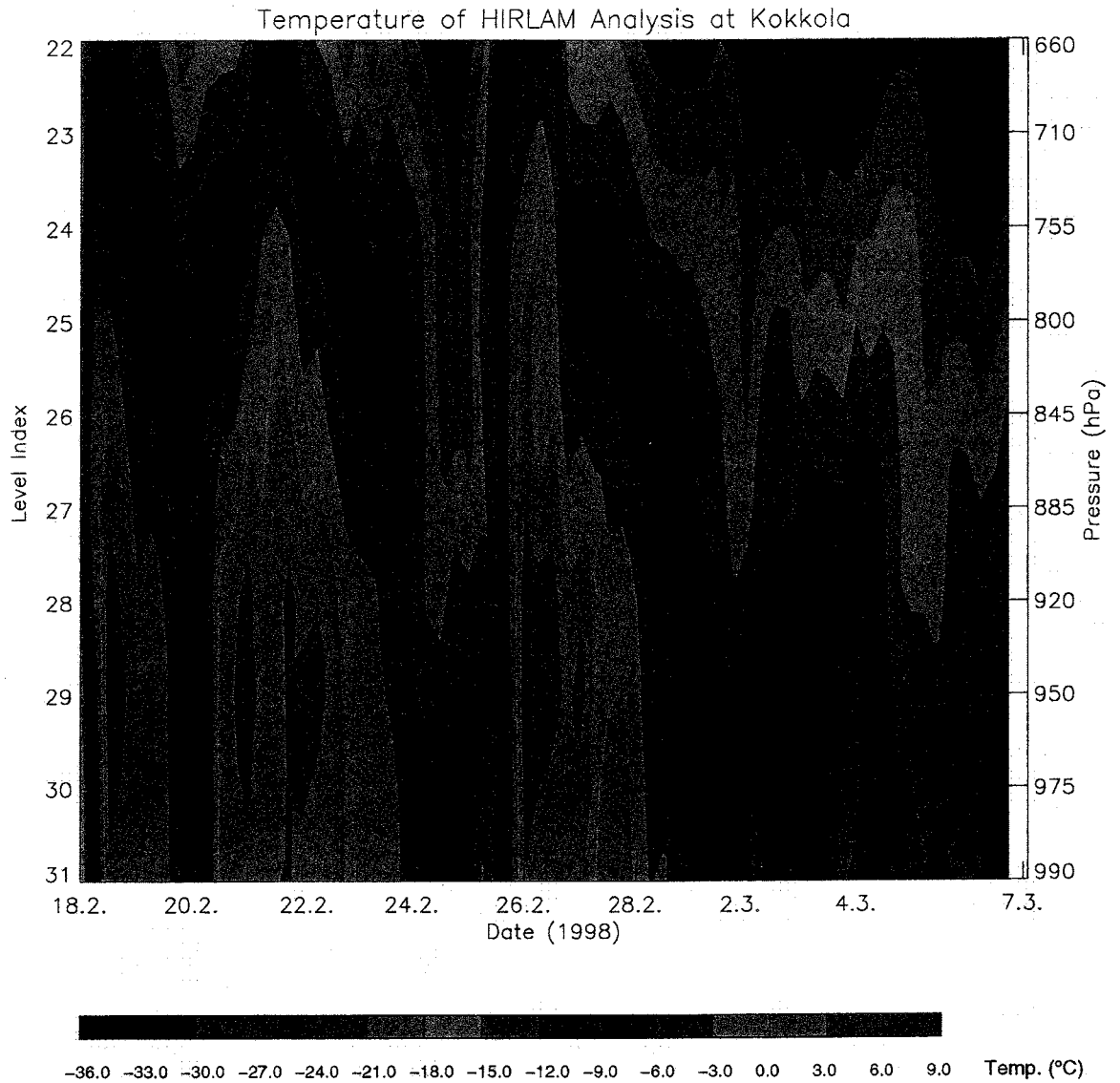


Figure 2: Vertical level mean of HIRLAM reanalysis temperatures, calculated for grid point Kokkola, drawn as contour plot in the time-level index plane. Horizontal axis: Date of verification. Left vertical axis: Level index of full levels of HIRLAM model. Right vertical axis: Typical values of pressure at full levels of HIRLAM model.

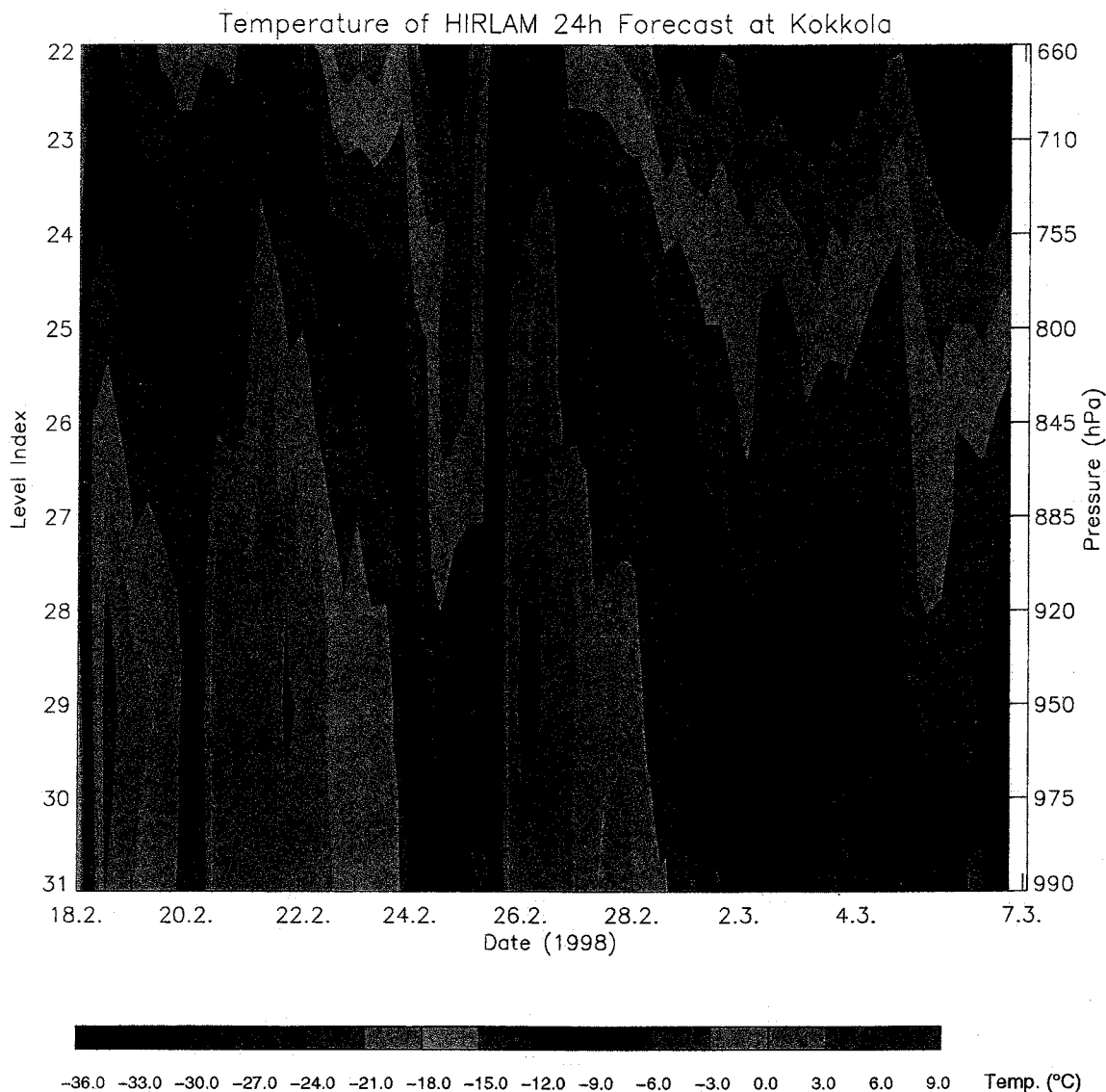


Figure 3: Vertical level mean of HIRLAM 24-hour forecast temperatures, calculated for grid point Kokkola, drawn as contour plot in the time-level index plane. Horizontal axis: Date of verification. Left vertical axis: Level index of full levels of HIRLAM model. Right vertical axis: Typical values of pressure at full levels of HIRLAM model

The differences of mean measured temperatures to those calculated with HIRLAM reanalysis and 24-hour forecast are largest within the levels closest to the ground. As an example Figure 4 shows a comparison of time series of temperatures of mean measured data, HIRLAM reanalysis data and forecast data at Kokkola. Large differences between mean measured temperatures and HIRLAM temperatures are always related to big changes in temperature, due to cold and warm fronts. As the qualitative behavior of the curves of measured temperature, HIRLAM reanalysis temperature and 24-hour forecast temperature are the same, differences are not due to phase errors of the calculated cold and warm fronts. In level 31 cooling and warming due to frontal passages is not correctly calculated by HIRLAM reanalysis and by 24-hour forecast. It must be mentioned that this quantitative behavior is also observed in level 30, but not in higher levels (not shown).

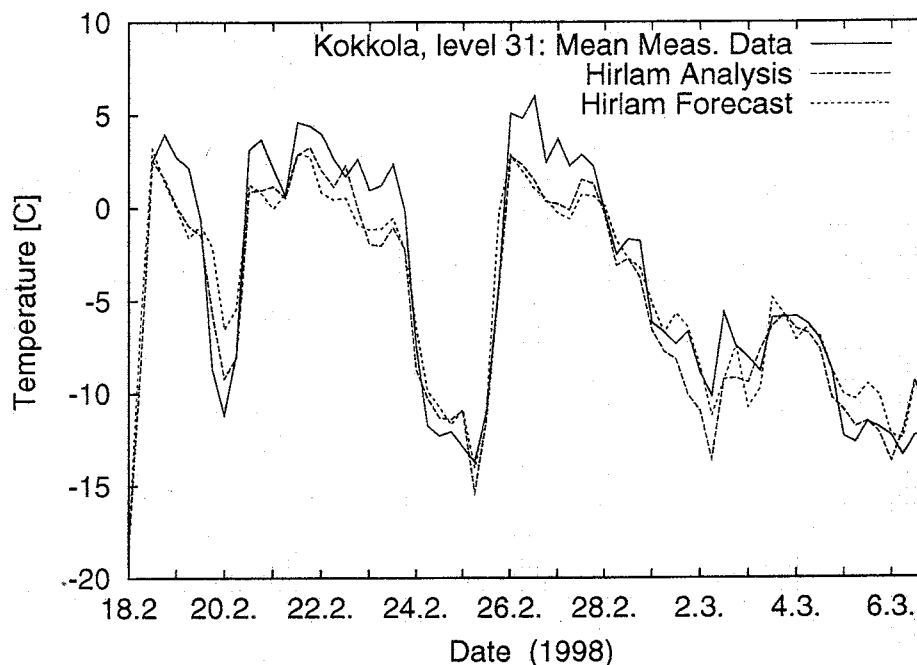


Figure 4: Time series of the results for level 31 of mean measured temperatures at Kokkola. For comparison time series of HIRLAM reanalysis, and HIRLAM 24-hour forecast temperatures, calculated for grid point Kokkola.

Figure 5 shows a comparison of HIRLAM model output temperatures in level 31 and mean measured temperatures at Kokkola. In most cases temperatures calculated with HIRLAM in level 31 are smaller than mean measured data. The results also show that differences of HIRLAM model output and measured data are not a function of the hour of the day, at which measurements were made. Results of the reanalysis made for nighttime do not differ by a larger or smaller amount from mean measured temperatures than reanalysis results for daytime. Also a dependence of the differences on wind directions could not be found (not shown).

The results of the comparison of mean measured temperatures to HIRLAM model output of analysis and 24-hour forecast at Kokkola are also typical for the measured and calculated results of the three stations Merikarvia, Umea and Aranda, even though the differences between measured and HIRLAM model output temperatures are in most cases largest at Kokkola. A comparison of temperatures, which were measured at the four meteorological stations, and HIRLAM model output for the corresponding grid points is shown for level 31 in Figure 6. The number of points, where the temperatures of HIRLAM reanalysis and 24-hour forecast are larger than mean measured temperatures is nearly as large as the number, where HIRLAM model output temperatures are smaller than mean measured ones. This is also the case for the comparison of temperatures in higher levels (not shown).



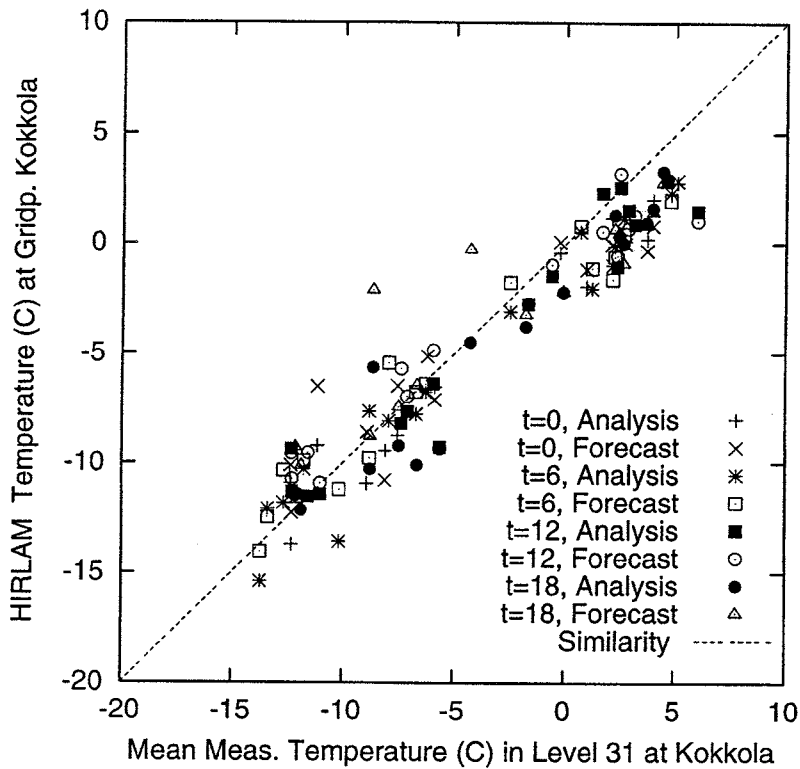


Figure 5: Comparison of results in level 31 of mean measured temperatures at Kokkola to HIRLAM model output of reanalysis and 24-hour forecast as functions of hour of the day, measured and calculated during the BASIS field experiment. For a guide for the eye the line of similarity of measured and calculated data is also drawn.

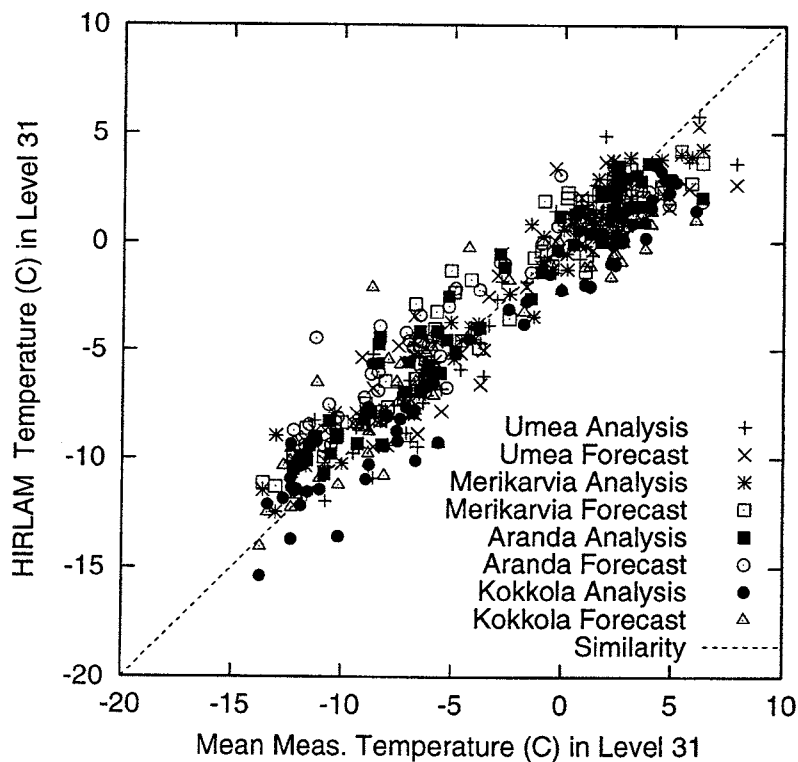


Figure 6: Comparison of results in level 31 of mean measured temperatures at Umea, Merikarvia, Kokkola, and above the Aranda to HIRLAM results of reanalysis and 24-hour forecast for the whole period of the BASIS field experiment. For a guide for the eye the line of similarity of measured and calculated data is also drawn

### 3.2 Wind Speed

Observations of boundary-layer structures at various sites in the Baltic Sea area over many years (Smedman et al. 1993 and 1995) and numerical studies (Sandström, 1997) showed that low-level jets occur in this region during the whole year. Therefore during the BASIS period many low level jets were observed, e.g. 64 low level jets above the site of the Aranda, see e.g. Vihma et al. (1999).

Again only the results for the wind speeds, measured and calculated at Kokkola, will be shown, since they are typical for the results of Merikarvia and Aranda. Low-level jets can be defined in a way that there exists a wind speed maximum, which exceeds the speed above and below it by at least 2m/s. Even though the vertical resolution of mean measured data is reduced, compared to radiosounding data, with the definition above 39 low level jets can be found in the mean measured wind speed of Kokkola. Figure 7 shows the contour plot of the wind speed in the time-level index plane at Kokkola, where low level jets can be observed e.g. at 21.2. 12 UTC, 25.2. 12 UTC and 3.3. 0 UTC. The intervals of the contour lines are 3m/s, and hence not all low level jets, observed in the mean measured data, can be found in the figure. Maximum wind speeds of low level jets reached values up to 36 m/s.

The corresponding HIRLAM reanalysis results for the wind speed are shown in Figure 8. A comparison of Figure 7 to Figure 8 shows that mean measured wind speed and HIRLAM reanalysis wind speeds are qualitatively the same. Nevertheless vertical gradients of wind speed are in many cases smaller in the HIRLAM reanalysis results than in the measurements. Therefore only 27 low level jets can be found in HIRLAM reanalysis data for the grid point Kokkola and 12 of them in Figure 8. Comparing at distinct time we find that jet core wind speed, calculated with HIRLAM reanalysis, is smaller than mean measured values. 12 of the low level jets that are found in the measured data can not be found in HIRLAM reanalysis data.

Figure 9 shows a contour plot of the wind speed, calculated with HIRLAM 24-hour forecast. Even though the structure of the function of wind speed is comparable to the mean measured data, values of vertical gradients of the wind speed of HIRLAM 24-hour forecast are in many points smaller than measured and also than those of the reanalysis. The number of low level jets, calculated with HIRLAM 24-hour forecast is 23, and 12 of them can be found in Figure 9. Comparing the results for reanalysis and forecast it is obvious that the differences of the forecast to mean measured data again is not only a result of errors in the reanalysis.

Also the deviations of mean measured wind speed from HIRLAM model output are mainly largest in the layers close to the ground. Therefore in Figure 10 a comparison of the wind speeds in level 31 is shown. As it was the case for the temperature the largest differences between mean measured wind speed and HIRLAM reanalysis and forecast data are not due to phase errors. Maximum wind speeds are in most cases overestimated by HIRLAM reanalysis data.

Figure 11 shows that at Kokkola differences of mean measured data to HIRLAM data do not depend on the hour of the day. 38 values of wind speed, calculated with HIRLAM reanalysis, are larger than mean measured data and 18 values are smaller. For the forecast 25 values of wind speed are larger than measured data, and 31 wind speeds are smaller. A dependence of the differences of the wind speeds of measured and HIRLAM model output on the wind direction could not be found (not shown). This is not very astonishing, as largest differences are connected to low level jets and Smedman et al. (this issue) found, that hardly no low level jets, measured during the BASIS experiment, were connected to sea-land/ice breeze

Comparing the calculated wind speeds in level 31 for Kokkola, Merikarvia and Aranda in Figure 12, it can be seen that calculated wind speeds of the HIRLAM model are in most cases smaller than mean measured wind speeds. Statistics of wind speeds, calculated with HIRLAM forecast for the three stations, showed that forecasted wind speeds in levels 27 – 30 are in

most cases smaller than mean measured wind speeds. Analyzed wind speeds in levels 30 and 29 are in most cases smaller and in levels 28 and 27 larger than mean measured data (not shown).

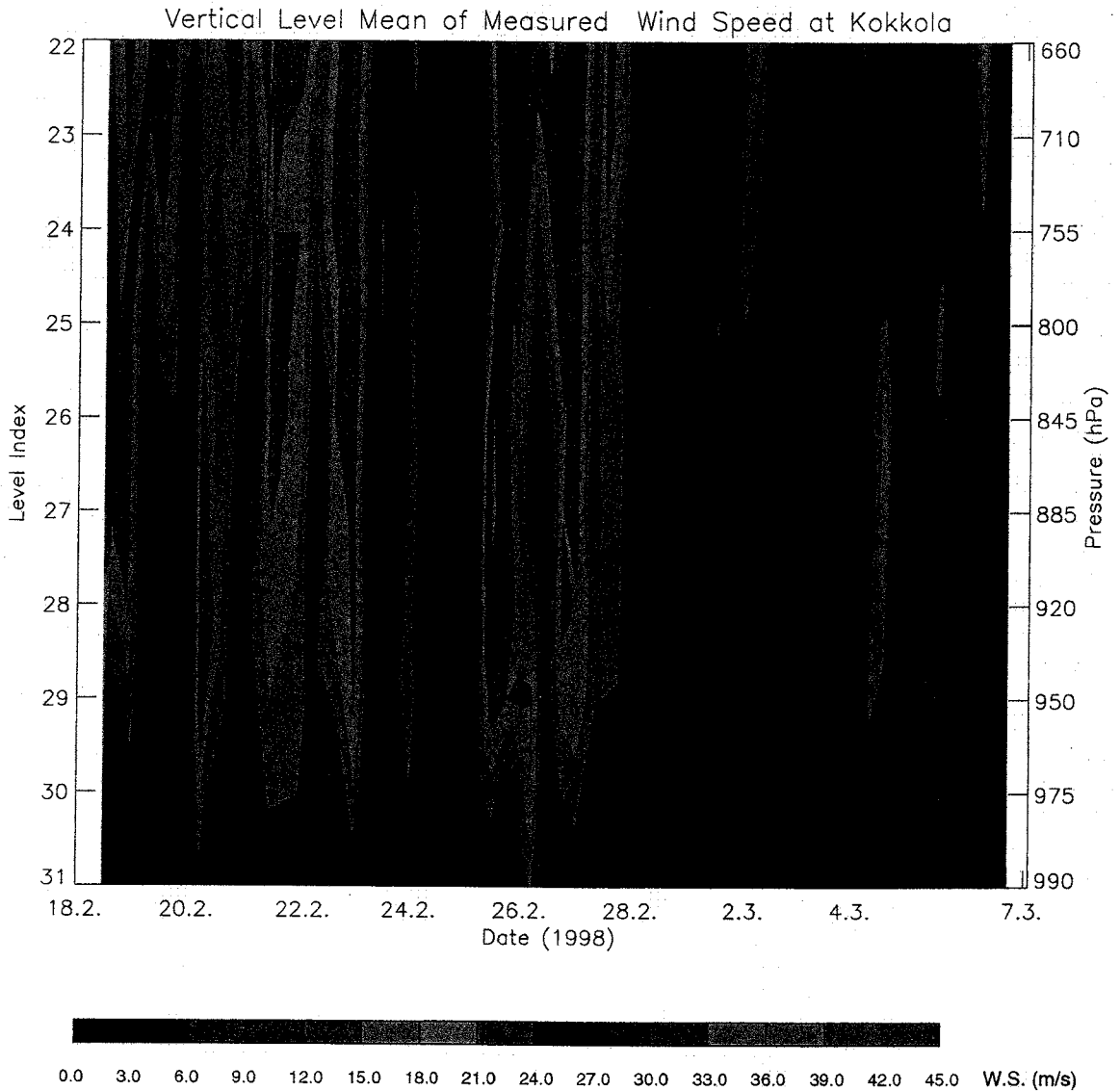


Figure 7: Vertical level mean of measured wind speeds at Kokkola, drawn as a contour plot. Horizontal axis: Date of measurement. Left vertical axis: Level index of full levels of HIRLAM model. Right vertical axis: Typical values of pressure at full levels of HIRLAM model.

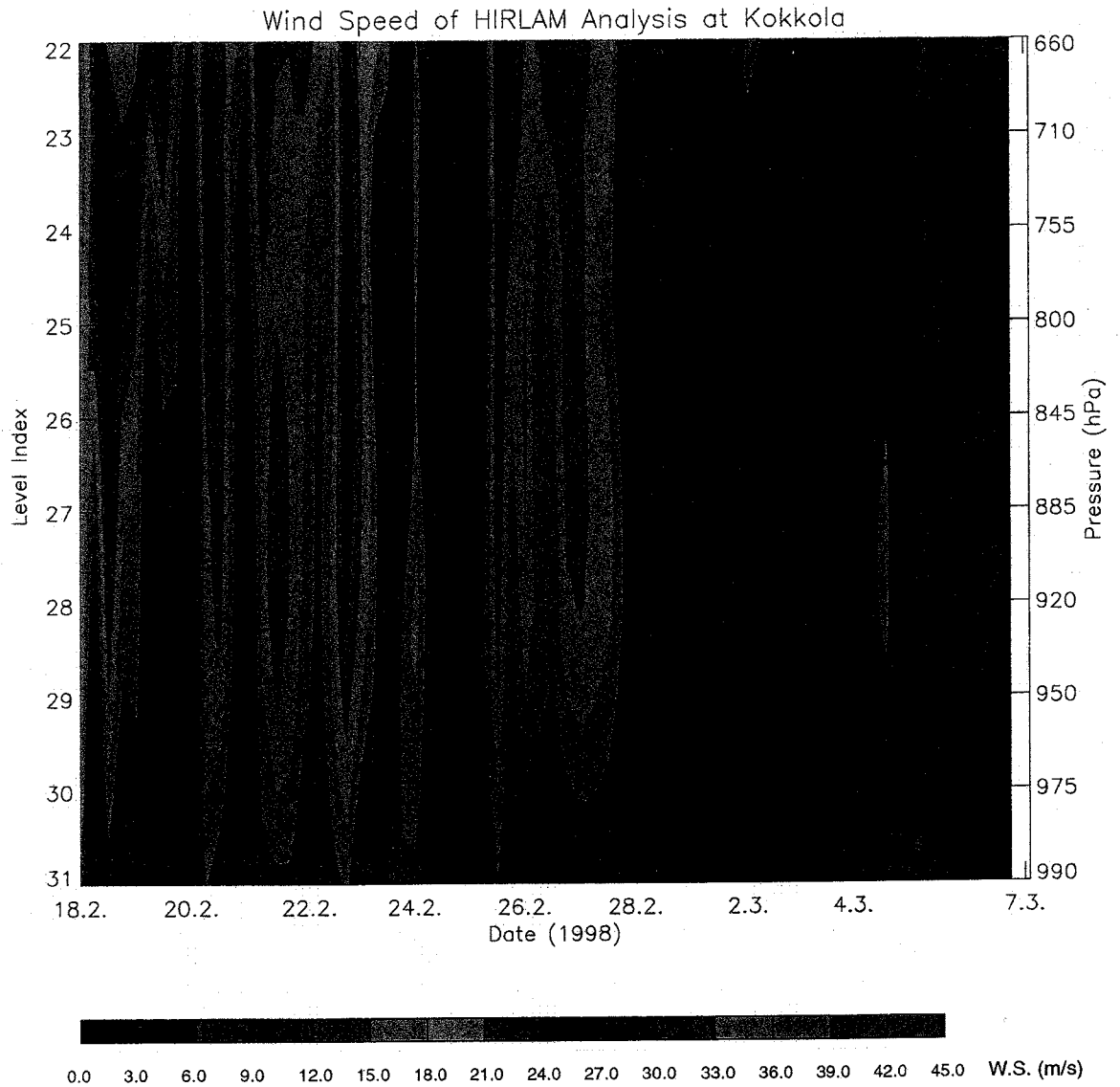


Figure 8: Vertical level mean of HIRLAM reanalysis wind speeds, calculated for grid point Kokkola, drawn as contour plot in the time-level index plane. Horizontal axis: Date of verification. Left vertical axis: Level index of full levels of HIRLAM model. Right vertical axis: Typical values of pressure at full levels of HIRLAM model.

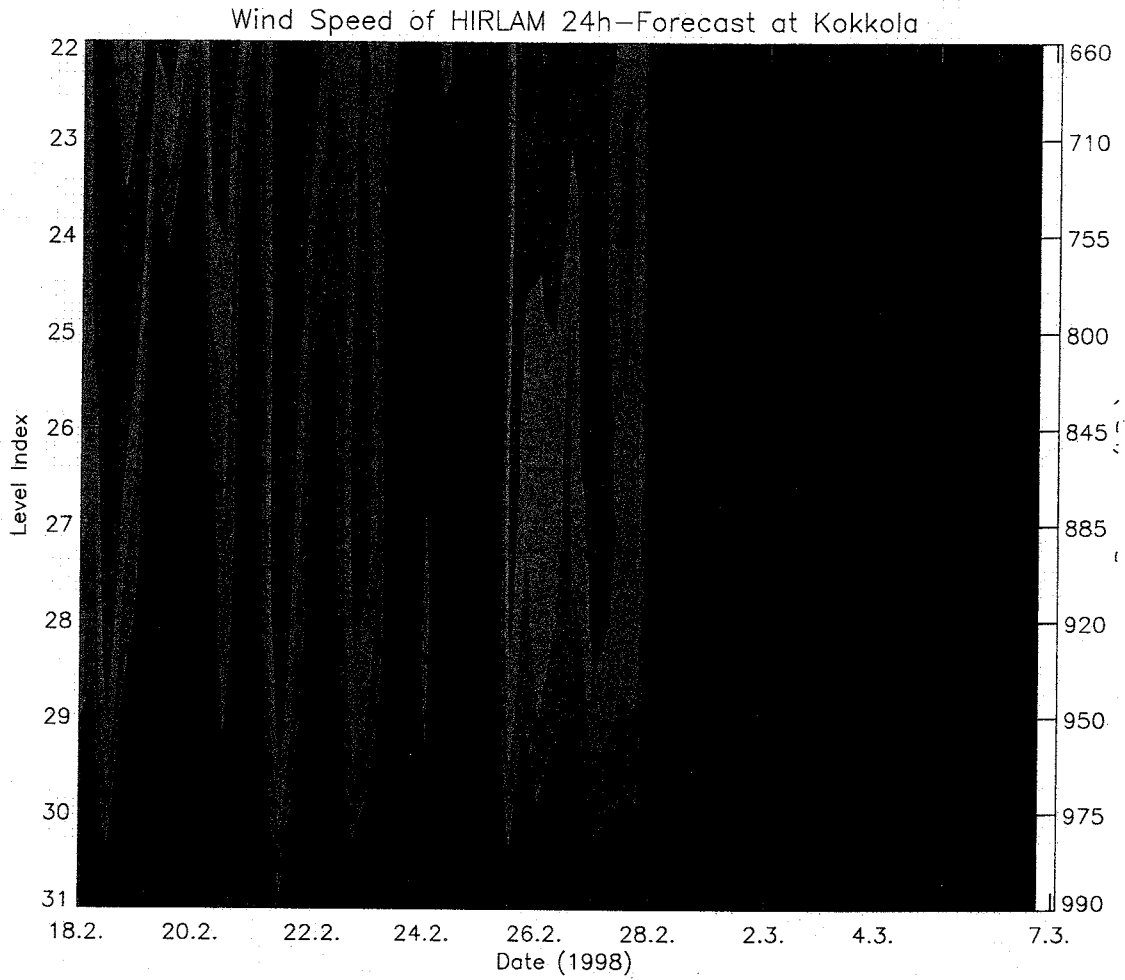


Figure 9: Vertical level mean of HIRLAM 24-hour forecast wind speeds, calculated for grid point Kokkola, drawn as contour plot in the time-level index plane. Horizontal axis: Date of verification. Left vertical axis: Level index of full levels of HIRLAM model. Right vertical axis: Typical values of pressure at full levels of HIRLAM model

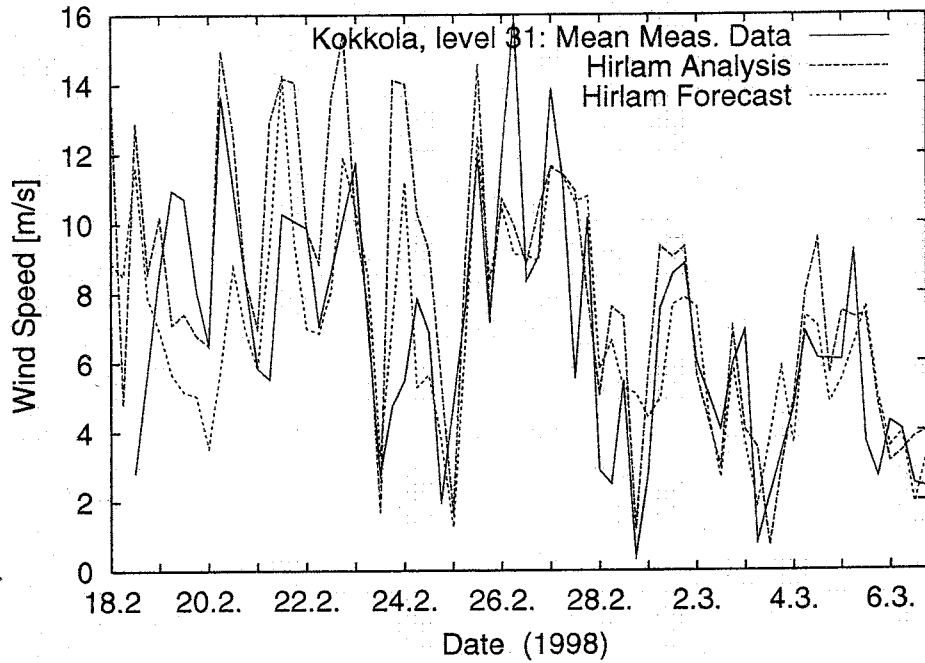


Figure 10: Time series of the results for level 31 of mean measured wind speeds at Kokkola. For comparison time series of HIRLAM reanalysis, and HIRLAM 24-hour forecast wind speeds, calculated for grid point Kokkola.

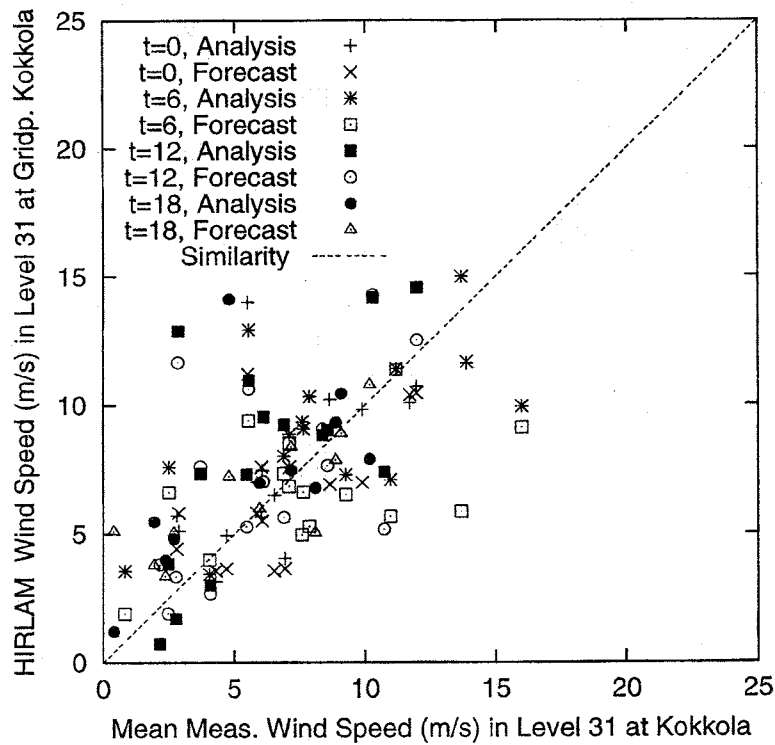


Figure 11: Comparison of results in level 31 of mean measured wind speeds at Kokkola to HIRLAM results of reanalysis and 24-hour forecast as functions of hour of the day, measured and calculated during the BASIS field experiment. For a guide for the eye the line of similarity of measured and calculated data is also drawn.

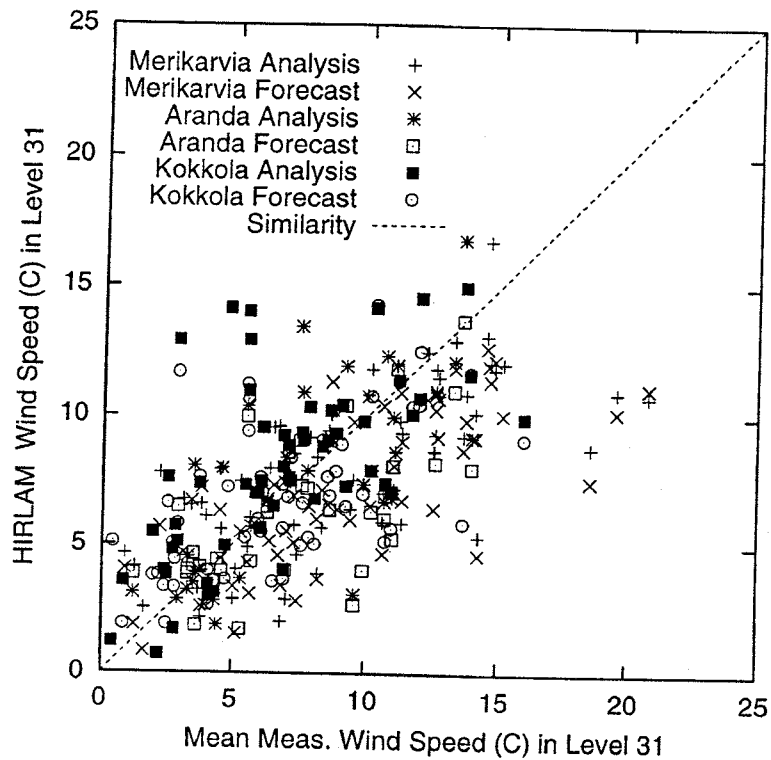


Figure 12: Comparison of results in level 31 of mean measured wind speeds at Umea, Merikarvia, Kokkola, and above the Aranda to HIRLAM results of reanalysis and 24-hour forecast for the whole period of the BASIS field experiment. For a guide for the eye the line of similarity of measured and calculated data is also drawn.

#### 4. Conclusions for the radiosonde comparison

The qualitative structure of the contour plots of temperature in the time-level index plane is the same for HIRLAM reanalysis, HIRLAM 24-hour forecast data, and mean measured data. Differences of HIRLAM model output temperatures from the mean measured temperatures are mostly related to large changes of temperatures with time, due to passages of cold and warm fronts. Especially in level 31 cooling and warming caused by fronts is not calculated correctly by the HIRLAM forecast and reanalysis. Also at constant time vertical gradients of temperature are smaller in HIRLAM reanalysis data than in mean measured temperatures and smallest in HIRLAM 24-hour forecast data.

The results of the HIRLAM 24-hour forecast wind speeds differ in larger amount from mean measured data than the results of HIRLAM reanalysis. Vertical gradients of wind speed are both in reanalysis and forecast results smaller than in mean measured data. Therefore the number of observed low level jets is smaller in reanalysis results than in measurements and smallest in forecast results, compared to reanalysis and measurements.

As low level jets are closely related to boundary layer structures (see e.g. Smedman et al. 1995) the decreasing number of detected low level jets in HIRLAM reanalysis and forecast, compared to mean measured data, shows that boundary layer turbulence is not correctly represented in the HIRLAM model. The reduction of vertical gradients in both HIRLAM temperature and wind speed profiles gives a hint that vertical mixing within the lower boundary layer is too strong, compared to mixing in the atmosphere.

## 5. Comparison with aircraft measurements

During the field experiment BASIS six aircraft missions were flown covering the ice edge zone between Kokkola in the north and locations up to 100 km south of RV Aranda over the open water. The low level flight legs between 10 and 30 m above the surface are compared with HIRLAM model results. The turbulent fluxes of sensible and latent heat,  $H$  and  $E$ , are calculated over 4 km length intervals applying the eddy correlation technique. Albedo  $Alb$ , wind speed  $FF$ , wind direction  $DD$ , surface temperature  $T_s$ , air temperature  $T$ , surface humidity  $q_s$ , and humidity  $q$  are averaged over the same distance. The ice cover is calculated based on a critical surface temperature of  $-0.26$  °C. The location of the flight patterns and the model gridpoints on 44 km resolution are presented in Figure 13. Each cross represents one 4 km average. These gridpoints, which are representatively covered by aircraft measurements, are chosen (grey shades) and gridpoint averages of the measurements are calculated. The equipment of the research aircraft Falcon is described by Brümmer et al. (2001, this issue).

Reanalysis of the BASIS period were performed by SMHI using HIRLAM on 44 km resolution based on extra ice observations, but not based on BASIS measurements. The turbulent surface fluxes are calculated by the mosaic method. A fraction of land and of water and for the water part a fraction of ice and open water are given for each gridpoint. Thus, two surface temperatures exist: one for the open water part and one together for the land and ice part. While  $T_s$  is constant over open water,  $T_s$  over the land/ice part is determined by a 3-layer surface model. A detailed description of the model can be taken from Källén (1996).

For this study 6h-forecasts based on ECMWF analysis are chosen. All six forecasts to be compared are valid for 12 UTC. Thus, there is time difference between the model results and the measurements, because the flight missions took place approx. around 10 UTC. The comparison between model results and aircraft measurements is presented in Tables 2a-c and 3. Table 2a compares the open water gridpoints ( $n_{ice}(\text{Aircraft measurement}) < 0.1$ ), Table 2b the ice covered gridpoints ( $n_{ice} > 0.9$ ) and Table 2c the partly ice covered gridpoints. The mean values and the deviations are shown in Table 3.

Over open water (Table 2a) the model results and the aircraft observations agree well concerning  $n_{ice}$ ,  $T_s$  and  $T$ , but  $FF$  and  $DD$  differ considerably. The RMSE-values amount to  $3.6 \text{ ms}^{-1}$  and  $92^\circ$ , respectively (Table 3). Deviations to both directions show that the different heights (model: 10 m and observation: 14 to 90 m) are not the reason for that. The errors of  $FF$  lead to an overestimation of  $H$  and  $E$  by 180 and 80 %, respectively, on 3 March (No. 4) and to an underestimation of  $H$  and  $E$  by 45 % on 6 March (No. 1).

Over the ice (Table 2b) there is again consistence between the ice distribution of the model and the observed one. The  $T$ -values show minor differences apart from one assumption on 3 March (No. 8). Over the land-fast ice in the south of RV Aranda,  $T$  and  $T_s$  are overestimated by 3.5 K and 6.1 K. In general, the modeled  $T_s$  is smaller than the observed one. The largest deviations occur when the albedo values are quite small: on 2 March (No. 10)  $T_s$  is underestimated by 4.4 K and on 6 March (No. 8) by 3.1 K, while albedo values of 0.38 and 0.40 were observed. It cannot be excluded that the differences are increased by the fact that the measurements may not really be representative for a whole grid point over an inhomogeneous ice surface in some cases, but it is confirmed that grey ice affects considerably the surface energy balance. Concerning the vertical temperature gradient  $T-T_s$ , the absolute differences between modeled and observed values are small, but in 5 out of 8 cases the sign and thus the stratification are opposite. This leads to  $H$ -fluxes of different direction, but small amounts. The extreme modeled  $E$ -values of 60 to  $80 \text{ Wm}^{-2}$  (positive



outward from the surface) compared to  $-1$  to  $26 \text{ Wm}^{-2}$  observed cannot be explained by the humidity stratification.

The partly ice covered gridpoints (Table 2c) are even more difficult to discuss, because the ice concentration given in the model does not agree well with the observed one. Yet,  $T_s$  and consequently H and E strongly depend on the ice concentration. Thus, major discrepancies to both directions occur.

The comparison of the mean values in Table 3 show that the model results of  $n_{ice}$ , T and q agree quite well with the observations, although the synoptic situation is not properly reproduced as demonstrated by RMSE-value of  $3.3 \text{ ms}^{-1}$  for FF and  $55^\circ$  for DD. The mean values of  $T_s$  show no systematic errors, but the RMSE-value over ice amounts to 3.2 K. The same amount of  $21 \text{ Wm}^{-2}$  is modelled and observed for the mean H-flux, but a RMSE-value of the same amount documents the discrepancies of the individual cases. Concerning the E-flux the modelled mean value of  $33 \text{ Wm}^{-2}$  is 50 % larger than the observed one due to some unrealistic large values (see Table 2b). It is striking that the observed H- and E-fluxes are of same size – increasing both from  $9 \text{ Wm}^{-2}$  over ice to  $42 \text{ Wm}^{-2}$  over open water.

Taken together, it can be concluded that no systematic differences between model results and aircraft observations can be determined. In spite of many difficulties in comparing these model results with aircraft measurements – 44 km grid size and line measurements, different heights and different time -, it is demonstrated that the occurring wind deviations influence considerably the surface heat fluxes and that the surface temperature is a crucial value underestimated over grey ice parts. A more precise model verification based on aircraft measurements requires a grid resolution of 10 km to 20 km.

## References

- Källén, E. (Ed.): 1996, 'HIRLAM Documentation Manual, System 2.5' .
- Launiainen, J. (Ed): 1999, 'BALTEX-BASIS Data Report 1998'. BALTEX Publ. No 14.
- Sandström, S.: 1997, 'Simulations of the Climatological Wind Field in the Baltic Sea Area Using a Mesoscale Higher-Order Closure Model'. *J. Appl. Meteor.* **36**, p. 1541 – 1552.
- Smedman, A., Tjernström, M. and Högström, U.: 1993, 'Analysis of the Turbulence Structure of a Marine Low-Level Jet'. *Boundary-Layer Meteorol.* **66**, p. 105 – 126.
- Smedman, A., Bergström, H. and Högström, U.: 1995, 'Spectra, Variances and Length Scales in a Marine Stable Boundary Layer Dominated by a Low Level Jet'. *Boundary-Layer Meteorol.* **76**, p. 211 – 232.
- Uotila, J., Vihma, T. and Launiainen, J.: 1997, 'Marine meteorological Radiosoundings in the Northern Baltic Sea from R/V Aranda in 1994-95'. *Report Series of the Finnish Institute of Marine Research* **30**.
- Vihma, T., Uotila, J., Cheng, B., Purokoski, T., Kosloff, P., Launiainen, J. and Schrum, C.: 1999, 'Marine meteorological, sea ice and oceanographic observations by the Finnish Institute of Marine Research'. *BALTEX-BASIS Data Report 1998*, International BALTEX Secretariat, Publication No. 14.

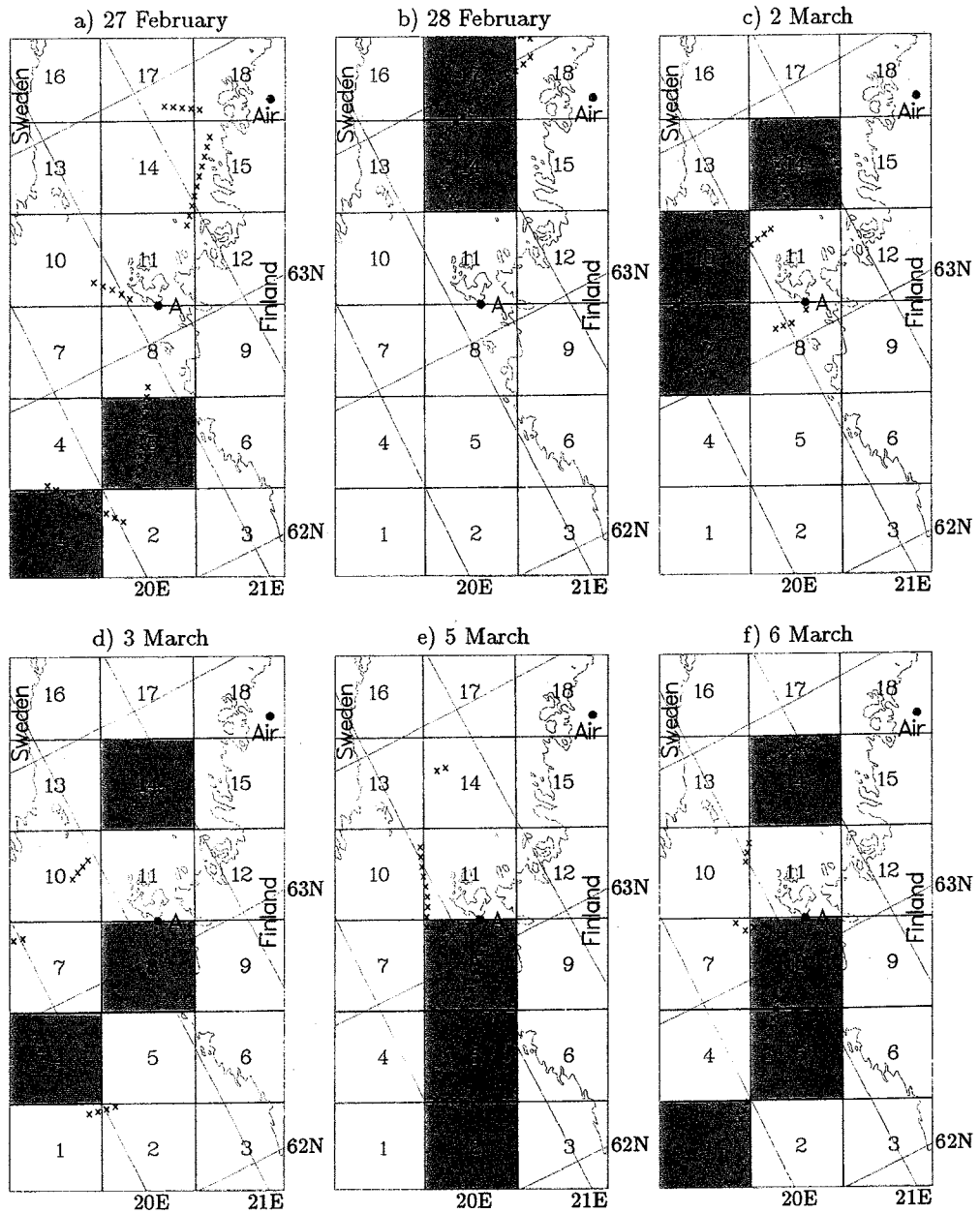


Figure 13: The location of the six missions of research aircraft Falcon in the ice edge zone of the Northern Baltic Sea. The flight operation field, Kokkola airfield (Air), and the location of RV Aranda (A) are marked by a dot. The crosses represent 4km-averages of the low level flight legs. 18 gridpoints of the HIRLAM model on 44 km resolution - from which the grey shades are chosen for comparison - are shown.

**Table 2a.** Comparison between HIRLAM model results (M) and aircraft measurements (A) for open water gridpoints ( $n_{ice}(A) < 0.1$ ).

Shown are data for ice cover  $n_{ice}$ , Albedo Alb, wind speed FF, wind direction DD, surface temperature  $T_s$ , air temperature T, air-surface temperature difference  $T-T_s$ , air humidity q, air-surface humidity difference  $q-q_s$ , sensible heat flux H, and latent heat flux E (positive outwards from the surface). The day in 1998 and the number of the gridpoint (see Figure 1) are given in the first two lines. The measurement height is shown in the third line; concerning the model heights FF and DD are 10m-values,  $T_s$ ,  $q_s$ , H, and E surface values, and T and q 30m-values.

a)			27 Feb.	3 March	5 March	6 March
No.		M	1	4	2	1
h	m	A	90	14	33	21
$n_{ice}$		M	0.00	0.00	0.00	0.03
		A	0.00	0.01	0.00	0.00
Alb		M				
		A	0.10	0.13	0.06	0.06
FF	$ms^{-1}$	M	11	5	8	3
		A	15	2	9	8
DD	°	M	196	210	332	312
		A	208	32	14	309
$T_s$	°C	M	1.1	0.1	1.0	1.0
		A	1.1	0.5	0.7	1.2
T	°C	M	2.4	-1.9	-8.7	-5.2
		A	2.4	-2.0	-8.7	-4.0
$T-T_s$	K	M	1.3	-2.0	-9.7	-6.2
		A	1.3	-2.5	-9.4	-5.2
q	$gkg^{-1}$	M	3.8	1.7	1.4	1.5
		A	4.2	2.6	1.6	2.2
$q-q_s$	$gkg^{-1}$	M	-0.2	-2.1	-2.6	-2.6
		A	0.1	-1.3	-2.4	-1.8
H	$Wm^{-2}$	M	-29	16	167	27
		A	-10	9	121	48
E	$Wm^{-2}$	M	1	42	121	27
		A	5	15	102	47

**Table 2b.** As Table 2a, but for ice-covered grid points ( $n_{ice}(A) > 0.9$ ).

b)			28 Feb.	2 March	2 March	3 March	3 March	5 March	6 Mar	6 Mar
No.		M	17	10	14	8	14	8	8	14
h	m	A	17	12	13	15	16	32	16	13
$n_{ice}$		M	0.83	1.00	0.97	1.00	0.97	1.00	1.00	0.97
		A	1.00	0.98	1.00	1.00	1.00	1.00	0.99	1.00
Alb		M								
		A	0.41	0.38	0.60	0.82	0.62	0.66	0.40	0.63
FF	$ms^{-1}$	M	6	4	4	3	1	4	2	2
		A	8	3	3	5	5	10	7	5
DD	$^{\circ}$	M	215	185	192	188	56	327	321	300
		A	226	223	255	183	9	7	351	358
$T_s$	$^{\circ}C$	M	-1.8	-8.4	-9.8	-1.9	-6.6	-10.5	-7.5	-11.8
		A	-2.3	-4.0	-8.0	-8.0	-4.1	-8.8	-4.4	-10.7
T	$^{\circ}C$	M	-2.7	-8.0	-9.3	-2.0	-5.9	-11.0	-8.4	-11.8
		A	-1.5	-6.4	-7.7	-5.5	-4.7	-11.8	-7.4	-11.8
T- $T_s$	K	M	-0.9	0.4	0.5	-0.1	0.7	-0.5	-0.9	0.0
		A	0.8	-2.5	0.3	2.4	-0.6	-2.9	-3.0	-1.1
q	$gkg^{-1}$	M	2.6	1.5	1.4	2.6	2.2	1.3	1.6	1.3
		A	3.1	1.7	1.7	2.3	2.3	1.3	1.7	1.2
q- $q_s$	$gkg^{-1}$	M	-0.7	-0.5	-0.3	-0.7	-0.1	-0.3	-0.5	-0.2
		A	-0.1	-1.1	-0.4	0.2	-0.4	-0.7	-0.9	-0.4
H	$Wm^{-2}$	M	4	-6	-8	-9	-1	20	37	-2
		A	-2	8	2	-3	4	29	24	6
E	$Wm^{-2}$	M	19	7	3	80	0	64	65	1
		A	8	12	4	-1	5	26	17	4

**Table 2c.** As Table 2a, but for partly ice-covered grid points.

c)			27 Feb.	28 Feb	2 Mar	5 Mar	6 Mar
No.		M	5	14	7	5	5
h	m	A	98	19	13	30	17
$n_{ice}$		M	0.00	0.31	0.00	0.97	0.04
		A	0.33	0.69	0.35	0.54	0.45
Alb		M					
		A	0.08	0.18	0.18	0.30	0.25
FF	$ms^{-1}$	M	11	7	5	8	3
		A	16	9	4	10	5
DD	$^{\circ}$	M	181	223	174	326	310
		A	195	227	212	8	328
$T_s$	$^{\circ}C$	M	1.2	-0.3	0.1	-5.0	0.1
		A	0.0	-0.8	-0.7	-2.6	-1.3
T	$^{\circ}C$	M	1.1	-1.8	-6.2	-10.1	-6.4
		A	2.4	-1.1	-4.9	-9.6	-5.3
T- $T_s$	K	M	0.0	-1.4	-6.3	-5.1	-6.6
		A	2.3	-0.2	-4.1	-7.0	-4.0
q	$gkg^{-1}$	M	3.9	2.8	1.5	1.3	1.5
		A	4.3	3.1	1.7	1.5	2.1
q- $q_s$	$gkg^{-1}$	M	-0.2	-0.8	-2.3	-1.3	-2.3
		A	0.6	-0.4	-1.9	-1.6	-1.3
H	$Wm^{-2}$	M	-6	20	55	38	35
		A	-13	6	16	86	25
E	$Wm^{-2}$	M	1	26	50	26	30
		A	3	18	22	67	20

**Table 3.** The mean values (M: model results, A: aircraft measurements) and the root mean square errors (RMSE) of all quantities compared in Table 2a-c. The results are given separately for the open water gridpoints, the ice-covered gridpoints, the partly ice-covered gridpoints, and for the total gridpoints.

			Water (Table 2a)	Ice (Table 2b)	Broken Ice (Table 2c)	Total
$n_{ice}$		M	0.01	0.97	0.26	0.53
		A	0.00	1.00	0.47	0.61
		RMSE	0.02	0.06	0.38	0.21
FF	$ms^{-1}$	M	6.8	3.3	6.8	5.1
		A	8.5	5.8	8.8	7.3
		RMSE	3.6	3.5	2.8	3.3
DD	$^{\circ}$	M				
		A				
		RMSE	92	41	27	55
$T_s$	$^{\circ}C$	M	0.8	-7.3	-0.8	-3.5
		A	0.9	-6.3	-1.1	-3.1
		RMSE	0.3	3.2	1.4	2.3
T	$^{\circ}C$	M	-3.3	-7.4	-4.7	-5.6
		A	-3.1	-7.1	-3.7	-5.2
		RMSE	0.6	1.7	1.0	1.3
T-T <sub>s</sub>	K	M	-4.1	-0.1	-3.9	-2.2
		A	-4.0	-0.8	-2.6	-2.1
		RMSE	0.6	2.0	2.1	1.8
q	$gkg^{-1}$	M	2.1	1.8	2.2	2.0
		A	2.6	1.9	2.5	2.3
		RMSE	0.6	0.3	0.4	0.4
q-q <sub>s</sub>	$gkg^{-1}$	M	-1.9	-0.4	-1.4	-1.0
		A	-1.3	-0.5	-0.9	-0.8
		RMSE	0.6	0.5	0.6	0.6
H	$Wm^{-2}$	M	45	4	28	21
		A	42	9	24	21
		RMSE	27	9	29	21
E	$Wm^{-2}$	M	46	30	27	33
		A	42	9	26	22
		RMSE	18	36	23	29

## 4. ICE AND SURFACE PROPERTIES

### Sea Ice Concentration Derived from Radarsat data

Maria Lundin

Swedish Meteorological and Hydrological Institute

#### 1. Introduction

A sea ice concentration algorithm determining sea ice concentration from SAR data have been developed and applied on Radarsat SAR scenes from the BASIS winter experiment period. The algorithm is based on local threshold, developed in Dokken et al. (2000), where the thresholds are partly manually extracted.

#### 2. Data Set

Radarsat scenes of the type ScanSAR Narrow have been used in this study. Each image covers an area of  $300 \times 300 \text{ km}^2$  with a resolution of 50 m. The Radarsat SAR instrument operates with the frequency 5.3 GHz and HH polarisation. The SAR scenes were downloaded to SMHI Norrköping by ftp from Tromsø Satellite Station (TSS) during the BASIS field campaign.

#### 3. Sea Ice Concentration Algorithm

The sea ice concentration algorithm is based on local threshold in order to work on non-calibrated SAR data (Dokken et al., 2000). The thresholds are determined from manually extracted water and ice values typical for the area each threshold is working on. Since the SAR sensor looks sideways there is a range dependency in the SAR data. Influence from the range dependency is avoided when several thresholds are defined along the range direction in the image.

The upper diagram in Figure 1 shows backscatter values of open water and ice for different incidence angles from a Radarsat scene from February 18, 1998. The values have been extracted manually from typical water and ice areas. In order to reduce the influence of speckle, each point represents a mean value of several pixels. The blue and green line represent water mean backscatter and standard deviation from mean, respectively. The red line represents the chosen threshold between water and ice. In order to achieve as true separation as possible between water and ice the threshold is optimised at 1.9 times the standard deviation. Least number of the manually chosen pixels are miss-classified at that level. The optimisation is illustrated in the lower diagram where number of miss-classified water and ice pixels are shown for different threshold levels. The minimum point is found at standard deviation factor 1.9. The quality factor shows number of miss-classified pixels of the extracted pixels for the chosen threshold.

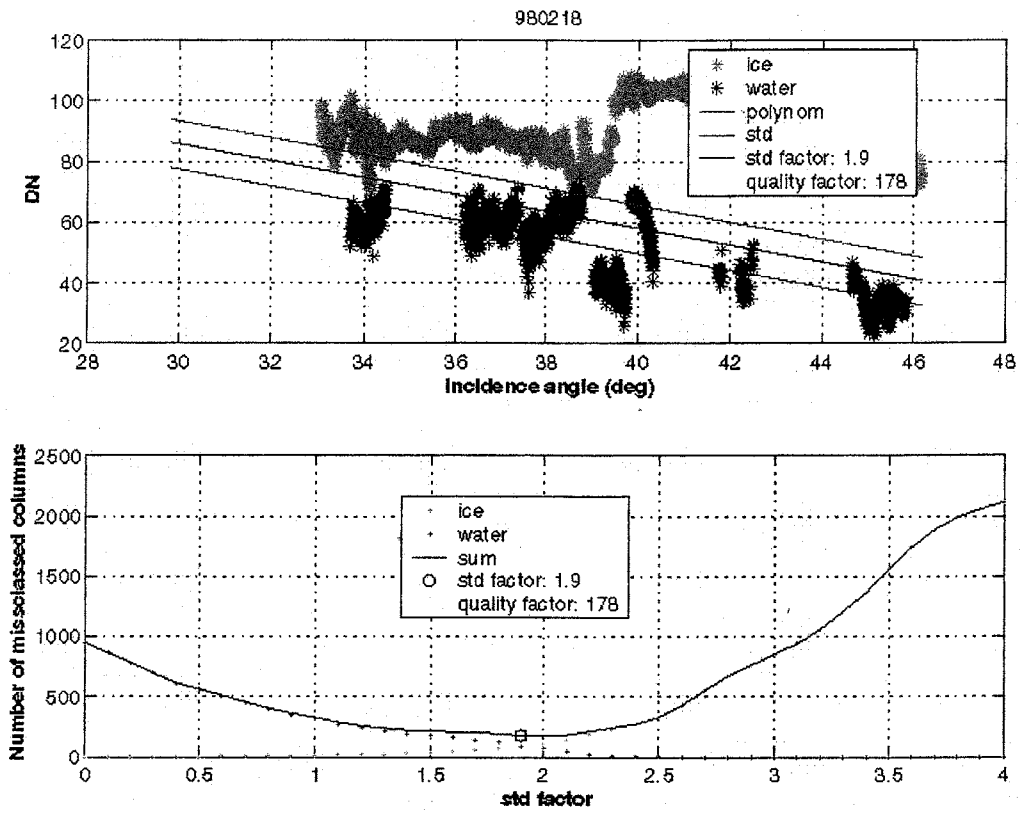


Figure 1. Threshold extraction for a Radarsat scene from February 18, 1998.

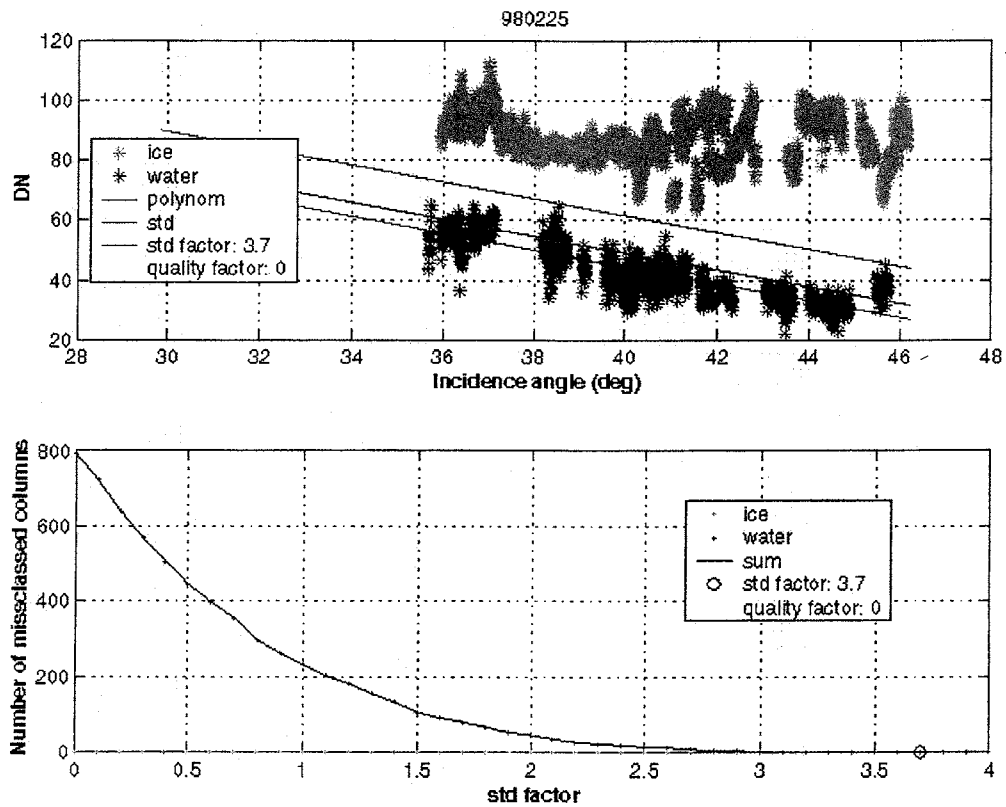


Figure 2. Threshold extraction for a Radarsat scene from February 25, 1998.

The range dependency in the SAR data is clearly seen in the upper diagram in Figure 1, where water pixel value increases with decreased incidence angle. The range dependency is more difficult to see in the ice data due to many different ice types that conceal the range effect, see Figure 4 below. The range dependency can also be seen in Figure 2 that shows the threshold for a Radarsat scene from 25 February. In this case there is a clear separation between open water and ice backscatter values which is due to the weather condition with very low wind and low air temperature that increases the contrast in the image. That weather condition is not only an advantage since it the production of new ice increases on large areas, which is difficult to distinguish from open water by a threshold.

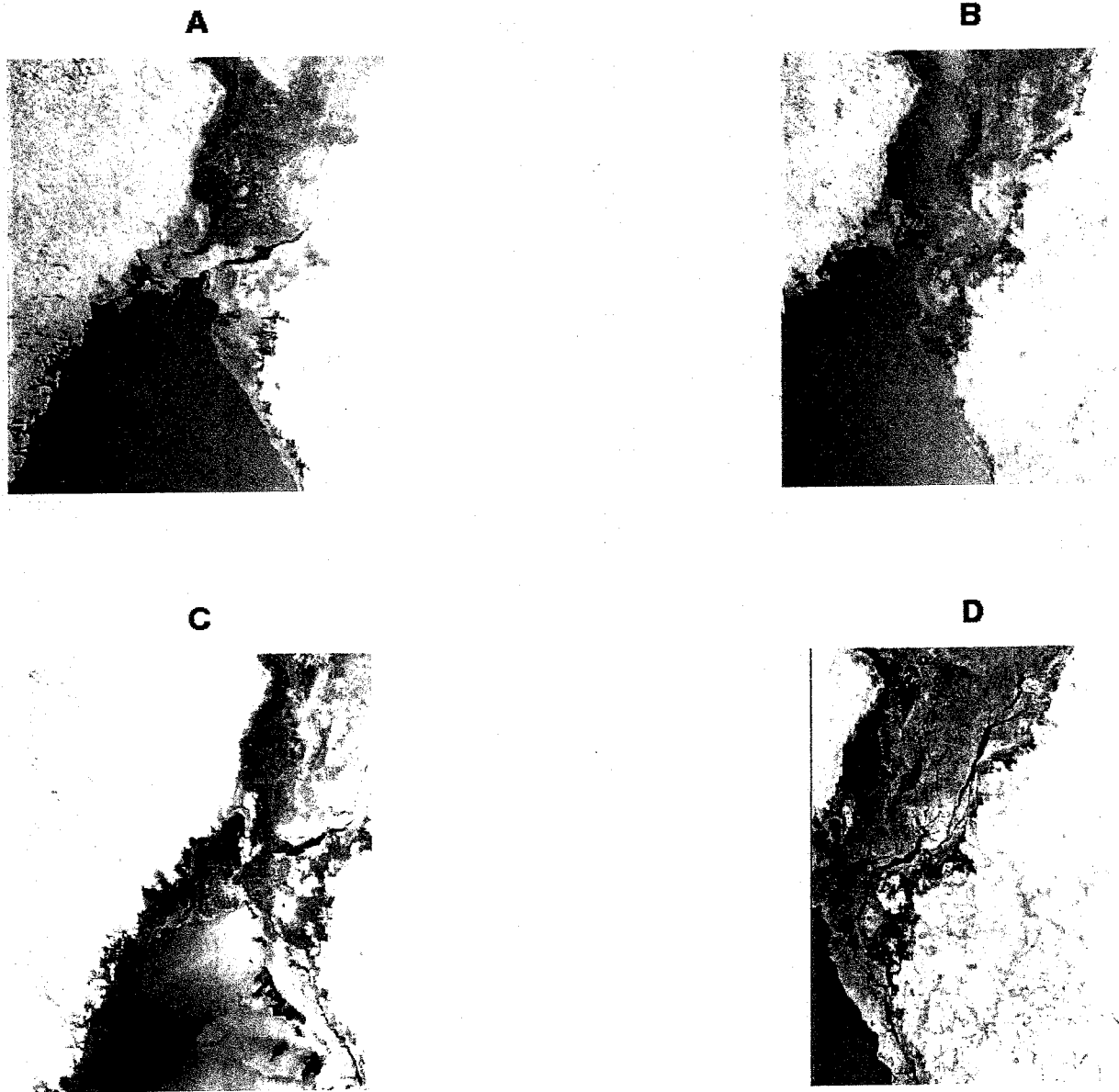


Figure 3. A) Range dependency in image. B) Air temperature above zero decreases the contrast. C) Rough sea ice as same backscatter values as large open water areas during high wind condition. D) Newly formed sea ice during cold and clam conditions.



In the same way level fast ice is sometimes miss-classified into water. In order to prevent that the land fast ice is masked by the 10-metre bathymetry data that is assumed to cover the main part of land fast ice areas. Furthermore large open water areas are manually masked. Such areas have a higher backscatter value than smaller water areas due to wind influences.

As mentioned above there are some cases where water and ice is difficult to separate by simply a threshold method. Figure 3 shows four examples of such cases. Image A illustrates the range dependency, mentioned above, which is solved by local thresholds. SAR images are strongly dependent on meteorological parameters as air temperature (Lundin, 1999) and wind conditions. In image B the air temperature is above zero which drastically decreases the contrast in the image. This makes it more difficult to discriminate between water and ice pixels. The problem in differing between rough sea ice and large open water areas during high wind conditions is a critical moment in determining sea ice concentration from SAR data. This is illustrated in image C. Different attempts have been made to find parameters that differ between ice and water in those cases, but still areas of open water with high wind have to be classed manually. The last image D shows an example of newly formed ice during cold and calm conditions as mentioned above. New ice is easily discriminated from calm open water of a trained eye but difficult to catch by a threshold method. The importance of finding the new ice areas depends on the application. For icebreakers using SAR images, open water or new ice does not make any difference while it is crucial within forecast modelling where new ice or open water makes a large difference concerning the heat transports.

#### 4. Results

The sea ice concentration algorithm has been applied on 12 Radarsat scenes. The image covers the northern part of Gulf of Bothnia and mainly the area of the BASIS winter experiment in the Northern Quark.

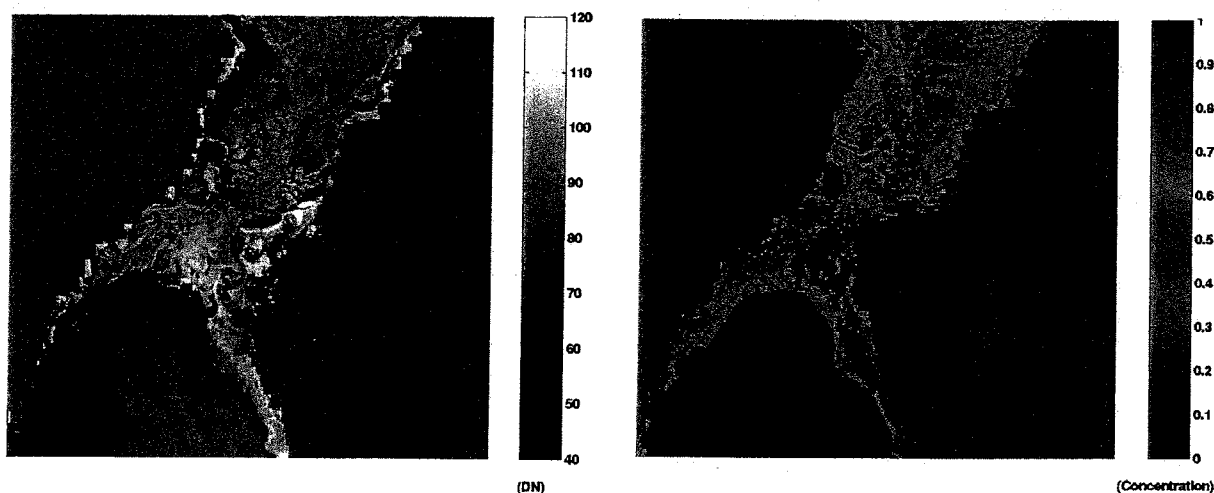


Figure 4: Left) Radarsat ScanSAR Narrow scene from February 18, 1998. Right) Sea ice concentration algorithm applied.

Two examples of the sea ice concentration algorithm applied to Radarsat images can be seen in Figure 4 and 5. When applying the threshold each pixel get the value ice or water with a resolution of 50 metres. In Figure 4 and 5 the data have been averaged into ice concentration between 0-1.

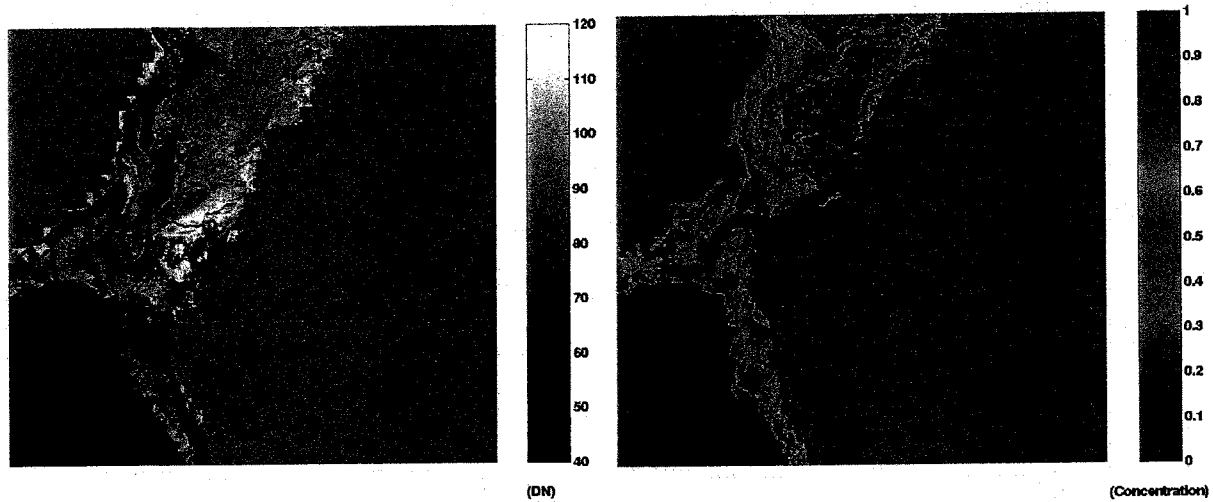


Figure 5. Left) Radarsat ScanSAR Narrow scene from February 25, 1998. Right) Sea ice concentration algorithm applied.

The threshold determined in Figure 1 and 2 have been used on the Radarsat scenes that cover southern part of Bothnian Bay and northern part of Bothnian Sea. Open water south of the ice edge in Bothnian Sea has been classified manually. As illustrated in previous section large open water areas are more affected by the wind and can not be separated from ice by simply a threshold. Land fast ice has been masked by 10-metre bathymetry data.

## References

- Dokken, S., Håkansson, B., and Askne, J.: 2000, Inter comparison of arctic sea ice concentration using Radarsat, ERS, SSM/I and in-situ data, *Canadian Journal of Remote Sensing*, December, 1-16.
- Lundin, M.: 1999, Time Series Analysis of SAR Sea Ice Backscatter Variability and its Dependence on Weather Conditions, *Reports Oceanography SMHI*, 25.

## BASIS Study of Wind Speed from SAR Images

J. Askne<sup>1)</sup>, N. Gustafsson<sup>2)</sup>, B. Håkansson<sup>2)</sup>, and S. Mugnier-Pollet<sup>1)</sup>

<sup>1)</sup> Chalmers Technical University, Gothenburg, Sweden

<sup>2)</sup> Swedish Meteorological and Hydrological Institute, Norrköping, Sweden

### 1. Introduction

Wind information over the ocean or partly ice covered areas is important for many reasons. Today we have localised measurements from buoys and weather stations but satellites can provide area extensive information from the open sea. By means of radar observations wind can be determined under certain conditions, which still have to be investigated. Such investigations have been performed during the BASIS project. The area extensive SAR estimates of wind are derived from more or less instantaneous measurement. In 15seconds a 100x100 km<sup>2</sup> large area is covered, and there are obvious differences between traditional wind measurements

Below a short summary of wind measurements from radar satellites is given. Validation of the relation between radar backscatter and wind is given based on comparison with weather stations, with the numerical model HIRLAM, and wind masts. Also some limited measurements from within the ice cover and the ice edge are reported. Further results are found in (Mugnier-Pollet et al, 1997, Mugnier-Pollet, 1998).

#### *ERS-1/2 scatterometer and wind estimates*

The ERS-1/2 scatterometer is used operationally for deriving wind information from the ocean surface. The radar backscatter,  $\sigma^0$ , from ocean surfaces is dependent on wind speed and direction, and empirical relations have been established for the scatterometer onboard ERS-1/2, see Figure 1 for one of these models (IFREMER, 1996).

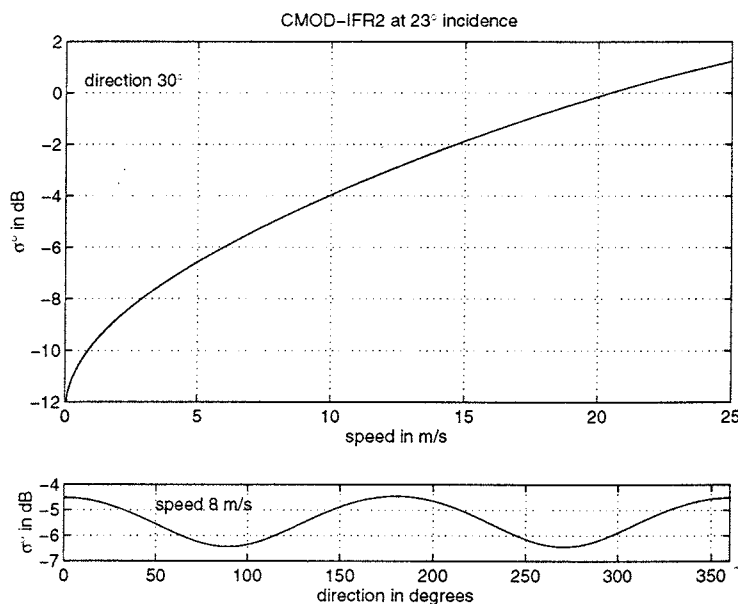


Figure 1. Backscattering coefficient with respect to speed and direction for a fixed incidence angle using the CMOD-IFR2 model (IFREMER, 1996).

### ERS-1/2 SAR and wind estimates

The ERS-1/2 scatterometer was designed for wind estimates in 50x50 km<sup>2</sup> areas and consequently the scatterometer is not very suitable for the Baltic Sea. Instead the SAR offers the possibility to determine the backscatter with a resolution of 25x25 m<sup>2</sup> but from only one direction. The wind speed then has to be determined by other means, such as forecasts or actual observations in the SAR image. Some air movement features like roll vortices can appear in the planetary boundary layer (the lowest atmospheric layer). These are helical circulations of the second order, mainly due to thermal instability, superimposed to the dominant wind field. They modulate the wind and create parallel features called wind rows or wind streaks in the SAR images (Wackerman *et al.* 1996, Vachon *et al.* 1997). Those features allow the estimation of the wind direction with a variable accuracy depending on their strength and the quality of the image. However, one should be careful not to mistake them for effects of internal waves. Typical figures and configurations are found in (Vachon *et al.* 1995) and (Dokken *et al.* 1998b).

With a resolution of 25x25 m<sup>2</sup> we can also discuss the possibility to obtain wind information in partly ice covered areas or estimate the backscatter from the openings in between the ice floes. Then the risk of problems for ice concentration estimates, which are dependent on the contrast between the ice backscatter and the ocean backscatter, can be judged.

## 2. Wind from SAR in the Baltic Sea.

The empirical wind estimates derived from the ERS-1/2 scatterometer are assumed to be possible to apply also for the SAR. One method to compare wind estimates derived from the scatterometer and the SAR is to compare observations done with a short time interval between the sensors during the ERS tandem mission (Furevik and Korsbakken 1998). However, the comparison between scatterometer and SAR is not fully investigated so far in all its aspects. There are also some special aspects of SAR derived winds worth studying in the Baltic Sea, where the fetch is not fully developed. We may also have effects of the coast line, especially if we have some topography. It is therefore important to verify the applicability of the CMOD-relation as illustrated by e.g. Figure 1.

In the Baltic Sea we have small islands, small enough not to disturb the wind roughened ocean surface very much, and with meteorological stations on the islands. During the BASIS experiment we also had wind masts available for more detailed measurements of the wind field. These observations can be used for comparison with SAR observations.

## 3. Dataset

The image set is composed by 18 images from ERS-1/2 over or very close to some weather stations, fixed (islands) or mobile (wind masts, ships). The wind estimation was made over samples of 10x10 km<sup>2</sup>. Some characteristics of the SAR images set are summarised in Table 1.

Table 1: image set characteristics

<i>in situ</i> data type and number of samples	satellite used	image to <i>in situ</i> time delay	number of images
fixed island stations (3)	ERS-1	45 minutes	3
fixed island stations (1, 2 or 3)	ERS-2	45 minutes	9
fixed island stations (3)	ERS-2	30 minutes	3
wind masts (2 or 3)	ERS-2	simultaneous	2
ice-breaker data (1)	ERS-2	simultaneous	1

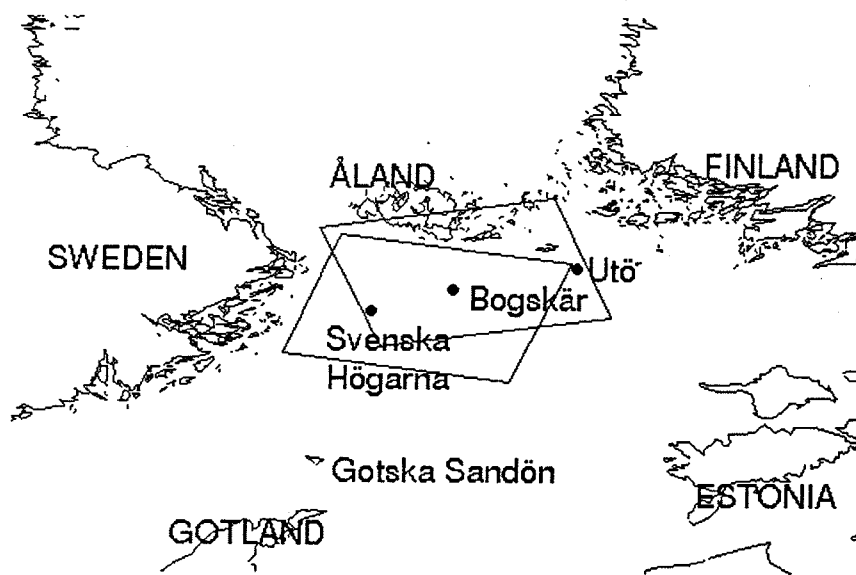


Figure 2: Map of the main test area with two ERS SAR frames used and the location of weather stations.

Most of the images corresponding to these data contain three *in-situ* samples: the manned meteorological stations of Utö (Finland) and Svenska Högarna (Sweden) and the automatic one of Bogskär (Finland), see Figure 2. The *in situ* data from the fixed island stations consists of 10 minute averaged wind speed and direction every three hours. The images were acquired at different times so an interpolation of the wind vector at the right time had to be done. This estimation leads to a separation of the data set in three groups. The first group contains good quality data, when a linear interpolation is possible. The second group contains fair quality data. A typical example is when the speed or direction is varying noticeably (2-3 m/s, 20-30 degrees) but the second order variation indicates that a linear interpolation looks reasonable. The third group contains low quality data, and will not be further discussed.

The wind masts data correspond to two images taken during the Baltic Air-Sea-Ice Study (BASIS), held in February and March 1998 in the framework of BALTEX/GEWEX. They were situated on the ice covering the North of the Baltic Sea near to the northern straits, quite close to the ice edge. The measurements were averages over 10 minute periods. There was thus a perfect time matching but a difference in location of 30 to 110 kilometres. This distance was then the parameter deciding the quality of the *in situ* data interpolation.

Finally, in order to study wind observations within the ice field, one site is situated 10 km away from the ice-breaker Oden during the International Arctic Ocean Expedition ARCTIC'96 and measurements were made at the image acquisition time (Dokken et al 1998a).

## 4. Results

### 4.1 Comparison with meteorological stations on islands

The wind speed has then been estimated near weather stations, using C-band models and using the direction from the *in situ* data as an input. This gave the best possible direction estimate and

helped the validation of the use of scatterometry C-band models on SAR images. Here we only report the comparison with the CMOD-IFR2 estimated wind speed against *in situ* speed for samples with good and fair quality ground truth interpolation, see Figure 3. The results, although limited in number, illustrate a reasonable agreement with the  $\pm 2$  m/s limits, although the results indicate a certain underestimation of wind speed at high wind speeds.

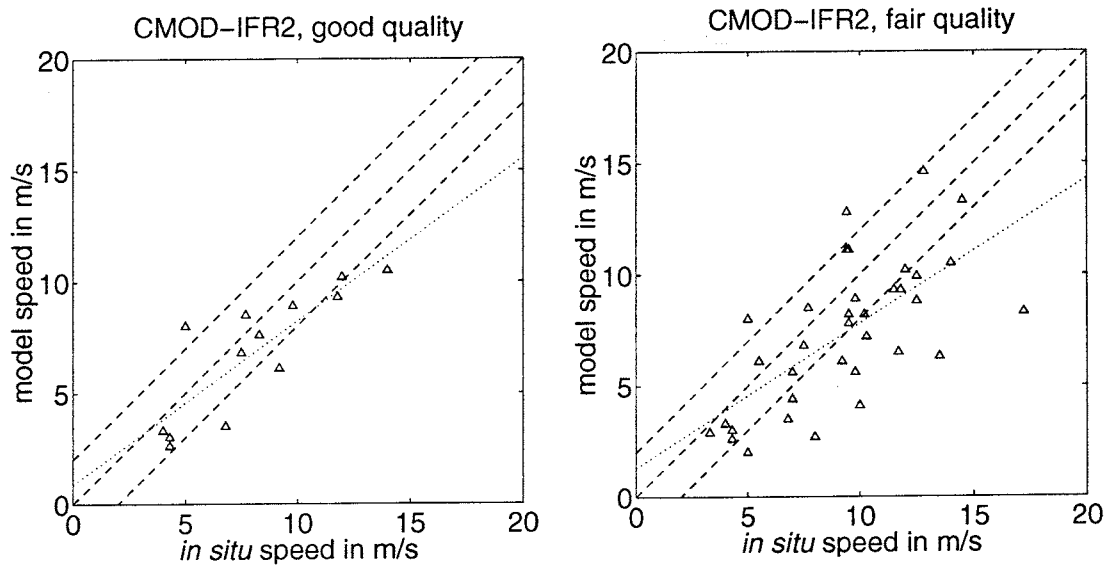
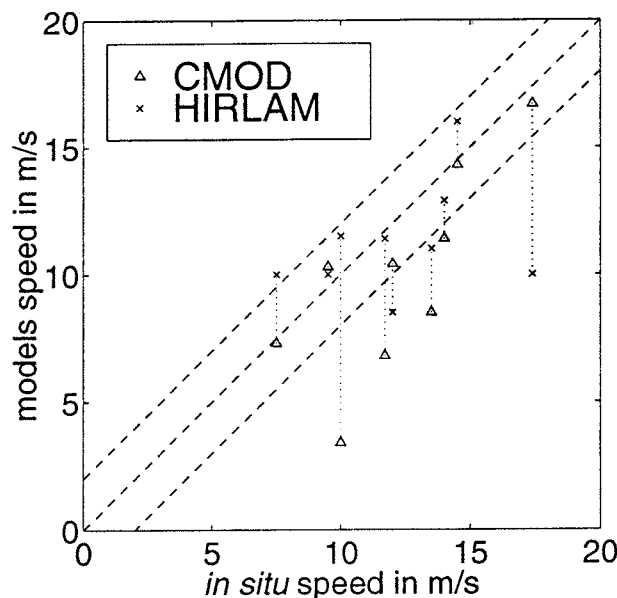


Figure 3: CMOD-IFR2 estimated wind speed against *in situ* speed for samples with good and fair quality ground truth interpolation. In each plot, the three dashed lines indicate the ideal case and the  $\pm 2$  m/s acceptable limits. The dotted line is the linear interpolation of the data points.

#### 4.2 Comparison with HIRLAM

For some of the investigation, a weather forecast model has been used instead of the *in situ* data. This model was the High Resolution Limited Area Model (HIRLAM), developed in co-operation with several European meteorological institutes including the Swedish Meteorological and Hydrological Institute (SMHI) from which one part of the *in situ* data and the HIRLAM charts were obtained. The model has presently a resolution of 22 km (called HIRLAM 22) but the version used here, which is not the latest, has a resolution of 55 km (called HIRLAM 55). The



speed accuracy of the model is not yet well established but is estimated to be of the order of 2 m/s for a 12 hour forecast. The direction accuracy is not known.

Figure 4: CMOD-ECMWF5 (using HIRLAM direction) and HIRLAM estimated wind speed against *in situ* speed. The three dashed lines indicate the ideal case and the  $\pm 2$  m/s acceptable limits. For every *in situ* measurement, the two corresponding model speeds are linked with a dotted line.

It appears that using a C-band model with HIRLAM direction at the input gives acceptable results in most of the cases. As a matter of fact, the three cases where the C-band model underestimates largely the speed correspond to cases with snow fall when it can be expected that CMOD underestimates the wind speed.

### 4.3 Comparison with mast measurements

Wind estimates from different methods are not easy to compare. The SAR is doing "instantaneous" measurements, covering a  $100 \times 100 \text{ km}^2$  in approximately 15 seconds. Instead of temporal averaging as done normally in measurements carried out in a specific point we have to consider spatial averaging. An important question is the minimum size of the area for which the empirical relation between backscatter and wind can be applied.

The standard deviation of the *in situ* speed during the 10 minutes averages was determined for one of the masts used during BASIS. The mast had a height of 3 m. Both standard deviations of the  $200 \times 200 \text{ m}^2$  cells inside the SAR image and the single measurements from the mast during averaging periods are presented in Figure 5.

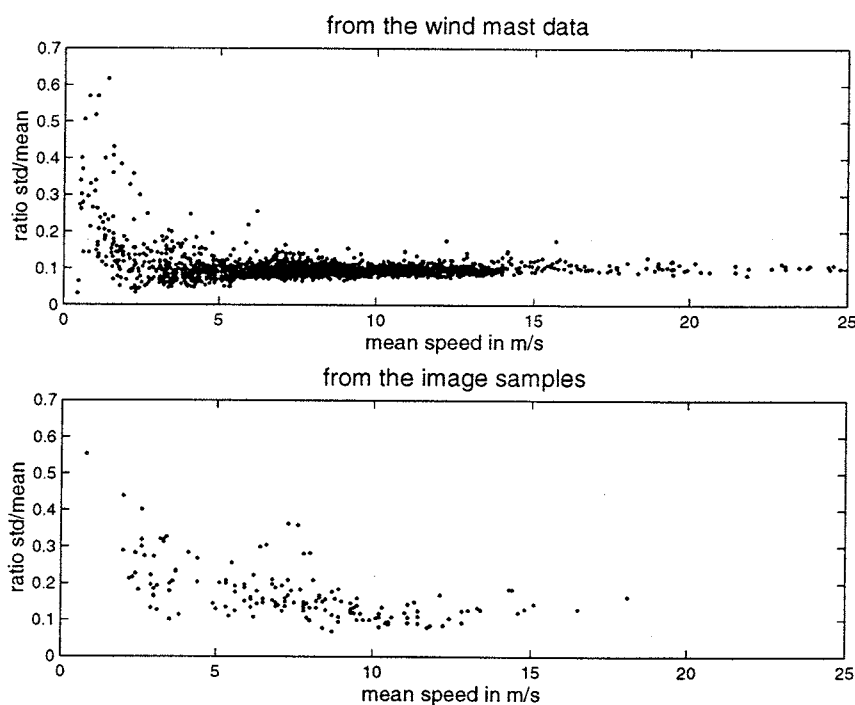


Figure 5. Ratio of the standard deviation over the mean for sets of wind speed measurements as function of time from a mast and sets of measurements as function of space from the images samples (estimated speeds using CMOD4, CMOD-ECMWF5 and CMOD-IFR2). Every set from the mast is averaged over 300 single measurements and over 2500 for the image samples

The behaviour in the two cases was very similar, with a slightly higher value for the radar measurements. Based on this result a  $10 \text{ by } 10 \text{ km}^2$  area was chosen as the averaging area in the earlier comparison between island observations and SAR observations.

In the best case, the two random variables describing the *in situ* speed and the SAR retrieved speed have Gaussian distributions and with the same variance, so comparing their means is most relevant. This can be summarised as follows: *the wind variability in one point during 10 minutes is the same as over  $10 \text{ by } 10 \text{ km}^2$  at one instant.*

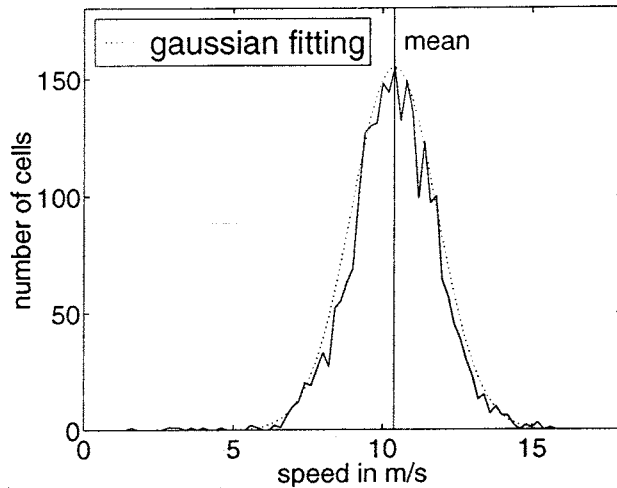


Figure 6. Histogram of the cells speeds from one image sample. The Gaussian approximation using the mean and variance of the histogram is plotted, as well as the mean. The data set contains 2500 points.

Another wind mast was set up during BASIS and recorded wind speed averages over 10 minute periods and the corresponding gust speeds. Those are maxima recorded during 2 seconds, which corresponds approximately to the acquisition time of a 10 km image area. The recording was done at 10 m height for this mast. When plotting the difference between gust speed and mean speed, with respect to the mean speed, a linear relation appears with a slope of 0.25 (see Figure 7).

This shows that the gust speed is comparable in many cases to the 2 m/s margin accepted for the estimation. However, a 30 m/s gust (maximum observed during the 17 days of BASIS) recorded during 2 s represents 60 metres in size, which can influence the retrieval from one cell ( $200 \times 200 \text{ m}^2$ ) but not on the whole sample of 2500 cells.

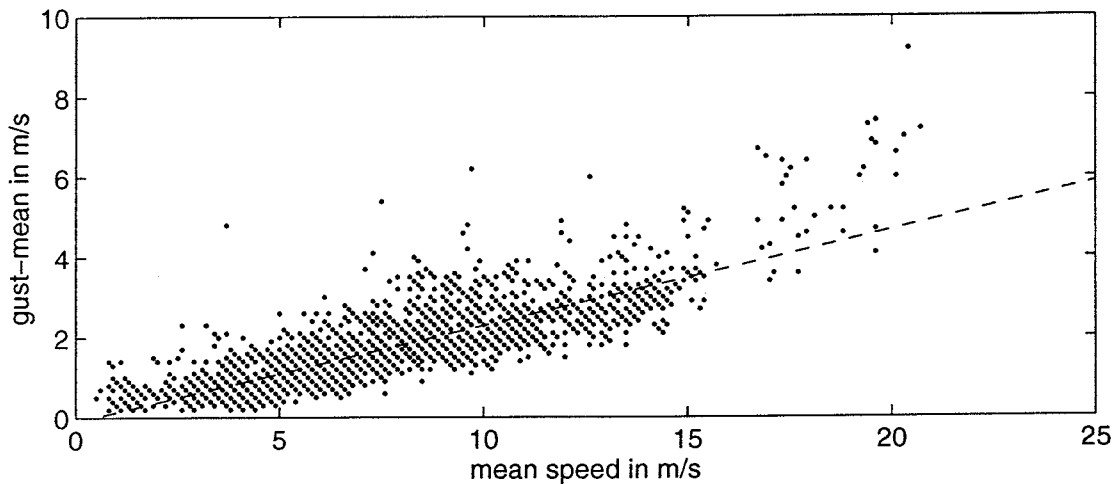


Figure 7: Difference between gust wind speed and mean speed as function of mean speed for 10 minute averaged samples from a wind mast. The gusts last 2 seconds.

#### 4.4 Ice edge transition

Figures 8 and 9 present plots of the backscattering coefficient and SAR retrieved wind speed along profiles across the ice edge. These plots show clearly the influence of ice on the backscatter. In those cases, the speed was correctly extracted even very close to the ice edge, which then seems not to have any influence on the retrieval.



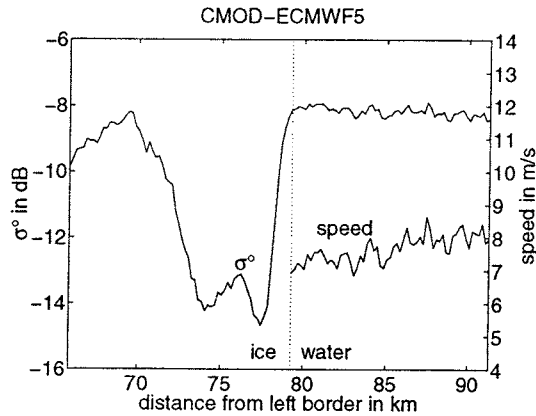


Figure 8: Plot of  $\sigma^0$  and the retrieved wind speed along a profile across the ice edge on the 1<sup>st</sup> of March 1998..

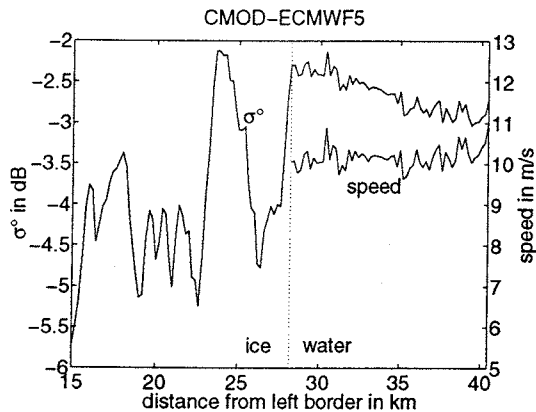


Figure 9: Plot of  $\sigma^0$  and the retrieved wind speed along a profile across the ice edge on the 4<sup>th</sup> of March 1998.

## 5. Discussion and conclusion

From the results, SAR seems to be a good tool for high-resolution wind speed estimation over the sea. The agreement between *in situ* data and SAR extracted wind speed lies within 2 m/s in the most reliable cases, using the wind retrieval models designed for scatterometers and the wind direction from *in situ* data. The variability with time according to most observations has been compared with the spatial image variations, and they are showing similarities.

The results from BASIS illustrate that SAR has potential to complement scatterometers over areas like the Baltic Sea. Since the SAR is sensitive to the wind just above the surface we also have to take the stratification problem into account. This is of importance near coasts as the stratification is often not neutral in this case (Janssen *et al.* 1998) and the C-band models are designed for neutral stratification. This problem can be handled (Korsbakken 1996), provided that temperature data are available, e.g. through HIRLAM.

The results are not extensive enough to make sure the smallest area for which the CMOD relation is applicable, i.e. the smallest opening between ice floes for which wind conditions can be retrieved, but investigations at the ice edge illustrate a quick transition.

The CMOD relation can be used to determine conditions when the backscatter from ocean and ice are similar and cause problems for e.g. ice concentration estimates.

## References

- Dokken, S., Håkansson, B. and Askne, J.: 1998a, 'Sea ice in the climate system monitored with satellite borne SAR', *Proceedings of 27th international symposium on remote sensing of environment: information for sustainability held in Tromsø, N, 1* (ISRSE), pp. 266-269.
- Dokken, S. T., Wahl, T. and Vinje, M.: 1998b, 'Identification and characterisation of internal waves along the coast of Norway', *Proceedings of 27th international symposium on remote sensing of environment: information for sustainability held in Tromsø, N, 1* (ISRSE), pp. 205-208.
- Furevik, B. and Korsbakken, E.: 1998, 'Wind field retrieval from synthetic aperture radar compared with scatterometer wind field during the ERS tandem phase', *Proceedings of 27th international symposium on remote sensing of environment: information for sustainability held in Tromsø, N, 1* (ISRSE), pp. 201-204.

- IFREMER: 1996, 'Off-line wind scatterometer ERS products, user manual', C2-MUT-W-01-IF, IFREMER CERSAT.
- Janssen, P. A. E. M., Wallbrink, H., Calkoen, C. J., van Halsema, D., Oost, W. A. and Snoeij, P.: 1998, 'VIERS-1 scatterometer model', *J. Geophysical Research*, **103**, 7807-7831.
- Korsbakken, E.: 1996, 'Quantitative wind field retrievals from ERS SAR images', ESA Earth Science Division.
- Mugnier-Pollet, S., Askne, J. and Håkansson, B.: 1997, 'Retrieval of wind from ERS-1/2 SAR', *Proceedings of CEOS wind and wave validation workshop held in Noordwijk, NL*, 1 (ESA), pp. 209-214.
- Mugnier-Pollet, S.: 1998, 'Retrieval of wind speed over the Baltic Sea from Synthetic Aperture Radar', Research Report No. 182, Dept of Radio and Space Science, Chalmers University of Technology.
- Vachon, P. W., Campbell, J. W. M. and Dobson, F. W.: 1997, 'ERS and RADARSAT SAR images for wind and wave measurements', *Proceedings of CEOS wind and wave validation workshop held in Noordwijk, NL*, 1 (ESA), pp. 9-21.
- Vachon, P. W., Johannessen, J. A. and Browne, D. P.: 1995, 'ERS-1 SAR images of atmospheric gravity waves', *IEEE transactions on geoscience and remote sensing*, **33**, 1014-1025.
- Wackerman, C. C., Rufenach, C. L., Shuchman, R. A., Johannessen, J. A. and Davidson, K. L.: 1996, 'Wind vector retrieval using ERS-1 synthetic aperture radar imagery', *IEEE transactions on geoscience and remote sensing*, **34**, 1343-1352.

## Sea Ice Kinematics Using Argos Buoys and SAR Imagery

Bertil Håkansson<sup>1)</sup>, Sverre Dokken<sup>2)</sup>, and Juha Uotila<sup>3)</sup>

<sup>1)</sup> Swedish Meteorological and Hydrological Institute

<sup>2)</sup> Chalmers University of Technology

<sup>3)</sup> Finnish Institute of Marine Research

### 1. Introduction

Ice drift is a primary parameter in ice dynamics influencing ice growth/melt, ice deformation and exchange of energy and momentum between the sea and the atmosphere. It is a major obstacle for ship transport in ice infested waters. However, it is a difficult parameter to measure. In this study ice-drifters were used, transmitting position and time using the Argos-system. In addition, an algorithm was used to calculate ice drift from consecutive SAR imagery and compared with simultaneous ice drifter data. The purpose was to evaluate this particular technique in relatively small-scale surroundings, as is the case in the northern Gulf of Bothnia.

In general, free ice drift is governing the sea ice movement far from the coasts (Uotila, 2001), meaning that the ice drift is not hindered by other forces. Approaching the coast, the external forces come into the play besides those from wind and currents. In shallow areas ice drift can be reduced by bottom friction, generation of hummocks and pure appearance of physical boundaries. Pressure inducing areas can be the coast, the fast ice or at any place where the ice drift is hindered. At these places the ice drift can overcome the plasticity of ice, resulting in ice deformation i.e. ridge formation.

The data gathered during the BASIS field experiment shows that in the central areas of the Bay of Bothnia the ice drift is governed by wind forcing and friction against underlying water under influence from the Coriolis force, according to Uotila (2001). The balance of forces changes closer to the coast. Hence, drift calculations using SAR imagery, which are based on image patterns conserved between two consecutive images, will ultimately fail in areas of ice deformation. It is most likely that the image-based technique will in general be successful in areas where free ice drift occurs.

In this study the combined SAR image and drifter data is evaluated. In Section 2 the methods and are shortly introduced, followed by results and discussions focused on ice velocity variance, SAR image drift calculations and ice lead variability. Finally, a short summary of conclusions is presented.

### 2. Methods

Several Argos-drifters were deployed during the BASIS field campaign (i.e. BALTEX BASIS Data Report 1998). In addition, a few GPS-drifters were used to get high temporal resolution data of ice drift. This study however, focuses on the Argos type drifters, using meteorological satellites for positioning. In general a temporal resolution of two hours is obtained in which case the lowest period that can be resolved is about four hours, according to the Nyquist frequency. Data was treated according to general procedures for Argos drifters (Håkansson & Rahm, 1993 & Launiainen et al., 1993). In Fig. 1 some of the drifter patterns are shown. The drifters were deployed on loose ice close to the ice edge just outside the Fast Ice campus operated from the R/V Aranda. The storm event between 20 to 21 February carried the ice drifters toward Northeast, where after calm winter conditions prevailed. The Argos drifters were recovered at the end of the experiment, whereas one was left in the Bay of Bothnia up to the beginning of June 1998.

RADARSAT ScanSAR NARROW C-band imagery was obtained from Tromsø Satellite Station. It has been shown in several studies (cf. Dierking et al., 1999) that C-band is most sensitive to ice roughness and snow wetness. The data covered the main areas of the Bay of Bothnia and the Bothnian Sea of interest for the project (cf. BASIS-BALTEX Data Report 1998). RADARSAT imagery (Lundin et al., 1998) and simultaneous drifter data were found at three occasions of which the first took place during the storm event. The ice drift was exceptionally large, ice deformation severe and melting snow conditions all made image pattern recognition in the images very difficult. Hence, two occasions remained for evaluation, covering in all five drifters.

### 3. Results and discussions

#### 3.1 Ice drift and velocity variance

Typically for all ice drifters are the large-scale drift patterns, which mainly takes place along the main axis of Bay of Bothnia in a NO to SW direction (Figure 1). Slightly shorter displacements and smaller

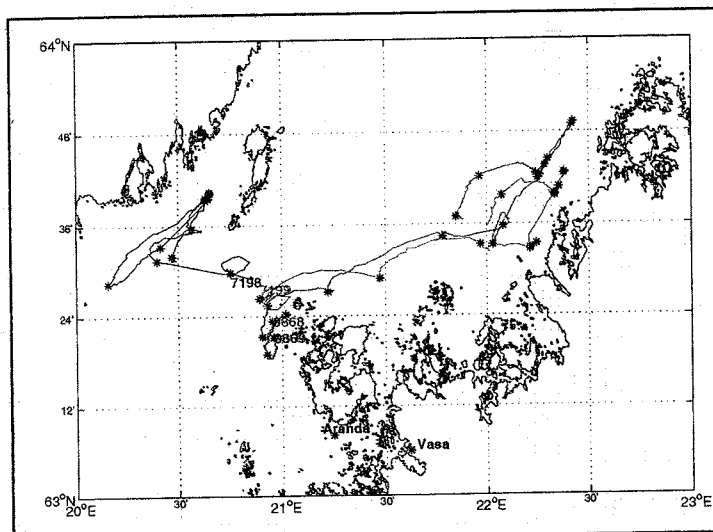


Figure 1: Drifter trajectories during the BASIS field.

Table 1: Drifter (#9868) data statistics during the period February to June 1998.

Parameter	Long-shore	Cross-shore
Mean velocity:	$0.9 \pm 15.2 \text{ cm/s}$	$-0.2 \pm 13.7 \text{ cm/s}$
Variance:	$232 \text{ (cm/s)}^2$	$188 \text{ (cm/s)}^2$
Kinetic Energy:	$197 \pm 352 \text{ (cm/s)}^2$	

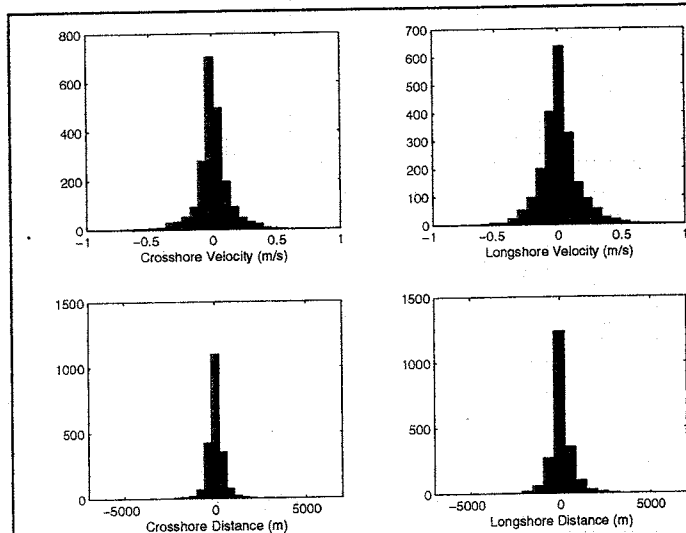


Figure 2: Histogram of velocities and distances of drifter #9868.

meters respectively.

velocities take place in the cross-shore direction compared to the long-shore (Figure 2). It is interesting to note that no one of the drifters escaped the Bay. Even the drifter in the Southwest part of the Northern Quark (Figure 1) was trapped. The mean drift velocity was also of no significance, taking into account the long lasting drifter #9868 (Table 1). Hence, contrary to what is expected no ice appears to be exported southward into the Bothnian Sea despite a weak but persistent estuarine circulation. These results are an indication that ice export from the Bay of Bothnia towards the Bothnian Sea is of minor importance in comparison to other sources and sinks in the ice mass balance, at least during the period of investigation.

The kinetic energy is an important parameter of ice drift. The kinetic energy per unit area and unit mass is given by the velocity variance. The time series of the parameter for the #9868 is presented in Figure 3. The velocity variance varies substantially and maximal values ( $\cong 4500 \text{ (cm/s)}^2$ ) were obtained during the storm event February 21 – 22. On average the velocity variance is close to  $200 \text{ (cm/s)}^2$  with a standard deviation 1.5 times larger than the mean.

Compared to Arctic conditions the Baltic Sea First Year ice does have much higher velocity variance on average. Thorndike (1986) presented data on velocity variance varying on average close to  $42 \text{ (cm/s)}^2$  in most cases. The difference between the Arctic and Baltic ice velocity variance can partly be attributed to differences in forcing mechanisms and magnitudes and partly on ice thickness, which are typically 3.3 (Zakharov, 1997) and 0.4

Assuming that a fraction ( $\kappa$ ) of the Arctic kinetic energy is balancing the Baltic sea ice kinetic energy per unit area, the following formula is obtained:

$$\rho h_B \frac{\overline{(v_B - v_B)^2}}{2} \cong \kappa \rho h_A \frac{\overline{(v_A - v_A)^2}}{2}.$$

The index A and B refer to the Baltic and Arctic sea-ice, respectively. The ice thickness is given by  $h_i$  and the ice velocity by  $v_i$ . It results in a kinetic energy per unit area ( $\kappa$ ) 60 % lower in the Baltic compared to the Arctic, assuming a constant ice density. Both wind, meso-scale ocean circulation and eddies force the sea ice drift to a larger extent in the Arctic than in the Baltic, where mainly inertial currents and sea level changes provide input to the velocity variance, beyond wind forcing.

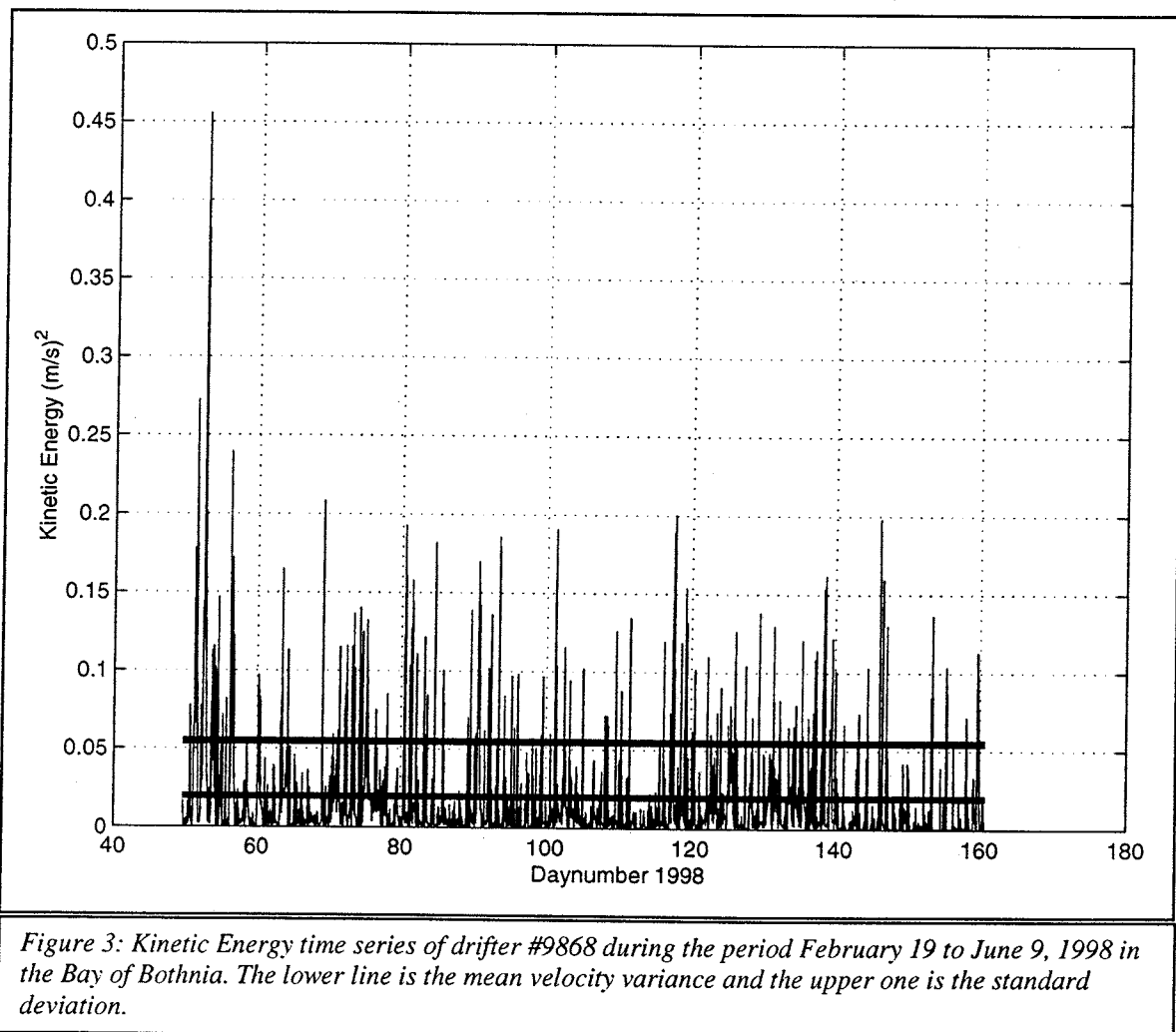


Figure 3: Kinetic Energy time series of drifter #9868 during the period February 19 to June 9, 1998 in the Bay of Bothnia. The lower line is the mean velocity variance and the upper one is the standard deviation.

### 3.2 SAR image ice drift calculations

The objective is to investigate the usefulness of SAR image data for ice kinematics in Baltic Sea ice, and in particular in the marginal ice zone. Coincident drifter observations and SAR imagery was used to evaluate velocity retrievals from consecutive images. However, the inter-comparison of drifter and image data is hampered mainly by coastlines, which inhibited buoy drift between the image acquisition intervals. This interval should be sufficiently short finding features in two successive images. The ice motion algorithm is described in Sun et al., (1995) but some minor modifications regarding the operational use of the algorithm have been added. The algorithm searches for signatures with similar backscatter and texture in two corresponding images. The retrieval accuracy is therefore

dependent on finding signatures that can be recognised between two images. The examples studied are chosen at the buoy positions furthest away from the ice edge and preferably when two images are acquired within a maximum of one-day difference. The buoys and the time intervals are divided into three groups, not possible to use, possible to use, and used. The results presented here are based on buoys #1154 and #7198 during 24-25 February, and buoys #7199, #9868, #557 and #559 from 3 - 4 March. Two methods were used; a local and a global approach (cf. Sun, 1995 & Li, 1997). In the former approach the images are divided into smaller areas around the buoy position. In the latter approach, the mean rotation and translation between two entire images are first calculated, followed by a small-scale calculation, which compensates for the deviation from the mean rotation and translation. The SAR algorithm derives approximately the same drift as indicated by the drifters for the former approach, while the global approach is shown to be less suitable close to the shore fast sea ice. The result from 3 - 4 March using buoys 7199 and 9868 is illustrated in Figure 4 and some statistics on the

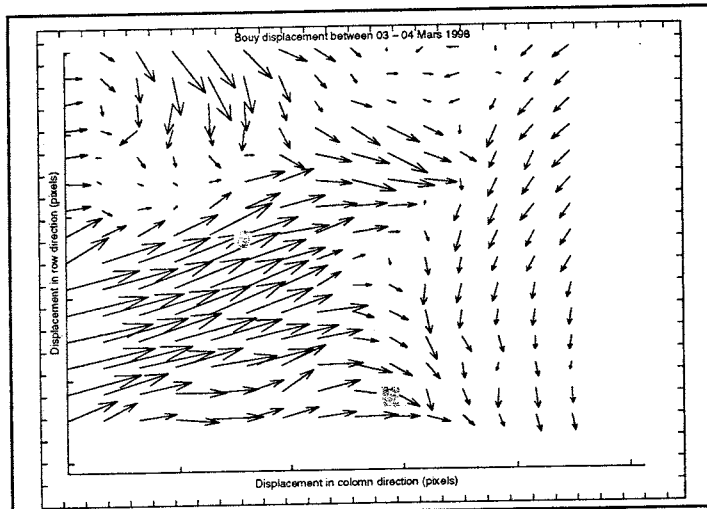


Figure 4: SAR drift algorithm plot of the area around buoy 7199 (top) and 9868 (bottom). The buoy locations at the first acquisition time (980303) are indicated with a gray rectangle. The SAR algorithm is applied on two Radarsat images from 980303 and 980304 with acquisition time around 05:00 UTC. The indications on the axis correspond to 100 pixels and North is down in the plot.

correspondence is presented in Table 2 and 3. The rms-error in drift distances between image data and the ice drifters is  $\pm 350$  meters, which is good in comparison to the accuracy of the drifter positions. Probably more data are needed to fully evaluate the SAR image ice drift, but this study provides some positive results.

The preliminary conclusion is that the SAR ice motion algorithm works for cases where there are possibilities to recognise similar features in two successive images, meaning that ice roughness patterns and snow wetness are conserved during the period of drift retrievals. It is shown in a few cases when there are short time lapses (less than 2 days) between the images and when the areas of interest are located some few kilometres inside the ice edge. Otherwise the changes in the ice surface

conditions are too fast and it is not realistically possible to recognise (even with the human eye) features in two successive SAR images. This simply indicates the need to obtain images with shorter time intervals (i.e. less than a day).

Table 2: Calculated ice drift from SAR and buoy data from the period 980303 - 980304.

Time period:	980303 - 980304				980304 - 980305
Buoy number:	7199	9868	557	559	559
SAR Distances (m):	1680	3081	914	1182	3416
Buoy Distances (m):	1000	3400	2200	900	4300
SAR direction:	W	NNW	S	S	S
Buoy direction:	WNW	W	S	S	SSW

Table 3: Statistics of differences between SAR and buoy drift.

Rms-error in drift distance:	$\pm 350$ m
Relative rms-error in distance:	0.37
Rms-error in direction:	$\pm 12^\circ$

### 3.3 Ice leads and drifter interpretation

The lead dynamics are important, since they govern the large-scale distribution of low albedo values from open water as compared to high albedo values from sea ice and determine the areas and therefore strongly influence the magnitude of heat, momentum and water exchange between the atmosphere and the ocean.

Offshore ice drift generates leads along coastlines. The width of the lead should be proportional to the offshore ice drift and the time span of the event. The drift trajectories between the March 4 and 5 show an offshore ice drift, which eventually turns toward south (cf. Figure 1). The westward drift between these two days is about the same size as the lead width on March 5. On the other hand ice should accumulate along the islands in the southern Bay of Bothnia during the southward ice drift. This is easily recognised in the image data showing that the open lead on March 4 is closed on the day after along the southern part of the Bay.

It is also of interest to note that leads in the open sea of the Bay tend to be localised perpendicular to the ice drift. During March 4 the leads are mainly oriented in the North-South direction when the main ice drift is towards West, whereas on March 5 the leads are oriented in East-West direction during ice drift towards South. It is surprising that within 24 hours the leads have changed both orientation and position in the open sea where free ice drift dominate the dynamics.

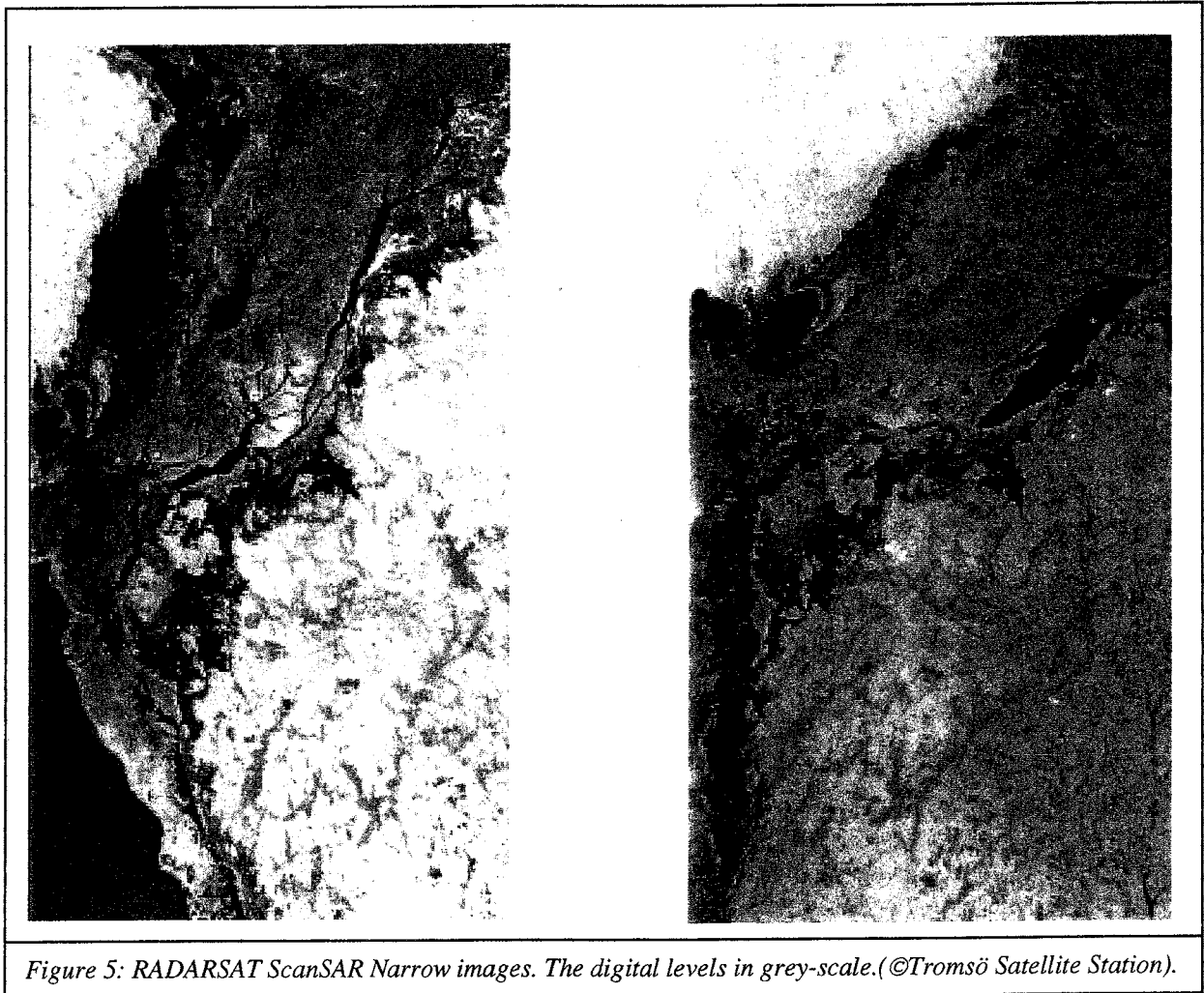


Figure 5: RADARSAT ScanSAR Narrow images. The digital levels in grey-scale. (©Tromsö Satellite Station).

#### 4. Conclusions

The remote sensing and ice drifter data gathered during the BALTEX-BASIS experiment, demonstrates how useful combined data sets can be. It provides superior information on ice kinematics, ice leads and ice concentrations of great value for coupled air-ice-sea model verification studies. The ice drifter data shows the typical velocity variance found in semi-enclosed basins with seasonal ice cover, whereas the radar image data shows closing/opening of leads and where ice deformation takes place. Consecutive radar images can also be used to derive ice velocity if roughness patterns are conserved. This requirement restricts the usefulness of the method to cases and areas where no ice deformation takes place and where snow moisture is low. On the other hand, this restriction can easily be reduced by obtaining SAR images more frequent in time, such as obtaining several images per day. The ice drifter data verify the SAR velocity estimates, even though more data is needed to obtain significant accuracy in the estimates, in particular, since we here consider thin First Year Ice. In addition, the combined data set improves interpretation and understanding of leads, which governs to a large extent the exchange processes in the air-ice-water system.

#### References

- Dierking, W., Pettersson, M. I. And J. Askne 1999. Multifrequency scatterometer measurements of Baltic Sea ice during EMAC-95. *Int. J. Remote Sensing*, Vol. 20, No. 2, 349-372.
- Håkansson, B. and L. Rahm 1993. Swedish Lagrangian current experiments. In *Gulf of Bothnia Year 1991* (Ed. J. Murthy), SMHI, R.O., No. 15, 41-54.
- Launiainen, J., Stipa, T., Grönvall, H. and T. Vihma 1993. Finnish Lagrangian current experiments. In *Gulf of Bothnia Year 1991* (Ed. J. Murthy), SMHI, R.O., No. 15, 55-66.
- Li, A. 1997. A matching method used for the estimation of sea ice motion from ERS-1/2 SAR image pairs. *Proceedings The European Symposium on Aerospace Remote Sensing, England*, 36-47.
- Lundin, M., Moberg, M., Håkansson, B. and M. Granskog 1999. Ground, air and satellite data obtained during BASIS field experiment by the SMHI. In *BALTEX-BASIS Data Report* (Ed. J. Launiainen), Int. BALTEX Secretariat Publ. No. 14, 72-87.
- Sun, Y. 1994. A new correlation technique for ice-motion analysis. *EARSeL International Journal Advances in Remote Sensing*, Vol. 3, No. 2, 57-63.
- Thorndike, A. S. 1986. Kinematics of sea ice. In *The Geophysics of Sea Ice*, Ed. N. Untersteiner, Plenum, New York, 489 - 549.
- Uotila, J. 2001. Observed and modelled sea-ice drift response to wind forcing in the northern Baltic Sea. *Tellus*, 2001, In press, reprinted in this issue.
- Zakharov, V. F. 1997. Sea ice in the climate system. *WMO/TD-No. 782*, pp 80.



Reprinted by a permission of *Tellus*.

## Observed and modelled sea-ice drift response to wind forcing in the northern Baltic Sea

J. Uotila

Finnish Institute of Marine Research,  
P.O.Box 33, FIN-00931, Helsinki, Finland.  
email: uotila@fimr.fi

### Abstract.

The wind dependence of sea-ice motion was studied on the basis of ice velocity and wind observations, and weather model output. The study area was a transition zone between open water and the ice-covered ocean in the northern Baltic Sea. In the centre of the basin the sea-ice motion was highly wind-dependent and the linear relationship between the wind and the drift velocities explained 80% of the drift's variance. On the contrary, the wind-drift dependence was low near the coast. The wind-drift coherence was significant over a broader frequency range in the central part of the basin than for the coastal drift. The ice motion was simulated by a numerical model forced with five types of wind stress and with two types of current data, and the outcome was compared with the observed buoy drift. The wind and the wind-induced surface current were the main factors driving the ice in the basin's centre, while internal ice stresses were of importance in the shear zone near the fast ice edge. The best wind forcing was achieved by applying a method dependent on atmospheric stability and ice conditions. The average air-ice drag coefficient was  $1.4 \times 10^{-3}$  with the standard deviation of  $0.2 \times 10^{-3}$ . The improvement brought about by using an accurate wind stress was comparable with that achieved by raising the model grid resolution from 18 km to 5 km.

## 1. Introduction

The ice-covered sea surface forms a complex boundary between the atmosphere and the underlying ocean. The sea ice strongly modifies the air-sea energy exchange, especially in winter when relatively cold air lies over a warm ocean. In these conditions, even small open water fractions are of importance. Accordingly, it is vital to know the sea-ice condition reliably when estimating the regional energy balance of ice-covered oceans. The wind is usually the most important forcing factor for the sea-ice drift, especially when the ice concentration is low. In high concentration conditions, usually near the fast-ice zone, internal ice stresses may play a significant role in modifying the sea-ice dynamics. In addition, sea-surface currents affect the motion of sea ice.

Several wind-drift studies have been published in recent years, for example by Kottmeier and Sellmann (1996), Vihma et al. (1996), Geiger et al. (1998), Thomas (1999) and Uotila et al. (2000) on the basis of buoy observations from the Arctic or Antarctic regions. The wind forcing applied in the analyses has usually been the output of large-scale weather models, and uncertainties and the differences between the applied models may be significant. Thus it is important to be aware of the possible errors in the wind forcing and the parameterization of the momentum flux when modelling sea-ice velocities.

In the Baltic Sea, Leppäranta (1981) investigated the motion and mechanics of pack ice in the Bothnian Bay, and more recently Leppäranta et al. (1998) compared the ice velocity fields derived from satellite imagery with modelled ones. Leppäranta and Omstedt (1990) modelled the drift of a ship in the Bothnian Bay with a coupled ice-ocean model, while Gustafsson et al. (1998) presented a coupled atmosphere-ice-ocean model for the Baltic Sea.

Highly accurate forecasts of ice conditions are important for the northern Baltic Sea, which is frequently navigated by shipping in winter. Accordingly, accurate wind forcing together with a well-suited dynamic ice model are necessary when forecasting the ice conditions. In the Baltic Sea the meteorological observation network is much denser than in the Arctic and especially in the Antarctic, providing a good opportunity to compare the effect of the wind data on the sea-ice modelling results.

In February-March 1998, a comprehensive field experiment was carried out in the northern Baltic Sea. The overall objective of this Baltic Air-Sea-Ice Study (BASIS) was to create and analyze an experimental data set for the optimization and verification of coupled atmosphere-ice-ocean models (Launiainen, 1999). BASIS is a subprogram of the Baltic Sea Experiment (GEWEX/BALTEX). One of the specific objectives covers the investigation of forcing at air-ice and ice-water boundaries, the topic which is addressed in this paper. Another specific objective of BASIS is the modelling of sea-ice dynamics. In the study, this was partly done by simulating the ice drift during the main field experiment and comparing the model outcome with the ice drift observed by buoys. The BASIS data set provided a very good observational base from which to study the wind-drift relationship and compare that with the modelling results.

In section 2 the data applied in the study is introduced. In section 3 the relationship between the measured drift and the wind is investigated. In section 4 a numerical model for the sea ice velocity is presented and the modelled velocities are compared with the observed ones. Finally, in section 5 some conclusions are drawn from the analysis.

## 2. Data

### 2.1. Ice conditions, concentration and thickness

The study area was located at the transition zone between the open ocean in the Bothnian Sea and the ice-covered ocean in the Bothnian Bay (Figure 1). The strait that connects these two basins is relatively shallow and narrow with a complex archipelago. Weak advective exchange can be expected through the strait between the basins (see for example Omstedt, 1990). Near the coasts the land-fast ice connected the archipelago to the main land, while there were drifting pack ice in the central part. The pack ice ridged and rafted against the fast ice mainly in the eastern side and central part, while regions of low ice concentration were opened up in the western side of the basin. The fast-ice thickness was 20-35 cm and the thickness of undeformed pack ice varied from 10 to 40 cm. The complex topography and many ice-types requires a sufficiently high resolution model to resolve the ice motion. On the other hand, the commonly applied ice rheology parameterization follow the continuum approximation of Hibler (1979), which requires many ice floes in a single gridcell. The large ice floes in the Baltic Sea are commonly 1-3 km in diameter (Leppäranta et al., 1998). The BASIS buoys were deployed on ice floes of around 1 km in diameter, which was found to be apparently more than the common size of the ice floes in the region. With the information of ice floe sizes during the BASIS experiment and results of Zhang et al. (1999), it seems that the continuum approximation of Hibler (1979) is not violated by applying the grid size of 5 km. The grid size is still one order of magnitude greater than ordinary floe size.

The ice concentration and thickness were derived from the daily SMHI and FIMR ice charts. Although the overall agreement between the analyses was quite good, the ice thicknesses in particular seemed to have a systematic difference. Occasionally the ice concentrations differed a lot, for example when buoy 5893 was surrounded by open water or a new ice region. In these cases the RADARSAT satellite images were studied. Additionally, mean values of the ice concentration and thickness from the two institutes were applied in such cases. The resolution of the FIMR ice concentration fields was 18.5 km, and that of the SMHI fields was 16.5 km.

### 2.2. Sea-ice velocity

Between 18 and 22 February 1998, six drifting buoys were deployed in the Gulf of Bothnia, five on sea ice floes and one in open water. Two of the buoys were equipped with the Global Positioning System (GPS) receivers, otherwise buoy positions were determined by the CLS Argos system. The accuracy of the GPS was of the order of 100 m, while the accuracy of CLS Argos was within the range of 100 to 700 m, typically 200 metres. Another buoy with a 4 m high meteorological mast was deployed on fast ice on 18 February, but the ice broke up on 24 February and the buoy began to drift. Locations of this buoy were also included in the study. The trajectories of the drifters during the experiment are presented in Figure 1.

The buoy positions determined by Argos were interpolated at three-hourly intervals, while GPS positions were interpolated hourly. The higher accuracy of the GPS locations made possible a reliable interpolation of the positions more frequently. The buoy positions were interpolated with a method known as 'Kriging', as described by Hansen and Herman (1989) and Hansen and Poulain (1996), who applied the method for open ocean drifters. Uotila et al. (2000) adapted the method to sea ice drifters in the Weddell Sea. One benefit of the method is that it provides individual error estimates for the quantity at each interpolated point. Knowledge of the accuracy of interpolated velocities e.g. due to gaps in the original non-interpolated time series is thus obtained. The sea ice velocities were then calculated from the interpolated positions.

One GPS-drifter and one Argos-drifter functioned for only a few days, and the velocity time series from these were considered to be too short for the most part of the study. One GPS-drifter (Argos ID 5893) functioned between 19 and 26 February 1998, and produced high-quality hourly locations. The two drifters on ice floes with Argos positioning, 7199 and 9868, functioned from 18 February until 5 March and 20 May 1998, respectively. These buoys drifted near GPS-drifter 5893, but closer to the fast ice. The open water drifter (7198) functioned until 16 March 1998, and gave some approximate information about the surface currents during the experiment. There was no drogue installed on 7198, and thus its motion did not represent the pure ocean current: the windage, i.e. the direct effect of wind on the buoy hull, and wave effects may have been significant. However the mean ratio between the 7198 speed and the geostrophic wind speed was 1.2%, which is about the same than observed speed ratios for drifters with a drogue at a depth of 5 m in the Bothnian Sea in November, 1991 (Uotila et al., 1995). The drift of the buoys was compared with sea level data in section 4 to see how the drift followed the barotropic ocean currents. As a whole the combined data from the four buoys 5893, 7198, 7199 and 9868 was very suitable for studying the wind-drift relationship and the coastal effects modifying the relationship, and for verification of the dynamic sea ice model.

### 2.3. Wind speed and direction

During the expedition, observations were available from several coastal meteorological stations (Figure 1). The wind observations were interpolated to the buoy sites. First, the wind at the 10 m level was estimated from the observations made at various heights. The 10 m wind components were then interpolated to the buoy sites, weighting each observation with its inverse distance from the buoy positions. Four meteorological stations were used in the interpolation: Kokkola, Umeå, the meteorological mast of Uppsala University, and buoy 3335 (see Figure 1).

In addition to the coastal meteorological data, fields from an operational mesoscale analysis system (MESAN) were obtained from the Swedish Meteorological and Hydrological Institute (SMHI). The MESAN fields were estimated by applying meteorological fields from the High Resolution Limited Area Model (HIRLAM) as first guesses and then verifying the fields with surface observations and satellite data (Häggmark et al., 2000). The MESAN fields were calculated at every third hour with a resolution of 11 km in both meridional and zonal directions. The 10 m wind and the geostrophic wind from the atmospheric pressure gradient were calculated at the buoy sites from the MESAN fields. The gradient components were derived from atmospheric pressure subfields of four grid point values around the buoy locations. The observations of the BASIS stations were not included in MESAN, and therefore winds interpolated to the buoy sites from these two sources of data were mutually independent. The weather conditions during the BASIS field expedition were rather variable because of passing cyclones, which crossed the research area from west to east. The 10-m wind time series in Figure 2a is characterized by varying speeds of up to 20 m/s following largely the pattern of the geostrophic wind. Westerly winds prevailed, but the wind turned to blow from the north after the cyclones had passed eastwards over the area on 24 February, and on 1 and 5 March 1998 (Figure 2b). Before 5 March cyclones crossed to the north of the research area, but on that date a cyclone passed to the south of the area, causing winds to blow from the east and south. The weather was generally mild during the expedition with large temperature fluctuations (Figure 2c). During the cold air outbreak on 24 February, however, the air temperature rapidly decreased from around 0°C to almost -15°C. Following this, the temperature returned to its initial level with the prevalence of westerly winds. On 28 February a cyclone was centred just north of the research site over the Bothnian Bay, causing cold air

originating in the north to flow over the area. Due to this, the temperature gradually decreased until 2 March.

The MESAN 10 m wind was about 42% of the geostrophic wind, turning on average  $37^\circ$  left of it. The BASIS wind was 48% of the geostrophic wind, deviating on average  $33^\circ$  left. The difference in speed ratio can be explained by the fact that the MESAN wind represented average values over a grid square, while the BASIS wind was derived from point observations. The roughness of a grid square that was partly over land, included the higher roughness of the land areas, and further reduced the surface wind from the geostrophic wind speed. To verify this, the speed ratio and turning between the MESAN surface and geostrophic wind were calculated for a point in the middle of the Bothnian Sea, i.e. at  $62^\circ\text{N}$ .,  $20^\circ\text{E}$ . The speed ratio now increased to 53%.

The agreement between the BASIS and MESAN winds was fairly good. The correlation coefficient between the vector time series of the winds was 0.95 (between 0.92 and 0.97 at the 95% confidence level). The BASIS and the MESAN winds correlated with the geostrophic wind with coefficients of 0.76 and 0.73, respectively. In addition, daily HIRLAM analyses (at 12 UTC) and forecasts every 6 hour from the Finnish Meteorological Institute (FMI) were utilized when the numerical ice model runs were made in section 4. The HIRLAM wind was originally input to the Finnish Institute of Marine Research (FIMR) operational ice model when forecasting ice conditions in the Baltic Sea.

### 3. Wind-drift relationship

The drift speed of the buoys followed the general weather patterns, although internal ice stress close to the coastline reduced the wind-drift dependence. Accordingly, it is important to include the ice concentration and thickness into the analysis. A closer look at the drift of the three buoys is presented in Figure 3. The buoys drifted mostly in the same ice field and the differences in their motion were due to the differences in the ice movement near the coast and the open ocean. The drift period was divided into subperiods characterized by the various wind and ice conditions. During the first days of the drift, between 19 and 23 February, the buoys drifted northeast, forced by the winds from the southwest (Figures 4 and 2). In Figure 4a, time series of the sea-ice drift speed observed by the buoys are presented. The speed varied a lot, up to a maximum of 0.7 m/s. The ice concentration at the buoy sites was relatively low (see Figure 4c). In addition, some periodic motion near the inertial frequency occurred, a fact especially evident for buoy 5893, which drifted furthest from the coast. This motion could not be explained by the wind and was probably connected with the sea surface currents (see section 4.1). Buoys that drifted near the coast (7199, 9868) moved in some cases at a higher speed than the buoy away from the coast (5893).

Between 23 and 25 February, the two buoys nearest the coast (i.e. 7199 and 9868) were stuck close to the fast ice border (Figure 3). The ice concentration around the third buoy (5893) remained low, (see Figure 4c) and it drifted back to the southwest. At the time the wind blew from the north. On 25 and 26 February, the wind turned again to blow from the southwest, and the buoys drifted northeast. During these days, the ice concentration around 5893 increased from 50% to compact, and the drifter was destroyed. The two remaining buoys were stuck near the coast, and responded only weakly to the varying winds until 4 March, when seaward winds from the east prevailed and the ice motion was directed towards the open ocean.

### 3.1. Linear dependence between the wind and the drift

By assuming a linear dependence between the complex wind vector  $\mathbf{u}_a$  and the drift vector  $\mathbf{u}_i$

$$\mathbf{u}_i = s e^{i\varphi} \mathbf{u}_a + \mathbf{C}, \quad (1)$$

the scaling factor  $s$ , turning angle  $\varphi$ , and additive term  $\mathbf{C}$  were estimated. In (1)  $i = \sqrt{-1}$  is the imaginary unit. The linear relationship is physically valid when a thin ice floe has steady-state free drift (see for example Thorndike and Colony, (1982)). Temporal changes of these quantities are presented in Figure 5 for the buoys 5893, 7199, 9868, and reflect the temporal changes in wind, currents and ice conditions, while Table 1 summarises estimates of  $s$ ,  $\varphi$  and  $\mathbf{C}$ . The explainability  $R^2$  gives the fraction of the variance of the ice velocity accounted for by the regression model (1).

The highest  $R^2$  and the highest  $s$  in Table 1 were obtained for 5893, which drifted mostly in low-concentration ice conditions. The open water drifter 7198 had the second highest  $s$ , while the remaining values were on average less than 2%. As discussed in section 2.2, the high  $s$  for 7198 may have resulted from the windage effect and waves. The high  $s$  for 5893 also gives the impression that the wind-dependent surface currents and waves increased the ratio in the central basin, but did not affect the ice motion so much near the coast (compare to the  $s$  of 7199 and 9868). In addition, the  $\mathbf{C}$  for 5893 was relatively high compared with those of the other drifters in Table 1. The turning angle  $\varphi$  of the ice drifters was about  $25^\circ$  and that of the open water drifter was  $30^\circ$ . These turning angles are comparable with the sea-ice drift in the summer in the Weddell Sea (Martinson and Wamser, 1990; Uotila et al., 2000), with the ice drift in the Bothnian Bay (Leppäranta and Omstedt, 1990), and with the open water drift in the Bothnian Sea (Uotila et al., 1995).

In Figure 5 the time evolution of the linear model parameters is illustrated. The scaling factors for the three buoys were highest on 19 and 20 February, almost 6%. The drift velocity was turned about  $30^\circ$  to the right of the surface wind and the linear relationship explained the ice motion well. During the first two days the wind-drift correlation was quite high. After that, as the buoys moved closer to the coast and the pack ice was pushed against the fast ice, the scaling factor and the correlation decreased, and the deviation of the turning angle increased.

### 3.2. Time-frequency analysis

The vector coherence and phase were calculated from the drifter velocities and the BASIS wind observations following the method given by Gonella (1972). The method produces the correlations and spectral relations for the clockwise and counterclockwise components between two time series. The vector coherence and the phase between the wind and the drift are presented in Figure 6. The wind-drift coherence was lower for the buoy that drifted near the coast (7199), and for the open water drifter (7198) than for the most remote buoy from the coast (5893). The coherence for 5893 was significant for the clockwise periods longer than 7 hours, i.e.  $-3.4 \dots 0$  cycles per day (cpd), but that for 7199 was significant only between periods of 16 and 30 hours ( $-1.5 \dots -0.8$  cpd). Thus, the wind-drift coherence near the coast was decreased in both at long and the short period regimes. The open water drift was coherent with the wind at periods longer than 30 hours and at periods near the inertial motion, i.e. between 11 and 13 hours ( $\sim -1.8$  cpd). The coherence between the counterclockwise wind and drift components was apparent only at the longest periods of 5893 and 7198, and the phase deviated more than at the clockwise frequencies. The coherence of 5893 is very similar to that observed by Leppäranta and Omstedt (1990). They found that low frequencies were dominated by the wind, whereas high frequencies were dominated by the current. They also observed very high ice-current coherence and a low peak in the wind-drift coherence at about  $-7$  cpd ( $\sim 3$  h). A similar low peak is apparent in the coherence for 5893 (see Figure 6).

For the period, the clockwise coherence between the wind and the drift was higher than for the counterclockwise component (Figure 6). The clockwise components of the wind and the drift had more energy, especially at periods between 20 and 48 hours, than for the corresponding counterclockwise periods. The energy of the counterclockwise component of the wind was high at periods longer than two days, but then the drift's response to wind was probably restricted by the basin's size and form. Between 23 and 24 February, the counterclockwise wind component had high energy when the surface wind turned from south to west and then to north (Figure 2b). However, the drift's response to this was quite low, because at that time buoy 5893 drifted in quite compact pack ice, near the shear zone, which decreased the wind-drift response. The lower wind-drift coherence of the counterclockwise component resulted from the wind and ice conditions and basin's dimensions.

#### 4. Drift modelling

We applied a numerical model for the ice velocity, ice concentration, and thickness to simulate the drift of the buoys. The basic equations of the dynamic ice model are the momentum and mass balance equations (Hibler, 1979; Leppäranta, 1981).

$$\rho h(d_t \mathbf{u}_i + f \mathbf{u}_i) = \tau_a + \tau_w + \nabla \cdot \boldsymbol{\sigma} + \mathbf{F} \quad (2a)$$

$$\partial m / \partial t = -\nabla \cdot (m \mathbf{u}_i) + \Phi \quad (2b)$$

$$m = \rho h A = \rho (h_l + h_r) A \quad (2c)$$

In (2)  $\rho$  is the ice density,  $h$  is the mean ice thickness,  $\mathbf{u}_i$  is the ice velocity vector,  $f$  is the Coriolis parameter,  $\tau_a$  and  $\tau_w$  are the air-ice and ice-water stresses,  $\nabla \cdot \boldsymbol{\sigma}$  is the force due to the gradients in the internal ice stress, and  $\mathbf{F}$  is the gravitational force due to the sea surface tilt. In addition,  $m$  is the ice mass per unit area,  $\Phi$  is the thermodynamic ice growth rate,  $A$  is the ice concentration, and  $h_l$  and  $h_r$  represent the level and the ridged ice thicknesses. Boldface characters represent vectors, and  $d_t$  denotes the total derivative operator with respect to time. Here  $i = \sqrt{-1}$  is the imaginary unit and (two-dimensional) vectors with magnitude  $|\mathbf{X}|$  and direction  $\delta$  have the notation  $\mathbf{X} = |\mathbf{X}|e^{i\delta}$ .

The drag terms are parameterized with a quadratic formulation

$$\tau_a = \rho_a C_a |\mathbf{u}_a| \mathbf{u}_a = \rho_a C_g e^{i\phi} |\mathbf{u}_g| \mathbf{u}_g \quad (3a)$$

$$\tau_w = \rho_w C_w e^{i\xi} |\mathbf{u}_w - \mathbf{u}_i| (\mathbf{u}_w - \mathbf{u}_i), \quad (3b)$$

where  $\mathbf{u}_a$  and  $\mathbf{u}_g$  are the surface wind and geostrophic wind velocities, respectively. In (3b)  $\mathbf{u}_w$  is the current velocity beneath the ice-water boundary.  $C_a$ ,  $C_g$ , and  $C_w$  are the drag coefficients with respect to the surface wind, geostrophic wind, and ocean current beneath the ice-water boundary, respectively;  $\phi$  is the turning angle in the atmospheric boundary layer and  $\xi$  is that in the oceanic boundary layer.

We applied two different versions of the numerical ice models in our analysis. The first version was the ice model for the Baltic Sea by Leppäranta and Zhang (1992), which is in operational use in the Finnish Ice Service of FIMR. The model has a spatial grid resolution of 18.5 km, and its time step is 6 hours. The internal ice stress is parameterized following the viscous-plastic rheology of Hibler (1979). The second version was introduced by Zhang et al. (1999), having a grid resolution of 5 km, a time step of 15 minutes, and a more realistic ice rheology with a truncated elliptical yield curve (see Hibler and Schulson, 1997) and more effective calculation routines proposed by Zhang and Hibler, (1997). The truncated elliptical yield curve is a modification of the viscous-plastic elliptical yield curve that eliminates the

tensile stress, which is physically realistic at the geophysical scale (for more details, see, for example, Geiger et al., 1998). The FIMR operational ice model set the velocity of fast-ice to zero and ice concentration to 1. On the contrary, the model of Zhang et al., (1999) has a boundary condition, where the ice velocity towards the boundary is set to zero, otherwise the velocity is the average value of the velocities of adjacent pack ice points. At the ice/water boundary Zhang et al., (1999) treated the ice velocity correspondingly by setting the free drift velocity if directed away from the pack ice interior.

The ice strength parameter  $P^*$  was set to  $1.5 \times 10^4 \text{Nm}^{-2}$ , which was considered to be the most representative for the ice edge zone in the Baltic Sea (Zhang Z., personal communication, 1999). Additionally, the ice model was run with several  $P^*$ s between  $1.0 \times 10^4 \text{Nm}^{-2}$  and  $2.0 \times 10^4 \text{Nm}^{-2}$ , but this did not change the outcome significantly.

#### 4.1. Simulations

With the aid of the three different wind data sets, i.e. HIRLAM, MESAN, and the BASIS observations, the significance of the atmospheric forcing on sea-ice modelling was studied. The sea-ice velocities were simulated and then compared with the buoy observed drift.

Simulation cases:

1. Linear dependence (1) between the wind and the drift using the BASIS wind and the regression parameters of Table 1.
2. Routine forecast, with the operational FIMR ice model forced by HIRLAM winds. The forcing parameters were:  $C_{a10} = 1.8 \times 10^{-3}$ ,  $C_w = 3.5 \times 10^{-3}$  and  $\xi = 18^\circ$ .  $\mathbf{u}_w$  was set to zero. These values were applied in operational model runs.
3. Same as case 2, but with the geostrophic winds derived from the MESAN air pressure fields. Atmospheric forcing parameters were:  $C_g = 3 \times 10^{-4}$  and  $\phi = 30^\circ$ . These values were obtained by fitting the  $\mathbf{u}_a$  of the drifters and the  $\mathbf{u}_g$  of MESAN according to (3a) in the least squares sense.
4. Same as case 2, but with the 10 m winds derived from the MESAN fields.
5. Same as case 2, but with the BASIS winds.
6. Same as case 5, but  $\tau_a$  was calculated by including the stability effects (air temperatures at two levels), and the effects of ice floes (ice concentration and thickness).
7. Same as case 6, but the velocity of the open water buoy 7198 was substituted for  $\mathbf{u}_w$  in (3b) to estimate the  $\tau_w$ .

The atmospheric momentum flux was estimated according to (3a), and in cases 2 to 5  $C_a$  was assumed to be a constant. In cases 6 and 7,  $C_a$  was not constant and depended on the stability of the atmospheric boundary layer and on the form drag due to ice floe edges (which can be estimated knowing the ice concentration and ice and snow thicknesses) following Uotila et al. (2000). In cases 6 and 7 the geometrical roughness of the drifting ice floes was estimated to be 5 cm, resulting in a  $C_{aN10}$  of  $1.46 \times 10^{-3}$  (Banke et al., 1980). The atmospheric boundary layer was usually stably stratified, which decreased the mean  $C_{a10}$  to  $1.3 \times 10^{-3}$ . The stability information was obtained from the weather mast measurements at the Aranda site. The effect of ice floe edges increased the  $C_{a10}$  of 5893 and 9868 to about  $1.4 \times 10^{-3}$ . This effect may still be underestimated because of the omission of narrow leads and open water areas smaller than the resolution of the initial ice concentration fields.



The momentum flux time series in the cases 2 to 6 at the 5893 location are presented in Figure 7. Because the momentum flux depends on the square of the wind speed, the deviation between the cases is especially large in high wind conditions. Case 5 seems to overestimate  $\tau_a$  compared to the stability-dependent case 6. The MESAN-winds-based estimate (case 4) follows case 5 quite well, as would be expected from the high correlation between the BASIS and MESAN winds (see section 2.3). Case 3 gives quite satisfactory estimates, but also deviates a lot from other estimates, as for example on 23 and 24 February. Case 2 has difficulties in following the other cases. For example, on 21 and 24 February the high wind conditions were not forecast by HIRLAM, resulting in too low  $\tau_a$  estimates on these days.

Magnitudes of complex vector correlation coefficients (Kundu, 1976) and average velocity differences for the simulation cases are presented in Table 2 for the three buoys. Kundu (1976) defined the complex vector correlation coefficient as a normalized inner product  $\langle w_1 w_2^* \rangle / (\langle w_1 w_1^* \rangle \langle w_2 w_2^* \rangle)^{1/2}$  between two complex vector time series  $w_1$  and  $w_2$ . Here the \* denotes the complex conjugate and the  $\langle \rangle$  represents an ensemble average. For the 18 km ice model only simulations 2 and 6 are presented in Table 2, marked as o2 and o6, because the mutual differences with the remaining cases were about the same as with the 5 km ice model.

The drift of buoy 5893 was highly wind-dependent with a correlation of 0.9. When the 5893 drift was modelled with the 18 km model (simulation o2 in Table 2), the correlation dropped to 0.5, and  $\overline{\Delta V}$  between the modelled and observed velocities doubled. In this simulation the wind was underestimated, as was shown in Figure 7. Additionally, the coarse grid of 18 km and the time step of 6 hours were not fine enough to simulate the ice motion, and the sea surface currents were excluded. Simulation 2 with the 5 km model increased the correlation from 0.5 to 0.7, which is about as much as the increase of correlation by applying the 18 km model with the most correct wind forcing in simulation o6. Between simulations o6 and 6 the correlation increases from 0.7 to 0.9, which is (again) about the same as the increase achieved using the best wind forcing in simulation 6 compared to simulation 2. The velocity differences between the observed and modelled velocities  $\overline{\Delta V}$  decreased by  $0.03 \text{ ms}^{-1}$  and by  $0.02 \text{ ms}^{-1}$ : compare simulations o2 and 2, and simulations o6 and 6, as the effect of the grid resolution increase. The enhanced wind forcing reduced  $\overline{\Delta V}$  at least as much as the finer grid. The differences between simulations o2 and o6, and simulations 2 and 6 were  $0.05 \text{ ms}^{-1}$  and  $0.03 \text{ ms}^{-1}$ , respectively.

In simulation 3 the modelled velocity of buoy 5893 correlated more with the observations than in simulation 2, because the time step between the MESAN analyses was 3 hours and the MESAN analysis fields provided better forcing than the operational HIRLAM analyses and forecasts. There were no great differences between simulation 3 based on  $u_g$ , and simulations 4 and 5, based on MESAN and BASIS surface winds. In simulation 6, the correlation increased practically to the same level as in simulation 1. This is expected to be the case, because the BASIS winds were utilized in both simulations 1 and 6. The relationship between the drift and the wind was close to linear, which is satisfied by simulation 1 and by the ice model. In addition, the parameters (scaling factor, turning angle and additive term) of simulation case 1 were statistically optimized for each drifter, which explains the relatively high correlation and small  $\overline{\Delta V}$  when compared to those of the numerical ice model.

The probability that the correlation increased between simulation 5 ( $C_a$  was constant) and simulation 6 ( $C_a$  was not constant) was 96%. Thus a  $C_a$  depending on stability and ice conditions produces better coherence with the observed drift of 5893. However,  $\overline{\Delta V}$  still remained almost as high as in simulation 2. This seemed to be due to the lack of the surface currents, because  $\overline{\Delta V}$  in simulation 7 was about the same as in the simulation 1.

In simulations 2 to 6  $u_w$  was set to zero, because no reliable current estimates were available for the analysis. The operational ice forecasts of FIMR were made with the same assumption.

If the real  $\mathbf{u}_w$  had been observed and had applied in the simulations, the differences between simulated  $\mathbf{u}_i$  with various  $\tau_a$  would have been smaller because  $\mathbf{u}_i$  would have followed more  $\mathbf{u}_w$ . Therefore the comparisons by assuming the zero  $\mathbf{u}_w$  produce greater differences between simulated ice velocities than the simulations with varying  $\mathbf{u}_w$ . The significance of  $\mathbf{u}_w$  was demonstrated in simulation case 7, where the velocity of 7198 was used as a crude estimate. This case is presented for buoy 5893, because the inclusion of  $\mathbf{u}_w$  only improved the modelled motion of this drifter.

The undrogued drift of 7198 and the drift of 5893 were compared with the sea level fluctuations in the Bothnian Bay. The hourly time series from Pietarsaari and Raahe stations (both at the Finnish coast) were averaged to provide the mean sea level in the Bothnian Bay and the resulting time series was filtered with 24 hours Gaussian filter. The time difference of the filtered sea level time series was then compared with the buoy velocities, which were divided (i.e. rotated  $50^\circ$  clockwise from the north) to the along coast and perpendicular to the coast components.

The correlations between the sea level fluctuations and the along coast components of the buoy velocities were calculated. The 7198 and 5893 along coast components and the sea level time difference correlated with the coefficients of 0.9. The high correlation reveals the high significance of the ocean current on the sea-ice motion in the central part of the basin. In addition, the high correlation between the open water drifter and the sea level fluctuations indicate that the undrogued open water drift at least roughly followed the sea surface current. The buoy velocities were also compared with the sea level gradient between the Bothnian Bay and the Bothnian Sea, but the resulted correlation coefficients were less than 0.6. The importance of the sea surface current for the 5893 drift is illustrated in Figure 8, where the difference between simulations 6 and 7 is evident before 21 February and on 24 and 25 February. The inclusion of the current apparently improved the modelled speed. On 25 February the buoy speed was too high in simulation 7 and the velocity of 7198 no longer represented the current velocity of the region.

The difference between the velocity directions of simulations 6 and 7 (Figure 8b) was not as apparent as that between the magnitudes. This may follow from the guiding effect of the basin's coast and the wind, when both the wind-dependent ice motion and the currents were forced to be in the same direction. There were still large deviations between the observed and modelled directions on 21 and 22 February, when the drift magnitude was weak. The observed rotational cycles lasted about 12 hours, had a radius of about 750 m (see Figure 3, the circle of 5893 on 21 February) and were probably inertial oscillations. The theoretical radius of the inertial circle is  $u_i/f$ . For a speed of 0.1 m/s it is less than 800 m in this area, which is below the resolution of the 5 km ice model. The buoy motion of 7199 and 9868 was also simulated by including the 7198 velocities as the current estimates, but this did not improve the modelled velocities. In addition, the correlations between the along coast velocities of 7199 and 9868 and the sea level fluctuations remained below 0.5.

Simulation 1 did not explain the drift near the coastline (buoys 9868 and 7199) as well as in the central basin (buoy 5893, Table 2). The 18 km model was not able to simulate the ice motion near the coastline because of its coarse grid. The correlation between the 18 km model and the observations was for 9868 0.5. The correlation was even worse for 7199 and was therefore not included in Table 2. The simulations of 7199 and 9868 are much more realistic with the 5 km model. By using any wind forcing from cases 2 to 6, the simulated velocities correlate equally well or better with the observations compared with simulation 1. When simulating 9868 drift, simulations 5 and 6, based on the BASIS wind, correlated better with the observed drift than simulations 2 to 4, based on HIRLAM or MESAN fields. By contrast, the differences between  $\overline{\Delta V}$  in the corresponding simulations for 9868 were small. For 7199, no

significant differences in correlation or  $\overline{\Delta V}$  between the simulations were found.

Near the coast the initial fields of the ice concentration and thickness had more influence than the wind field. The initial ice field information resolution was about 18 km, and was not able to separate the narrow leads and channels of low ice concentration where the buoys may have been drifting at a relatively high speed. In some cases such conditions were identified from RADARSAT images (see section 2.1). Thus the best correlations achieved with the numerical model were about 0.8 and 0.7 for 9868 and 7199, respectively. In the central basin, the wind forcing and the wind-induced surface currents had more influence on ice motion, and the numerical model correlated with observations with a coefficient of 0.9.

In Figure 9 the dependence between the simulated and observed sea ice speeds is presented. The free drift simulation was optimized for each buoy separately and provided the best linear fit between the wind and the drift in the least squares sense. Accordingly, the linear model overestimated low observed speeds and underestimated high observed ones (see Figure 9a). When the 18 km model was applied, the coastal fast-ice zone caused the low modelled speed to be roughly as small as that observed, but the deviation was very high (Figure 9b). In particular, the simulated speed was often zero, while the observed speed was high, which was due to the coarse resolution of the model near the fast ice zone. The situation improved when the ice model resolution was increased to 5 km (Figure 9c). There were cases when the ice model resulted in too high or too low speeds because of erroneous wind forecasts, and the modelled speed approached that observed by using the most sophisticated wind forcing of simulation 6 and the surface current estimate of simulation 7 (Figure 9d). Finally, there remained cases in which the ice condition information was incorrect due to the coarse input fields, resulting in lower modelled speeds than those observed.

## 5. Conclusions

The ice motion was primarily driven by the wind and the changing wind directions, and the ice mainly drifted along-shore or seaward. When the wind forced ice towards the fast ice zone, the pack ice moved slowly or was stuck near the coast. The internal ice stress became important and the motion of the buoys in the shear zone was only explained by the high-resolution numerical ice model including more realistic ice rheology. In moving pack ice, where the ice concentration was low, the ice motion was well explained by assuming a linear relationship between the wind and the drift. This is a physically valid relationship when thin ice drifts freely in steady-state conditions.

Occasionally the buoys moved at a relatively high speed near the coast, although the ice concentration derived from the ice charts was high. The modelled ice speeds were too low due to the high concentration of the input fields. In these cases it seemed that the buoys drifted in leads of low ice concentration. These openings were too narrow to be seen in the initial ice condition fields and the buoy drift did not represent the average ice motion in a model grid square.

The drifting ice responded most apparently to the wind at periods longer than 7 hours. Near the fast ice the wind-drift coherence was significant over a narrower frequency range than further away from the coast. In addition, the kinetic energy of the ice motion was highest at periods of about one to two days, because the dimensions of the basin restricted the drift at longer periods. The open water drifter velocity was coherent with the wind at periods longer than 30 hours, but also the periods near the inertial frequency. In addition, one ice buoy displayed inertial circles when the wind speed and the ice concentration were small. The radius of the circles was below the resolution of the 5 km ice model, which did not resolve the motion.

The significance of the sea surface currents on the open pack ice drift was apparently revealed

by the sea level fluctuations. The sea level time difference in the Bothnian Bay had the highest correlation with the buoy drift, while the sea level gradient between the Bothnian Sea and Bothnian Bay corresponded to the buoy speeds only during the strongest in/outflow events. The weak similarity of the sea level gradient and the observed buoy motion seem to support the conclusion that the water exchange between the basins was relatively small during the study period. However, the buoy trajectories reveal that the ice drifted from the northern Bothnian Sea to the Bothnian Bay thus transporting heat between the basins.

The scaling factor between the ice and the wind was relatively high in the centre of the basin because the ice was driven by the wind-induced sea surface current in addition to the direct wind stress on the ice surface. Accordingly, the ice motion was well modelled by applying the surface current estimate. While surface currents are not routinely measured, the necessity of a coupled ice-ocean model is apparent for solving the ice motion.

Winds derived from MESAN fields proved to provide accurate forcing to the ice drift. By using the most correct wind forcing compared to the wind applied in the operational model, the modelled ice velocities in the drifting pack ice were improved as much as by replacing the 18 km model by the 5 km one. In addition, the modelled drift clearly approached the observed drift when  $C_a$  was assumed to be dependent on the atmospheric stability and ice conditions in contrast to using a constant  $C_a$ . Near the fast ice the inclusion of the surface current and a non-constant  $C_a$  did not improve the modelled drift. The calculation of momentum flux following Uotila et al. (2000) can easily be included in a coupled atmosphere-ice model with information on the atmospheric surface layer stratification, ice concentration, and ice and snow thickness.

## 6. Acknowledgements

I wish to thank Zhanhai Zhang for allowing the use of his ice model for this study. Bertil Håkansson and Maria Lundin from SMHI are acknowledged for providing the MESAN analysis, SMHI digitized ice charts and the SMHI BASIS field data. Heinrich Hoerber from the University of Hamburg and Ann-Sofie Smedman from Uppsala University are acknowledged for providing their BASIS field measurements. The BASIS group of FIMR is gratefully acknowledged. Jouko Launiainen and Timo Vihma particularly are thanked for project co-operation, and discussions and comments on the manuscript. Jouni Vainio and Bin Cheng kindly assisted me with the operational FIMR ice model and the FMI HIRLAM fields. This study is part of the EC-funded project BALTEX-BASIS carried out under contract MAS3-CT97-0117.

## References

- Banke, E. G., Smith S. D., and Anderson R. J., 1980. Drag coefficients at AIDJEX from sonic anemometer measurements, in *Sea Ice Processes and Models*, edited by R. S. Pritchard, pp. 430-442, Univ. of Washington Press, Seattle, U.S.A.
- Geiger, G. A., Hibler W. D. III, and Ackley S. F., 1998. Large-scale sea ice drift and deformation: Comparison between models and observations in the western Weddell Sea during 1992, *J. Geophys. Res.*, 103, 21,893-21,913.
- Gonella, J., 1972. A rotary-component method for analysing meteorological and oceanographic vector time series, *Deep-Sea Res.*, 19, 833-846.
- Gustafsson, N., Nyberg L., and Omstedt A., 1998. Coupling of a High-Resolution Atmospheric Model and an Ocean Model for the Baltic Sea, *Mon. Wea. Rev.*, 126, 2822-2846.

- Hägmark, L., Ivarsson K.-I., Gollvik S., and P.-O. Olofsson, 2000. Mesan, an operational mesoscale analysis system, *Tellus*, 52A, 2-20.
- Hansen, D. V., and Herman A., 1989. Temporal sampling requirements for surface drifting buoys in the tropical Pacific, *J. Atmos. and Oceanic Technol.*, 6, 599-607.
- Hansen, D. V., and Poulain P.-M., 1996. Quality control and interpolations of WOCE-TOGA drifter data, *J. Atmos. and Oceanic Technol.*, 13, 900-909.
- Hibler, W. D. III, 1979. A dynamic thermodynamic sea ice model, *J. Phys. Oceanogr.*, 9, 815-846.
- Hibler, W. D. III, and Schulson E. M., 1997. On modeling sea-ice fracture and flow in numerical investigations of climate, *Annals of Glaciology*, 25, 26-32.
- Kottmeier, C., and Sellmann L., 1996. Atmospheric and oceanic forcing of Weddell Sea ice motion, *J. Geophys. Res.*, 101, 20,809-20,824.
- Kundu, P. K., 1976. Ekman veering observed near the ocean bottom, *J. Phys. Oceanogr.*, 6, 238-242.
- Launiainen, J. (Editor), 1999. BALTEX-BASIS Data Report 1998, *International BALTEX Secretariat, Publication No. 14*, 94 pp.
- Leppäranta, M., 1981. An ice drift model for the Baltic Sea, *Tellus*, 33, 583-596.
- Leppäranta, and Omstedt A., 1990. Dynamic coupling of sea ice and water for an ice field with free boundaries, *Tellus*, 42A, 482-495.
- Leppäranta, M., and Zhang Z., 1992. A viscous-plastic ice dynamics test model for the Baltic Sea, *Finnish Inst. of Marine Res., Internal Report*, 3.
- Leppäranta, M., Sun Y., and Haapala J., 1998. Comparisons of sea-ice velocity fields from ERS-1 SAR and a dynamic model, *J. Glaciology*, 147, 248-262.
- Martinson, D. G., and Wamser C., 1990. Ice drift and momentum exchange in winter Antarctic pack ice, *J. Geophys. Res.*, 95, 1741-1755.
- Omstedt, A., 1990. Modelling the Baltic Sea as thirteen sub-basins with vertical resolution, *Tellus*, 42A, 286-301.
- Omstedt, A., Nyberg L., and Leppäranta M., 1996. On the ice-ocean response to wind forcing, *Tellus*, 48A, 593-606.
- Thomas, D., 1999. The quality of sea ice velocity estimates, *J. Geophys. Res.*, 104, 13,627-13,652.
- Thorndike, A. S., and Colony R., 1982. Sea ice motion in response to geostrophic winds, *J. Geophys. Res.*, 87, 5845-5852.
- Uotila, J., Launiainen J., and Vihma T., 1995. Analysis of the surface drift currents in the Bothnian Sea, *Geophysica*, 31, 37-49.
- Uotila, J., Vihma T., and Launiainen J., 2000. Response of the Weddell Sea pack ice to wind forcing, *J. Geophys. Res.*, 105, 1135-1151.
- Vihma, T., Launiainen J., and Uotila J., 1996. Weddell Sea ice drift: Kinematics and wind forcing, *J. Geophys. Res.*, 101, 18,279-18,296.
- Zhang, J., and Hibler W.D. III, 1997. On an efficient numerical method for modeling sea ice dynamics, *J. Geophys. Res.*, 102, 8691-8702.
- Zhang, Z. H., Leppäranta M., Haapala J., and Stipa T., 1999. Numerical Simulation of Sea Ice Drift in the Bay of Bothnia, *POAC'99 Proceedings*, Helsinki University of Technology, Espoo, Finland, 488-496.

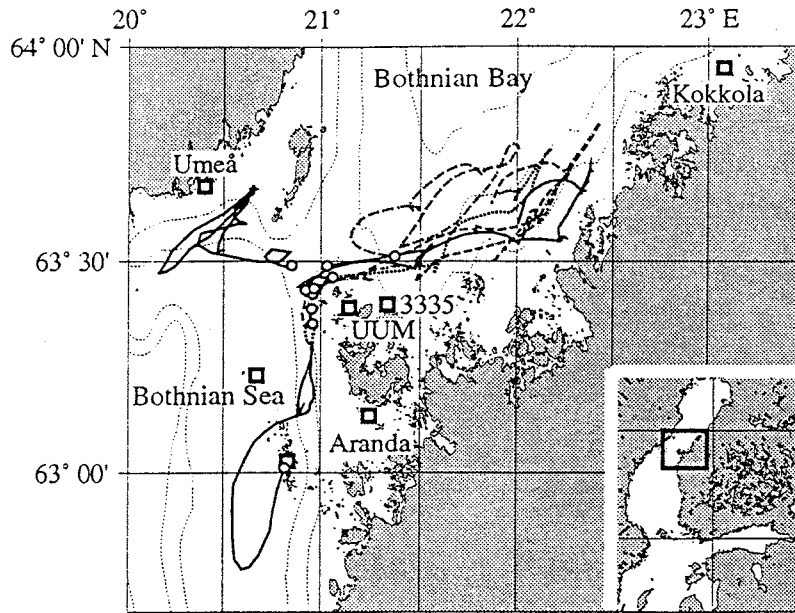


**Figure 1.** The drift trajectories (thick lines) and the initial positions (open circles) of the BASIS buoys, and the positions of the nearest meteorological stations (squares). UUM is the Uppsala University weather mast and 3335 is a weather buoy of the University of Hamburg. R/V Aranda was the main observing station of the BASIS experiment. Thin dashed lines give the depth countours with 20 m interval up to 20 m depth.

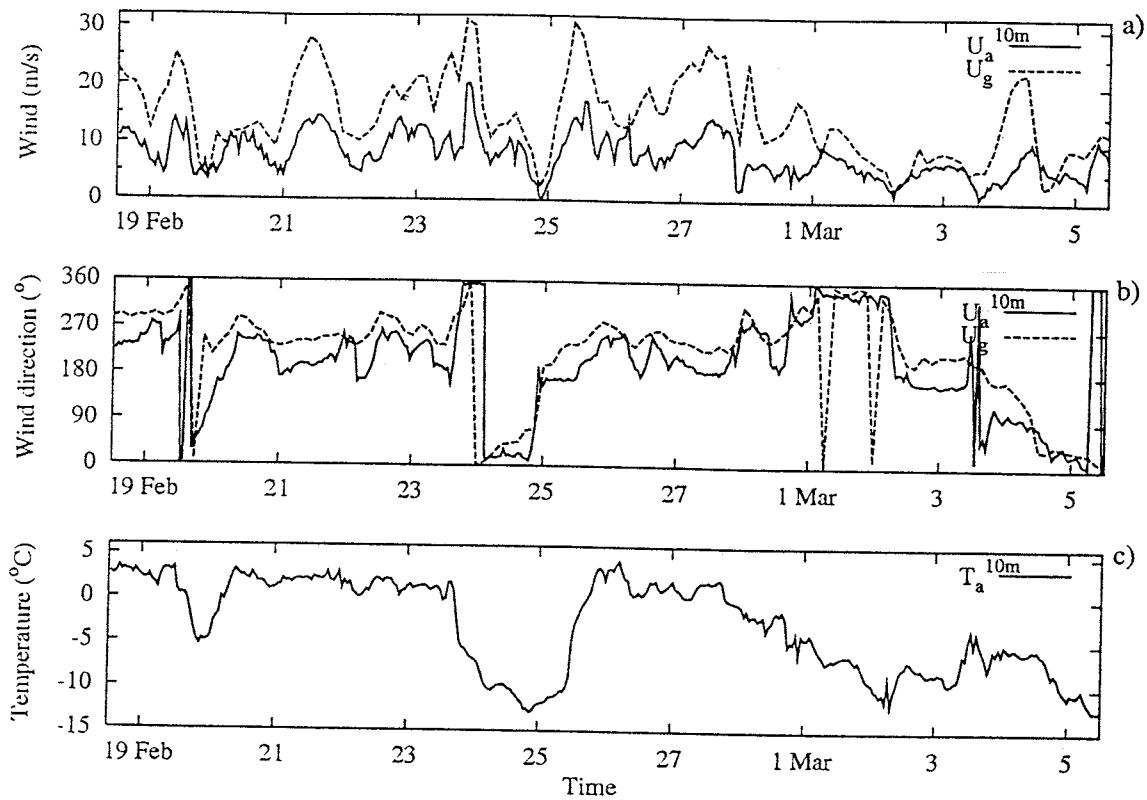


**Figure 2.** Time series of (a) the 10-m wind and the geostrophic wind speeds, (b) and directions and (c) the air temperature at a height of 10 m during the BASIS main field expedition in 1998 as measured at the location of R/V Aranda.

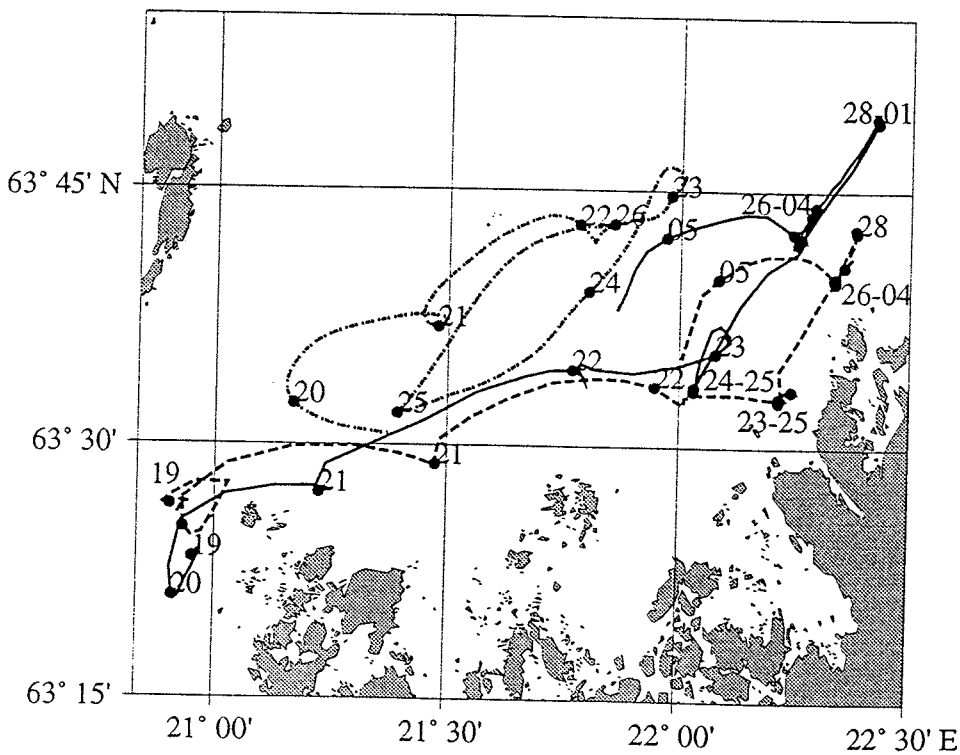


**Figure 3.** Trajectories of three drifters between 19 February and 5 March 1998. Daily positions are shown as dots, with dates in February and March. Buoy 9868 is plotted with a solid line, 7199 with a dashed line, and 5893 with a dash-dotted line.

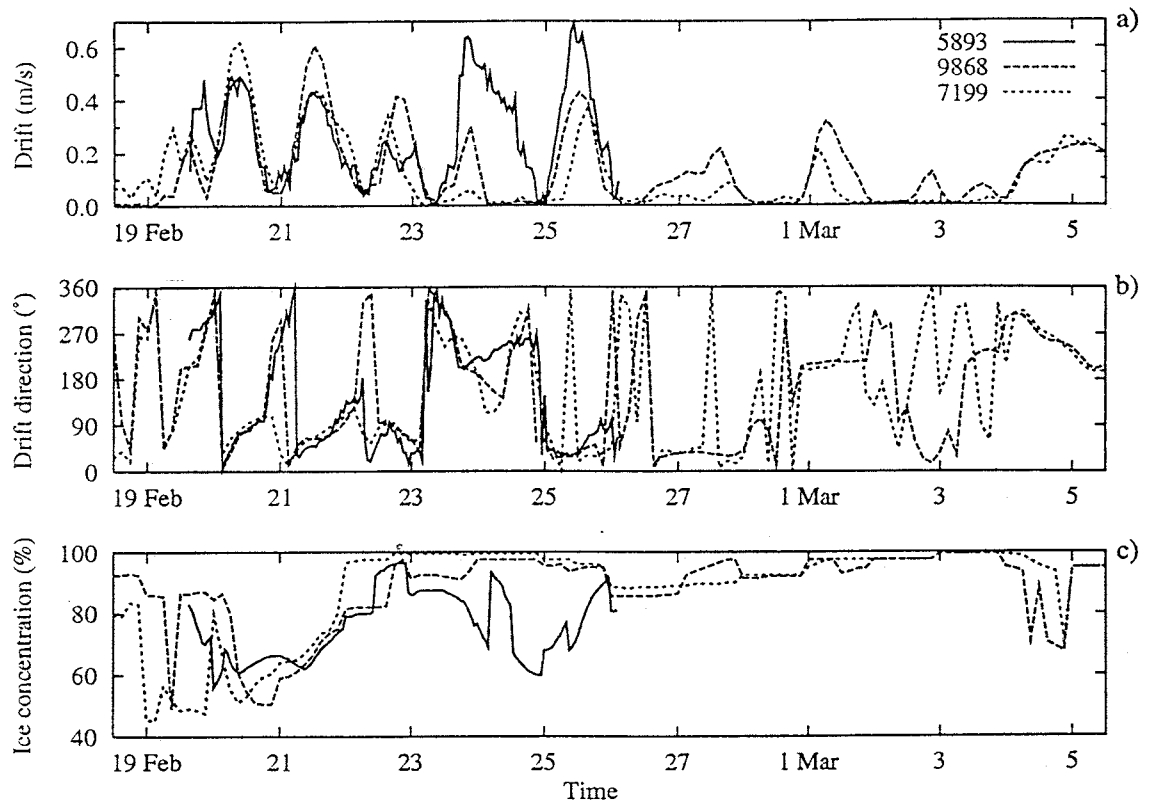


**Figure 4.** (a) Drift speeds, (b) directions, and (c) ice concentrations for the drifters 5893, 7199 and 9868.



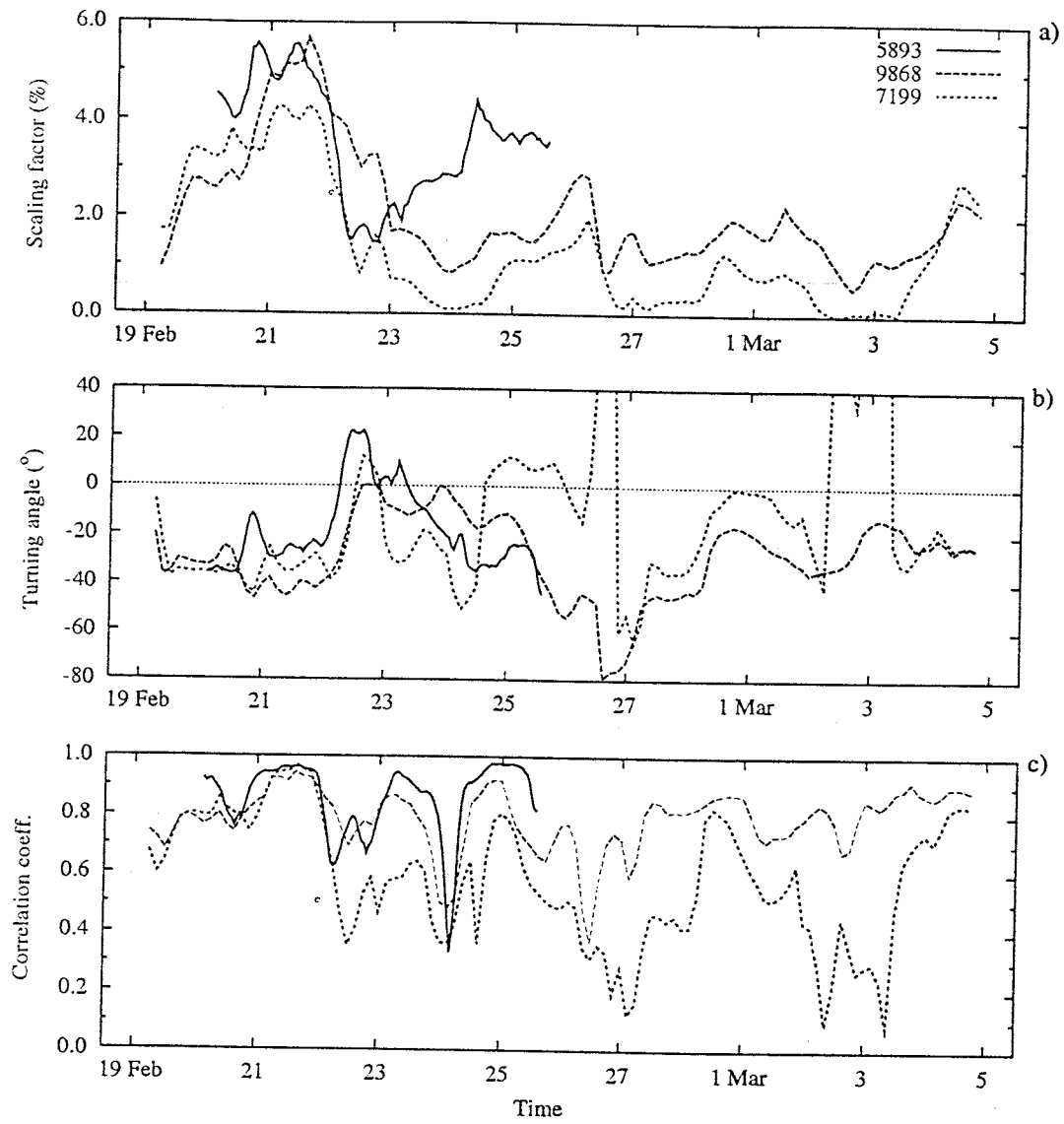


**Figure 5.** (a) scaling factor, (b) turning angle, and (c) correlation coefficient between the wind and the drift for the three drifters. A diurnal moving period was chosen for 5893 and 3-day moving periods for 9868 and 7199.

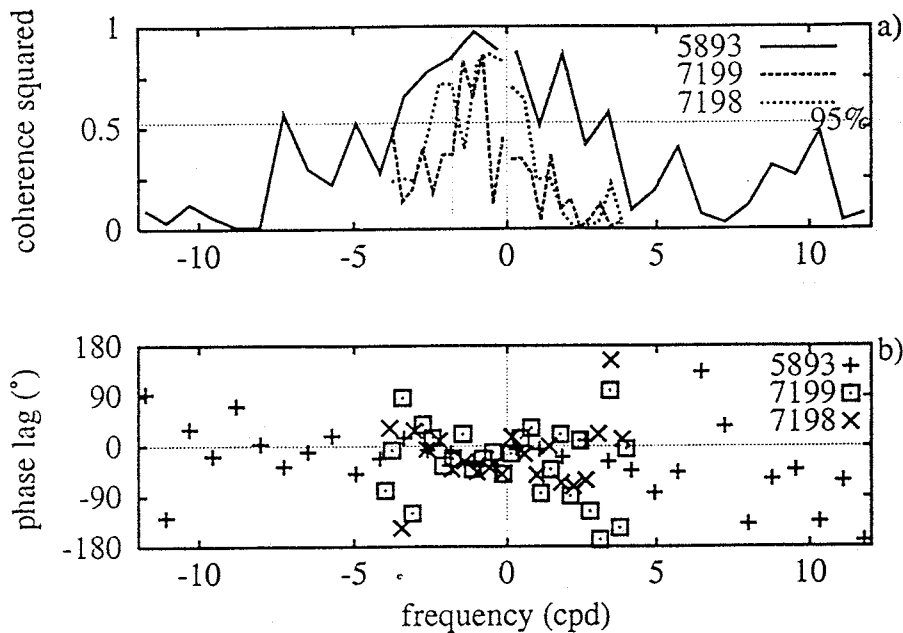


**Figure 6.** The wind-drift coherence (a) and phase lag (b) for 5893, 7199, and 7198. Negative frequencies represent a clockwise velocity component, while positive frequencies represent a counterclockwise component. The phase lag is a measure of the phase lead of the rotary component of drift velocity time series with respect to that of wind velocity time series. When the phase lag is positive (negative), the drift vector is directed counterclockwise (clockwise) from the wind. In (a) the vertical dashed line gives the inertial frequency.

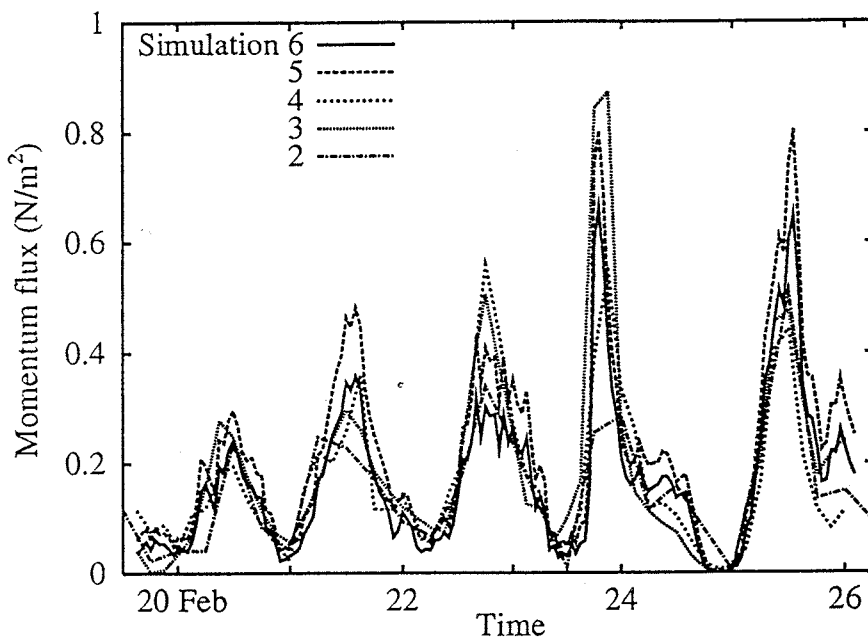


**Figure 7.** Momentum flux time series for 5893 from the simulation cases.

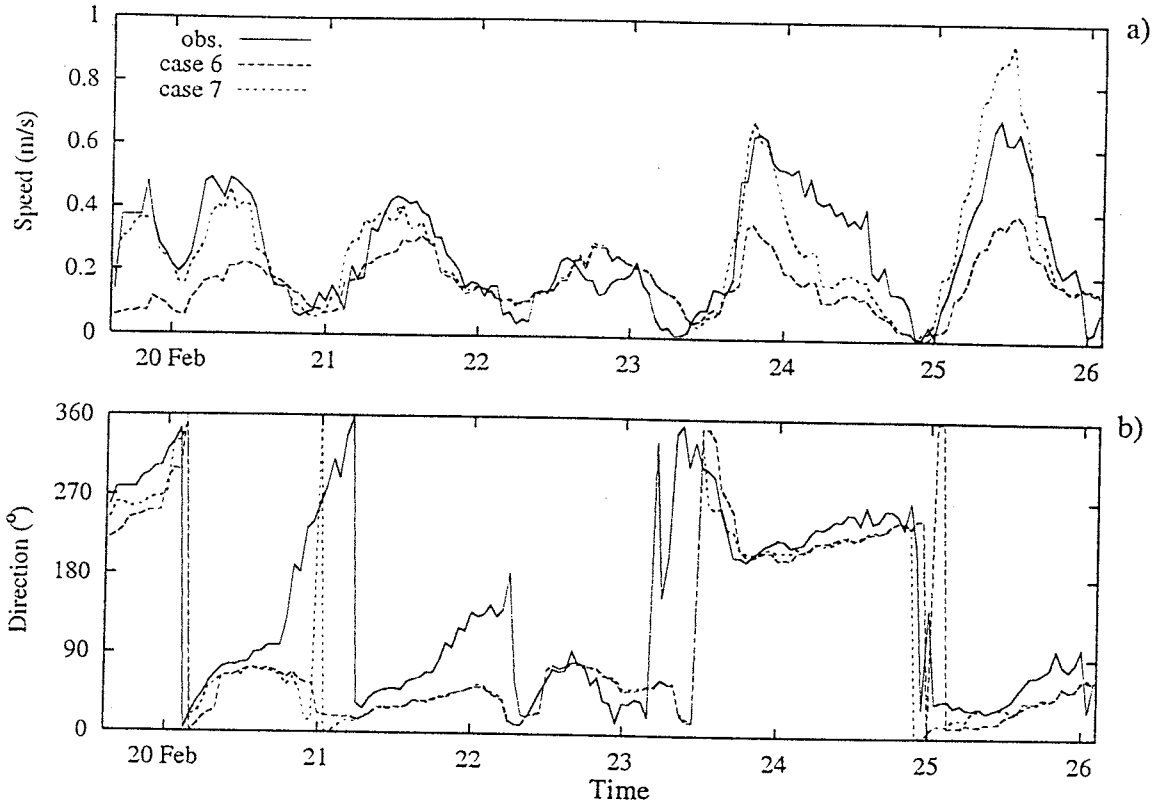


Figure 8. Comparison of the observed drift and the (a) speed and (b) direction of buoy 5893 in

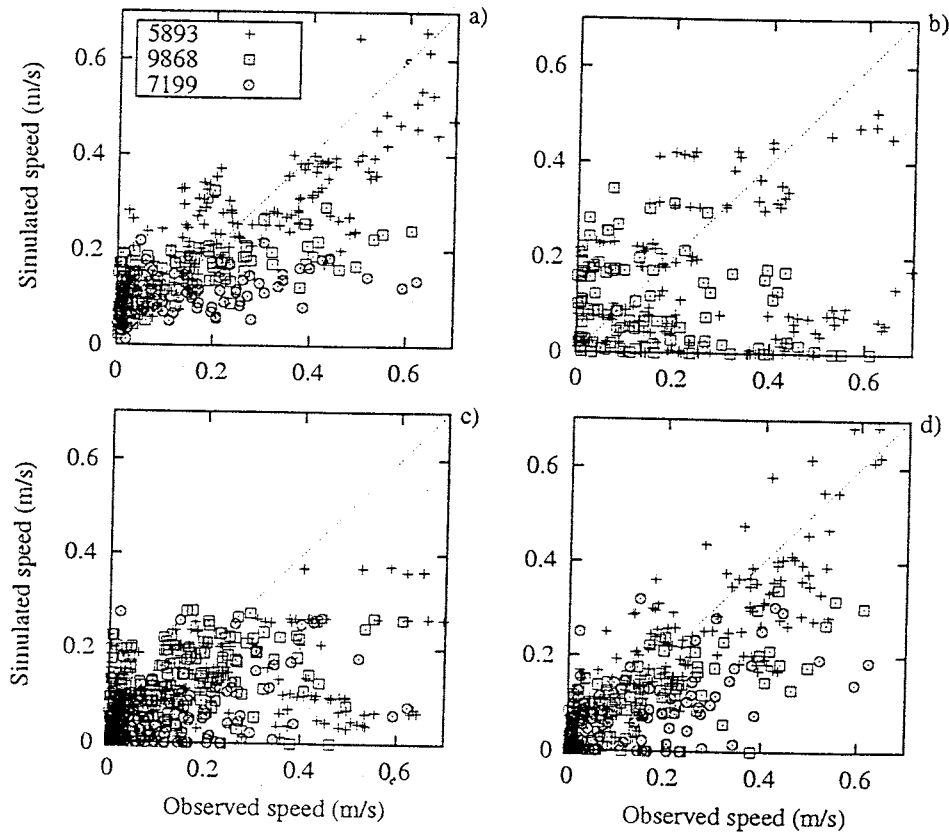


Figure 9. Relations between the observed (horizontal axis) and simulated speed (vertical) in (a) simulation 1, (b) simulation o2, (c) simulation 2, and (d) simulation 6 for buoys 7198 and 9868, and in simulation 7 for buoy 5893. The simulation o2 is the model run with the 18 km ice model, while the remainders are with the 5 km ice model.

**Table 1.** Scaling factor ( $s$ ), turning angle ( $\varphi$ ), and additive term magnitude ( $C$ ) between the buoy drift and the interpolated surface wind based on the BASIS meteorological stations.  $\varphi$  is negative if the drift is directed right from the wind. The values in brackets represent the standard deviations of the coefficients, and  $R^2$  gives the ratio of the explained variance of the regression model (1).

Buoy	$s$ (%)	$\varphi$ ( $^\circ$ )	$C$ (cm/s)	$R^2$
1154	1.96(0.25)	6(1)	2(4)	0.46
5893	3.25(0.12)	-25(1)	9(3)	0.80
7198	2.49(0.21)	-30(3)	2(2)	0.53
7199	1.25(0.14)	-23(3)	1(3)	0.39
9868	1.76(0.13)	-23(2)	2(2)	0.58
9869	1.68(0.33)	-23(5)	5(5)	0.35

**Table 2.** Complex vector correlation coefficient magnitude ( $r$ ) and the mean velocity difference ( $\overline{\Delta V}$ ) between the observed and modelled drift velocities. Simulations with the prefix "o" are model runs with the 18 km ice model, while the remainders are with the 5 km ice model. The correlation bounds are the 95% confidence limits of the coefficients.  $N$  gives the number of observations per simulation.

Buoy	Simulation	$r$	$\overline{\Delta V}$	$N$
5893	1	0.89 (0.92...0.85)	0.13	156
	o2	0.47 (0.58...0.33)	0.24	153
	2	0.72 (0.79...0.63)	0.20	156
	3	0.81 (0.86...0.75)	0.18	156
	4	0.82 (0.86...0.76)	0.19	156
	5	0.83 (0.87...0.77)	0.19	156
	o6	0.70 (0.77...0.60)	0.19	156
	6	0.87 (0.91...0.83)	0.17	156
9868	7	0.91 (0.93...0.88)	0.14	156
	1	0.75 (0.82...0.66)	0.11	121
	o2	0.50 (0.62...0.34)	0.11	114
	2	0.67 (0.73...0.61)	0.09	324
	3	0.74 (0.78...0.68)	0.08	324
	4	0.72 (0.77...0.66)	0.09	324
	5	0.82 (0.87...0.74)	0.09	121
	o6	0.42 (0.55...0.26)	0.12	121
7199	6	0.83 (0.88...0.76)	0.09	121
	1	0.59 (0.70...0.46)	0.11	121
	2	0.63 (0.73...0.51)	0.10	121
	3	0.62 (0.72...0.49)	0.10	121
	4	0.66 (0.75...0.54)	0.10	121
	5	0.67 (0.76...0.56)	0.10	121
	6	0.67 (0.76...0.55)	0.10	121

## Modelling of Snow Influence on Land-Fast Ice Thickness

Maria Lundin

Swedish Meteorological and Hydrological Institute

### 1. Introduction

Local variations of ice thickness were found in measurements made in land-fast ice in the Northern Quark during the BALTEX/BASIS winter experiment. The ice measurements show high negative correlation with snow thickness in the case where the snow dunes had been stationary for a while. In order to investigate the influence of snow on the fast ice thickness a simple one-dimensional ice model with snow cover and snow-ice was set up. Two cases were created. In the first case the mean ice thickness over a wide fast ice area were modelled. This case showed large agreement with measurements when snow ice formation was included. In the second case the ice thickness under a snow dune of varying snow thickness was simulated for a certain date. It was shown that locally variations in ice thickness are mainly dependent on the snow cover thermodynamics but not affected by snow-ice formation, since flooding leading to snow-ice formation is a large area phenomena.

### 2. Method

#### 2.1 Mathematical Formulation

A one-dimensional ice model was used which describes the ice growth through thermodynamic growth (Omstedt et al., 1996), snow-ice formation and sun radiation when melting.

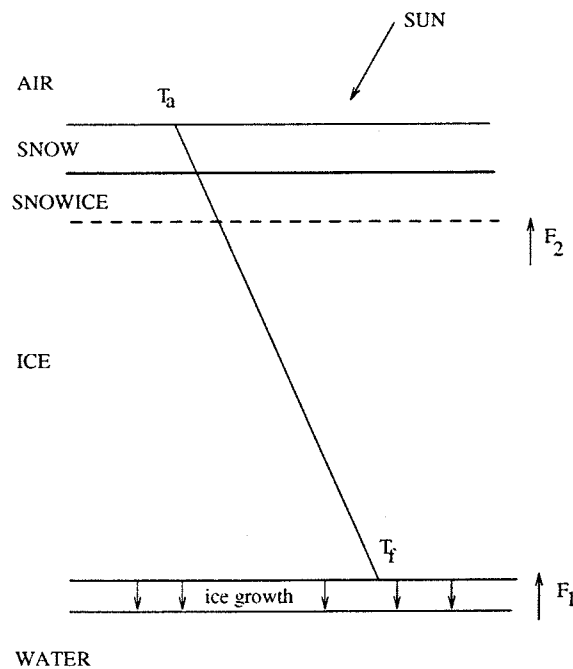


Figure 1. One-dimensional ice model

In Figure 1 the thermodynamic part is represented by the heat fluxes  $F_1$  and  $F_2$ . The heat flux  $F_1$  describes the amount of latent energy released when the ice thickness  $dh_i$  freezes

$$F_1 = \rho_i L \frac{dh_i}{dt}$$

where  $\rho_i$  is the density of ice and  $L$  the latent heat. The parameter values are shown in Table 1 below.  $F_2$  stands for the conducted heat transported through ice and snow due to the temperature gradient, which in this case is linear.

$$F_2 = \frac{k_i k_s}{k_i h_s + k_s h_i} (T_f - T_{surf})$$

The first factor is the total thermal conductivity for the ice and snow layers, where  $k_i$ ,  $k_s$ ,  $h_i$  and  $h_s$  stand for thermal conductivity and thickness for ice and snow respectively. The ice bottom temperature is set to freezing temperature,  $T_f$ .  $T_{surf}$  stands for the snow surface temperature and is the same as the atmosphere temperature,  $T_a$  when  $T_a$  is below freezing. When  $T_a$  is above zero,  $T_{surf}$  is the same as  $T_f$ . It means that the linear temperature gradient never becomes positive and melting is taken care by a sun radiation part.

In order to get the freezing up date, a turbulent model was solved by the equation solver PROBE (PROgram for Boundary layers in the Environment) (Svensson, 1998). When the water column reached the freezing temperature the ice growth started. Due to the small depth in the modelled near shore area the water column was assumed well mixed at temperature of freezing and no water heat flux is added from below. The ice growth is solved by

$$dh_i = \frac{k_i k_s}{k_i h_s + k_s h_i} \cdot \frac{(T_f - T_{surf})}{\rho_i L} dt$$

Snow-ice forms when the snow thickness  $h_s$  increases the pressure on the ice making sea water poring up through brine channels or cracks in the ice and a slush layer is created. In the model this layer freezes instantaneously into so called snow-ice.

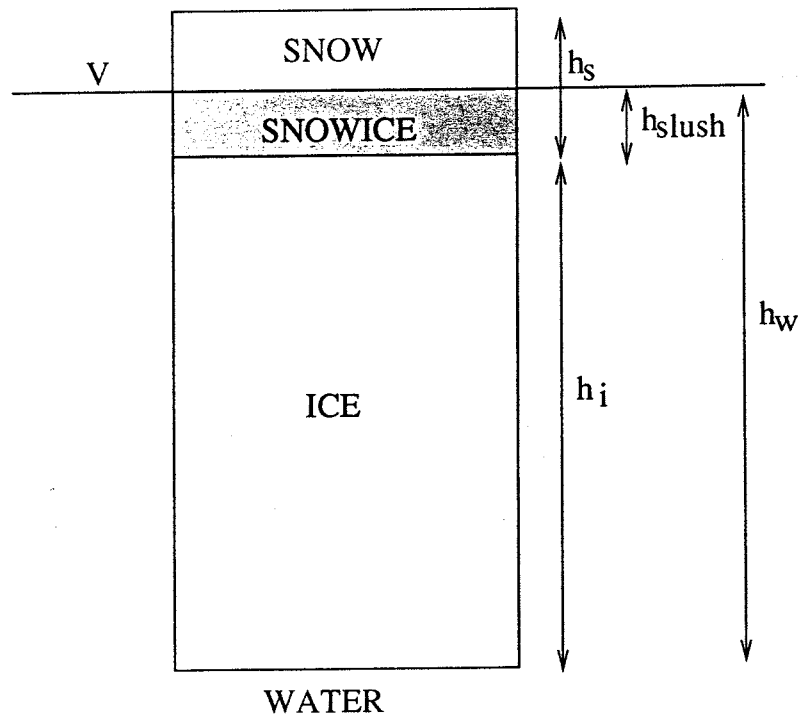


Figure 2. Snow ice formation

Snow ice formation is illustrated in Figure 2. Following equation describes equilibrium between water and the snow and ice column:

$$h_i \rho_i + h_s \rho_s = h_w \rho_w$$

where  $h_w$  and  $\rho_w$  stand for thickness and density of the repressed water column. The thickness of the slush layer is received from the difference between the height of the repressed water column and the ice thickness.

$$h_{slush} = \frac{h_i \rho_i + h_s \rho_s}{\rho_w} - h_i$$

The ice thickness equation including snow-ice is given by

$$dh_i = \frac{k_i k_s}{k_i h_s + k_s h_i} \cdot \frac{(T_f - T_{surf})}{\rho_i L} dt + \left( \frac{h_i \rho_i + h_s \rho_s}{\rho_w} - h_i \right)$$

The constants used in the calculations are shown in Table 1.



Table 1. Constants

Symbol	Name constant	Value	Unit
$\rho_I$	Density ice	910	kg/m <sup>3</sup>
$L$	Latent heat pure ice	$3.34 \cdot 10^5$	J/kg
$K_I$	Thermal conductivity ice	2	W/(m <sup>2</sup> ·K)
$\rho_s$	Density snow	300	kg/m <sup>3</sup>
$k_s$	Thermal conductivity snow	0.3	W/(m <sup>2</sup> ·K)
$\rho_w$	Density water	1003	kg/m <sup>3</sup>

## 2.2 Details of Calculations

The analysed period runs from June 1997 until May 1998 and intended to simulate the BASIS experimental area with land-fast ice around the Aranda location in the Northern Quark. Meteorological data extracted every third hour were used for running the model. In order to use the best estimate for the area, weather mast data from the BASIS experiment were used in combination with data from the mesoscale analyses system Mesan (Häggmark et al., 2000), which show high correlation with the mast data. Where no Mesan data were available for the period the synoptic weather station at Bjuröklubb were used. The last mentioned is available in SMHI database, which covers the area of Baltic Sea drainage. In the Mesan data base new snow occurrence is based on the wet bulb temperature and its density is determined from the atmosphere temperature (Häggmark et al., 2000). In order to calculate snow thickness two assumptions were made:

1. Snow cover was assumed to be one third of the precipitated snow thickness according to wind compression.
2. When the air temperature is above freezing, snow cover grows according to snowfall and melts at a rate of 1.28 cm snow/degree day.

The melt rate is based on snow measurements during BASIS experiment. This melt rate can be compared to the melt rate 3.5 mm water equivalent/degree day for snow cover on land, used in the HBV-model (Lindström et al., 1997). In this study the mean snow density is assumed to be 300 kg/m<sup>3</sup> which corresponds to a rate of 1.17 cm snow/degree day. In order to get correct snow thickness in the ice model the formed snow-ice thickness has to be subtracted from the snow thickness.

## 3. Results

During the BASIS winter experiment snow and ice thickness were measured every second metre along a line of hundred metres at nine occasions between 19 February to 6 March 1998. An example of snow and ice thickness along a line can be seen in Figure 3. Those measurements were made February 19 and the snow and ice thickness show high correlation. Later during the measuring period there was a melting period and the correlation between ice and snow thickness was lost. This study aims to investigate to what degree the snow cover causes the ice thickness variations.

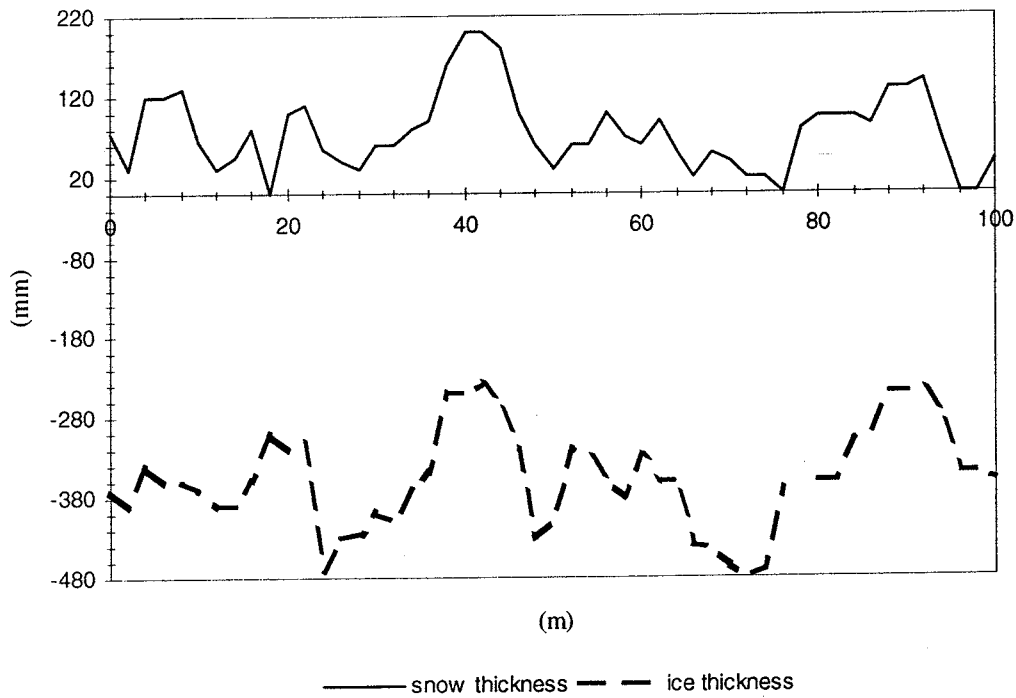


Figure 3. Snow and ice thickness along 100 m from February 19.

Modelled ice thickness from the investigated period is shown in Figure 4 together with snow thickness determined from database according to description above. The observations represent mean snow and ice thickness along the 100-meter line measured during BASIS winter experiment. Also the snow-ice limit is included in the diagram. According to snow ice equations above the condition for snow ice to form is:

$$h_s > \frac{\rho_w - \rho_i}{\rho_s} h_i \approx \frac{h_i}{\rho_s / 100}$$

The snow ice limit is of course sensitive to the varying density of snow, which varies between near zero up to  $600 \text{ kg/m}^3$ . In this study snow mean density is set to  $300 \text{ kg/m}^3$  according to measurements from the BASIS experiment and earlier (Lundin et al., 1999; Saloranta, 1999). This means that flooding occurs when snow thickness exceeds one third of the ice thickness.

The model shows good agreement to measured mean ice thickness during the main part of the BASIS experiment period. The difference between the model and the first two observed values could be due local variations in snow fall leading to snow-ice formation at different dates.

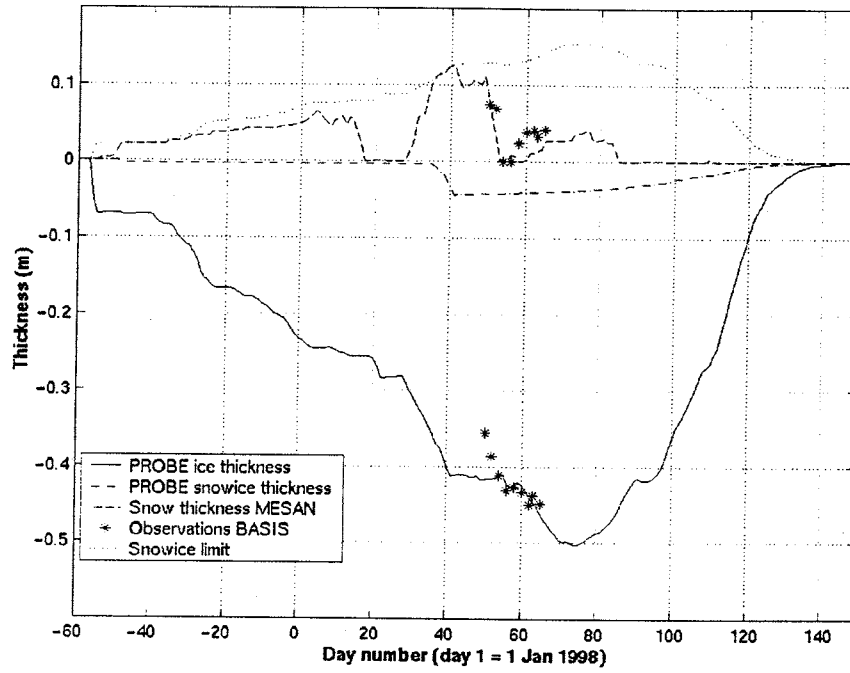


Figure 4. Ice and snow and snow-ice thickness from June 1997 – May 1998.

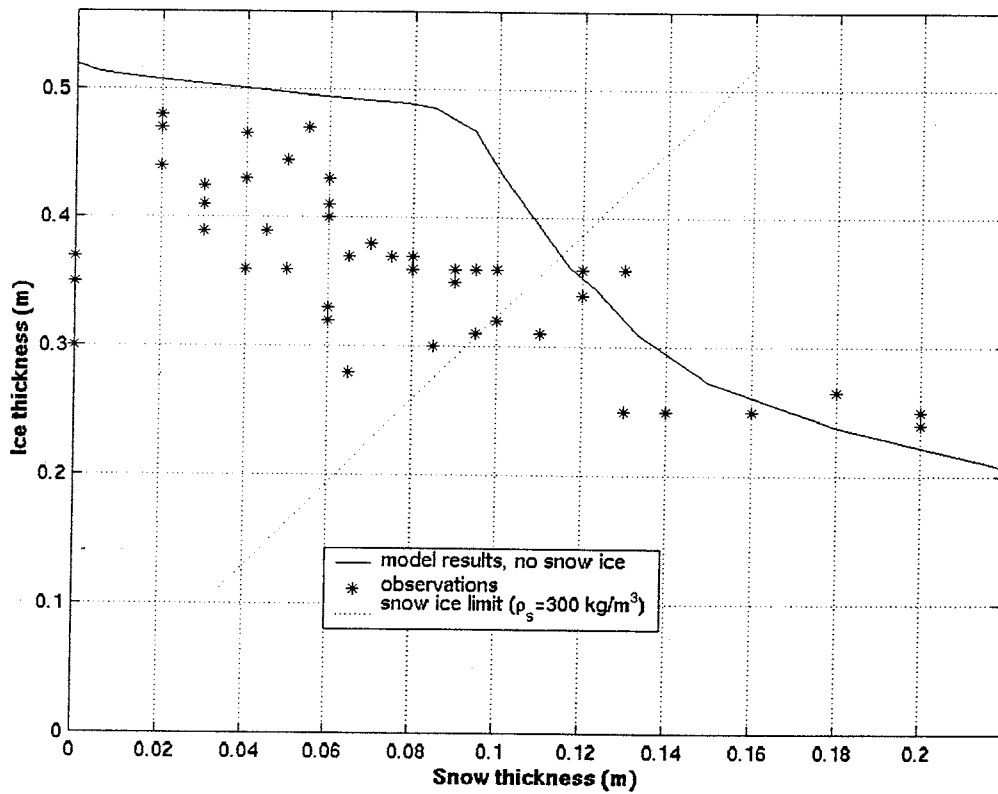


Figure 5. Ice thickness as a function of snow thickness from 19 February 1998.

In order to investigate how the snow influences the ice thickness variations on a local scale the snow thickness was varied in order to simulate different positions on a snow dune at a certain date. The snow thickness was constantly increased or decreased representing different parts of a snow dune. The results can be seen in Figure 5 where measured and modelled ice thickness is plotted versus snow thickness for February 19.

In order to simulate the small-scale variations there is no snow-ice formation included in this case. Flooding leading to snow-ice formation is dependent on the mean snow thickness over a larger scale. Due to the exclusion of the snow ice formation the snow thickness is larger in the modelled case. Although the modelled and observed data are displaced along the snow thickness axis, a decrease in snow thickness of near 0.2 m corresponds to an increase in ice thickness of near 0.3 m in both cases. This shows that the thermodynamics of the snow cover can be responsible for the rough water-ice surface of the land-fast ice observed during the BASIS experiment.

Running the model in the same way with snow ice formation included did not give any acceptable result. The ice growth becomes very sensitive to the snow thickness history.

#### 4. Summary and Conclusions

The purpose of this report is to investigate whether variations found in land-fast ice thickness are due to spatial snow thickness variations – i.e. snow dunes. A simple ice model including thermodynamic growth, snow-ice formation and sun radiation when melting has been used. Increased mean snow thickness over a wide area leads to flooding which leads to increased ice thickness via snow-ice formation. Snow thickness variation on smaller scales do not lead to flooding but effect the thermodynamics and works like more or less isolation to the heat transfer through the ice.

The conclusion from the results above is that the ice growth on a small scale depends strongly on the snow thermodynamics while snow-ice formation, depending on snow mean thickness, plays a larger role for large-scale areas of ice growth. Snow-ice formation is very sensitive to the snow thickness history.

#### 5. References

- Hägmark, L., Ivarsson, K.I., Gollvik, S. and Olofsson P.O.: 2000, Mesan, an operational mesoscale analysis system, *Tellus*, 52A, 2-20, 2000.
- Lindström, G., Johansson, B., Persson, M., Gardelin, M. and Bergström, S.: 1997, Development and test of the distributed HBV-96 hydrological model, *Journal of Hydrology*, 201:272-288.
- Lundin, M., Moberg, M., Håkansson, B., and Granskog, M.: 1999, Ground, air and satellite data obtained during BASIS field experiment by SMHI, in; Launiainen, J, (editor), *BALTEX-BASIS Data Report 1998*, Int. BALTEX Secretariat Publ. No. 14, Geesthacht, Germany, 94 pp.
- Omstedt, A., and Nyberg L.: 1996, Response of Baltic Sea ice to seasonal, interannual forcing and climate change, *Tellus*, 48A, 644-662.
- Saloranta, T.M., 1999: Modeling the evolution of snow, snow ice and ice in the Baltic Sea, *Tellus*, 52A, 93-108.
- Svensson, U.: 1998, PROBE Program for Boundary Layers in the Environment System description and Manual, Reports Oceanography SMHI, 24.

## 5. OCEAN BOUNDARY LAYER

### **Modelling the Bothnian Bay Water and Heat Balance: the BALTEX-BASIS Experiment**

Anders Omstedt

SMHI, Norrköping, and Department of Earth Sciences, University of Gothenburg, Sweden

#### **1. Introduction**

The winter research in the Baltic Sea has a long tradition and became rather active for about 25 years ago when a joint Swedish-Finnish Winter Navigation Research Program was started. In the beginning the research was mainly oriented towards ice drift and remote sensing. Later thermodynamic studies were started together with coupled atmosphere-ice-ocean modelling. In late 1990<sup>th</sup> the first coupled atmosphere-ice-ocean model system was put in operational use (Gustafsson et al., 1998). Since the BALTEX programme (BALTEX, 1995) started, more efforts are oriented towards the understanding of the water and heat cycles in the Baltic drainage basin and the development of coupled atmosphere-land-ice-ocean models. The BASIS experiment is the first major winter experiment within BALTEX addressing Baltic Sea winter conditions. The major field experiment was performed during the period 16 February to 6 March 1998 (Launiainen, 1999) in the sea ice zone in the southern part of Bothnian Bay. Both field data and models are used in BASIS and the specific objectives addressed by the present study are to perform water and heat budget calculations using a coupled ice-ocean model.

Using an ocean model when studying the water and heat balance is an important improvement compared to earlier studies. The reason is that the water and heat balances are solved together in a consistent way. Other reasons are that the results can be checked both with regard to the sea surface temperatures and ice, in- and out-flow properties and the fresh water content (salinity) in the system, Omstedt and Rutgersson (2000).

The rate of turnover of water in the Bothnian Bay has been estimated to 4-5 year. This implies that numerical integration's are influenced by the initial conditions for simulations less than 5 years. On the other hand long-term (more than the transient time) numerical integration's are strongly influenced by the lateral boundary conditions. In the present paper we use the PROBE-Baltic model (Omstedt and Nyberg, 1996) to analyse the water and heat cycles. We will use results from an 18 years validation period starting in November 1980 and covering the BASIS period in 1998. This means that initial conditions will not influence the results, this is therefore a major improvement compared to earlier studies. The water and heat balance for the whole Baltic Sea were analysed by Omstedt and Axell (2000).

In Section 2, a short description about the modelling is given. The results are then presented in Section 3. Finally a summary with some conclusions are given in Section 4.

## 2. Methods

### 2.1. Model description

In the model, which is called PROBE-Baltic (Omstedt and Nyberg, 1996), the Baltic Sea is divided into 13 sub-basins (Figure 1) and the properties in each sub-basin is calculated with horizontally averaged time-dependent advective-diffusive conservation equations for momentum, heat and salinity as well as conservation laws for volume and ice. The full model description is given in Omstedt and Axell (2000) and will not be repeated here. The model was run for an 18-year period, from November 1, 1980 to December 31, 1998, and initial profiles were approximated from available oceanographic measurements.

### 2.2. Model forcing and observational data

The meteorological forcing were taken from a gridded database developed at the Swedish Meteorological and Hydrological Institute (SMHI), see Omstedt and Axell (2000).

The water level forcing from the North Sea was calculated on the basis of daily mean sea levels from the Kattegat (water level station Viken). The river-runoff data were based upon observations and model calculations.

The vertical profiles of observed salinity and temperature were extracted from the national database SHARK (Swedish Ocean Archive). The ice data during the BASIS period were partly due to direct field observations and partly due to ice chart and satellite information.

## 3. Results

### 3.1 Long-term means

In the present study we will concentrate on the modelling of the Bothnian Bay. Omstedt and Axell (1998, 2000) present results from the other sub-basins in the Baltic Sea. Before making any water and heat balance studies we need to validate our ocean model. In Figure 2 and 3, the results from the 18 years integration are shown. The number of observations available in the Bothnian Bay as indicated in the figures is quit low, but increases during the end of the period. The calculated sea surface temperature follows the observation close with a bias of  $-0.6$  ( $^{\circ}\text{C}$ ) and a rms error of  $1.2$  ( $^{\circ}\text{C}$ ). The deep-water temperatures indicate a slight underestimation in the calculation, however, winter temperatures are not available in the Bothnian Bay and therefore the observed temperatures underestimate winter conditions. The corresponding results for salinity are given in Figure 3. The observed and calculated sea surface salinities follow each other close (except some observed low values which could be due to measuring errors) with a bias and rms error of  $+0.1$  and  $0.2$  (psu), respectively. The modelled deep-water salinities are slightly higher than observation, indicating a need for considering mixing of the dense bottom plume during inflow events.

The results illustrate that the model realistically calculates the water and heat cycles as examined from salinity and temperature respectively. The long-term estimation on these cycles is given in Tables 1 and 2. We could notice that the net precipitation (P-E) is positive both in the Baltic Sea as well in the Bothnian Bay. From the heat calculations we can also conclude that the Baltic Sea is almost in balance with the atmosphere. The Bothnian Bay, however, losses  $6$  ( $\text{Wm}^{-2}$ ) to the atmosphere. This heat loss must be compensated by heat gain

from the in- and out-flows between the Bothnian Bay and Bothnian Sea. We can thus conclude that the heat balance calculations indicate that on long term mean the Bothnian Bay import heat from the Bothnian Sea.

### 3.2 The BASIS period

#### 3.2.1 Sea ice

The winter 1998 was a mild winter and during the BASIS period the ice were mainly formed in the Bothnian Bay. From satellite and ice chart information the observed ice concentration was about 90 (%) in the Bothnian Bay during the BASIS period. The observed and calculated values are illustrated in Figure 4, showing a good agreement.

For the ice thickness several measurements were taken close to the Aranda camp (Lundin, 2001). As these observations represent fast ice conditions the calculation only need to consider level ice. In Figure 5, observed and calculated level ice thicknesses are given. As the observations represent a mean ice thickness over a distance of 100 meters, standard deviations from the mean are also given as dotted lines in the figure. The calculated mean ice thickness follows observations in a realistic way, but with a slight underestimation.

For the Bothnian Bay budget calculations we need also to consider the mean ice thickness in the whole bay, Figure 6. The mean ice thickness includes both level and ridged ice. In the figure we also give the estimated mean ice thickness based on ice chart information. The modelled result is within the estimated low and high limits based on ice chart information.

The calculations during the BASIS period are close to observations both with regard to ice concentration and thickness. We shall recall that the modelling is based on a run starting November 1980 and the results are analysed after more than 17 years simulation. The good agreement thus indicates that the heat balance is realistically modelled and could be used when analysing the heat balance.

#### 3.2.2 Heat balance

The calculated heat fluxes during the BASIS period are illustrated in Figure 7. From the figure we can notice that the Bothnian Bay loses heat during the BASIS period and the largest loss were due to the sensible heat flux. The latent heat flux and the net long wave radiation flux were also positive and thus in the direction from water to air. Even though that the BASIS experiment were taken place during February, sun radiation added heat to the Bothnian Bay.

The calculated heat balance is illustrated in Figure 8. The main heat sink for the water body was due to heat loss in the open ice regions. Heat flow from water to ice, increased the heat loss with values up to more than  $30 \text{ Wm}^{-2}$ . The fluxes all show a high degree of temporal variability. Data from surface stations and from aircraft (Brummer et al, 2001), also showed large temporal but also spatial variations.

## 4. Summary and Conclusions

In the present work we have examined the water and heat cycles of the Bothnian Bay by using the model PROBE-Baltic (Omstedt and Nyberg, 1996). Observed and numerically simulated data from an 18-year period (1981-1998) were first analysed, including temperature and

salinity profiles. Secondly, the observed and calculated ice concentration and thickness during the BASIS period were examined. Finally, we examined the heat balance of the Bothnian Bay during the BASIS period. The conclusions from the work are summarised as follows:

- The calculated long-term salinity and temperature structure are stable and in good agreement with observations.
- The calculated ice concentration and thickness during the BASIS period were quit close to observations, illustrating that the heat cycle was realistically calculated.
- The Bothnian Bay water body heat balance during the BASIS period showed high temporal variation and with major contributions from the sensible heat flux, the latent heat flux and the net long wave radiation from the open water surface.
- During the BASIS period the sun radiation as well as the heat flow from water to ice could not be neglected in the heat balance.
- From the heat balance calculations it was concluded that on long term mean the Bothnian Bay import heat from the Bothnian Sea

### References:

- BALTEX, : 1995, 'Baltic Sea Experiment. Initial implementation plan', *Internat. BALTEX Secretariat Publ. No. 2*, GKSS Research Center, Geestacht, Germany.
- Brummer, B., Schröder, D., Launiainen, J., Vihma, T., Smedman, A.-S., and Magnusson, M.: 2001, 'Temporal and spatial variability of surface fluxes over the ice edge zone in the northern Baltic Sea', this issue.
- Gustafsson, N., Nyberg, L. and Omstedt, A.: 1998, 'Coupling of a high-resolution atmospheric model and an ocean model for the Baltic Sea', *Monthly Weather Review*, **126**, 2822-2846.
- Launiainen, J. (Ed.): 1999, 'BALTEX-BASIS Data Report 1998', *International BALTEX Secretariat Publ. No. 14*, GKSS Research Center, Geestacht, Germany.
- Lundin, M.: 2001, 'Modelling of snow influence on land fast ice thickness', this issue.
- Omstedt, A. and Axell, L. B.: 2001, 'Modeling the Variations of Salinity and Temperature in the Large Gulfs of the Baltic Sea', Submitted.
- Omstedt, A. and Axell, L. B.: 1998, 'Modeling the Seasonal, Interannual, and Long-Term Variations of Salinity and Temperature in the Baltic Proper', *Tellus 50A*, 637-652.
- Omstedt, A. and Rutgersson, A.: 2000, 'Closing the water and heat cycles of the Baltic Sea', *Meteorol. Z.* **9**, 57-64.
- Omstedt, A. and Nyberg, L.: 1996, 'Response of Baltic Sea ice to seasonal, interannual forcing and climate change', *Tellus 48A*, 644-662.

Table 1. Mean water balance for the Baltic Sea (the Belt Sea and the Kattegat excluded) and the Bothnian Bay averaged over the 18-year period (From Omstedt and Axell, 2001). The symbols are : River runoff ( $Q_r$ ), precipitation (P), evaporation (E), inflow ( $Q_{in}$ ) and outflow ( $Q_{out}$ ). Units:  $10^3 \text{ m}^3 \text{ s}^{-1}$ .

Sea area	$Q_r$	P	E	P-E	$Q_{in}$	$Q_{out}$	Storage change
Baltic Sea	15.12	7.06	5.54	1.53	39.96	57.08	-0.47
Bothnian Bay	3.46	0.66	0.37	0.29	12.80	16.60	-0.05



Table 2. Mean heat balance for the Baltic Sea (the Belt Sea and the Kattegat excluded) and the Bothnian Bay averaged over the 18-year period (From Omstedt and Axell, 2000). The fluxes are positive when going from the water to the atmosphere. The symbols are: Sensible heat flux ( $F_h$ ), latent heat flux ( $F_e$ ), net long-wave radiation ( $F_l$ ), flux of short wave radiation reaching the open ocean ( $F_{so}$ ), heat flux from water to ice ( $F_w$ ), flux of short wave radiation reaching through the ice ( $F_{si}$ ) and  $F_{loss}=(1-A_i)(F_h+F_e+F_l+F_{so})+A_i(F_w+F_{si})$ , where the ice concentration is denoted by  $A_i$ . Unit:  $Wm^{-2}$

Sea area	$F_h$	$F_e$	$F_l$	$F_{so}$	$F_w$	$F_{si}$	$F_{loss}$
Baltic Sea	9	37	37	-88	4	-0	-1
Bothnian Bay	10	25	30	-66	7	-0	6

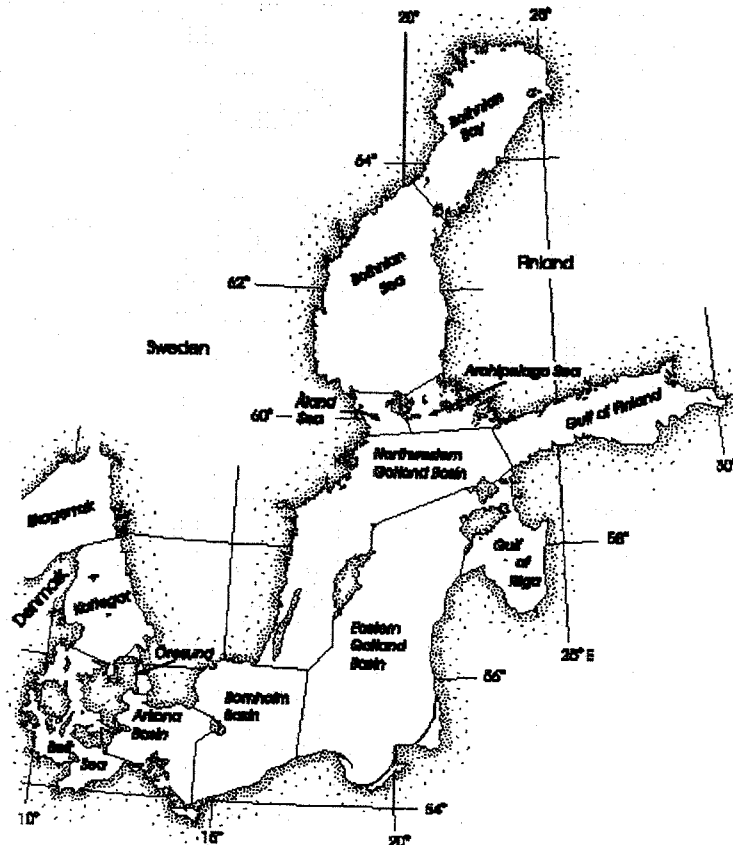


Figure 1. The division of the Baltic Sea into sub-basins as modelled by the PROBE-Baltic ocean model (Omstedt and Nyberg, 1996).

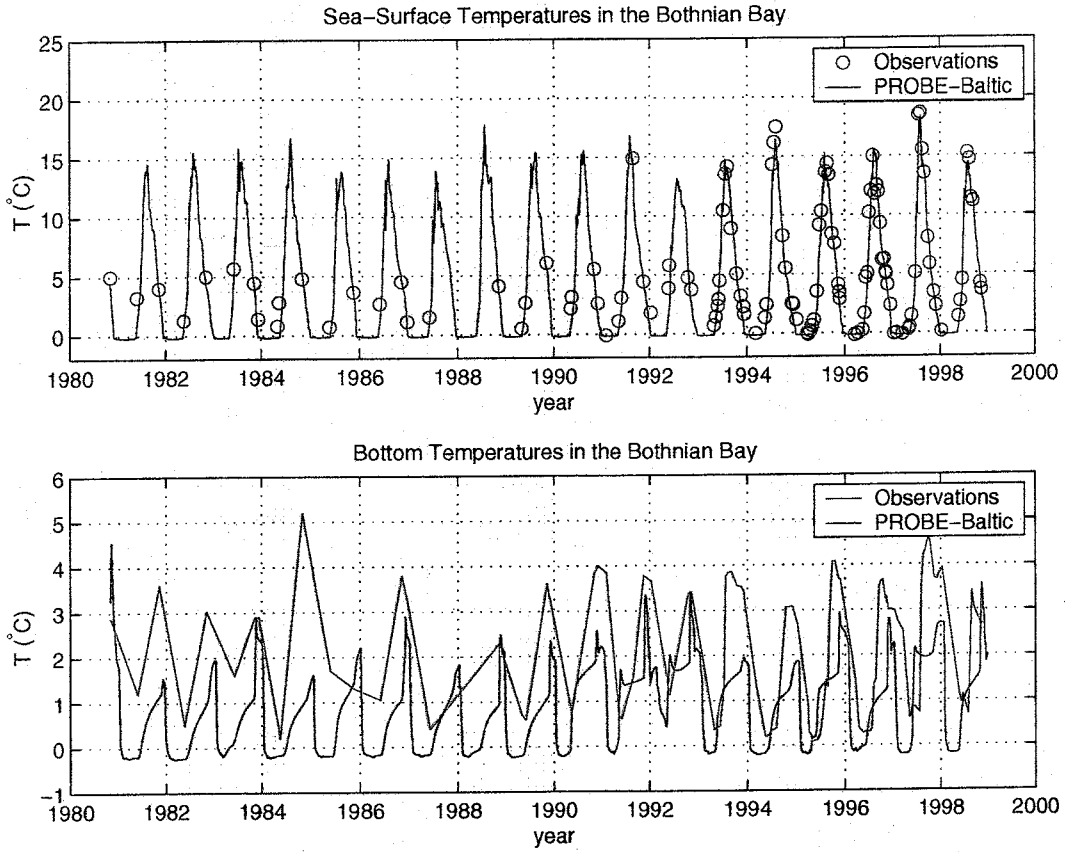


Figure 2. Observed (station F9) and calculated temperatures in the Bothnian Bay.

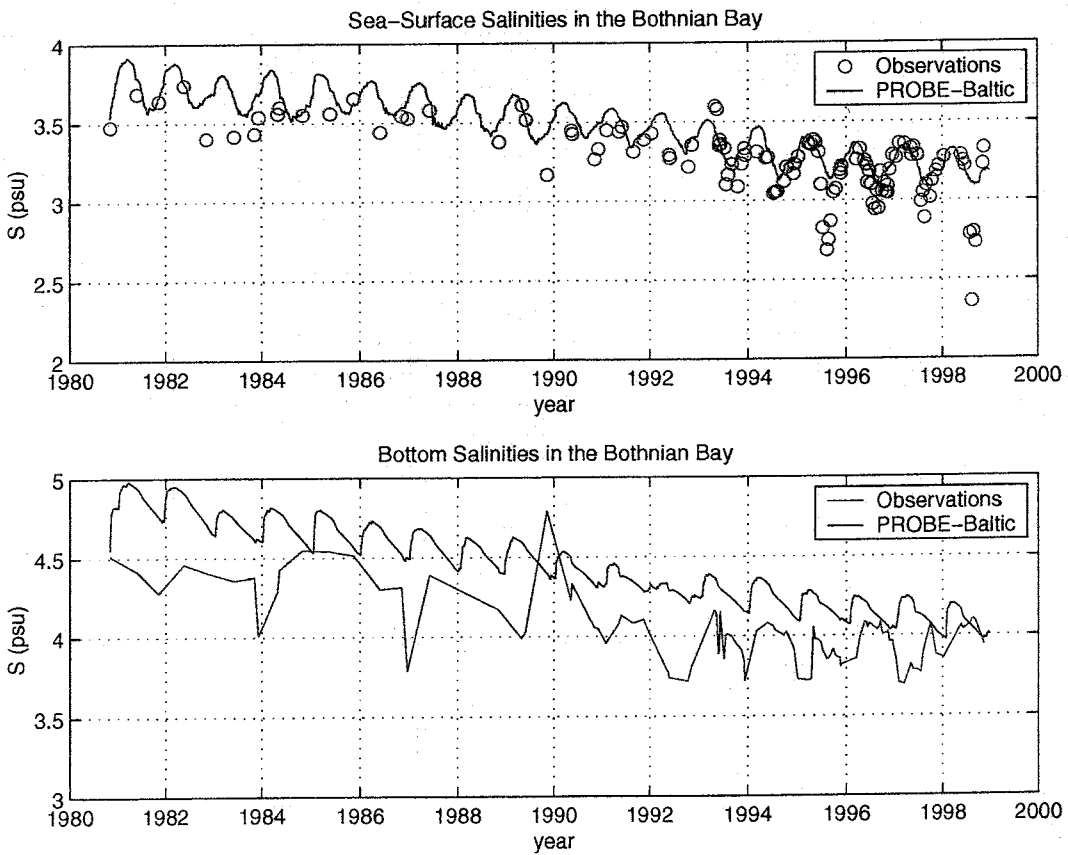


Figure 3. Observed (station F9) and calculated salinity in the Bothnian Bay.

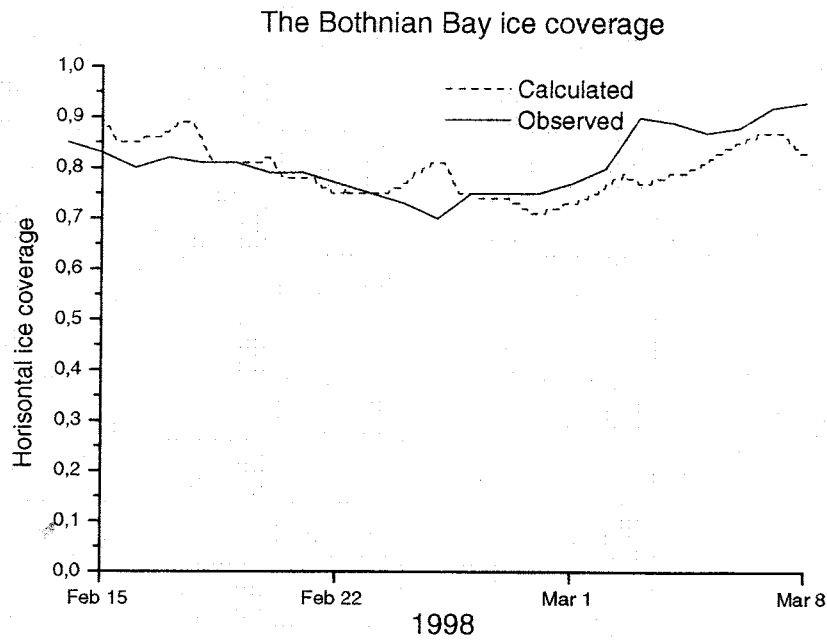


Figure 4. Observed and calculated ice coverage in the Bothnian Bay during the BASIS period.

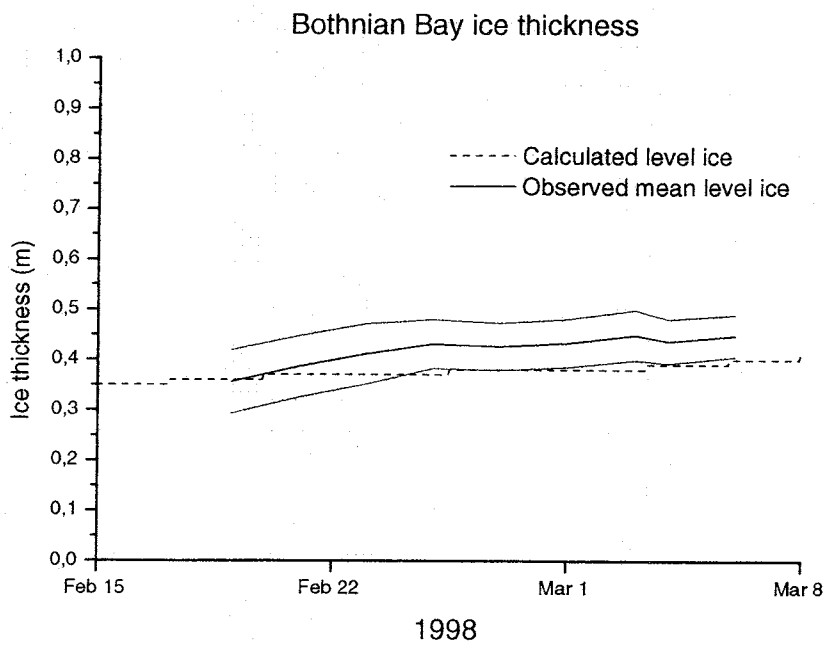


Figure 5. Observed and calculated level ice thickness in the Bothnian Bay during the BASIS period. The dotted lines indicate the standard deviation from the observed (Lundin, 2001).

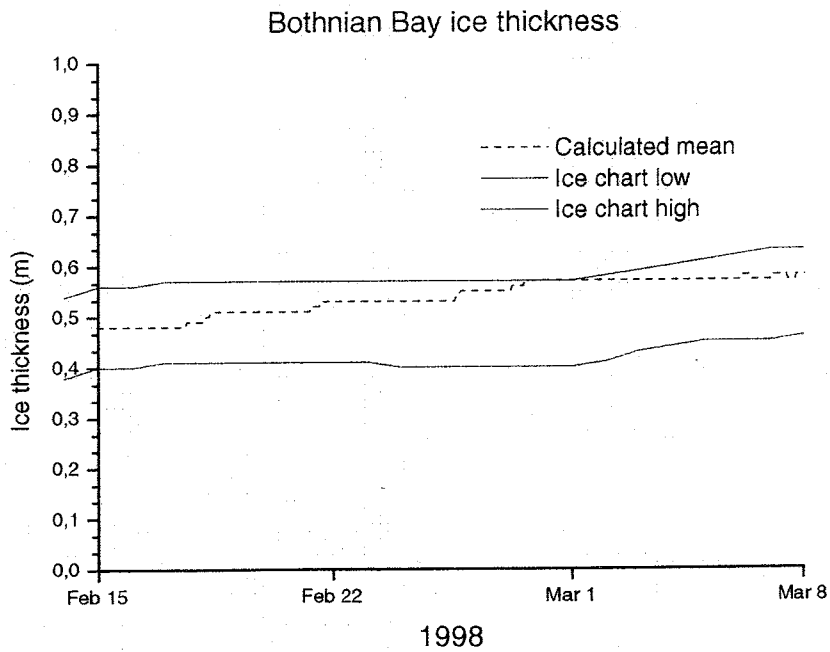


Figure 6. Observed and calculated mean ice thickness in the Bothnian Bay during the BASIS period. The observations are estimated from ice chart information and with low and high estimates.

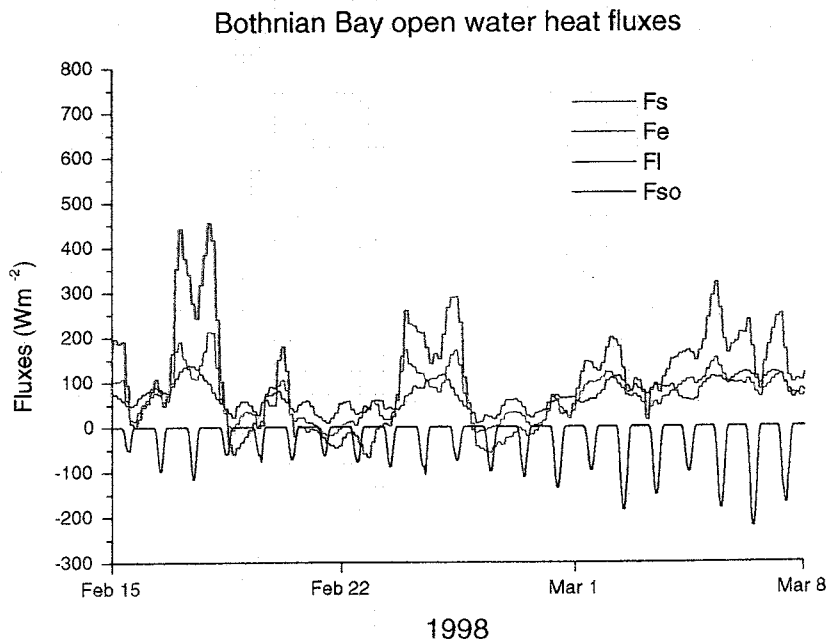


Figure 7. Calculated heat fluxes in the Bothnian Bay during the BASIS period.

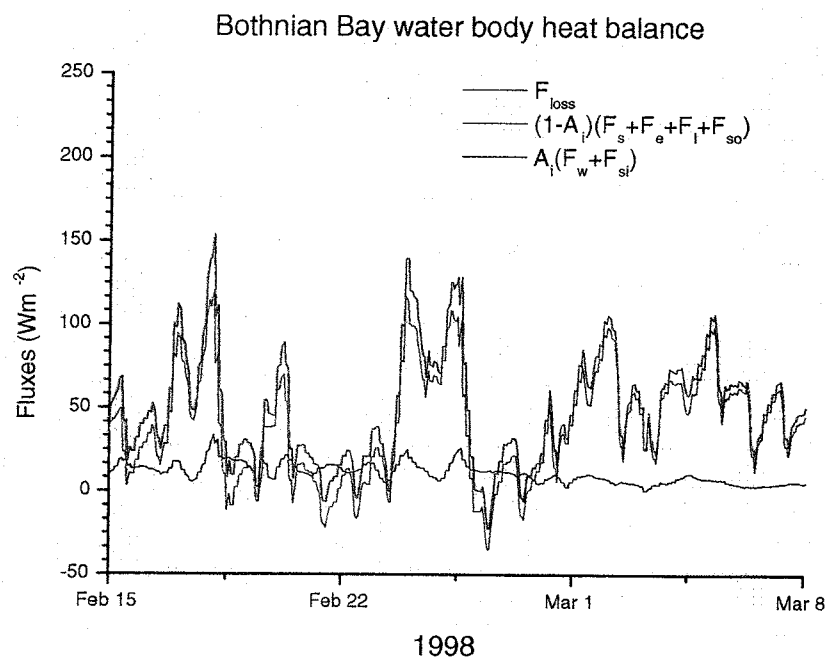


Figure 8. Calculated surface heat balance in the Bothnian Bay during the BASIS period, where  $F_{\text{loss}} = (1-A_i)(F_h + F_e + F_l + F_{so}) + A_i(F_w + F_{si})$ .

# Eddy Flux Measurements below Ice and Oceanic Boundary Layer Studies

Kunio Shirasawa, Kunio Kobinata and Toshiyuki Kawamura

Sea Ice Research Laboratory/The Institute of Low Temperature Science,  
Hokkaido University, Japan

## 1. Objectives

The objective of the field experiment was to measure turbulent fluxes of heat and momentum in the oceanic boundary layer (OBL) under the land-fast sea ice, and to study the OBL structure, ice-sea and air-sea interaction processes near the ice edge region in the Gulf of Bothnia during the BASIS 1998 field experiment. In particular, time series of the three-dimensional (3-D) currents, temperature and salinity were collected to estimate momentum and heat fluxes in the OBL under the sea ice. Temperature profiles through the air/ice/ocean were also measured to understand the heat conduction through the ice sheet. Ice cores were taken to analyze crystallographic structure and physical properties of sea ice.

## 2. Experimental Site

The main ice station was established in the land-fast sea ice region ( $63^{\circ}08.12'N$ ,  $21^{\circ}14.67'E$ ) westward from Vaasa. The ice-ocean study site of the Hokkaido University was located about 100 m from the FIMR (10m high) meteorological tower and about 280 m northwestward from *R/V Aranda*. The ice was about 42- to 45-cm-thick level ice at the ice-ocean study site at the beginning of the experiment on 18 February 1998. Ice cores were taken from several sites in the north, south, east and west from *R/V Aranda*.

## 3. Measurements and Methods

### 3.1. Under-ice current, temperature and salinity measurements

Development of under-ice current, temperature and salinity measurements is schematically shown in Figure 1. Two 3-D electromagnetic (EM) current meters (Model ACM32M, Alec Electronics Co. Ltd., Japan) were deployed from the 45-cm-thick ice at the depths of 0.5 m and 5 m below the ice-ocean interface on 19 February 1998. The water depth was 15.9 m. The EM current meters provide time series of fluctuations of 3-D currents ( $u$ ,  $v$ ,  $w$ ), temperature ( $T$ ) and conductivity ( $C$ ). Salinity ( $S$ ) is calculated from conductivity and temperature values. By sampling a bursting of 20 min in each hour, at a sampling rate of 1 sec, the data are collected of the duration of 8 days. The both EM current meters were recovered at 7:43 UTC on 27 February 1998, for changing memory and battery packs, and redeployed at the same site and depths at 12:38 UTC on 27 February. The ice thickness was 47.8 cm at that time. The both EM current meters were then finally recovered on 6 March 1998.

A frame consisting of a 3-D ultrasonic current meter (Model SD10, Union Engineering Co. Ltd., Japan) and a conductivity-temperature sensor (Model RD-CT, Union Engineering Co. Ltd., Japan) was deployed at the depth of 0.3 m below the ice-ocean interface near the EM current meter deployment site at 13:55 UTC on 20 February. The pair of the 3-D current meter and conductivity-temperature sensor provide time series of fluctuations of 3-D currents ( $u$ ,  $v$ ,  $w$ ), temperature ( $T$ ) and conductivity ( $C$ ) at a sampling rate of 0.2 sec. Those instantaneous values of currents, temperature and conductivity were recorded for the duration of 15 min in each every 30 min. The frame was recovered on 6 March 1998.

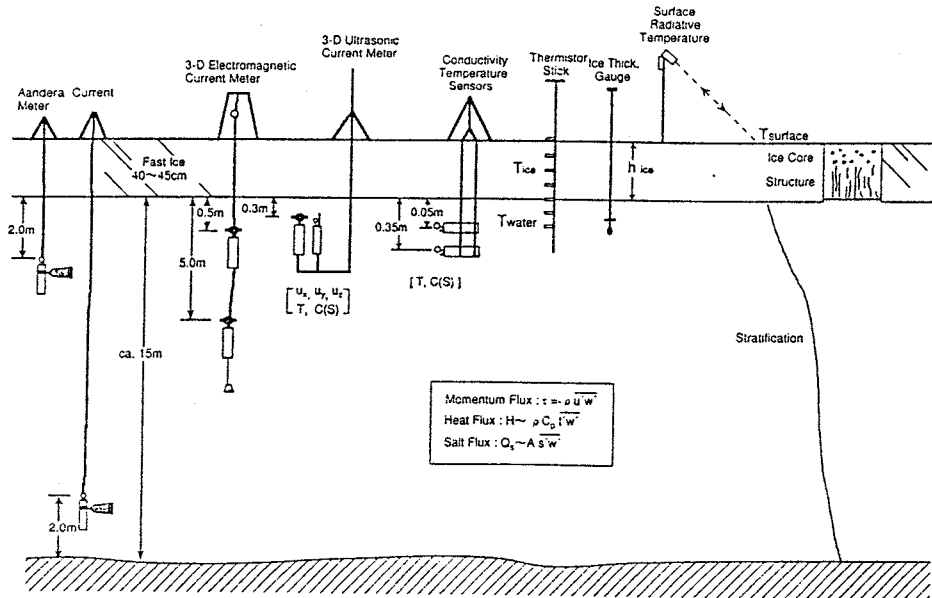


Figure 1A schematic picture of deployment of in- and under-ice measurements at the ice-ocean study site.

Two conductivity-temperature (C-T) sensors (Model RD-CT, Union Engineering Co. Ltd., Japan) were deployed at the depths of 0.05 and 0.35 m below the ice-ocean interface near the ultrasonic current meter deployment site on 20 February. The ice thickness was 42.6 cm. Time series of temperature and conductivity were recorded at a sampling rate of 0.2 sec for the duration of 15 min at every 30 min. The two C-T sensors were recovered on 6 March 1998.

The turbulent fluxes of oceanic heat, momentum and salt are to be calculated from the fluctuations of 3-D currents, temperature and salt by the eddy correlation method. The velocity data are used to calculate the mean vector and covariance (i.e., Reynolds stress/momentum flux) tensor in an east-north-vertical reference frame in which the mean vertical velocity component vanishes. The Reynolds stress components are  $\langle u'w' \rangle$  and  $\langle v'w' \rangle$ , where  $u'$ ,  $v'$  and  $w'$  are the downflow, cross-flow, and vertical flow fluctuations, respectively, and  $\langle \rangle$  denotes time averaging. Similar techniques are used for processing the fast response temperature data to get mean temperature and vertical heat flux,  $\langle w'T' \rangle$ , where  $T'$  is the temperature fluctuation.

### 3. 2. Ice thickness, temperature, salinity and structural properties

A thermistor string (Model SQ-1202, Grant Instruments, UK) was installed in the air and ocean through the ice sheet on 18 February 1998. One thermistor sensor was installed on a stick at a height of 1.5 m above the air-snow interface. Seven thermistor sensors were installed on the stick at the air-ocean interface (0 cm as the base of the depth meter), at the depths of 10, 20, 30 and 40 cm in the ice, and 45 and 55 cm in the ocean. The thermistor stick has been kept as it was at the setting up throughout the whole sampling period. A surface radiative temperature sensor (Tasco Co., Japan) was installed near the thermistor stick to measure the surface brightness temperature on 19 February 1998. The set of thermistors and radiative temperature sensor can provide time series of temperature profiles in the air, at the air-snow/ice surface, in the ice and in the ocean throughout the whole sampling period. The thermistor string was recovered on 6 March 1998.

Two ice thickness gauges were installed at the distance of 5 m from the EM current meter site; one towards the north and another towards the south on 19 February 1998. The ice thickness gauge is consisted of thin wire and electric cord with a stopper and a weight. The thickness of the ice can be measured manually by reading the length of the wire. The reading was made once a day throughout the whole sampling period. The thickness gauges were recovered on 6 March 1998.

Ice cores were taken from seven sites in the north, south, east and west from *R/V Aranda*. Those cores were analyzed at Hokkaido University in Japan, to understand crystallographic structure and physical properties of sea ice. The thicker sections allowed us to examine bubble and brine layer distributions under scatter light. Then, the sections were smoothed by planing to a thickness less than 0.1 cm and were illuminated under polarized light to identify individual grains and their structure. The ice core was also cut at about 4 to 5 cm-thick vertical sections along the entire core length. These samples were used to measure the density of each section. Thereafter, they were melted in a room temperature and their chlorinity values were determined by the titration method. The chlorinity values were converted to the salinity values by the formula  $S \sim 1.80655 Cl$ , where  $S$  is salinity and  $Cl$  is chlorinity (e.g., Bennett, 1976). The oxygen isotope composition ( $\delta^{18}O$ ) of selected melted samples was also determined with a mass spectrometer (Finnigan MAT 250, accuracy of 0.1‰).

## 4. Results

### 4. 1. Under-ice current, temperature and salinity measurements

#### 4.1.1 Current measurements

Time series of current speed and direction along with wind speed and direction are shown in Figs. 2 and 3, respectively. The currents at the depths of 0.5 and 5 m below the ice-ocean interface were obtained from the EM current meters, and the ones at the depth of 15.6 m were obtained from an Aanderaa current meter moored by FIMR. The wind speed and direction were obtained from *R/V Aranda*. The wind speed and air temperature depended on the synoptic weather conditions and wind direction. The winds were strongest during conditions of warm advection. The winds appeared to affect the under-ice currents. The maximum current speeds of 13 and 19  $\text{cm s}^{-1}$  at the depths of 0.5 and 5 m, respectively, on 23 February, appeared to correspond to the maximum wind speed of about 22  $\text{m s}^{-1}$  with a delay of 1-2 hours. Mean current speeds were 5-7  $\text{cm s}^{-1}$  at the depths of 0.5 and 5 m. For much of the sampling period the current speed at the depth of 15.6 m was below the threshold value of the Aanderaa current meter (1 to 2  $\text{cm s}^{-1}$ ).

The variability like a clockwise rotation in current direction appeared in 1-1.5 days period at the depths of 0.5 and 5 m. During a windy period the wind effect was felt in the under-ice currents after a delay of 1-2 hours. The currents between the west and northwestward were dominant at the depth of 0.5 m after 28 February. The current direction at the depth of 15.6 m was mainly the southwest to northwestward, and its variability was not pronounced, since the currents at that depth were too weak to detect for much of the sampling period. In addition to the wind, the under-ice currents were related to the variations in the water level.



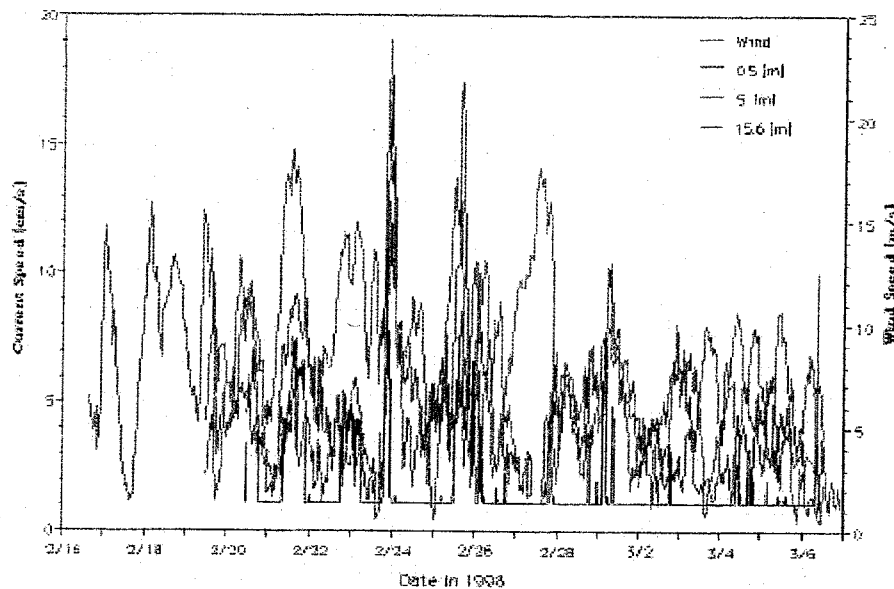


Figure 2 Time series of the under-ice current speed at the depths of 0.5, 5 and 15.6 m below the ice-ocean interface along with the wind speed obtained from *R/V Aranda*.

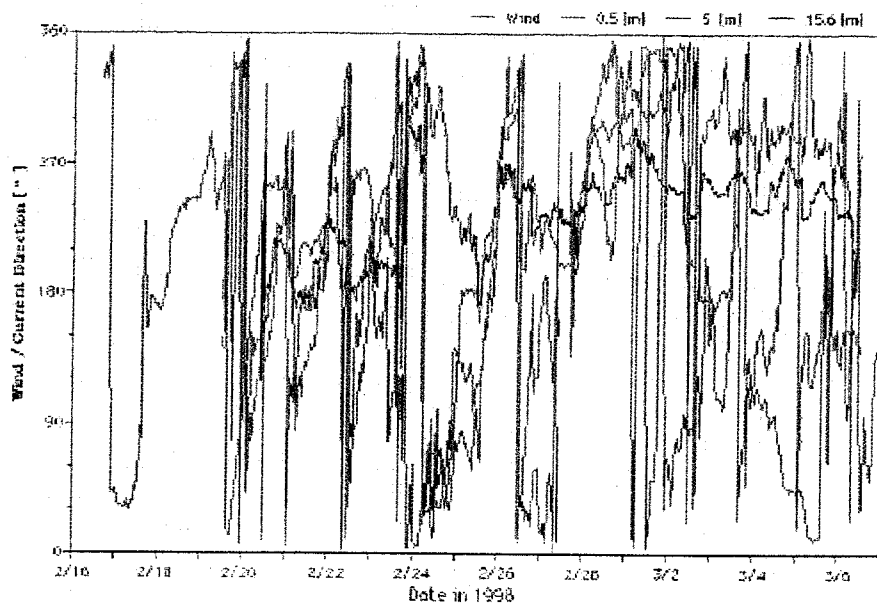


Figure 3 Time series of the under-ice current direction at the depths of 0.5, 5 and 15.6 m below the ice-ocean interface along with the wind direction obtained from *R/V Aranda*.

#### 4. 1. 2. Water temperature and salinity measurements

Characteristics of the temperature and salinity conditions below the ice along with the air temperature are shown in Figure 4. The temperatures in the air and water showed as a whole large variations. The generally warm conditions were interrupted by cold periods from 23 to 25 February and again from 28 February. The water temperatures showed a pronounced decrease from 28 February in the upper 0.5-m layer, which corresponded to that of the air temperature. The salinity showed also an overall decrease during the observational period in

the upper layer. The salinity at the upper 0.5-m layer showed a pronounced decrease from 28 February, which corresponded to the predominant currents altered to the west to northwestward at the upper layer (Figure 3). It is therefore suggested that the less saline water in the upper layer could be transported from the southeast, while the decreasing trend in temperature and salinity was not pronounced at the depth of 5 m.

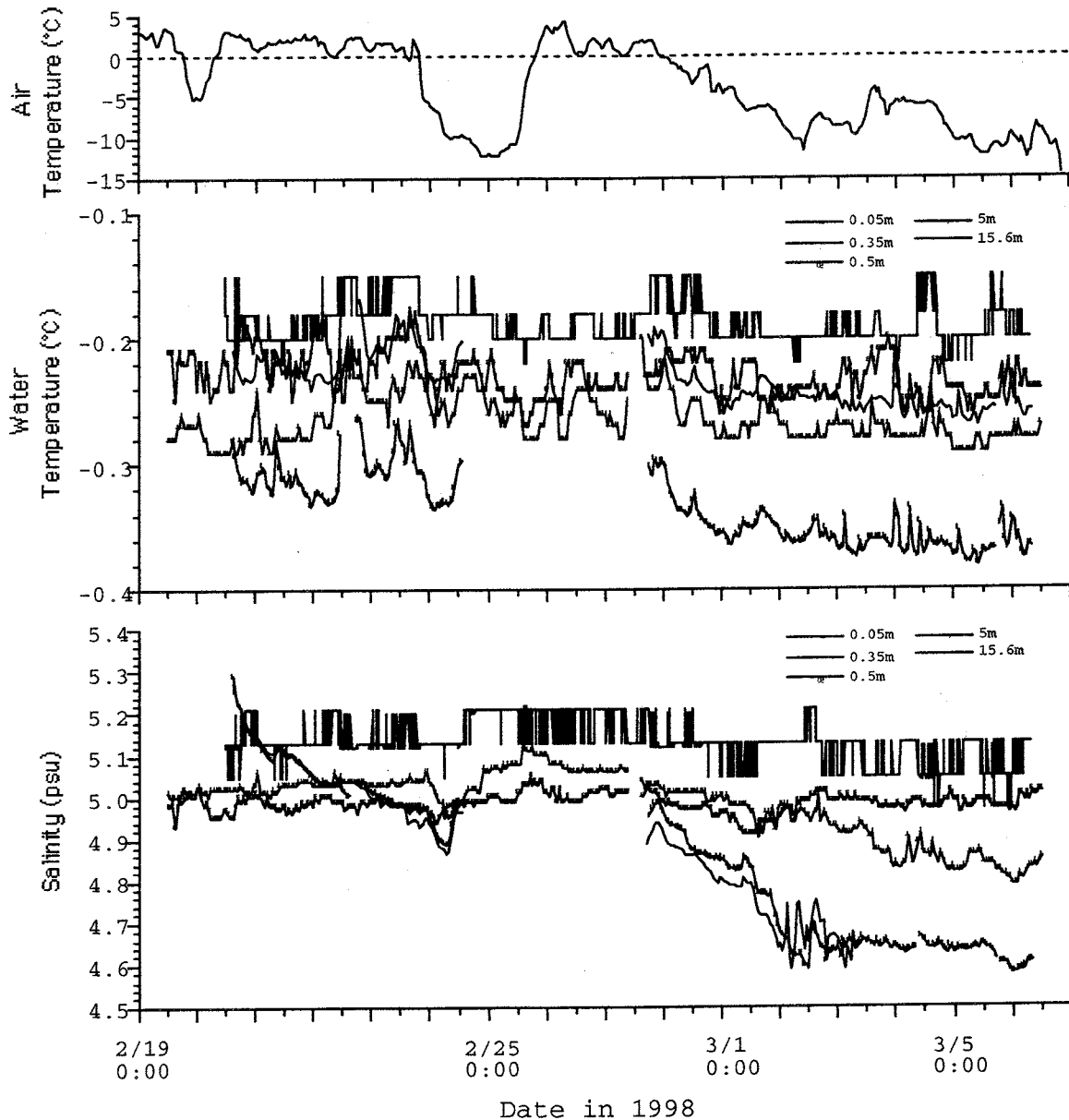


Figure 4 Time series of the water temperature and salinity at the depths of 0.05, 0.35, 0.5, 5 and 15.6 m below the ice-ocean interface along with the air temperature obtained from *R/V Aranda*

#### 4. 1. 3. Turbulent fluxes of momentum and heat

Time series plots of under-ice momentum flux (i.e., the Reynolds stress) and oceanic heat flux obtained at the depths of 0.5 and 5 m are shown in Figure 5. The Reynolds stress ( $\tau$ ) and the oceanic heat flux ( $F_w$ ) showed, as a whole, large variations. The Reynolds stress ( $\tau$ ) was within almost 0.02 and 0.1 Pa at the depths of 0.5 and 5 m, respectively (Figure 5a). The mean Reynolds stress during the sampling period was 0.004 and 0.05 Pa at the depths of 0.5 and 5 m, respectively. It is noticeable that the mean Reynolds stress at the depth of 5 m was one order larger than that at the depth of 0.5 m. The oceanic heat flux ( $F_w$ ) was within almost  $\pm 20$  and  $40 \text{ Wm}^{-2}$  at the depths of 0.5 and 5 m, respectively (Figure 5b). The mean oceanic heat flux during the sampling period was  $-0.2$  and  $-0.9 \text{ Wm}^{-2}$  at the depths of 0.5 and 5 m, respectively. The mean oceanic heat flux at the depth of 5 m was larger than that at the depth of 0.5 m.

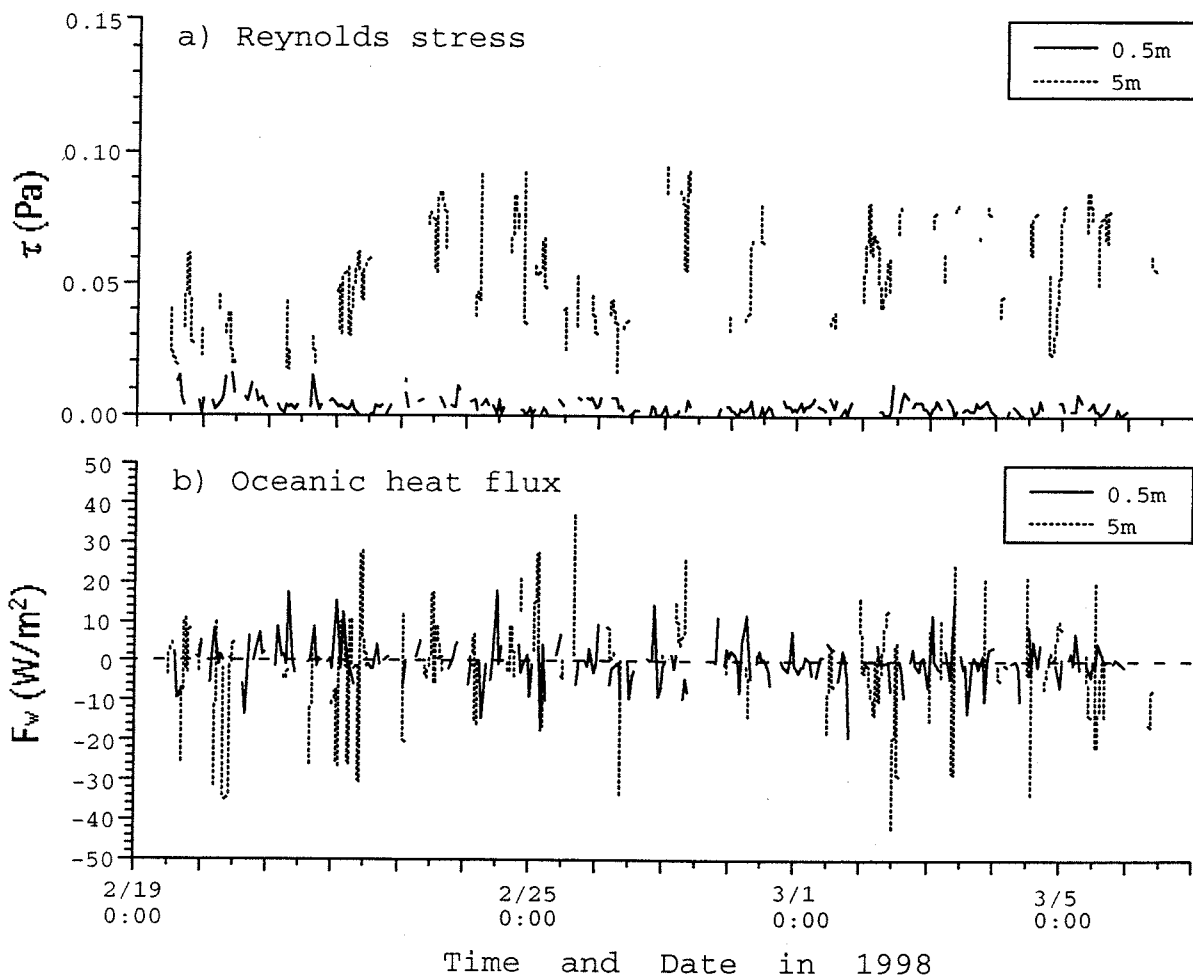


Figure 5 Time series of (a) the Reynolds stress and (b) oceanic heat flux obtained at the depths of 0.5 and 5 m below the ice-ocean interface.

The bulk transfer coefficient of momentum flux, i.e., the drag coefficient,  $C_w(0.5\text{m})$  was between 0.001 and 0.01, based on the depth of 0.5 m for the neutral condition ( $-0.1 < z/L < 0.05$ , where  $z$  is the depth and  $L$  is the Obukhov length). The mean  $C_w(0.5\text{m})$  for the neutral

condition was 0.0025. The mean bulk transfer coefficient of oceanic heat flux,  $C_h(0.5m)$  was 0.0054 based on the depth of 0.5 m for the neutral condition. The power spectra of wind, current, turbulent fluxes and water level are shown in Figure 6. The water level obtained from Vaasa showed the peak of 32.5-hour period, which can correspond to a period of seiche in that area (Kullenberg, 1981). The peak of the power spectrum of the Reynolds stress ( $\tau$ ) at the depth of 5 m corresponds to that of the water level. There are not found pronounced peaks in wind, current and heat flux, but found a little in the current direction at the depth of 5 m with about 70 hours period.

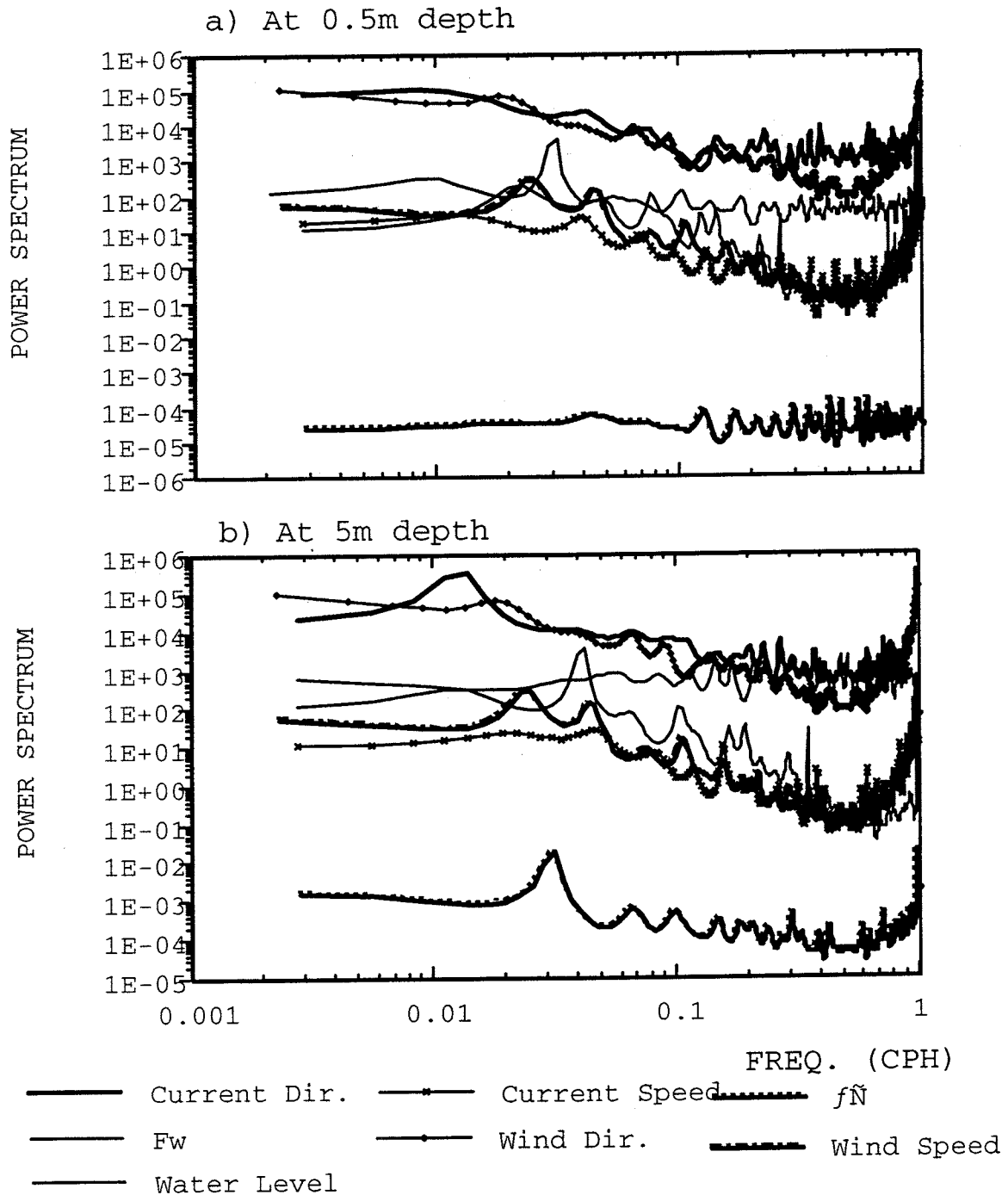


Figure 6 Power spectra of the wind, current, turbulent fluxes and water level obtained from Vaasa.

#### 4. 2. Physical properties and isotopic characteristics of sea ice

Photographs of vertical and horizontal sections, salinity, density, oxygen isotope composition ( $\delta^{18}\text{O}$ ) and porosity of sea ice were obtained at seven sites. One typical case obtained at the site 1 was shown in Figure 7. At all sites the columnar structure was predominant along the entire section except the granular structure at the top part of the core. The granular structure was also found at the bottom layer at the site 5 and at the thin layer at the bottom of the core at the site 7. The salinity was, as a whole, within 1.2 psu, and the density was almost consistent at  $900 \text{ kgm}^{-3}$  at the sites 1 (Figure 7), 2, 3, 5 and 6. The density of granular ice at the top layer was less than  $800 \text{ kgm}^{-3}$  at the site 4. The density at the site 7 was almost consistent at  $850 \text{ kgm}^{-3}$  for the granular ice predominant along the entire section except for  $900 \text{ kgm}^{-3}$  for the columnar ice at the bottom part of the core. The oxygen isotope composition ( $\delta^{18}\text{O}$ ) was, as a whole,  $-14$  to  $-15\text{‰}$  for the granular ice and  $-6$  to  $-7\text{‰}$  for the columnar ice. It is therefore suggested that the granular ice could be originated from snow cover and the columnar ice could be formed from sea water. At the site 1 there exists the pronounced boundary between the granular structure at the 9.5-cm top layer and the columnar structure at the underlying layer, where the  $\delta^{18}\text{O}$  and porosity change distinguishably from  $-15\text{‰}$  and  $5\%$  at the top layer to  $-7\text{‰}$  and  $2\%$  at the bottom layer, respectively (Figure 7).

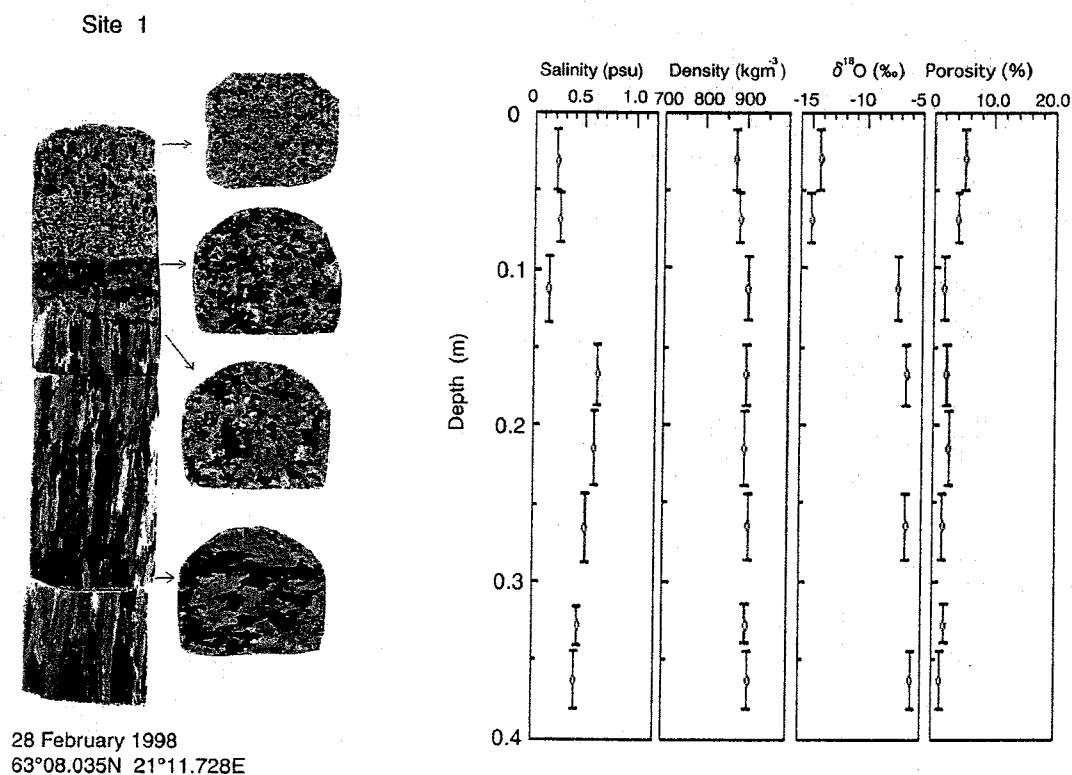


Figure 7. Photographs of vertical and horizontal sections, salinity, density, oxygen isotope composition and porosity of sea ice at the site 1.

**Acknowledgments.** We are grateful for all staff of the BASIS 1998 field experiment, the captain and crew of *R/V Aranda*, Osamu Matsubaya for analyzing oxygen isotope composition, and Toru Takatsuka, Takaharu Daibou and Eriko Uematsu for processing the field data.

**References**

- Bennett, A.S.: 1976, 'Conversion of in situ measurements of conductivity to salinity', *Deep-Sea Res.* **23**, 157-165.
- Kullenberg, G.: 1981, 'Physical Oceanography', in *The Baltic Sea*, A. Voipio (ed.), Elsevier Oceanography Ser., 30, Elsevier Scientific Publishing Co., Amsterdam, 135-181.

## 6. MODELLING

### Modelling of Sea Ice Thermodynamics

Bin Cheng, Jouko Launiainen, Timo Vihma and Juha Uotila  
Finnish Institute of Marine Research, Helsinki, Finland

#### 1. Introduction

The air-ice coupling and ice thermal variation are studied using a one-dimensional thermodynamic sea ice model (Launiainen and Cheng, 1998; Cheng and Launiainen, 1998) applied to the Baltic Air-Sea-Ice Study (BASIS) field data. The numerical integration of the vertical heat conduction equation is considered as an essential part of the model which resembles to those of Maykut and Untersteiner (1971) and Gabison (1987).

The boundary conditions of the heat conduction equation are however well considered and specified compare with those of the old models. The main physical processes expressed in the model involve the air-ice coupling, heat fluxes and heat balance at the surface and the ice bottom, heat conduction in the multi-layer snow and ice, and mass balances at the surface and the bottom. A schematic presentation of the model is given in Figure 1. Model solutions are obtained using the procedures briefly given below:

1) The radiative surface fluxes of the net downward short-wave radiation  $(1-\alpha)Q_s$ , the short-wave absorption in snow and ice ( $I$ ), the downward ( $Q_d$ ) and upward ( $Q_b$ ) long-wave radiation are calculated using various parameterization schemes. The turbulent air-ice fluxes of momentum ( $\tau$ ), the sensible heat ( $Q_h$ ), and the latent heat ( $Q_{le}$ ) are calculated on the basis of Monin-Obukhov similarity theory. An integration of the non-dimensional universal profile gradients of wind speed ( $V$ ), temperature ( $T$ ) and moisture ( $q$ ) yields the vertical profiles of  $V(z_a)$ ,  $T(z_a)$  and  $q(z_a)$  in the surface layer (SL) of the atmosphere. Those surface heat fluxes together with the surface conductive heat flux ( $F_c$ ) construct a heat and mass balance equation for the surface layer of snow or ice. This balance serves as the upper boundary condition needed for the heat conduction equation of snow or ice. The surface temperature ( $T_{sfc}$ ) is the critical quantity to be iterated in the solution of the surface heat balance. Surface melting ( $\Delta h_s$ ) is a response to the surface heat balance when the surface temperature tends to increase above the freezing point.

2) The temperature profile in the ice  $T_i(z,t)$  is numerically solved from the heat conduction equation with the boundary temperature ( $T_{sfc}$ ) at the surface and the freezing temperature ( $T_f$ ) at the ice bottom, respectively. Absorption of short-wave radiation  $I(z,t)$  in the snow and ice is an additional source term in the heat conduction equation. The volumetric heat capacity  $(\rho c)_{si}$  and the heat conductivity of sea ice ( $k_{si}$ ) are functions of ice salinity ( $s_i$ ) and temperature. In the case of a thin snow cover,  $0 < h_s < 0.01\text{m}$ , a single snow layer ( $Q_{si}$ ,  $h_s$ ) is coupled with ice. For snow thickness of over 0.01m, the heat conduction equation is also applied to calculate temperatures ( $T_{snow}$ ) at various depths in the snow. The snow-ice interface temperature ( $T_{in}$ ) is calculated according to the flux continuation assumption ( $F_c = Q_{si}$ ). If the snow melt is followed by freezing temperatures, the melt-water is assumed to refreeze to snow-ice on the basis of the mass conservation without delay.

3) The difference between the heat flux from the ocean mixed layer ( $F_w$ ) and conduction upwards from the ice bottom ( $Q_c$ ) determine the ice growth or melt ( $\pm \Delta h_i$ ) at the ice bottom.

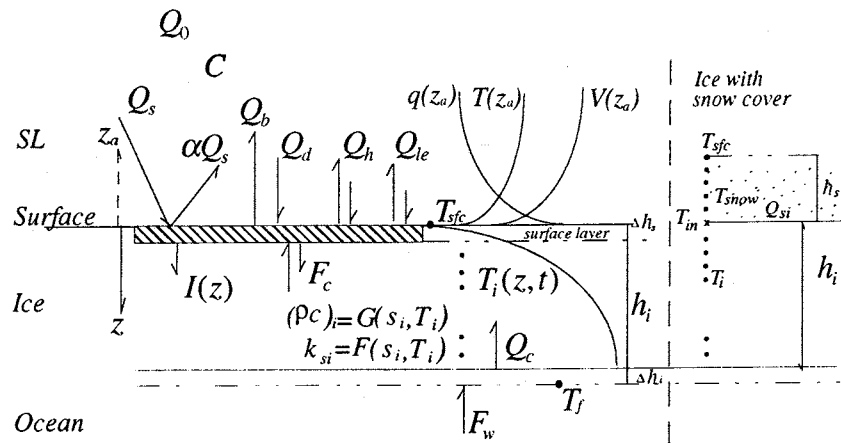


Figure 1. Structure of the FIMR one-dimensional thermodynamic sea ice model. For symbols, see the text.

## 2. Field data and model parameters

Observations for validation and optimization of the thermodynamic ice model were performed during the BASIS field campaign in the Northern Baltic Sea in 1998. Observations of wind speed, air temperature and relative humidity were made from a sea ice weather mast. The 10-minute averages of these quantities served as the forcing data for the ice model. The data time series are shown in Figure 2. Cloudiness ( $C$ ) was observed visually every 3 hours. Downward and upward short-wave and long-wave radiation were measured during BASIS, but some of these measurements are missing, nearly 27% of the total BASIS period, due to bad weather conditions. Large variations were observed in the surface albedo, and the measured short-wave radiation and albedo values were used for the model input. In the case of missing data, *R/V Aranda's* short-wave radiation measurements and an average albedo of 0.73 were used. A sonic anemometer was also deployed, and eddy fluxes of sensible heat and momentum were measured.

A thermistor string with 11 sensors was deployed vertically through the snow and ice. The temperatures of near-surface air, snow, ice, and sea water near the ice bottom were measured at various levels. The installation of the thermistor string and its sensors are shown schematically in Figure 3, indicating the initial and final stages in the ice. Snow and ice thickness were measured manually once a day at 10 locations near the thermistor string. The daily means of snow thickness were interpolated linearly and used as model input. For a short-period simulation, the model parameters were specified to correspond to the BASIS field characteristics; these are given in Table 1 (note that the salinity of the Baltic Sea ice is much less than that of the sea ice in the oceans). In this study, an oceanic heat flux was specified as an input for the model. Eddy flux measurements performed in the water near the ice bottom suggested that there was, on average, a small upward heat flux during BASIS. Its small magnitude ( $1.0 \text{ W m}^{-2}$ ) is explained by the strong water stratification below the ice in the Baltic Sea. In the simulation, we initialized the model with the weather forcing of BASIS and with the diurnal solar radiation until a stable vertical temperature profile in the snow and ice was achieved.



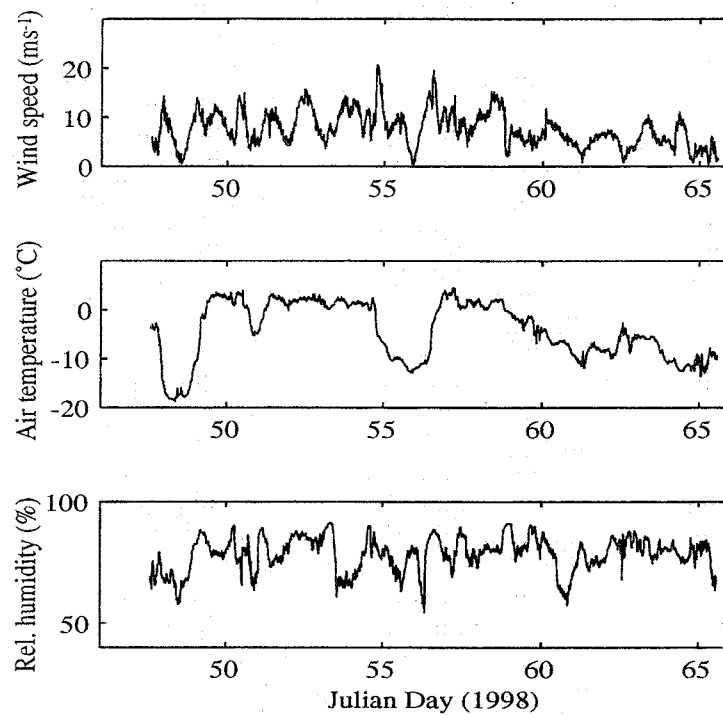


Figure 2. Time series of wind speed (at 10m), air temperature (10m) and moisture (4.6m) during BASIS.

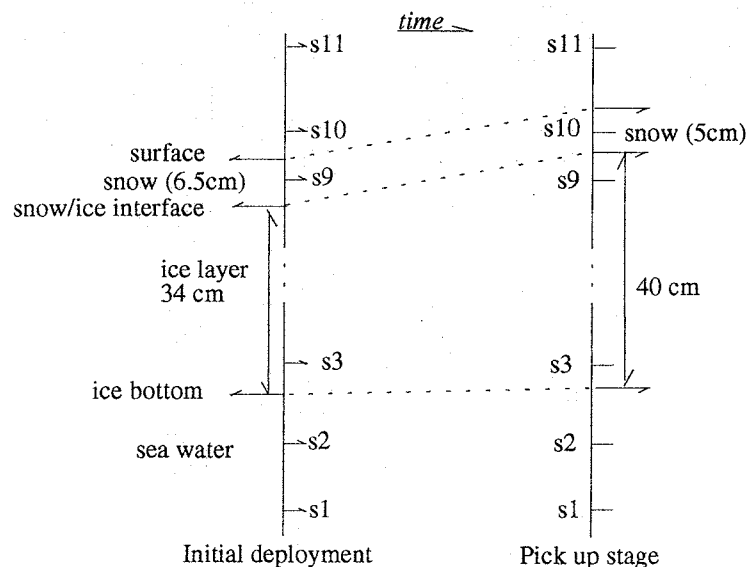


Figure 3. Geometric location of sensors attached to an ice thermistor string in the air/snow surface, snow/ice interface and ice/water. At the beginning, sensor s10 was 1.5 cm above the surface. The snow depth was 6.5 cm (3 cm soft snow + 3.5 cm hard snow) measured from the surface of the ice. The ice thickness was 34 cm. S3 was 5 cm from the ice bottom. At the end of BASIS, s10 was situated 3.5 cm below the snow surface. The snow-ice interface was 1.5 cm below s10 and the total ice thickness was 40 cm. A 4.5 cm distance in depth between s3 and the ice bottom was measured.

Table 1. Model parameters based on BASIS measurements and the literature.

Aerodynamic roughness ( $z_o$ )	$10^{-4}$ m	Launiainen et al.(2001)
Extinction coefficient of sea ice ( $\kappa_i$ )	1.5 - 17 $m^{-1}$	modified from Maykut and Grenfell (1977)
Extinction coefficient of snow ( $\kappa_s$ )	25 $m^{-1}$	Perovich (1996)
Freezing point ( $T_f$ )	-0.26 °C	$T_f \approx -0.054 \cdot s_w$
Sea ice volumetric heat capacity ( $\rho \cdot c$ ) <sub>i</sub>	$G(T_i, s_i)$	Maykut and Untersteiner (1971)
Heat capacity of ice ( $c_i$ )	2093 J $kg^{-1}$ K <sup>-1</sup>	
Latent heat of freezing ( $L_i$ )	$0.33 \times 10^6$ J $kg^{-1}$	
Oceanic heat flux ( $F_w$ )	1.0 W $m^{-2}$	BASIS eddy measurement (average)
Sea ice density ( $\rho_i$ )	910 $kg\ m^{-3}$	
Sea ice salinity ( $s_i$ )	0.59 - 0.75 ppm	BASIS ice core measurement
Sea water salinity ( $s_w$ )	4.9 ppm	BASIS measurement (average)
Snow density ( $\rho_s$ )	310 $kg\ m^{-3}$	BASIS measurement (average)
Surface emissivity ( $\epsilon$ )	0.97	
Sea ice heat conductivity ( $k_{si}$ )	$F(T_i, s_i)$	Maykut and Untersteiner (1971)
Thermal conductivity of ice ( $k_i$ )	2.03 W $m^{-1}$ K <sup>-1</sup>	
Thermal conductivity of snow ( $k_s$ )	0.24 W $m^{-1}$ K <sup>-1</sup>	calculated according to Yen (1981)
Time step of model ( $t$ )	10 minutes	
Number of layers in the ice	10	
Number of layers in the snow	5	

### 3. Results and discussion

The observed surface fluxes are compared with the modelled results. The measured downward solar radiation in the midday period showed several large peaks. Although the measured value were used as the input data for the model run, the short-wave radiation calculated by an empirical sinusoidal formula were compared with the measurement. The calculated short-wave radiation was obtained by  $Q_s = Q_0(1-0.52 \cdot C)$ , where  $Q_0$  is the result of Shine's (1984) formula for clear skies, and  $(1-0.52 \cdot C)$  is a cloudiness factor given by Bennett (1982).

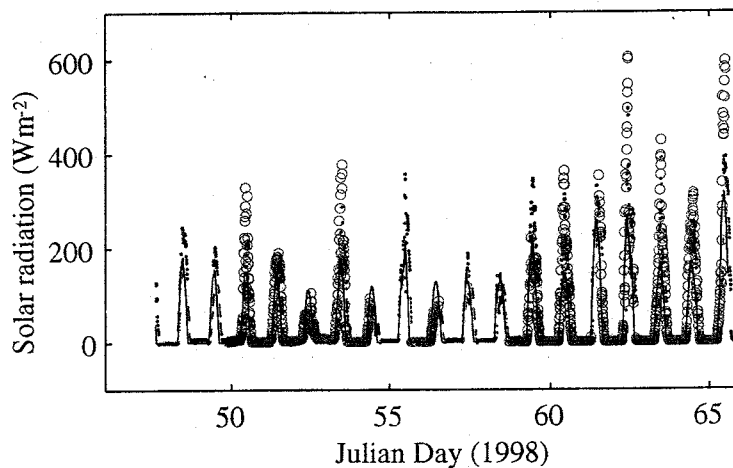


Figure 4. Measured and estimated short-wave radiation. Circles (red) indicate measurements by the radiometer over the sea ice and solid dots (green) measurements on the *R/V Aranda*. The solid line (black) gives the results calculated using an empirical formula. The model input uses the measured values.

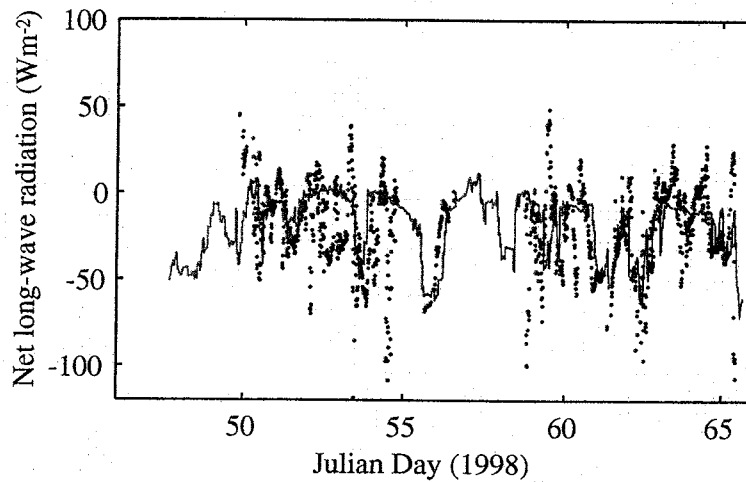


Figure 5. Net long-wave radiation flux comparison. The solid line (red) gives the ice model estimate and dots (blue) are the observed values.

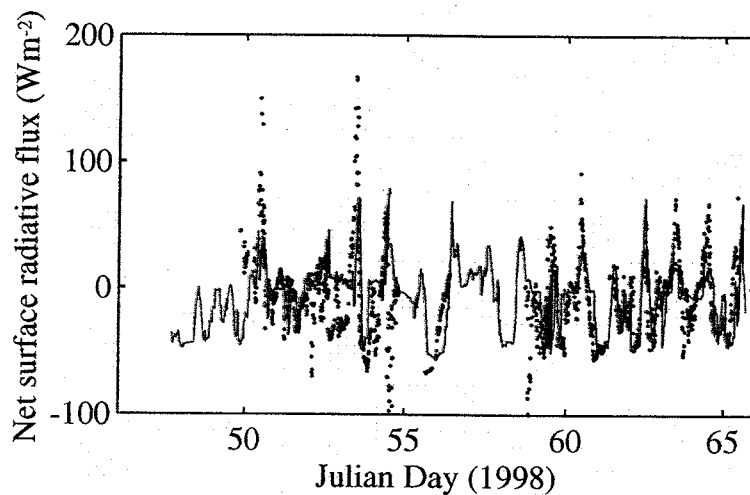


Figure 6. Net surface radiative flux (short-wave + long-wave radiation flux) comparison. The solid line (red) gives the calculated value and dots (blue) are the observed ones.

Figure 4 gives the comparison of measured and calculated short-wave radiation. The difference may be due to multiple reflections between the snow surface and clouds. During the occurrence of the large peaks, the cloud cover was between 0.5 and 1, and large peaks were also present in *R/V Aranda's* shortwave radiation data. According to several authors (Schneider and Dickson, 1976; Shine, 1984; Wendler and Eaton, 1990) neglect of multiple reflections may lead to errors of 30-60% in the surface shortwave radiation flux. Several parameterizations of downward long-wave radiation are included in the ice model code for comparison. That of Prata (1996) combined with the cloudiness factor of Jacobs (1978) was selected in this study. Comparison of the observed and calculated net long-wave radiation flux is given in Figure 5. The difference was mainly related to the estimation of downward long-wave radiation, especially during the period before day 55, when the air temperature was above freezing point and melting was found by the model. In the later part of the period, the calculation compares somewhat better with the measurements. The time series of calculated and observed net surface radiation flux indicate a reasonable comparison for most of the time (Figure. 6). Additionally, the model gives a good estimation of surface turbulent flux of

momentum and sensible heat (Figure. 7). The mean values of the various surface fluxes are given in Table 2.

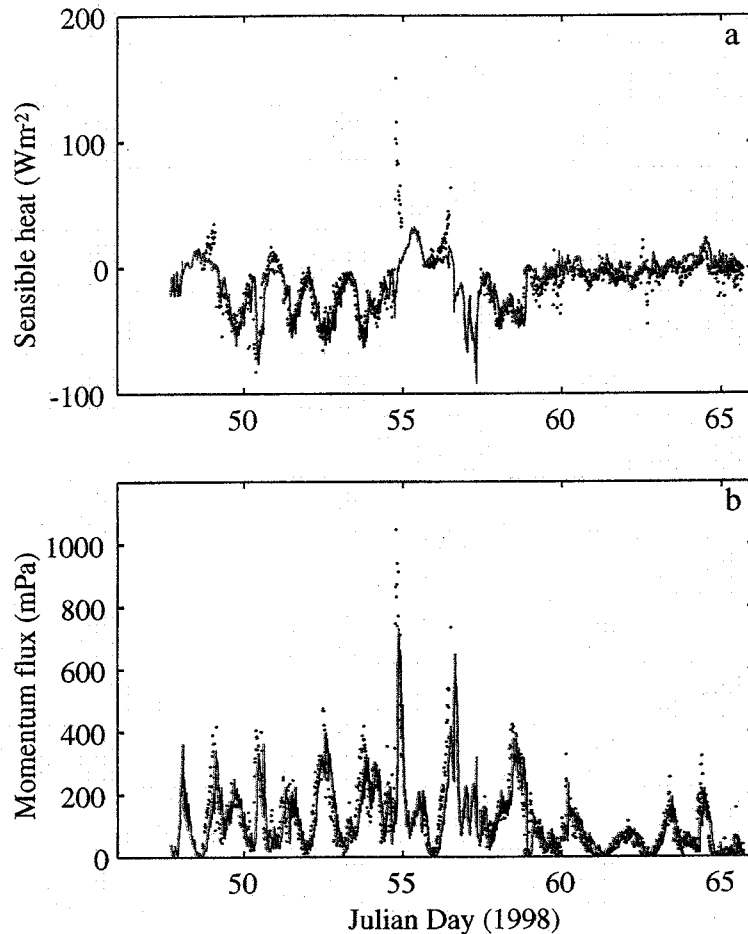


Figure 7. Modelled (red line) turbulent surface fluxes of sensible heat (a) and momentum (b) compared with those measured as eddy fluxes by the sonic anemometer (blue dots).

Table 2. Observed and calculated mean values of various surface heat fluxes.

	$Q_s(\text{down})$	$Q_s(\text{net})$	$Q_d$	$Q_b$	$Q_d + Q_b$	$Q_{net}$	$T_{sfc}$	$Q_h$	$\tau$
<i>Obs.</i>	50	11	262	-282	-20	-9	-6.3	-11	113
<i>Cal.</i>	34	9	270	-287	-17	-8	-4.4	-10	105

A comparison of the observed and modelled in-ice temperatures is given in Figure 8. The thermistor string measurements indicated a snow-ice formation near the surface (Fig. 3). At the beginning of the period, a large vertical gradient is seen in the experimental in-ice temperature profile (Fig. 8a), indicating a rapid freezing around the thermistor string after its installation. This was not well simulated by the ice model (Fig. 8b), because the installation of the thermistor string caused water flooding near surface, which was not taken into account in the model initialization. The modelled average in-ice conductive heat flux was  $10.7 \text{ W m}^{-2}$  upward, while the thermistor string measurement indicated an average upward heat flux of  $8.1 \text{ W m}^{-2}$  in the ice. The difference may be due to the inaccuracy of the estimated heat conductivity and the complexities of a snow cover above ice. However, the results (Fig. 8b) still indicate an encouraging agreement with the observed thermal structure and its time development. The modelled air-snow interface temperature was compared with the radiation measurement-derived surface temperature, and with estimates derived from the flux-profile

relationships (Launiainen et al., 2001). The results indicate that the ice model can generally reproduce the surface temperature well. However, in cases of small surface heat fluxes, the surface boundary being flux-controlled in the model, the modelled surface temperature may be less accurate.

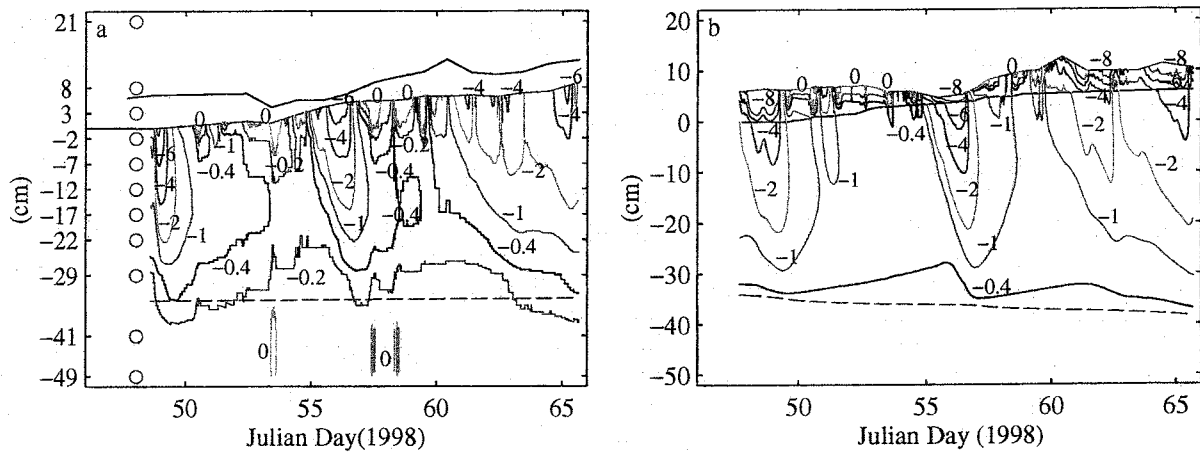


Figure 8. Internal ice temperatures ( $^{\circ}\text{C}$ ) during the BASIS experiment. a) Observed in-ice temperatures. Circles indicate the locations of sensors attached to the thermistor string. b) In-ice temperatures calculated by the ice model. The three horizontal lines show the average observed (a) and modelled (b) evolution of the height/depth of the snow surface, the snow/ice interface and the ice bottom.

The measured snow and ice and modelled ice thickness variations are given in Figure 9. The measurements of snow and ice show distinct areal and temporal variations in the test area, due to the highly variable weather during the BASIS experiment. The surface melting largely occurred when the measured air temperatures were above freezing. Figure 9b shows the time series of the modelled surface melting, producing a cumulative snow thickness change of about 12 cm. Figure 9c gives the modelled ice growth at the ice bottom, leading to an increase in thickness of 3 cm. Figure 9d shows the simulated ice thickness compared with the measurements. Assuming the surface meltwater is totally refrozen, and the density ratio between the snow and sea ice is 0.35, the above modelled melting would correspond roughly to about 5 cm of snow-ice formation. In practice, however, instead of immediately re-freezing, melting water percolates into the snow/ice interface and may be mixed with snow forming a slush layer, which later will be refrozen under the proper weather conditions. Such a layer of slush or snow-ice will affect the heat conduction and heat flux through the whole ice layer. These uncertainties may cause discrepancies between the measurements and modelling of ice temperature and ice thickness. Further studies on this aspect are needed.

The ocean flooding is another source for slush layer and snow-ice formation. In general, the ocean flooding depends on the density of sea water ( $\rho_{sw}$ ), sea ice ( $\rho_{si}$ ), and snow ( $\rho_s$ ), as well as the depth of snow  $h_s$  and ice  $H_i$ . Assuming that  $\rho_{si} \approx 0.9 \rho_{sw}$  (Baltic Sea is almost fresh water body, since the average salinity is low), according to the Archimedes law, the criterion (ice surface start to merge below water level) for ocean flooding would be:

- (a)  $h_s \geq 0.6 H_i$  for very fresh (soft) snow, i.e.  $\rho_s < 0.15 \rho_{sw}$
- (b)  $h_s \geq 0.2 H_i$  for very old (hard) snow, i.e.  $\rho_s < 0.5 \rho_{sw}$

In this study, we assumed that the snow density was about  $0.3 \rho_{sw}$ , and  $h_s$  should accordingly be larger than approximately  $0.3 H_i$  for ocean flooding. During BASIS experiment, in addition to the snow and ice thickness measurement, the water level was also measured from the ice holes in order to see if the snow loading was heavy enough for ocean flooding. The individual measurements indicated that there were few data with (b) satisfied and the water level simultaneous positive, i.e. water above ice surface. For most data of water level positive, the snow thickness matched neither (a) nor (b). We further looked at the weather data and found that the air temperature were above or close to zero during these water flooding measurements indicating that the water may have come due to the surface melting. As to the average of the measurements, the snow thickness did not reach the range from  $0.2 H_i$  to  $0.6 H_i$ , and the average water level was positive only for the period of days 52-54 when the air temperature was above zero. If we look at the temperature gradient (Fig. 8), the measurement and model calculation both indicated a downward heat flux during the period of these single water flooding events. This downward heat flux may be considered as a result of a warm surface, i.e. surface melting. The overall effect of ocean flooding is important in understanding sea ice thermodynamics. According to our analyses, it seems that its contribution to snow-ice formation in this study is minor.

Some comparative estimates can be made from the measured ice thickness and ice temperature data (Wettlaufer et al., 1990). At the ice bottom, a heat balance is achieved between heat conduction, latent heat of fusion and oceanic heat flux. Accordingly, the heat/mass balance reads:  $\rho_i L_i \partial h_i / \partial t = k_i \partial T_i / \partial z - F_w$ . The thermistor string measurements (Fig. 3) indicate an approximate mass equilibrium during BASIS with no effective thickness change at the ice bottom. Using the modelled thermal structure and heat conduction near the ice bottom, this equilibrium corresponds to an average oceanic heat flux of  $0.63 \text{ W m}^{-2}$ . On the other hand, assuming a small average oceanic heat flux and calculating the heat conduction near the ice bottom from the measured temperature profile, the ice thickness controlled by the bottom heat/mass balance would be in approximate equilibrium for  $F_w = 1 \text{ W m}^{-2}$  and indicates a melting of about 1 cm for  $F_w = 2 \text{ W m}^{-2}$  (Fig. 9d). The ice equilibrium for  $F_w = 1 \text{ W m}^{-2}$  agrees with the ice thickness measurements by the thermistor string and with the below-ice eddy flux measurements.

Next we look at the vertical temperature profiles in the near-surface air, snow and ice. As an example, Figure 10 gives the daily variation of temperature profiles in two different cases. The diurnal temperature variation in (a) represents a modest cold air break a successive warming during 19 - 20 February, while (b) represents a strong cold air outbreak during 23 - 24 February. The modelled results will be further compared with the *in situ* measurement. This study is still in progress and a journal paper is under preparation.

The model input quantities for this simulation showed large temporal variations, especially in solar radiation and surface albedo. The ice model was forced by the observed short-wave radiation, and this produced better results than a control run using the parameterized values. This was judged from comparisons of the observed and modelled surface temperature and net radiation, which were measured independently of the short-wave radiation. As for the model initialization, if we assume a constant vertical temperature profile of  $-0.5 \text{ }^\circ\text{C}$  in the ice, the in-ice temperature adjustment would cause a difference in ice growth rate in the first 2 days of simulation and eventually a change in the overall ice thickness by 20% compared with the current model run. In addition, the estimation of the thermal heat conductivities of ice and snow is of primary importance for the modelling of ice thermodynamics. In this study we

used a simple parameterization. Potential errors due to this inaccuracy may remain in the model results with respect to the in-ice conductive heat flux. Further data on the heat conductivity are needed.

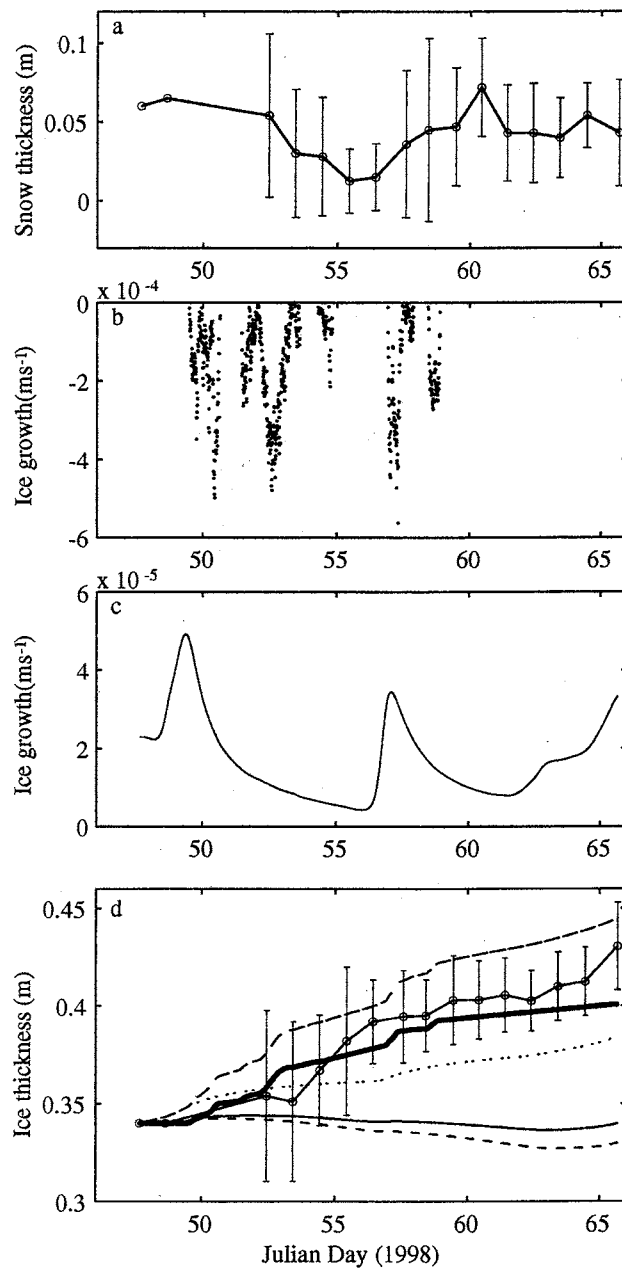


Figure 9. a) Observed mean snow thickness (circle-connected line) with  $\pm$  standard deviation (vertical bars). b) Modelled melting rate at the surface. c) Modelled freezing at the ice bottom. d) Observed mean ice thickness (circle-connected line) with  $\pm$  standard deviation (vertical bars) The dotted line gives the modelled ice growth at the bottom, and the thick line gives the ice growth solely due to snow-ice transformation. The broken line on top is the cumulative ice growth. The lowermost two lines (solid and broken) give the ice thickness variation calculated from the ice bottom heat mass balance using thermistor string temperature data with an assumed average oceanic heat flux of 1 and 2  $\text{W m}^{-2}$ , respectively.

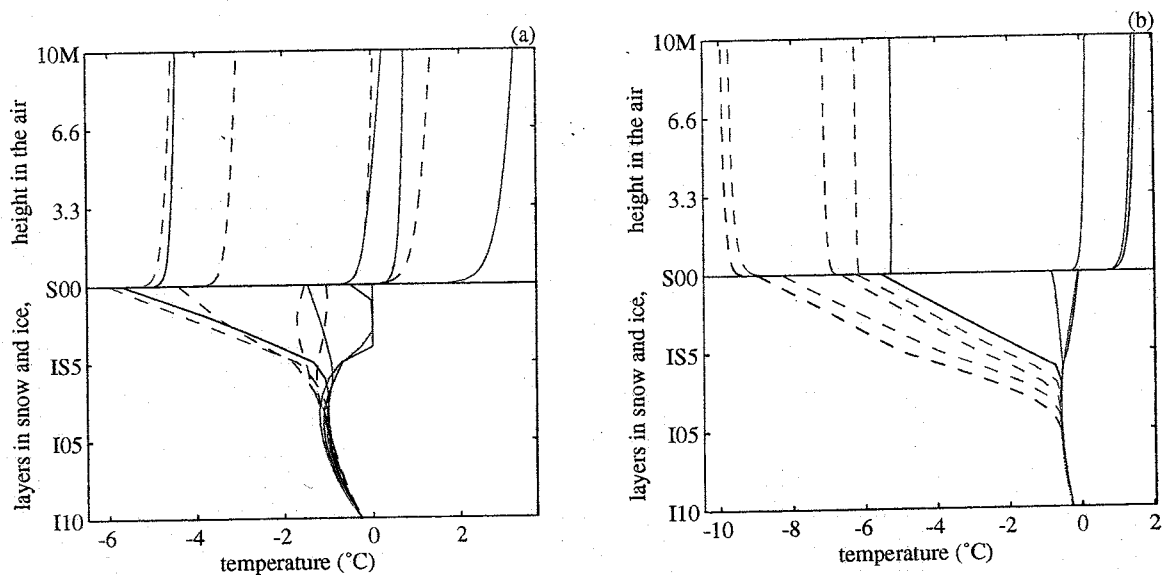


Figure 10. Modelled temperature profile in near surface air, snow, and ice. The sub-figures are for 19 - 20 February (a) and 23 - 24 February (b). Various lines indicate a temperature profile of local time 15:00 (solid red); 18:00 (solid green); 21:00 (solid blue); 00:00 (solid black); 03:00 (broken red); 06:00 (broken green); 09:00 (broken blue); and 12:00 (broken black).

#### 4. Conclusion

An 18-day ice model simulation was carried out using the BASIS field data. In general, the overall results of the ice model were encouraging, which were made during mild weather conditions with distinct areal and temporal variations in the snow and ice thickness. The *in situ* field data provided a good opportunity to verify the model parameters and indicated that high-quality field data are a prerequisite for model validation. The air-ice turbulent fluxes were well estimated by the model, indicating an accurate simulation of the air-ice coupling. The total amount of re-frozen ice calculated from the surface melting water gives a first-order estimate of snow-ice formation during the BASIS experiment, and this agreed well with the total observed variation in ice thickness. Results indicate that the surface meltwater is an important source for snow-ice formation during a mild winter. The in-ice temperature simulation indicated reasonable agreement of the thermal structure and its time development. Accurate model initialization is important for a short-period simulation of the overall ice thickness. The model slightly overestimated the ice growth at the ice bottom. This may be due to uncertainties in the estimation of sea ice thermal properties, affected by a slush layer between the snow and ice, or to the lack of ice-ocean interaction in the model and the lack of a coupled ocean model.

#### Acknowledgments

We are grateful to the participants in the BASIS-98 field experiment. In particular, Kunio Shirasawa provided us with his under-ice heat flux data.



## References

- Bennett, T.J. 1982. A coupled atmosphere-sea-ice model study of the role of sea-ice in climatic predictability. *J. Atmos. Sci.* **39**, 1456-1465.
- Cheng, B. and J. Launiainen. 1998. A one-dimensional thermodynamic air-ice-water model: technical and algorithm description report. MERI-Report series of the Finn. Inst. of Mari. Res., **37**, 15-36.
- Ebert, E.E. and J.A. Curry. 1993. An intermediate one-dimensional thermodynamic sea ice model for investigating ice-atmosphere interaction. *J. Geophys. Res.* **98**(C6), 10085-10109.
- Gabison R. 1987. A thermodynamic model of the formation growth and decay of first-year sea ice. *J. Glaciol.* **33**(113), 105-109.
- Grenfell, T.C. and G.A. Maykut. 1977. The optical properties of ice and snow in the Arctic Basin. *J. Glaciol.* **18**(80), 445-463.
- Jacobs, J.D. 1978. Radiation climate of Broughton Island. In: Barry, R.G., and Jacobs, J.D.(eds): Energy budget studies in relation to fast-ice breakup processes in Davis Strait. Occas. Pap. 26: 105-120. Inst. of Arctic and Alp. Res., Univ. of Colo., Boulder.
- Launiainen, J., ed. 1999. *BALTEX-BASIS Data Report 1998*. Geesthacht, Germany. International BALTEX secretariat. (Publication14).
- Launiainen, J. and B. Cheng. 1998. Modelling of ice thermodynamics in natural water bodies. *Cold Reg. Sci. Technol.*, **27**(3), 153-178.
- Launiainen, J., B. Cheng, J. Uotila, and T. Vihma. 2001. Turbulent surface fluxes and air-ice coupling in BASIS. *Ann. Glaciol.*, **33** in press.
- Maykut, G.A. and N. Untersteiner. 1971. Some results from a time dependent thermodynamic model of sea ice. *J. Geophys. Res.*, **76**(6). 1550-1575.
- Perovich, D.K. 1996. The optical properties of sea ice. *CRREL Rep.* 96-1.
- Prata, A.J. 1996. A new long-wave formula for estimating downward clear-sky radiation at the surface. *Q. J. R. Meteorol. Soc.*, **122**. 1127-1151.
- Schneider, S. H., and R. E. Dickson. 1976. Parameterization of fractional cloud amounts in climate models. The importance of modelling multiple reflections. *J. Appl. Meteorol.*, **15**. 1050-1056.
- Shine, K.P. 1984. Parameterization of short wave flux over high albedo surfaces as a function of cloud thickness and surface albedo. *Q. J. R. Meteorol. Soc.*, **110**. 747-764.
- Wendler, G., and F. Eaton. 1990. Surface radiation budget at Barrow, Alaska. *Theor. Appl. Climatol.*, **41**. 107-115.
- Wettlaufer, J.S., N. Unterstiner and R. Colony. 1990. Estimating oceanic heat flux from sea-ice thickness and temperature data. *Ann. Glaciol.*, **14**, 315-318.
- Yen, Y.-C. 1981. Review of thermal properties of snow, ice and sea ice. *CRREL Rep.* 81-10.

## Case Studies of On-Ice and Off-Ice Air Flow Over the Gulf of Bothnia

Timo Vihma<sup>1)</sup> and Burghard Brümmner<sup>2)</sup>

<sup>1)</sup>Finnish Institute of Marine Research, Helsinki, Finland

<sup>2)</sup>Meteorologisches Institut, Universität Hamburg, Germany

### 1. Introduction

The Baltic Sea influences the overlying atmospheric boundary layer (ABL) via the turbulent and radiative surface fluxes, and the degree of influence depends on the state of the surface (open water or sea ice) and on the origin of the flow (off-land, off-ice, off-sea). A stable stratification is typical in the atmospheric surface-layer over a compact ice cover. The ice cover is, however, often fractured, and the upward sensible and latent heat fluxes from leads modify the properties of the ABL. Off-shore winds bring continental air-masses over the sea, which may be open or covered by a compact or fractured ice field. Off-ice winds bring cold air from the sea ice over the open ocean, where a convective boundary layer develops. In the reverse situation, on-ice winds bring warm and moist air over the ice, where downward turbulent fluxes consequently take place.

In this report, two cases of on-ice and off-ice airflow characterizing the extreme weather conditions over the northern Baltic Sea are analyzed. We present aircraft observations on the ABL modification. A two-dimensional mesoscale model is then applied to simulate the observed modification and to study the sensitivity of the modification on fetch characteristics and turbulence parameterizations.

### 2. Aircraft Observations

The experimental part of this study was based on data gathered by the German Falcon research aircraft over the ice-covered and open part of the Gulf of Bothnia. Two cases, that on 27 February, 1998, in a warm on-ice airflow situation, and that on 5 March, 1998, in a cold off-ice air flow situation, are presented here. The measurements and data are described in Brümmner and Müller (1999). The flight patterns of Falcon in the two cases studied are shown in Figures 1 and 2. They were arranged along the mean wind direction, and consisted of vertical profiles in the lowest 1-3 km and of horizontal flight legs at different levels. The horizontal legs were arranged as vertical stacks oriented perpendicular to the wind direction. The transits from one stack to another were flown at low levels between 20 and 90 m

On 27 February (Figure 1), an extensive low with its centre close to the Lofote Islands produced a south to south-westerly airstream over the region of the Gulf of Bothnia. This day was characterised by weak temperature differences between the ice and the water surface. The mean surface temperature over open water was  $T_w = 1.1^\circ\text{C}$ , the ice surface temperature  $T_i$  was  $-0.3^\circ\text{C}$ , and the low-level air temperatures were around  $+2^\circ\text{C}$ . The air mass modification over a total distance of 190 km between P2 and P5 was rather small due to the weak contrast between  $T_w$  and  $T_i$ . The stable layer was about 250 m high, and characterised by large wind shear and a pronounced low-level jet (around 20 m/s) at its top.

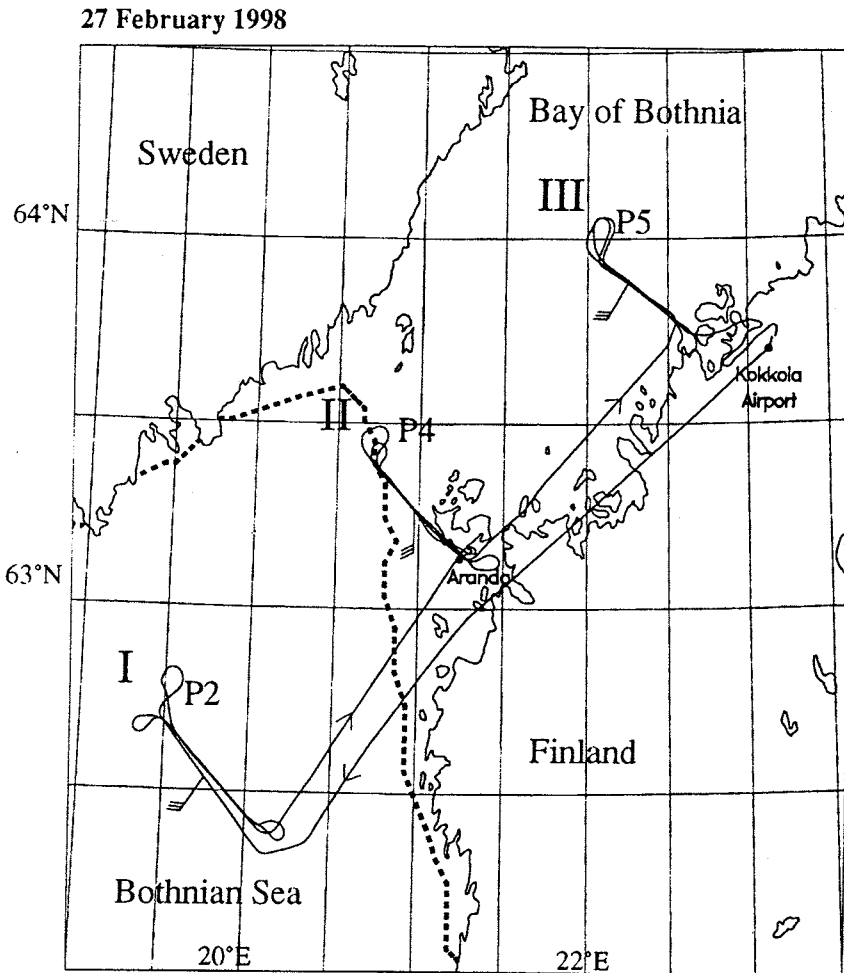


Figure 1. Flight patterns of the Falcon research aircraft on 27 February. Locations of vertical stacks (I-III) and profiles (P2-P5) used in this paper are marked. The approximate position of the ice edge is dashed, and the near-surface wind is marked at each stack. The operations base was at Kokkola airport.

On 5 March (Figure 2), the experimental area was influenced by a depression with its centre over the White Sea, and the wind was from the north over the Gulf of Bothnia. The air temperatures were between  $-10$  and  $-15^{\circ}\text{C}$ . The mean surface temperature over ice was  $T_i = -11^{\circ}\text{C}$ , while the water surface temperature was about  $T_w = 0.7^{\circ}\text{C}$ . Even over the ice, the air temperature was mostly below that of the ice surface, so that the boundary layer was unstably stratified both over the ice (weakly) and over the water (strongly). The depth of the boundary layer increased downwind, from 300 m at P1 to 470 m at P4, and further to about 550 m at P7. Here, a 3-5 octas cloud layer was present between 400 m and 1200 m. Along with the increase in the depth of the boundary layer, its temperature also increased.

The two cases of ABL modification during on-ice and off-ice air flow presented here are probably typical of the two extreme situations occurring in wintertime over the Gulf of Bothnia in the region of the ice edge zone.

5 March 1998

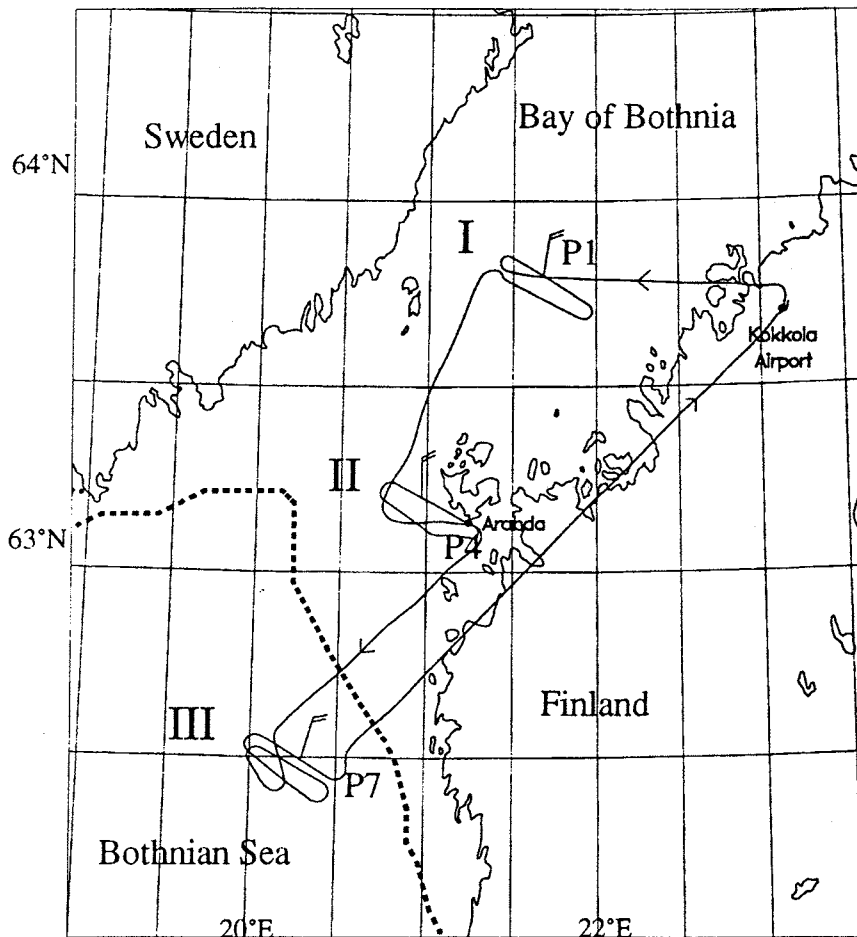


Figure 2. Flight patterns of the Falcon research aircraft on 5 March.

### 3. Mesoscale Model

In order to understand the physics of on-ice and off-ice flows and to verify the parametrization schemes for stable and unstable conditions over sea ice and its edge zone, the ABL flow over the Gulf of Bothnia was simulated using a two-dimensional hydrostatic ABL model developed in the University of Helsinki, Department of Meteorology. The equations of the model dry dynamics are as given in Alestalo and Savijärvi (1985), but the physical parameterizations are as in Savijärvi (1997) with the air moisture, clouds, and a radiation scheme included. The thermodynamic ice model of Launiainen and Cheng (1998) is coupled with the ABL model. For the present simulations, we improved the description of turbulence by applying a non-local closure with a parameterization for the counter-gradient transport of heat and moisture in convective conditions (Holtslag and Moeng, 1991). The model is well validated (Savijärvi, 1991) and also previously applied for ice-edge regions (Vihma, 1995; Vihma and Kottmeier, 2000).

#### 4. Modelling of On-Ice Flow on 27 February, 1998

The air mass observed by the aircraft had its origin over a land area. Hence, the air mass trajectory was estimated by analyzing the 06 and 09 UTC wind fields of the Mesoscale Analysis system (MESAN) of the SMHI. It appeared that the air mass had departed from the Swedish coast at approximately  $18.0^{\circ}\text{E}$ ,  $60.5^{\circ}\text{N}$  about 3 hours before arriving at P2 (Figure 1). Accordingly, the model domain was set such that it included 40 km patch of land surface followed by 282 km of open water upwind of P2 (i.e. upwind of the ice edge there was a total of 378 km of open water). For the upwind boundary conditions we used the MESAN values of 80% for relative humidity (constant with height), and  $4^{\circ}\text{C}$  for the land surface and 2-m air temperature, and applied a constant lapse rate of  $7.5 \text{ K km}^{-1}$ . The initial inflow wind profile was set as an Ekman-Taylor spiral. The model was then run for 12 h to reach a steady state. The first simulations were made by forcing the flow by a geostrophic wind constant in height. Then the baroclinicity was taken into account by estimating the air temperature gradient on the basis of the rawinsonde sounding data from six stations around the Gulf of Bothnia, and new simulations were made with a height-dependent geostrophic wind.

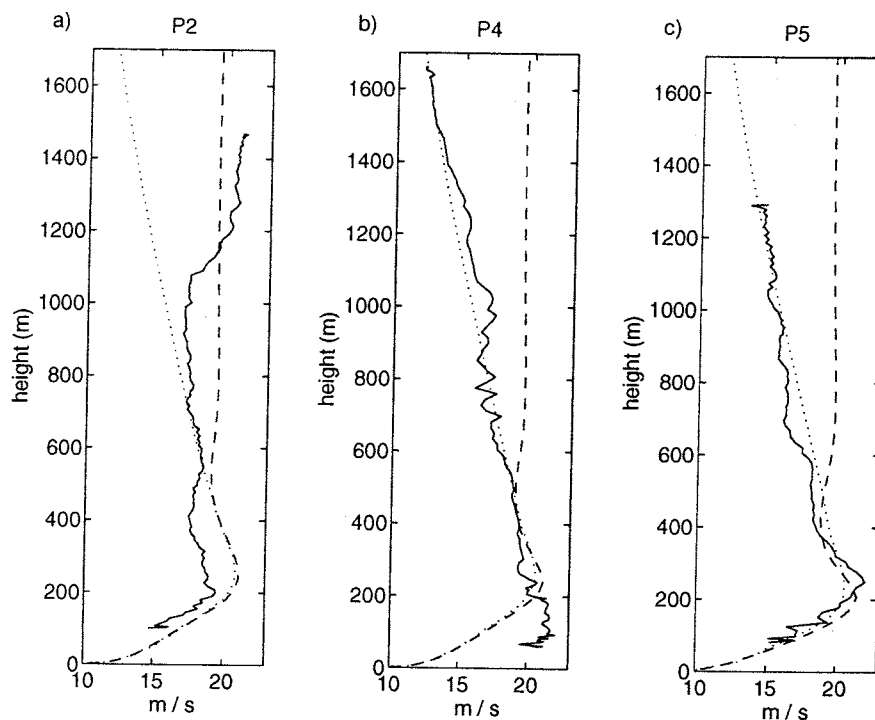


Figure 3. Observed (continuous lines) and modelled wind speed profiles at (a) 95 km upwind of the ice edge, (b) the ice edge, and (c) 95 km downwind over the ice during the on-ice flow on 27 February, 1998. The model included a 40-km-long patch of land surface with its coastline 378 km upwind of the ice edge. The barotropic model results are shown as dashed lines, and the baroclinic ones as dotted lines.

The resulting wind profiles at P2, P4, and P5 included an LLJ (Figure 3) that fitted the observations reasonably well. We see that the baroclinicity explains the shape of the wind profile above the stable boundary layer, but the LLJ is also generated without the baroclinic effect, and this seems to be related to inertial oscillations in space. In the model results, the LLJ is clearly a spatial feature: it is stationary, it does not exist over the upwind land surface,

and it is most pronounced 500 km downwind of the coast. This follows from the theory of Thorpe and Guymer (1977) that the maximum LLJ occurs after half an inertial period, i.e. after 6.7 h at a latitude of  $63^\circ$ . With a wind speed of  $20 \text{ m s}^{-1}$  advecting the air mass, this corresponds to a distance of 482 km. Further, it was confirmed by a 120 h long control run that the jet did not evolve in time, and is thus not associated with inertial oscillations in time (like the classical nocturnal jet). The generation of the jet was sensitive to the parameterization of turbulence. It was essential to use an upper limit for the mixing length that was about 10% of the ABL height, and a strong stability-dependence of the transfer coefficients in the interior of the ABL (not at the surface) produced the best results.

## 5. Modelling of the Off-Ice Flow on 5 March, 1998

The off-ice flow on 5 March, 1998, was modelled applying inflow vertical profiles of wind speed, air temperature, and humidity over ice as observed by the aircraft at site P1 (Figure 2). The flow was forced by the observed geostrophic wind of  $8 \text{ m s}^{-1}$  at a height of 3 km. This value was taken from the rawinsonde soundings made at R/V Aranda (close to P4) and Kokkola (close to P1) between 6 and 12 UTC. The model was run for 12 hours to reach a steady state.

### 5.1 Reference run

The surface boundary conditions were set according to the Falcon data and the FIMR and SMHI ice charts. The surface was estimated to be a mosaic of ice and water with an open water fraction of 0.2 between P1 and P4, zero over the land-fast ice 16 km downwind from P4, and then 0.3 until the southernmost ice edge. Below the air-mass trajectory from P1 to P4 there were a few islands, with a total length of 16 km. The islands were covered by pine and spruce forest, and hence their roughness length ( $z_0 = 0.8 \text{ m}$ ) and energy balance were different from those of the sea ice. We therefore developed a simple subroutine to calculate the energy balance of the forest following Ni and Woodcock (2000). According to the aircraft observations, in addition to the liquid water cloud droplets, ice crystals were present over almost the entire experimental area (Brümmer and Müller, 1999). In modelling the condensation and cloud formation, the saturation specific humidity was therefore calculated as an average of the saturation humidities with respect to water and ice, using the equations of Buck (1981).

The observed and modelled vertical profiles of the air temperature and specific humidity are shown in Figure 4. We see that, in the lowest 300 m, the air mass is already heated by about  $1.5^\circ\text{C}$  over the fractured ice cover and the forest between P1 and P4, and this heating is rather well reproduced by the model. The inversion base at the height of 480 m at P4 is, however, not as sharp in the model results as in the observations. Still more warming, about  $3^\circ\text{C}$ , takes place from P4 to P7, and this the model reproduces well. The air humidity profiles are also good, except that the air above the ABL is a somewhat too dry at P5. The modelled vertical fluxes at different levels at stacks I, II, and III agreed reasonably well with the observed ones. This model run, the results of which are shown in Figure 4, is referred to in the following as the reference run.

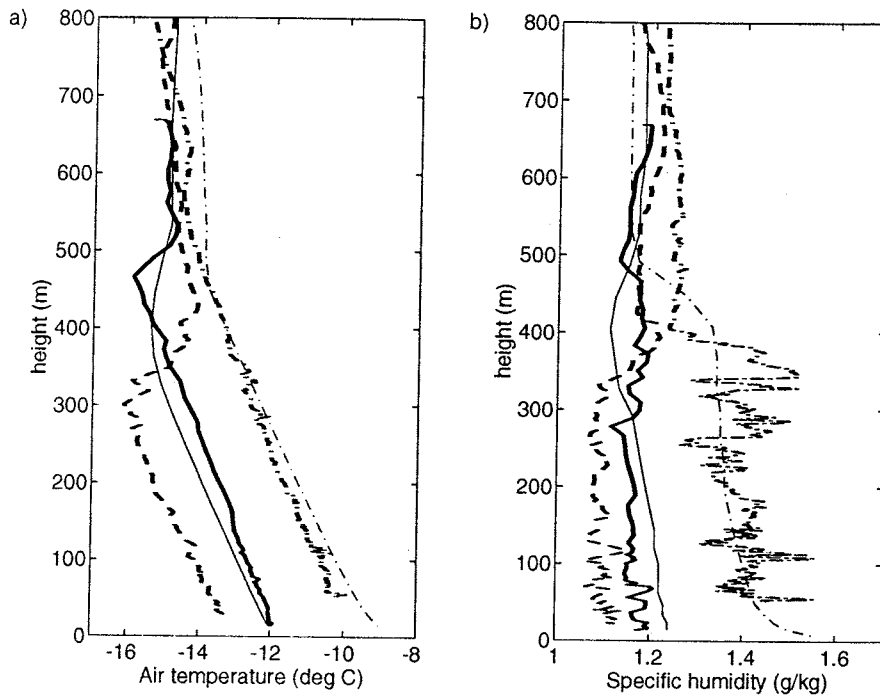


Figure 4. Observed (thick lines) and modelled (thin lines) vertical profiles of (a) air temperature, and (b) specific humidity at P1 (dashed line, observed profile used as the model inflow boundary condition), P4 (solid lines), and P7 (dot-dashed lines) during the off-ice flow on 5 March, 1998. See Figure 2 for the locations of P1, P4, and P7.

## 5.2 Sensitivity tests

It appeared that it was important for three topics to be taken into account to reach realistic results. These were (1) recognition of the effect of the forest on the surface energy balance in the archipelago, (2) parameterization of the heat and moisture fluxes from the subgrid-scale leads within the sea ice, and (3) recognition of the presence of ice crystals in the parameterization of the air saturation humidity. To demonstrate the importance of these effects, we present four sensitivity runs: (1) without forest but with a snow cover on the archipelago ( $z_0 = 0.01$  m), (2) with a compact ice cover without any leads, (3) with the air saturation humidity calculated with respect to water only, and (4) neglecting all three effects: with neither forest nor leads, and the saturation calculated with respect to water only. In other respects the sensitivity runs were similar to the reference run. The principal results of the sensitivity runs are shown in Figure 5.

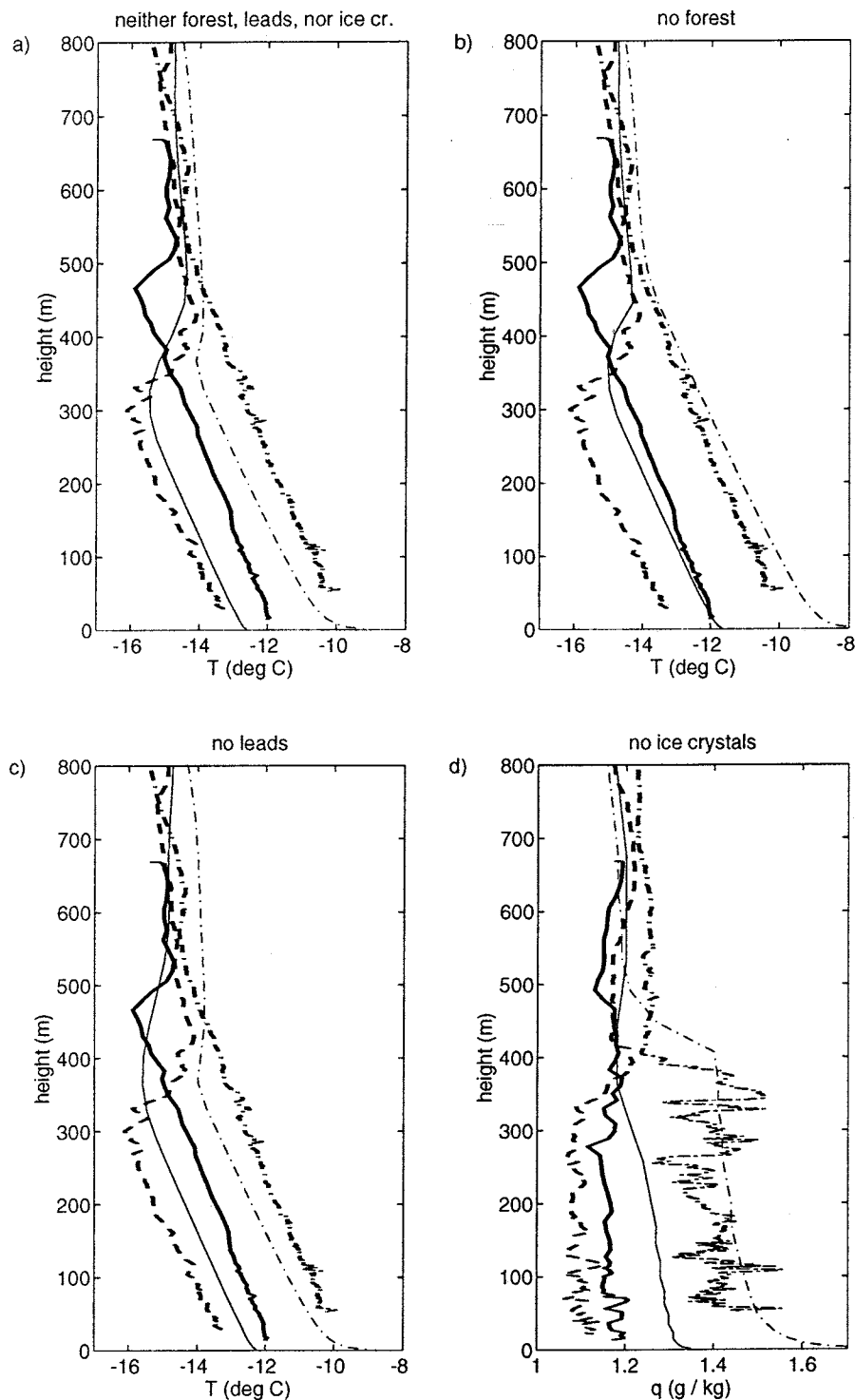


Figure 5. Observed (thick lines) and modelled (thin lines) vertical profiles of air temperature (a) in sensitivity run 4, (b) in run 1, and (c) in run 2, and (d) specific humidity in run 3, at P1 (dashed line; observed profile used as the model inflow boundary condition), P4 (solid lines), and P7 (dot-dashed lines) during the off-ice flow on 5 March, 1998.

In run 4, the heating and growth of the boundary layer are seriously underestimated at both P4 and P7. There is very little difference between the modelled profiles at P1 and P4 (Figure 5a). Between P4 and P7 some heating takes place due to the open sea. Run 1 without forest



is fine with respect to the ABL temperatures, but the ABL height is underestimated in P4: from 350 m upwards the temperature profile almost equals to that at P1 (Figure 5b). In run 2 without leads, the most evident results are the reduced heating and lack of ABL growth between P4 and P7 (Figure 5c). Due to the forest, the lowest 300 m at P4 are heated half as much as observed. Heating from the open water upwind of P7 originates from a fetch of 15 km, which seems to be too short to cause ABL growth. In the reference run, the surface heat flux and counter-gradient transport through the mixed layer over the fractured ice (50 km with a 30% open water fraction) and open water cause much more boundary-layer growth between P4 and P7. The boundary layer evolution between P1 and P4 seems to be due to the combined effect of the forest and the leads. Compared to this effect, the air-ice exchange was of minor importance in this case. In run 3, where the saturation was calculated with respect to water only, the air humidity was too high in the lowest 360 m at P4 (Figure 5d). In the lower levels, too high a humidity remains in the air, because the saturation humidities are higher when condensation to ice crystals is neglected.

Comparing the observed and modelled vertical profiles of the turbulent fluxes (not shown), with the lack of leads the sensible and latent heat fluxes were too large near the surface at P7 (the air was cold when reaching the ice edge). In sensitivity run 4, both the evaporation and boundary layer growth were reduced and the latent heat flux already fell to zero at a lower height than observed.

## 6. Discussion

We have presented two cases of air flow over the ice-edge zone: on-ice and off-ice flow. In many respects, they represent the two extreme situations occurring in wintertime over the ice edge zone in the Baltic Sea. The stable boundary layer during the on-ice flow exhibited little thermal modification but interesting wind features, due to the frictional decoupling with the surface. During the off-ice flow, the coupling between the surface and the air was strong, and hence the boundary layer became strongly unstable over the open water and the thermal modification was large. Common to both cases was, however, the importance of the vicinity of the land surface on the ABL.

During on-ice flows in general, the ABL over the upwind open sea is typically close to thermal equilibrium with the surface. After crossing the ice edge, the warm air mass provides heat to the snow surface, and the snow temperature increases. This process had apparently already taken place before the Falcon observations on 27 February, 1998, as southerly winds had prevailed for two days before the flight mission. The air-surface temperature difference and the turbulent exchange were therefore small over the ice, as in the study of Brummer et al. (1994). Hence, in contrast to the case of 5 March, the results of this case were not sensitive to the parameterization of the subgrid-scale heat and moisture fluxes.

The wind field showed a low-level jet that was most pronounced over the ice. In the model, the LLJ was associated with inertial oscillations. The mechanism is a spatial analogy to the classical nocturnal jet development in time, and is in agreement with the observations of Smedman et al. (1993) over the open Baltic Sea in spring and summer. Although an LLJ associated with inertial oscillations is a well-known feature in stable boundary layers, relatively few studies before BASIS (Smedman et al., this issue) have documented it over sea ice. A few studies have shown other mechanisms for the generation of LLJs over the sea ice

or its edge zone: the ice-breeze (Langland et al., 1989), baroclinicity as the main mechanism (Vihma et al., 1998), and katabatic or barrier winds (King and Turner, 1997).

Although the observed LLJ was most pronounced over the ice, the modelling suggests that the jet was not generated by the ice edge but by the coastline, where a much more drastic change in the thermal stratification and surface roughness took place. The observed and modelled location of the maximum jet approximately 500 km from the coast followed the theory of Thorpe and Guymmer (1977). The generation, maintenance, and strength of the LLJ was very sensitive to the parameterization of turbulent mixing in the model. In particular, the upper limit for the mixing length and the stability dependence of the transfer coefficients in the interior of the ABL were important.

In the case of the off-ice flow on 5 March, 1998, the modification of the air-mass and the development of a convective boundary layer over the open sea were reasonably well simulated. The sensitivity runs suggested that in this case it was essential to take into account the effects on the ABL of the subgrid-scale leads and the archipelago forest. The local surface sensible heat flux over leads was up to  $120 \text{ W m}^{-2}$ , yielding grid-averaged sensible heat fluxes of about  $40 \text{ W m}^{-2}$ . These fluxes were particularly important for the heating of the ABL. Without the forest these large fluxes were not, however, effective enough to reproduce the observed growth of the ABL at P4. In the presence of the forest in the archipelago, the boundary layer growth was better simulated, and even without the leads the forest, together with the small upward heat flux from the ice, provided half of the heating observed at P4.

The aircraft observations indicated that ice crystals were present over almost the entire experimental area on 5 March. Taking them into account in a very simple manner, by calculating the saturation humidity as the average of saturation with respect to water and ice, clearly improved the modelled humidity profile at P4. In addition to the sensitivity tests described in detail, we may note that the counter-gradient transport was important for the heating and growth of the ABL at P7, where the convection was strongest. This effect has been well documented in several studies (Chrobok et al., 1992; Lüpkes and Schlünzen, 1996).

### Acknowledgements

We thank the coordinator and scientists of BASIS for good cooperation. The assistance by David Schröder and Stefan Thiemann and discussions with Hannu Savijärvi and Mikael Magnusson are acknowledged. Maria Lundin provided us with the MESAN fields and sea ice concentrations from the SMHI.

### References

- Alestalo, M., and Savijärvi, H.: 1985, 'Mesoscale circulations in a hydrostatic model: coastal convergence and orographic lifting', *Tellus* **37A**, 156-162.
- Buck, A. L.: 1981, 'New equations for computing vapour pressure and enhancement factor', *J. Appl. Meteorol.* **20**, 1527-1532.
- Brümmer, B., Busack, B., Hoerber, H., and Kruspe, G.: 1994, 'Boundary-layer observations over water and Arctic sea ice during on-ice air flow', *Boundary-Layer Meteorol.* **68**, 75-108.

- Brümmer, B., and Müller, G.: 1999, 'Boundary layer measurements with research aircraft Falcon', In: J. Launiainen (Ed.): BALTEX-BASIS Data Report 1998, *Int. BALTEX Secretariat Publ.* **14**, Geesthacht, Germany, pp. 26-38.
- Chrobok, G., Raasch, S., and Etling, D.: 1992, 'A comparison of local and non-local turbulence closure methods for the case of a cold air outbreak', *Bound.-Layer Meteorol.* **58**, 69-90.
- Holtslag, A. A. M., and Moeng, C.-H.: 1991, 'Eddy diffusivity and countergradient transport in the convective atmospheric boundary layer', *J. Atmos. Sci.* **48**, 1690-1698.
- King, J. C., and Turner, J.: 1997, '*Antarctic Meteorology and Climatology*', Cambridge University Press, Cambridge, U.K., 409 pp.
- Langland, R. H., Tag, P. M., and Fett, R. W.: 1989, 'An ice breeze mechanism for boundary-layer jets', *Bound.-Layer Meteorol.* **48**, 177-195.
- Launiainen, J., and Cheng, B.: 1998, 'Modelling of ice thermodynamics in natural water bodies', *Cold Reg. Sci. Techn.* **27**, 153-178.
- Ni, W., and Woodcock, C. E.: 2000, 'Effect of canopy structure and the presence of snow on the albedo of boreal conifer forests', *J. Geophys. Res.* **105**, 11879-11888.
- Savijärvi, H.: 1991, 'The United States Great Plains diurnal ABL variation and the nocturnal low-level jet', *Mon. Wea. Rev.* **119**, 833-840.
- Savijärvi, H.: 1997, 'Diurnal winds around Lake Tanganyika', *Quart. J. Roy. Meteorol. Soc.* **123**, 901-918.
- Smedman, A.-S., Tjernström, M., and Högström, U.: 1993, 'Analysis of the turbulence structure of a marine low-level jet', *Bound.-Layer Meteorol.* **66**, 105-126.
- Thorpe, A. J., and Guymer, T. H.: 1977, 'The nocturnal jet', *Quart. J. Roy. Meteorol. Soc.* **103**, 633-653.
- Vihma, T.: 1995, 'Subgrid parameterization of surface heat and momentum fluxes over polar oceans', *J. Geophys. Res.* **100**, 22,625-22,646.
- Vihma, T., Uotila, J., and Launiainen, J.: 1998, 'Air-sea interaction over a thermal marine front in the Denmark Strait', *J. Geophys. Res.* **103**, 27,665- 27,678.
- Vihma, T., and Kottmeier, C.: 2000, 'A modelling approach for optimizing flight patterns in airborne meteorological measurements', *Bound.-Layer Meteorol.*, **95**, 211-230.

## Large-Eddy-Simulation of an Off-Ice Airflow Case.

D. Etling<sup>1)</sup>, G. Harbusch<sup>1)</sup> and B. Brümmer<sup>2)</sup>

<sup>1)</sup> Institut of Meteorology and Climatology, University Hannover, Germany

<sup>2)</sup> Meteorological Institute, University Hamburg, Germany

### 1. Introduction

Large Eddy-Simulation (LES) models are by now quite common for boundary layer research. In contrast to mesoscale models, which are described in Vihma and Brümmer (2001, this issue), only subgrid turbulence is parameterised and all large scale eddies are resolved explicitly. This demands grid resolutions as low as 10 - 30 m in all directions. LES models have been applied to the problem of polar boundary layers, e.g. flow over leads or sea ice, by Glendening (1995) or Raasch and Harbusch (2000).

Here we report simulations performed with the LES model of the University of Hannover. The model is described in detail in Raasch and Etling (1998) and has been applied to the boundary layer development over variable sea-ice concentrations by Raasch and Harbusch (2000).

### 2. Model results

The purpose of this study is to simulate the development of the boundary layer during the off-ice flow situation in the BASIS field experiment on 5 March 1998. On this day, aircraft observations have been performed (see article by Brümmer et al. (2001) in this report) and hence comparison between simulations and observations are possible. Due to the periodic lateral boundary conditions and small grid size of the LES model it is not possible to treat the off-ice flow situation as spatial problem over the whole observation distance of 70km. Instead, the model domain (a box of 3 x 3 km horizontally and 2 km in the vertical) is moving with the mean boundary layer wind as observed on this day. The spatial change in surface conditions (from ice to sea ice to open water) is simulated by a temporal variation of the lower boundary condition. In this case, the surface temperature as observed by the aircraft (Figure 1, top) is prescribed at the lower boundary of the model domain (Figure 2, top).

The model run is started with the observed vertical profiles of wind, temperature and humidity as measured near the research vessel Aranda. (The temperature profile is shown in Figure 3.) The first part of the flight track is then simulated by applying a small air-ice temperature difference of  $\Delta T = 2$  K (Figure 2) at the lower boundary. The "ice edge" is introduced to the model by a surface temperature jump of  $\Delta T = 8$  K, which corresponds to the average surface temperature observed by the aircraft (Figs. 1 and 2 top). This is of course a simplification of the real situation which shows variations in the surface temperature. But the main aspect of the LES simulations was to capture the principle development of the boundary layer during this off-ice flow situation.

The effect of increased surface temperature on air temperature at flight level of about 30m and on turbulent fluxes of sensible and latent heat as well as on surface shear stress as observed by the aircraft is shown in Figure 1. The results from the LES model simulations are displayed in Figure 2. For comparison, the temperature jump in the model at horizontal position 0 km in Figure 2 is equivalent to the observed jump at  $x = 20$  km in Figure 1.

The simulated sensible heat flux increases from about  $30 \text{ Wm}^{-2}$  over the ice to about  $150 \text{ Wm}^{-2}$  after the 'ice edge'. The observed values are somewhat lower with about  $120 \text{ Wm}^{-2}$  after the surface temperature jump. The simulated latent heat flux compares quite well with the observations, with about  $20 \text{ Wm}^{-2}$  over the ice and about  $90 \text{ Wm}^{-2}$  after the 'ice edge'.

In general, the temporal (spatial) development of fluxes as well of air temperature is captured quite well by the model simulations. More agreement could be obtained, if the small scale variations of the surface temperature as observed (Figure 1, top) would be also applied to the model boundary condition.

Concerning the development of the vertical boundary layer structure, model results for virtual potential temperature are given in Figure 3. Due to the increased surface heat flux, the boundary layer is heated and the capping inversion is increased from about 500m at Aranda about 750m at 36 km down wind the "ice-edge". Concerning comparison to aircraft measurements, the inversion height was reported to be 900m at the end of the flight leg.

### 3. Conclusions

An LES model has been applied to an off-ice airflow case as observed during the BASIS field experiment. The boundary layer modification was simulated by following the air mass trajectory with observed surface temperature as lower boundary condition in the model domain. Despite the well known limitations of the LES approach for spatial varying surface conditions, the development of observed air temperature, sensible and latent heat flux and shear stress was simulated in reasonable agreement with the aircraft observations.

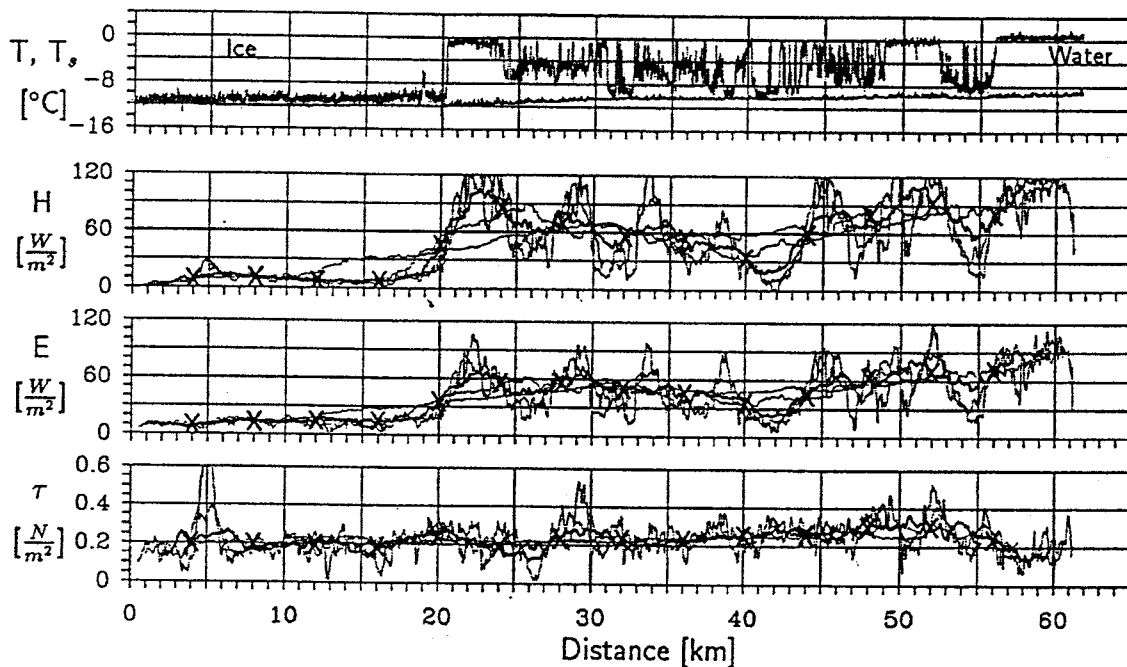


Figure 1. Aircraft observations for day 5 March 1998 of surface temperature  $T_s$ , air temperature  $T$ , sensible heat flux  $H$ , latent heat flux  $E$  and shear stress  $\tau$ . All data except for  $T_s$  are taken at flight level  $z = 30\text{m}$  height.

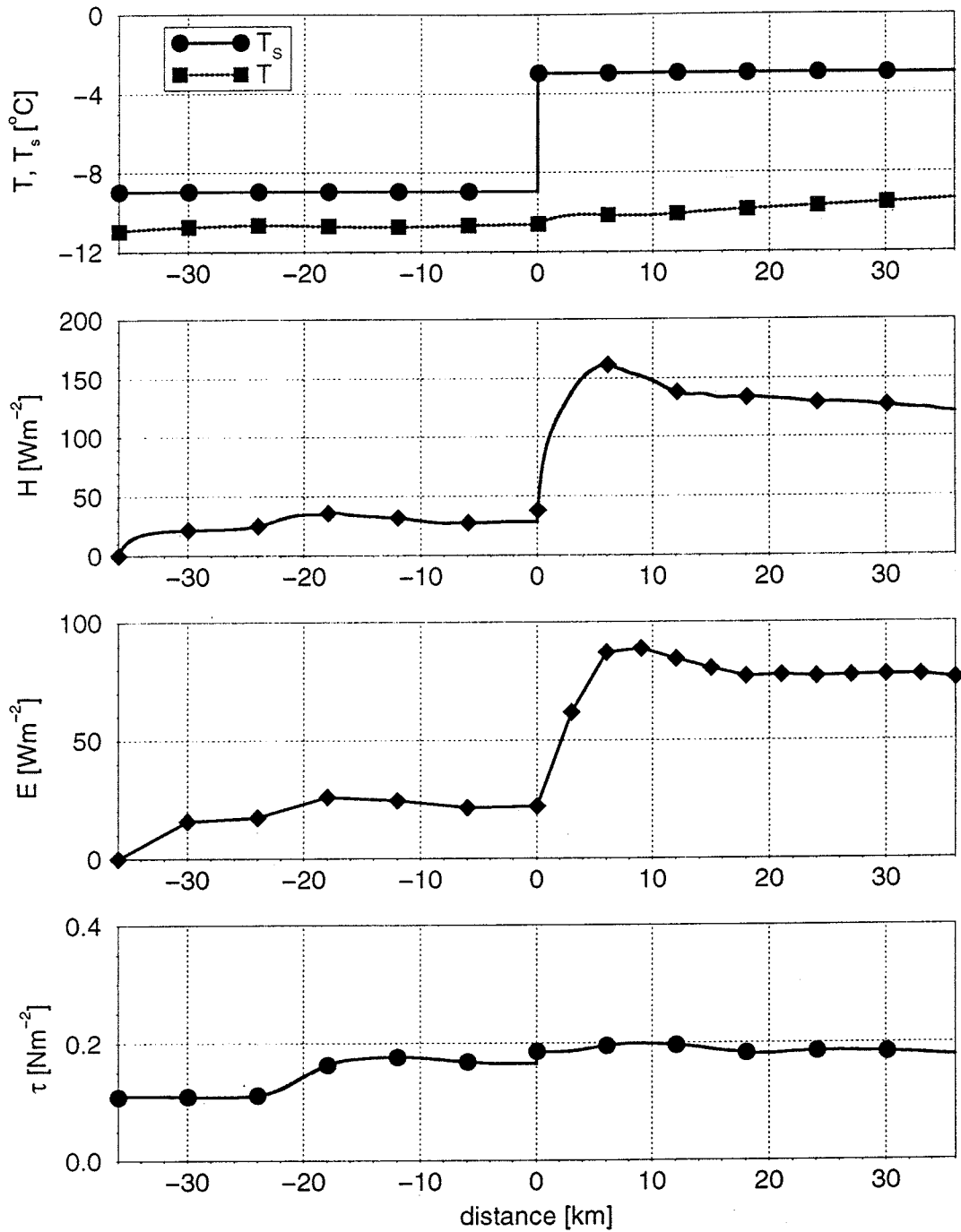


Figure 2. Results of the LES model for surface temperature  $T_s$ , air temperature  $T$ , sensible heat flux  $H$ , latent heat flux  $E$  and shear stress  $\tau$ . All data (except for  $T_s$ ) are taken at  $z = 30\text{m}$  height, corresponding to mean flight level of the research aircraft (observations in Figure 1).

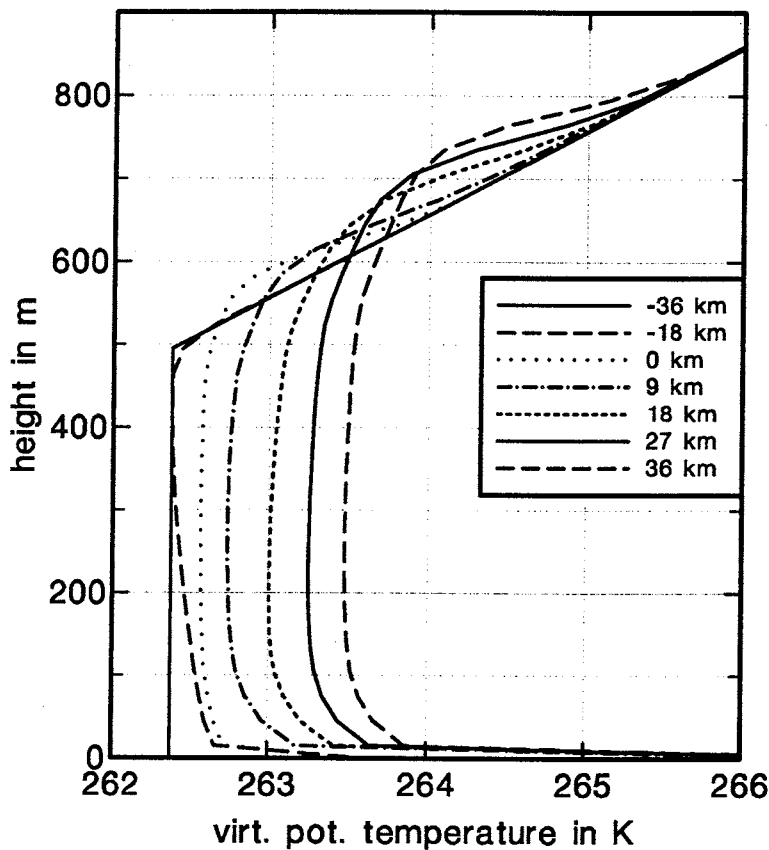


Figure 3. Vertical profiles of the virtual potential temperature at various horizontal positions as simulated by the LES-model.

#### 4. References

- Brümmer, B., Schröder, D., Launiainen, J., Vihma, T., Smedman, A. S., and Magnusson, M.: 2001, 'Temporal and spatial variability of surface fluxes over the ice edge zone in the Gulf of Bothnia.', this issue.
- Glendening, J.W.: 1995, 'Horizontally integrated atmospheric heat flux from an Arctic lead'. *J. Geophys. Res.* **100**, 4613 - 4620.
- Raasch, S. and Etling, D.: 1998, 'Modeling deep ocean convection: large eddy simulation in comparison with laboratory experiments'. *J. Phys. Oceanogr.* **28**, 1786 - 1802.
- Raasch, S. and Harbusch, G.: 2000, 'An analysis of secondary circulations and their effects caused by small-scale surface inhomogeneities using large-eddy simulations'. *Boundary-Layer Meteorol.*, in review.
- Vihma, T., and Brümmer, B.: 2001, 'Case studies of on-ice and off-ice air flow over the Gulf of Bothnia', this issue.

## Three-dimensional mesoscale modelling in BASIS

Mikael Magnusson

Department of Earth Sciences, Meteorology, Uppsala University, Sweden  
Current address: SMHI, 60176 Norrköping, Sweden

### Introduction

A numerical model has been used in order to simulate phenomena observed during the field campaign in the Gulf of Bothnia. The model used in the investigation is a non-hydrostatic 2.5 order closure model developed at the department of Meteorology Uppsala, the MIUU-model, (Enger 1988). Four different days during the campaign were simulated; 25 and 27 February, and 3 and 5 March. These days were chosen because different kind of phenomena were observed. On 25 February a low-level jet was observed at more than one station, and this situation will be denoted as case A. Case B is the situation that occurred on 27 February, which is an off-ice flow situation. There were aircraft measurements performed in the area during this day. There were also airborne measurements on 3 March, when there was an on-ice flow situation, case C. The last day studied was 5 March, on which an ice breeze was observed at the Umeå station. This situation is hereafter denoted as case D.

### Model Description

Numerical simulations were performed with a mesoscale model, the MIUU-model. The model is a non-hydrostatic 2.5 order closure model developed at Uppsala University. The model was run using an energy balance scheme for all cases except case D. Input data was a typical temperature in the ground for the period and the stratification of the atmosphere was given by the data from the radios soundings at 9.00 LST. The model was started at 18.00 LST the day before the time of interest. For the simulation performed for case D another scheme was used where the temperature at 2m is prescribed as function of time in the model, as the lower boundary.

### Case A:

There were rather frequent occurrences of low-level jets detected in the wind profiles measured during the campaign. A low-level jet was detected in approximately 30% of the measured profiles, and wind maximum was found in more than 60% of the measured profiles.

In the radiosonde measurements performed at 12 o'clock LST on 25 February, one case of low-level jet was detected in the measurements performed at Aranda. Another type of low-level jet was detected at Kokkola. The first jet was governed by the roughness/temperature difference between the open water and the ice, and the second jet was generated by the effect of an upstream land area.

The result used from the model is the wind profile at 12.00 at the site. An example of comparison between measurements and model results is presented in Figure 1 for the Aranda site. The difference in magnitude between the measured and modelled winds is probably a result of the magnitude of the geostrophic wind speed used. In the model the geostrophic



wind was the same for the whole domain, but during the investigated cases there was a synoptic weather system which modified the pressure field. As a result it was difficult to find a general synoptic wind speed. Figure 1 shows that the wind speed at the jet maximum is 32 m/s, while the geostrophic wind speed can be estimated to be 20 m/s. This increased wind speed is a result of the temperature difference between the open water and ice.

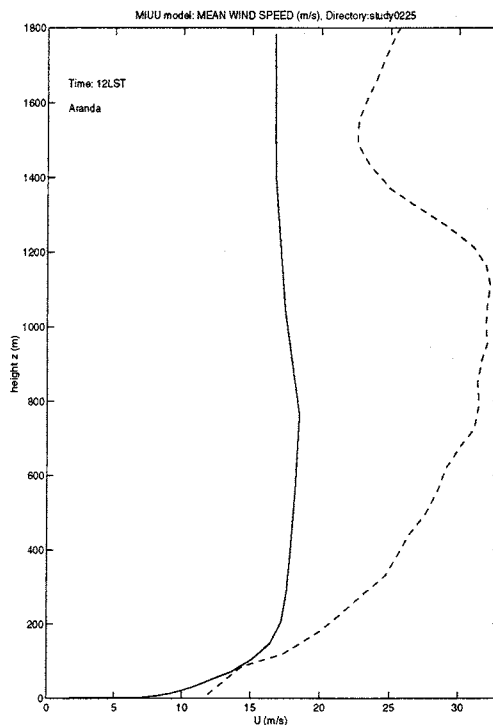


Figure 1. Wind profile measured and simulated at the Aranda site.  
 ---: measurements, - -: model

### Case B and C.

The horizontal variability of the heat flux has been studied for two days, with the aid of the MIUU model. For one of the days there was an on-ice flow, 27 February, while on 3 March there was an off-ice airflow. The magnitudes of the fluxes have been compared with aircraft measurements at different locations in the domain. The agreement was satisfactory. The on-ice case is presented in Figure 2 and the results for off-ice case are presented in Figure 3. From the figures it can be seen that when there is an on-ice flow the magnitude of the fluxes over ice and water are of the same order. For the off-ice case the fluxes over the open water are much larger. These high values of the fluxes can be found at rather high levels over the water. Hence we have a rather good mixing of the advected air. The result from the model agrees with the aircraft measurements (Brummer et al., this issue) except for the ice-covered area in the off-ice case. The aircraft measurements give a positive heat flux while the model gives a negative heat flux. This is probably a result of the coarse resolution of the model. Hence the leads cannot be resolved. They create a convective region close to the surface.

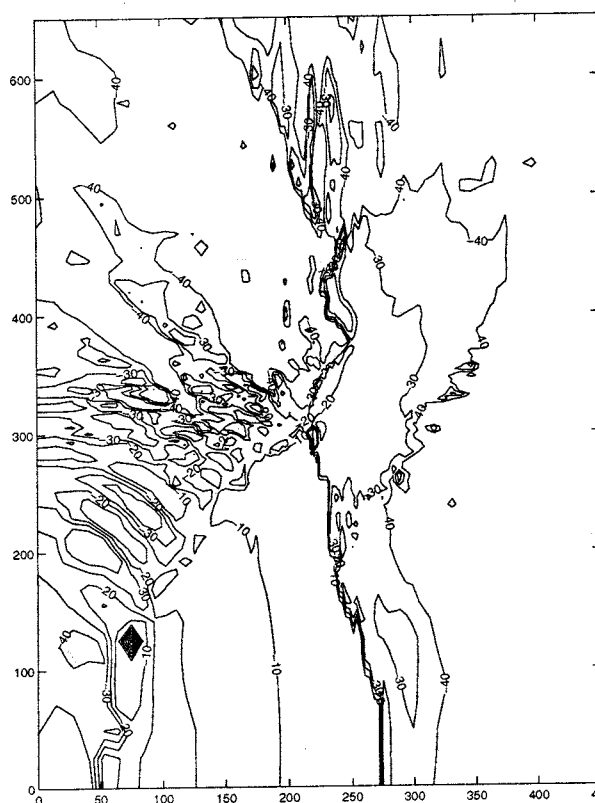


Figure 2. Sensible heat flux calculated at 30m height for the on-ice flow on 27 February, 1998, 12.00 LST.

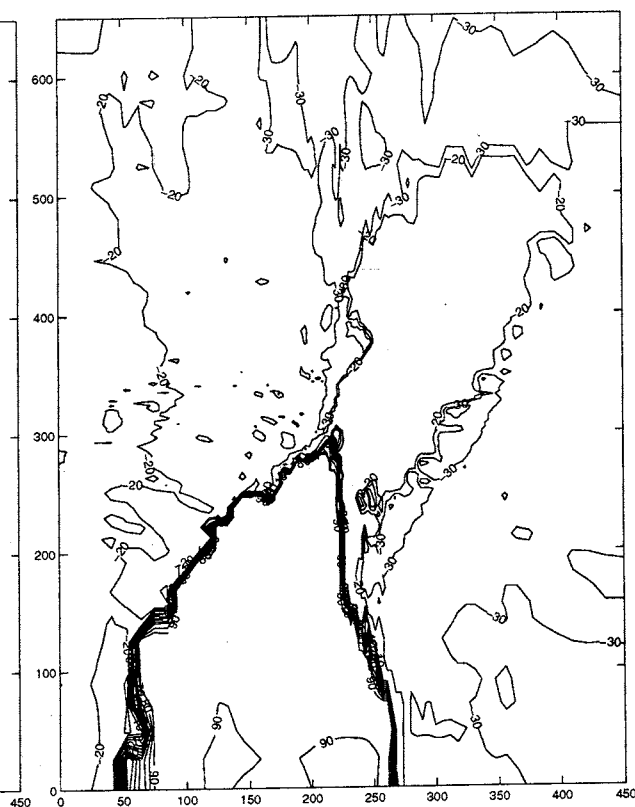


Figure 3. Sensible heat flux calculated at 30 m height for the off-ice flow case on 5 March, 1998, 12.00 LST.

#### Case D:

The 'ice breeze' at the coast of Sweden was detected with the aid of pibal tracking technique. Figures 4 and 5 show the temperature, humidity, wind speed and wind direction profiles for the ice breeze case. The difference between the land surface temperature (LST) and the sea surface temperature (SST) is the driving force for this phenomenon. The ice-covered area in-between contributes to the high wind speeds due to the low friction. The event seems to be independent of the time of the day since the criteria for the event to occur is that the temperature difference is large enough and this can happen at any time of the day depending on the synoptic weather conditions in combination with the cloud cover.

The difference between SST and LST during March the third, 1998, can be approximated with the temperature measured at the lowest level in the tower,  $t_1$ , (1 m asl) since the SST  $\approx$  0. The largest difference between LST and SST occurs at the time were the 'ice breeze' was observed with the pibal technique, see Figure 6.

The MIUU model was run for three different winter conditions over the Bothnian bay area. In the first run there were no ice on the Bay of Bothnia in the second case the whole of Bothnian bay was frozen. Finally the ice conditions were as they were observed at the time.

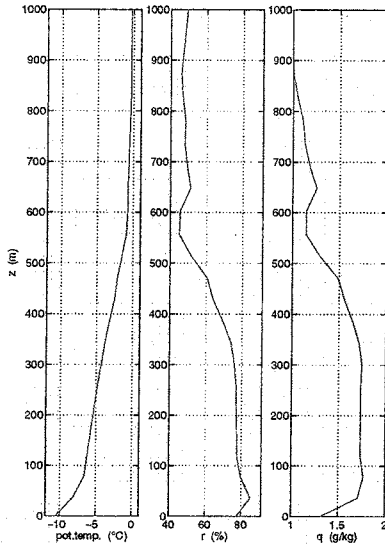


Figure 4. Temperature and humidity profile measured with radio sounding technique at Lövöudden 980303 6.30 LST.

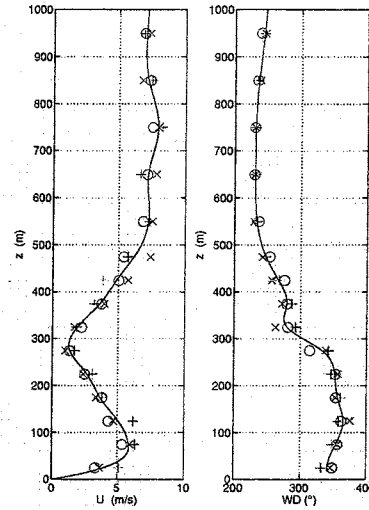


Figure 5. Wind speed and wind direction profile from pibal measurements performed at Lövöudden 980303 6.30 LST. The different symbols indicates the three individual balloons.

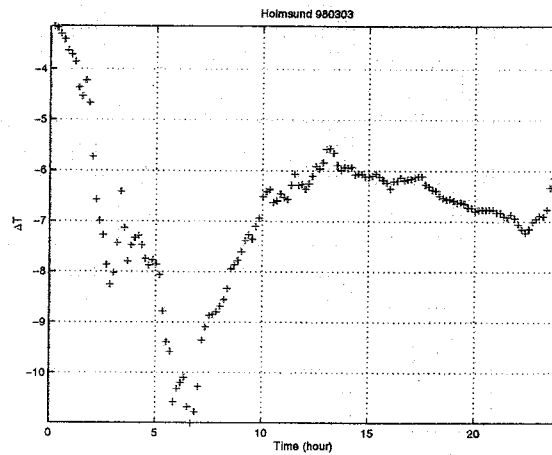


Figure 6. Temperature difference between sea surface and the temperature above the snow.

In all simulations the temperature was kept constant at a value of  $+0.1$  °C. The temperature at 2m height was prescribed as a function of the time following the pattern as was observed at the Umeå station. The results from the numerical simulations will be presented in three figures. Figure 7 shows the simulated wind field for the case when we have simulated a situation with no ice, for this scenario there is no significant turning of the wind, and the wind pattern is rather homogenous. The other extreme situation is the one where the whole Bay of Bothnia is covered with ice, Figure 8. Also in this situation the wind field is rather large-scaled. There is a turning of the wind at the coast line as a result of the change of roughness. The scenario with most variable wind is the last, where the ice condition are as they were during the measurements, Figure 9. The sharpest turning of the wind is occurring at the ice edge, this is a result of the combined effects of different temperatures and roughness.

Open U=5, V=2, Time=06, z=29m

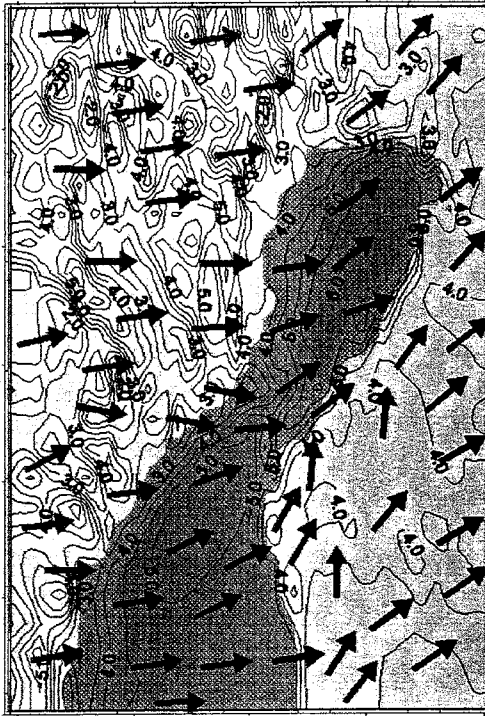


Figure 7. Open water in the Gulf of Bothnia. The sea surface temperature is kept at a constant value.

Ice U=5, V=2, Time=06, z=29m

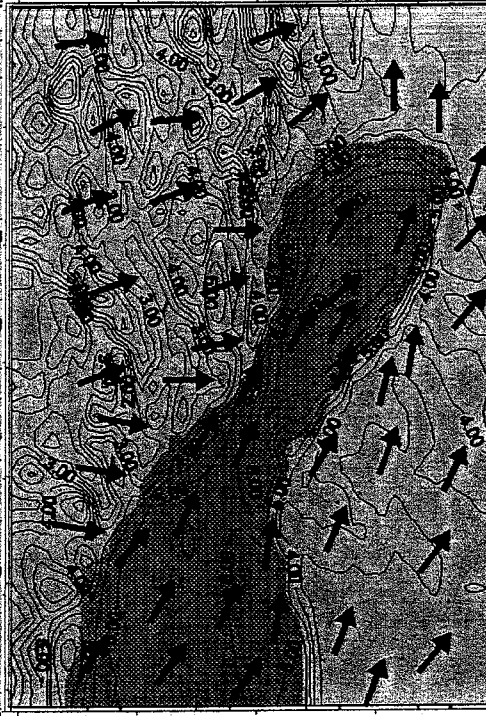


Figure 8. The whole Gulf of Bothnia is covered by ice. The temperature at 2 m asl follows the temperature variations at land.

Half ice U=5, V=2, Time=06, z=29m



Figure 9. Both open water and ice in the Gulf of Bothnia as observed during the situation. The sea surface temperature is kept at a constant value.

## Conclusions

A partly ice-covered lake or sea will generate a number of mesoscale phenomena. A wind maximum at lower levels were detected for more than 60 % of profiles collected during one month of measurements around the Gulf of Bothnia. 30% of the measurements could be classified as different classes of low-level jet. Knowledge of the amount of low-level jets and their structure is of interest for calculations of the wind energy potential in an area. The phenomena are also of interest concerning dispersion studies. The numerical model developed at MIUU was able to generate the low-level jets, although the magnitude of the jet was higher. This was probably a result of a homogenous geostrophic wind in the model boundaries, which then was too high at the location of the jet. A special kind of a low-level jet is the 'ice breeze' which was observed during the campaign. It was also possible to simulate it with the mesoscale model, if the ice distribution was correct.

Numerical calculations of the heat flux over the ice and water gave the same result as was observed from aircraft measurements. However the effects of leads could not be included in the model and the result was that the stratification over the ice in the off-ice flow situation was reversed.

## References

- Enger L.: 1990, 'Simulation of dispersion in moderately complex terrain – part A. The fluid dynamic model', *Atmospheric Environment*, 24A, 2431-2446.
- Brümmer, B., Schröder, D., Launiainen, J., Vihma, T., Smedman, A.-S., and Magnusson, M.: Temporal and spatial variability of surface fluxes over the ice edge zone in the northern Baltic Sea, this issue.

## 7. SUMMARY

The data-analyses in BASIS concentrated into three main branches: (1) the atmospheric boundary layer, (2) the ice and surface properties and, (3) the ocean boundary layer. In addition, process oriented modelling was made applying the field data as a reference. Part of the results still remain as objectives of further study, but a summary of the most essential results read as follows.

The analyses of atmospheric surface-layer turbulence, based on the measurements at Umeå, Kokkola, and Aranda, yielded physical results that are of importance also from the point of view of modelling. In stable stratification conditions, the normalized standard deviations of the wind components increased during strong stability. The behaviour of the buoyancy length scale and the ratio of the standard deviations of the vertical and horizontal wind components showed that the wall effect is important for the turbulence structure in the stable surface layer. The analyses of the stable boundary-layer depth agreed with new theoretical predictions, and slightly modified parameter values for the theoretical equation were suggested. In near-neutral conditions, the analyses demonstrated the effects of inactive turbulence, and they were explained in terms of 'top-down' mechanisms: eddies brought down from above into the surface layer strongly contribute to the momentum transport and cause the increase of the dimensionless vertical velocity variance with height.

The profile and turbulence measurements on land-fast ice confirmed the validity of the Monin-Obukhov similarity theory, and yielded a new formula for the ratio of local roughness lengths for momentum and heat. The ratio depends on the local roughness Reynolds number. The analyses further yielded a new formula for the flux-profile relationships in conditions of a stable stratification. Different methods, based on radiation, turbulence and profile measurements, to determine the ice surface temperature were compared, and the comparison demonstrated the applicability of a thermodynamic ice model in estimating the surface temperature. The model was also fairly accurate in reproducing the temporal development of the temperature profile through the ice and snow in conditions of rapidly varying weather.

The airborne, land-based, and ice-based observations of the turbulent and radiative fluxes in the atmospheric surface layer showed a good agreement. The agreement was, in fact, better than usually achieved in field experiments over land surfaces, and this was perhaps partly due to the low aircraft flight altitudes that were reached over the ice and open sea. The study revealed significant spatial and temporal variations in the surface fluxes: the fluxes depended above all on the large-scale weather conditions and on the state of the surface, which was either open water, compact land-fast sea ice, or broken sea ice. The spatial variability of the heat fluxes in the ice edge zone was small during warm air advection and large under cold-air advection conditions. It was, however, often exceeded by the spatial variability of the net radiation flux caused by inhomogeneous cloud fields. Spatial variability from aircraft showed that area-representative fluxes for the whole ice edge zone cannot be derived from land-fast ice stations only. The effects of the surface temperature differences between thin, new ice and snow-covered land-fast ice were evident also in the formation and growth of an internal boundary layer at the Umeå measurement site.

The aircraft data were further applied in parameterizing the turbulent surface fluxes over a broken ice cover. The analyses revealed that in order to get realistic area-averaged fluxes the roughness lengths for heat and moisture must be 3 to 4 orders of magnitude smaller than the

roughness length for momentum. This is in agreement with the results of several field experiments over heterogeneous land surfaces. The measurements were made approximately at the height of the lowest grid level of regional and large-scale models (e.g. HIRLAM and REMO). The results are therefore applicable for the models, because in conditions of stable stratification the lowest level may often be above the constant-flux layer, and the flux-divergence should be taken into account as reduced roughness lengths.

The BASIS observations of the ABL were compared with the analyses and 24-h forecasts of the regional model HIRLAM. Comparisons based on the rawinsonde sounding data demonstrated that the differences were largest during passages of cold and warm fronts. The differences were largest near the surface, and the vertical gradients of air temperature and wind speed were smaller in HIRLAM than in the observations. The comparisons based on aircraft observations did not reveal systematic biases in HIRLAM, but in individual cases the surface temperature, wind speed and direction were strongly biased, and the latent heat flux was unrealistically large in HIRLAM.

The low-level jets (LLJ) were addressed in three studies: an analysis of the rawinsonde sounding data, a comparison with HIRLAM results, and a case study based on aircraft observations and mesoscale modelling. According to the sounding data from six stations, the LLJs can be classified to five categories with a characteristic structure and a most probable generation mechanism in each. In HIRLAM, particularly in the 24-h forecasts, the LLJs were less common than in the observations. This may have resulted from a boundary-layer parameterization producing too much mixing. The mesoscale modelling study supported this conclusion. The case study addressed a jet generated by the inertial oscillations in space, with an influence of baroclinicity in the shape of the wind profile higher in the ABL.

Most of the analyses of the ABL were related to a stable or near-neutral boundary layer. A convective boundary layer was addressed in detail in two cases. On 3 March, the warm surface of the open sea generated an ice-breeze, a mesoscale circulation resembling the classical land-breeze. The ice-breeze was also reproduced by a numerical model. On 5 March, a cold-air outbreak from sea ice to open water took place. The case was documented by an aircraft flight mission and further studied applying two models. In a mesoscale modelling study, it was important to take into account the leads among the sea ice, the counter-gradient transport of heat, a forest in an archipelago crossed by the air flow, and the water vapour condensation into ice crystals. In a large-eddy simulation of the same case, the convection was mostly resolved by the model grid, and the results were comparable to those in the mesoscale modelling study.

The analyses of the ice and surface properties concentrated on the ice motion, remote sensing of the ice and open ocean, and the snow influence in the ice thickness. The remote sensing and ice drifter data gathered during the BALTEX-BASIS experiment demonstrate how useful a combined data set can be. It provides information on ice kinematics, ice leads and ice concentrations of great a value for coupled air-ice-sea model verification studies. The ice drifter data show the typical velocity variance found in semi-enclosed basins with seasonal ice cover, whereas the radar image data show closing and opening of leads and where ice deformation takes place. Consecutive radar images can also be used to derive ice velocity, if roughness patterns are conserved. The ice drifter data verify the SAR velocity estimates. The combined data set improves interpretation and understanding of leads, which governs to a large extent the exchange processes in the air-ice-water system.

The study of the wind forcing on the ice drift showed that in the centre of the Gulf of Bothnia the ice drift was highly wind-dependent, and a linear relationship between the wind and drift velocities explained 80% of the drift's variance. The MESAN wind fields provided an accurate forcing. Close to the coast, internal ice stresses were important, and the modelling of the ice motion was only successful by using a high-resolution (5 km) model with a realistic ice rheology. In general, the improvement in the model results brought by using an accurate wind stress, depending on the thermal stratification and ice conditions, was comparable to that achieved by raising the grid resolution from 18 to 5 km.

A study of wind speeds over the open sea on the basis of ERS-1/2 SAR images showed that the method is a good tool for high-resolution wind speed estimation over the sea. The agreement between in situ data and SAR extracted wind speed lies within 2 m/s in the most reliable cases. Since the SAR is sensitive to the wind just above the surface the thermal stratification is important to be taken into account, in particular near coasts. This problem can be handled provided that temperature data are available, e.g. through HIRLAM.

An algorithm for determining sea ice concentration from Radarsat SAR was developed. The algorithm is based on local thresholds, which are partly manually extracted. The algorithm resolves the ice concentration with a resolution of 50 metres, and yielded good results for cases over the Gulf of Bothnia during the BASIS experiment.

A study on the snow influence in land-fast ice thickness revealed that an increased mean snow thickness over a wide area leads to flooding, which increases the ice thickness via snow-ice formation. Snow thickness variations on smaller scales do not lead to flooding but affect the ice thickness, because the heat transfer through the snow is sensitive to the snow thickness.

The water and heat cycles of the Bothnian Bay were examined on the basis of observations and by using the model PROBE-Baltic. Observed and numerically simulated data from an 18-year period (1981-1998) were first analysed, including temperature and salinity profiles. Secondly, the observed and calculated ice concentration and thickness during the BASIS period were examined. Finally, the heat balance of the Bothnian Bay during the BASIS period was examined. The results can be summarized as follows. (1) The calculated long-term salinity and temperature structure are stable and in good agreement with observations. (2) The calculated ice concentration and thickness during the BASIS period were quit close to observations. (3) The Bothnian Bay water body heat balance during the BASIS period showed high temporal variation and with major contributions from the sensible heat flux, the latent heat flux and the net long wave radiation from the open water surface. (4) During the BASIS period the solar radiation as well as the heat flow from water to ice cannot be neglected in the heat balance. (5) From the heat balance calculations it was concluded that on long term mean the Bothnian Bay import heat from the Bothnian Sea.

The eddy-flux measurements below the ice revealed interesting features: the momentum flux at the depth of 5 m from the ice bottom was ten times larger than at the depth of 0.5 m, and the heat flux from the water to the ice was very small, less than  $1 \text{ W m}^{-2}$ . Both these findings indicated the existence of a shallow very stable boundary layer just below the ice. This may be related to an inflow of river water into the sea at the measurements site in Vaasa archipelago. The small water-ice heat flux differs from the basin-scale observations reported



above, and demonstrates that spatial differences may be large not only in the ABL but also in the ocean boundary layer.

### **Acknowledgement**

In thinking up of the project BASIS, Prof. Dr. Peter Lemke, Intitut für Meereskunde an der Universität Kiel, and Prof. Dr. Anders Omstedt, Sveriges Meteorologiska och Hydrologiska Institut, had a role of a primary importance. Prof. Dr. Eberhard Ruprecht, Intitut für Meereskunde an der Universität Kiel and chairman of the BALTEX Working Group on Process Studies, is appreciated for promoting the realization of the project. Prof. Dr. Christoph Kottmeier is acknowledged for his comments in the scientific study plan. We pay our highest tribute to the role and contribution of our past distinguished colleague and project member, Professor Dr. Rainer Roth, Universität Hannover. Finally, we may note that during the BASIS field campaign and the project the cooperation between the various international scientists and institutions was exemplary good.

BALTEX-BASIS was financially supported by the European Commission through contract MAS3-CT97-0117.

## 8. DATA ARCHIVE

The structure of the BASIS Data Archive is shown below.

	FIMR	UHAM	UHAN	UUPP	UUPP / Östergarnsholm	SMHI
<b>1. Atmospheric data</b>						
<b>1.1 Surface layer</b>						
air pressure	1 level, 10 min intervals	1 level, 10 min intervals		1 level, 10 min intervals	1 level	
air temperature	2 + 3 levels, 10 min intervals	2 levels, 1 & 10 min intervals		2 + 3 levels, 10 min intervals	5 + 1 levels	
wind speed & dir	2 + 5 levels, 10 min intervals	2 levels, 1 & 10 min intervals		1 + 1 level, 10 min intervals	5 levels	
rel. humidity	2 levels, 10 min intervals	1 level, 2 sens, 10 min intervals		-	1 level	
sensible heat flux	1 level, 10 min intervals	1 level, 10 min intervals		2 levels, 10 min intervals	3 + 1 levels	
latent heat flux	-	-		-	1 level	
momentum flux	1 level, 10 min intervals	1 level, 10 min intervals		2 levels, 10 min intervals	3 levels	
radiation	2 x Ts-rad SWR up & down 2 x net radiation 10 min intervals	Ta-rad SWR up & down LWR up & down 10 min intervals		SWR up & down LWR up & down, 10 min intervals	SWR up & down	
buoy data	3 x p, 2 x Ta, 1 x V & Vdir, 1 x RH	2 x (p, V, Vdir, Ta, RH)				
Cloud data	total cover once an hour during daylight, rainfall	Total & various level cover Once an hour during daylight Base height and thickness, 10 min		total cover during soundings	rainfall	
<b>1.2 Radiosonde soundings</b>	FIMR, UHAM, UHANN: 1 station; p, Ta, V, Vdir, RH profiles up to 10 km, 2 second resol.					
	R/V Aranda	Kokkola	Merikarvia	Umeå V and Vdir from pibals up to 2 km with 25 m resol.		Sundsvall & Kallax, data from standard levels
<b>1.2 Airborne data</b>		p, Ta, V, Vdir, RH profiles, 1 s aver. (p, Ta, V, Vdir, RH, $\tau$ , H, LE, SWR $\uparrow$ , LWR $\downarrow$ ) horiz. leg averages, time, position				
		Falcon	Helipod, except no radiation			

	FIMR	SMHI	UHOK
<b>2. Ice and Surface Properties</b>			
<b>2.1 Ice Properties</b>			
<b>Ice thickness</b>	along 50 m (L-shape), 10 points, once a day, also water level	along 100 m line, 2 m intervals, every second day	2 thickness gauges, once a day
<b>Ice temperature and salinity</b>	7 profiles, once	2 profiles, 5 cm resolution, every second day, temperature only	
<b>Ice structure</b>			7 tomography cores
<b>2.2 Snow Properties</b>			
<b>Snow Thickness</b>	along 50 m line (L-shape), 10 points, once a day	along 100 m line, 2 m intervals, every second day	
<b>Snow Temperature</b>		8 profiles, 5 cm resolution, every second day	
<b>2.3 Thermistor Stick Air-Snow-Ice-Water</b>	7 thermistors in ice or snow, 2 in water, 2 in air, 10 min intervals	2 m, 12 thermistors, 1 h intervals	5 thermistors in ice or snow, 2 in water, 1 in air, 10 min intervals
<b>2.4 Buoy Data</b>	1 x Argos position 1 x GPS position	3*ARGOS-position, 10 times a day 3*GPS-position, 10 min intervals	
<b>2.5 Radarsat Images</b>		Sub scenes, 50 m resolution	
<b>2.6 Ice concentration</b>		Radarsat data, digitized ice charts (concentration and thickness)	
<b>2.7 Ice Roughness</b>	laser-profilometry data, 7 h	(Radarsat data)	
<b>2.8 Ice Drift</b>	2 buoys; time, location, drift speed and direction	6 buoys, time, location, drift speed and dir.; Radarsat velocity fields	
<b>3. Oceanic data</b>			
<b>3.1 Hydrographic ship CTD</b>	pre-exp. Gulf of Bothnia 38 stations, T,S -profiles past-exp. Bothnian Sea 19 stations, T,S -profiles	pre-exp. Gulf of Bothnia, 22 stations, T,S -profiles	
<b>ice station CTD</b>	T,S -profiles, 12 m, 2 stations, twice a day		
<b>thermistors</b>	1 chain, 12 m, 1 m interval, 10 min.	1 chain: -60 - -120 m, 2 m interval, 1h 1 chain: 12 m, 1 m interval, 30 min	T & S at -0.05 and -0.35 m, 15 min
<b>3.2 Currents</b>			
<b>Mechanical</b>	at -2 & -13 m, 10 min.		
<b>ADCP</b>	at 1-m intervals, 10 min		
<b>3.3 Turbulence</b>			3 instrum.: -0.15, -0.5, -5 m fluxes of heat, momentum, and salinity, T, S and current comp., 15-20 min averages

<b>4. Supporting data</b>		
<b>Coastal meteorological stations:</b>	8 FMI Stations	Atmospheric pressure, air temperature, wind speed and direction
	SMHI Stations	Atmospheric pressure, air temperature, wind speed and direction
<b>Mareographs</b>	3(-5) FIMR Stations	hourly sea level
	3(-5) SMHI Stations	hourly sea level

## 9. LIST OF PUBLICATIONS

### 1998

- Dokken, S., Håkansson, B. and Askne, J., 1998: "Sea ice in the climate system monitored with satellite borne SAR", *Proceedings of 27th International Symposium on Remote Sensing of Environment: Information for Sustainability, Tromsø, Norge, 1 (ISRSE)*, pp. 266-269.
- Launiainen, J., Vihma, T., Brummer, B., Roth, R., Wode, C., Smedman, A-S., Håkansson, B. and Omstedt, A., 1998: "Baltic Air-Sea-Ice Study - a field experiment of BALTEX", *Third European Marine Science and Technology Conference, Lisbon, 23-27 May, An extended abstract in the conference Project Synopses, Volume I: Marine Systems*, pp.354-357.
- Magnusson, M., 1998: Preliminary results from tower and radio-sonde measurements performed in the Northern part of the Baltic Sea during winter conditions. *Proc. BALTEX Second Study Conference, Rugen, Germany, May 1998*, pp. 146-147.
- Mugnier-Pollet, S, 1998: "Retrieval of wind speed over the Baltic Sea from Synthetic Aperture Radar", *Research Report No. 182, Dept of Radio and Space Science, Chalmers University of Technology*.
- Shirasawa, K., Kobinata, K. and Takatsuka, T., 1998: "Measurements of under-ice turbulent fluxes and oceanic boundary layer processes in the Baltic Sea", *Programme and Abstracts of the 21st Symposium on Polar Meteorology and Glaciology*, 25 - 26 November 1998, National Institute of Polar Research, Tokyo, Japan, pp. 70-71.

### 1999

- Launiainen, J. (Ed.) 1999: "BALTEX-BASIS Data Report", *International BALTEX Secretariat, Publication No. 14, 94 pp.*
- Launiainen, J., Cheng B., Uotila J., and Vihma T., 1999: "Air-ice coupling and thermodynamic modelling of sea ice".- In: Pettersson, H., and Rontu, L. (Eds.), *Workshop on Modelling of the Marine-Atmospheric Boundary Layer, Helsinki, 7-8 December 1998, Meri, Report Series of the Finnish Institute of Marine Research, 40, pp. 33-36.*
- Launiainen, J., Vihma T., and Omstedt A., 1999:"Baltic Air-Sea-Ice Study - A field experiment of BALTEX. - In: Järvet, A. (Ed.): *Publications of the Second Workshop on the Baltic Sea Ice Climate, Publ. Dept. Geogr. Univ. Tartu, No. 84, pp. 101-106.*
- Magnusson, M., 1999: "Mesoscale circulations observed in a coastal area during winter conditions", *Preprints of the 13th Symposium on Boundary Layers and Turbulence, 10-15 January 1999, Dallas, Texas, American Meteorological Society, pp. 640-641.*
- Shirasawa, K., Kobinata, K., Takatsuka, T. and Kawamura, T., 1999, "Measurements of under-ice turbulent fluxes and oceanic boundary layer processes in the Baltic Sea - BALTEX/BASIS 1998 Experiment-", *Proc. 14th International Symposium on Okhotsk Sea & Sea Ice and International Workshop on Rational Evolution of Ice Forces on Structures*, 31 January - 4 February 1999, Mombetsu, Japan, 90-94.
- Vihma, T., Uotila, J. and Launiainen, J., 1999: "Observations and modelling of the atmospheric boundary layer over sea ice".- In: Pettersson, H., and Rontu, L. (Eds.), *Workshop on Modelling of the Marine-Atmospheric Boundary Layer, Helsinki 7-8 December 1998, Meri, Report Series of the Finnish Institute of Marine Research, 40, pp. 37-41.*

**2000**

- Cheng, B., Launiainen, J., Uotila, J. and Vihma, T., 2000: "Modelling sea ice thermodynamics in BALTEX-BASIS", *Annals Glaciology*, in press.
- Dokken, S., Håkansson, B. and Askne, J., 2000: "Inter comparison of Arctic sea ice distribution using Radarsat, ERS and SSM/I and *in-situ* data". *Canadian Journal of Remote Sensing*, Vol. 26, No. 6, pp. 521-536.
- Launiainen, J., Cheng, B., Uotila, J. and Vihma, T., 2000: "Turbulent surface fluxes and air-ice coupling in BALTEX-BASIS", *Annals Glaciology*, in press.
- Launiainen, J., Cheng, B., Uotila, J. and Vihma, T., 2000: "Turbulent surface fluxes and air-ice coupling in BASIS", *The 15th International Symposium on Okhotsk Sea and Sea Ice, 6-10 February 2000, Mombetsu, Hokkaido, Japan*, pp. 286-294.
- Launiainen, J., Cheng, B., Uotila, J. and Vihma, T., 2000: "BASIS and air-ice coupling", In: Gustafsson, N. (Ed.) Parameterization of surface fluxes, atmospheric planetary boundary layer and ocean mixed layer turbulence for BRIDGE - What can we learn from field experiments?, *International BALTEX Secretariat, Publication No. 17*, pp. 87-91.
- Launiainen, J., Vihma, T., Brümmer, B., Etling, D., Håkansson, B., Omstedt, A., Smedman, A-S., Magnusson, M. and Shirasawa, K., Baltic Air-Sea-Ice Study (BALTEX- BASIS), *EurOCEAN 2000, The European Conference on Marine Science and Ocean Technology, Hamburg, 29 August - 2 September, 2000, Project Synopses, Vol. I: Marine processes, ecosystems and interactions*, pp. 326-330.
- Lundin, M. and Håkansson, B., 2000: "Time series analysis of SAR Sea Ice Backscatter. Proceedings of a Workshop on Mapping and Archiving of Sea Ice Data - the expanding role of radar", *JCOMM Technical Report No.7*.
- Magnusson, M., 2000: "Modelled and observed phenomena in a marginal ice zone, *14th Symposium on Boundary Layers and Turbulence, Aspen, USA*, pp. 600-601.
- Uotila, J., 2000: "Wind forcing on drifting sea ice during the Baltic Air-Sea-Ice Study", *The 15th International Symposium on Okhotsk Sea and Sea Ice, 6-10 February 2000, Mombetsu, Hokkaido, Japan*, pp. 279-286.

**2001**

- Brümmer, B., Schröder, D., Launiainen, J., Vihma, T., Smedman, A-S., and Magnusson, M., 2001: "Temporal and spatial variability of surface fluxes over the ice-edge zone in the northern Baltic Sea", *Submitted to J. Geophys. Res...*
- Högström, U., Hunt, J.C.R. and Smedman, A-S, 2001: "Theory and measurements for turbulence spectra and variances in the atmospheric neutral surface layer", *Submitted to Bound.-Layer Meteorology*.
- Vihma, T. and Brümmer, B.: 2001: "Observations and modelling of the on-ice and off-ice air flow over the northern Baltic Sea", *Accepted in Bound.-Layer Meteorology*.

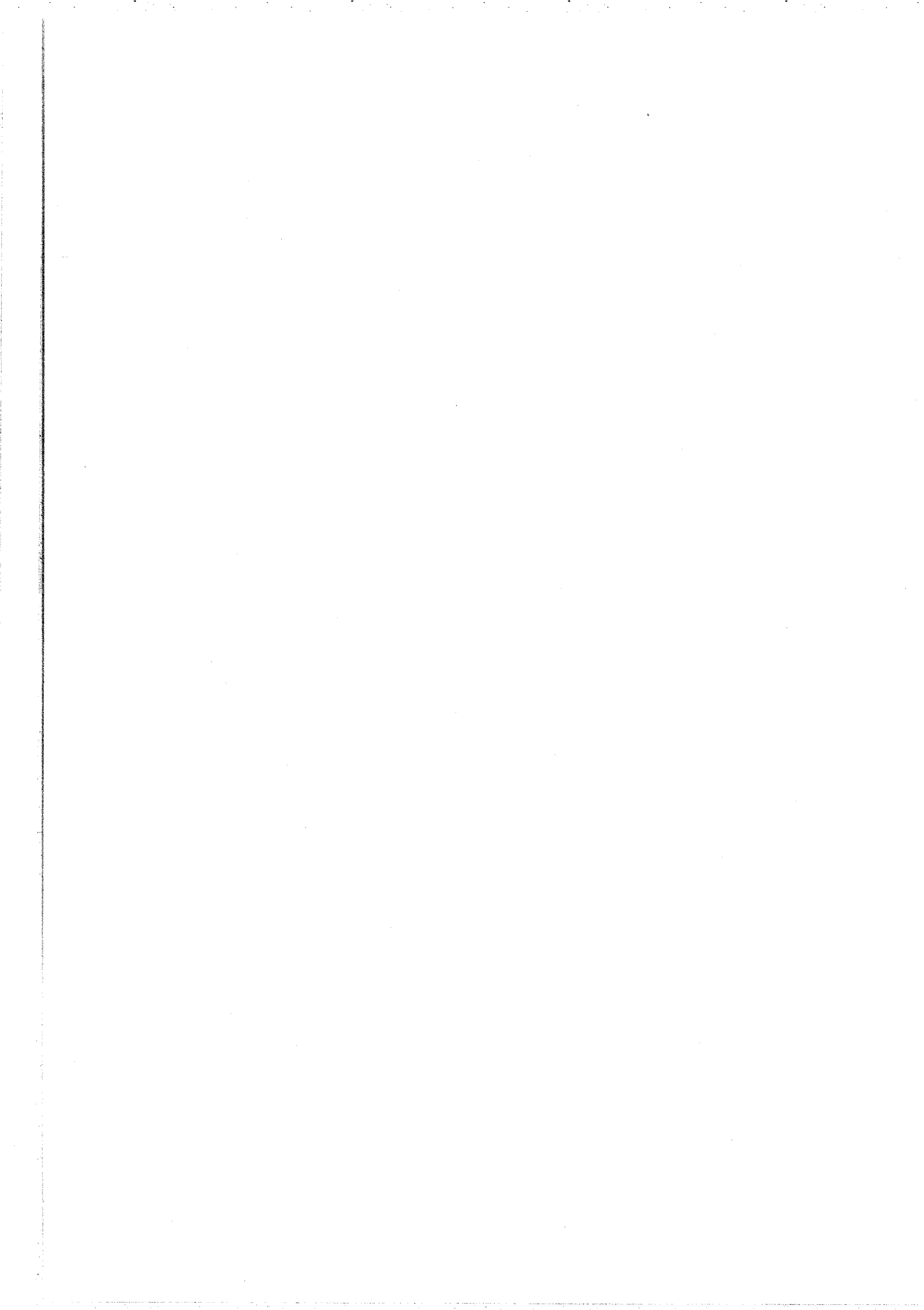
**Theses**

- Cheng, B., 1999: "Calculations of sea ice thermodynamics by an ice model coupled with the atmospheric boundary layer", *Ph. Lic. Thesis, University of Helsinki*. (partially based on BASIS experimental data).

- Kobinata, K., 1999: "Measurements of under-ice turbulent fluxes in the Baltic Sea and the North Water (NOW) polynya region", *Master of Environmental Earth Science Thesis, Graduate School of Environmental Earth Science, Hokkaido University, Japan, February, 1999, 30 p.*
- Rost, J., 1999: "Messungen in der atmosphärischen Grenzschicht über einer Eisfläche des Bottnischen Meerbusens", *Diplomarbeit, Univ. Hamburg, 119 p.*
- Schröder, D., 1999: "Vertikalstruktur und Wärmehaushalt der atmosphärischen Grenzschicht über dem Eisrand der Ostsee: Analyse durch Flugzeugmessungen und Vergleich mit dem Europamodell des Deutschen Wetterdienstes", *Diplomarbeit, Univ. Hamburg, 99 p.*
- Carlsson, M., 2000: "The Stable boundary layer over the ice covered Bothnian Bay", *Master thesis, Department of Earth Sciences, Meteorology, Univ. of Uppsala, Uppsala, Sweden.*
- Dokken, S., 2000: "Sea Ice and Ocean Environmental Applications of Spaceborne SAR", *PhD. Thesis. Dep. of Radio and Space Science, School of Electrical and Computer Engineering, Chalmers University of Technology, Gothenburg, ISBN 91-7197-969-7.*
- Uotila, J., 2001: "Observed and modelled sea-ice response to wind forcing in the northern Baltic Sea.", *Tellus, in press. Part of PhD Thesis, University of Helsinki.*







## International BALTEX Secretariat Publication Series

- No. 1:** Minutes of First Meeting of the BALTEX Science Steering Group at GKSS Research Center in Geesthacht, Germany, 16-17 May, 1994. August 1994
- No. 2:** Baltic Sea Experiment BALTEX – Initial Implementation Plan. March 1995, 84 pages
- No. 3:** First Study Conference on BALTEX, Visby, Sweden, August 28 – September 1, 1995. Conference Proceedings. Editor: A. Omstedt, SMHI Norrköping, Sweden. August 1995, 190 pages
- No. 4:** Minutes of Second Meeting of the BALTEX Science Steering Group at Finnish Institute of Marine Research in Helsinki, Finland, 25-27 January, 1995. October 1995
- No. 5:** Minutes of Third Meeting of the BALTEX Science Steering Group at Strand Hotel in Visby, Sweden, September 2, 1995. March 1996
- No. 6:** BALTEX Radar Research – A Plan for Future Action. October 1996, 46 pages
- No. 7:** Minutes of Fourth Meeting of the BALTEX Science Steering Group at Institute of Oceanology PAS in Sopot, Poland, 3-5 June, 1996. February 1997
- No. 8:** *Hydrological, Oceanic and Atmospheric Experience from BALTEX*. Extended Abstracts of the XXII EGS Assembly, Vienna, Austria, 21-25 April, 1997. Editors: M. Alestalo and H.-J. Isemer. August 1997, 172 pages
- No. 9:** The Main BALTEX Experiment 1999-2001 – **BRIDGE**. Strategic Plan. October 1997, 78 pages
- No. 10:** Minutes of Fifth Meeting of the BALTEX Science Steering Group at Latvian Hydrometeorological Agency in Riga, Latvia, 14-16 April, 1997. January 1998
- No. 11:** Second Study Conference on BALTEX, Juliusruh, Island of Rügen, Germany, 25-29 May 1998. Conference Proceedings. Editors: E. Raschke and H.-J. Isemer. May 1998, 251 pages
- No. 12:** Minutes of 7<sup>th</sup> Meeting of the BALTEX Science Steering Group at Hotel Aquamaris in Juliusruh, Island of RÜGEN, Germany, 26 May 1998. November 1998
- No. 13:** Minutes of 6<sup>th</sup> Meeting of the BALTEX Science Steering Group at Danish Meteorological Institute in Copenhagen, Denmark, 2-4 March 1998. January 1999
- No. 14:** BALTEX – BASIS Data Report 1998. Editor: Jouko Launiainen March 1999, 96 pages

- No. 15:** Minutes of 8<sup>th</sup> Meeting of the Science Steering Group at Stockholm University in Stockholm, Sweden, 8-10 December 1998, May 1999
- No. 16:** Minutes of 9<sup>th</sup> Meeting of the BALTEX Science Steering Group at Finnish Meteorological Institute in Helsinki, Finland, 19-20 May 1999
- No. 17:** Parameterization of surface fluxes, atmospheric planetary boundary layer and ocean mixed layer turbulence for BRIDGE – What can we learn from field experiments? Editor: Nils Gustafsson, April 2000
- No. 18:** Minutes of the 10<sup>th</sup> Session of the BALTEX Science Steering Group in Warsaw, Poland, 7-9 February 2000, April 2000
- No. 19:** BALTEX-BASIS: Final Report, Editors: Jouko Launiainen and Timo Vihma, May 2001

Copies are available upon request from the International BALTEX Secretariat.